

THESIS



This is to certify that the
thesis entitled
MEASUREMENT OF THE STRUCTURE
FUNCTION F_2 IN MUON SCATTERING AT 270 GEV
presented by

ROBERT CHARLES BALL

has been accepted towards fulfillment
of the requirements for

Ph.D. degree in Physics

A handwritten signature in cursive script, appearing to read "J. W. D.", written over a horizontal line.

Major professor

Date October 19, 1979



MSU

OVERDUE FINES ARE 25¢ PER DAY
PER ITEM

Return to book drop to remove
this checkout from your record.

--	--

MEASUREMENT OF THE STRUCTURE FUNCTION F_2
IN MUON SCATTERING AT 270 GeV

By

Robert Charles Ball

A DISSERTATION

Submitted to
Michigan State University
in partial fulfillment of the requirement
for the degree of

DOCTOR OF PHILOSOPHY

Department of Physics

1979

ABSTRACT

MEASUREMENT OF THE STRUCTURE FUNCTION F_2 IN MUON SCATTERING AT 270 GeV

BY

Robert Charles Ball

An experiment has been performed at Fermi National Accelerator Laboratory in which the nucleon structure function F_2 was measured. The experiment took place in the muon laboratory using a 270 GeV μ^+ beam incident on an iron-scintillator calorimeter-target. The primary detection counters used were proportional wire chambers and magnetostrictive wire spark chambers. The spectrometer consisted of toroidally shaped, wire wound magnets interleaved with the spark chambers and plastic scintillator trigger banks. Low angle muons were excluded by the use of veto counters centered on the toroid axis.

The data are compared to the QCD (Quantum Chromodynamics) model of Buras and Gaemers, wherein least squares fits to several parameters are performed. A disagreement with the model is seen in the region of $25 < Q^2 < 50 \text{ (GeV/c)}^2$ where the data events are more copious than the model allows. A threshold of production in the variable W^2 is considered, and dismissed as unlikely. The effect on the data of a variation of the value of $R = \sigma_L/\sigma_T$ is quantitatively examined.

Possible systematic errors in the experiment are checked. Included in the study are variations of the toroid magnetic field and the incident muon energy, and changes in the resolution of the scattered muon energy.

ACKNOWLEDGMENTS

I wish to thank many people for their aid in this endeavor. The members of the experiment were few but able, Adam Kotlewski, Larry Litt, Sten Hansen, Phil Schewe, K. W. Chen (thesis advisor), and particularly Jim Kiley and Dan Bauer, without whose work there would be no accurate monte carlo or data reconstruction programs. Larry Litt in particular has been highly encouraging.

The neutrino area staff at Fermilab deserve thanks for their cheerful faces, and for their aid during crisis situations. The computer center staff at Michigan State University are to be thanked for their unflinching aid (not another box of tapes?!).

I wish to thank Tom Pierce for his concern, advice, mathematical software, and general friendship, and with Mary Brake, for their help in editing this thesis.

Last, but hardly least, I wish to thank Mehdi Ghods for his time and help, and Delores Sullivan for typing this thesis, particularly the beautiful tables scattered throughout.

TABLE OF CONTENTS

Chapter	Page
I. THEORETICAL BACKGROUND	1
A) Introduction: Historical Development	1
B) Early Theorems and the Deep Inelastic Cross Section	4
C) The Move Away from Scaling	9
D) Asymptotically Free Gauge Theories	13
E) A Particular QCD Model	14
F) The Structure Function for Iron	18
II. EXPERIMENTAL EQUIPMENT	22
A) Beam Transport	22
B) Proportional Wire Chambers (PWC)	28
C) Beam Line Scintillation Counters	30
D) The Target	37
E) Wire Spark Chambers (WSC)	39
F) Magnets	44
G) Trigger Bank Counters (TBC)	44
H) Halo Vetoes (HV)	53
I) Beam Vetoes (BV)	53
J) Target Hodoscope	56
K) Fast Trigger Circuitry	56
L) The CAMAC Equipment	65

Chapter	Page
M) On-Line Computing	71
III. DATA EVENT RECONSTRUCTION	78
A) Track Finding	78
B) Program Initialization	86
C) The Momentum Fitting	88
D) Program Cross Checks	92
E) Raw Kinematic Distributions	95
IV. THE MONTE CARLO	104
A) Modelling the Data	104
B) Multiple Coulomb Scattering and Energy Loss	104
C) Radiative Corrections	112
D) Wide Angle Bremsstrahlung (WAB) Background .	115
E) Nuclear Fermi Motion	117
F) The Incident Beam	118
G) Computer Program Description	122
H) Event Weighting	129
I) Geometric Acceptance and Resolution . . .	132
V. ANALYSIS PROCEDURE	142
A) Normalization by Flux	142
B) The Filter Program COMPARE	147
C) The Comparison of Data to Monte Carlo . .	153
D) The Construction of $F_2(x, Q^2)$	160
E) Systematic Errors	178
VI. CONCLUSIONS	196

APPENDICES	Page
A. PROOF OF EQUIVALENCE OF THE STRUCTURE FUNCTION F_2 AND ITS MOMENTS	203
B. PRESCRIPTION FOR S AND C MOMENT EVALUATIONS	206
C. SUMMARY OF DETERMINED STRUCTURE FUNCTION VALUES	208
D. MAGNETIC FIELD AND INCIDENT ENERGY SYSTEMATICS	220
E. THE TOROID MAGNETIC FIELD	235
REFERENCES	239

LIST OF TABLES

Table		Page
I-1	Definitions of Kinematic Variables	2
I-2	Constants and Best Fit Parameters Used in the QCD Calculation of νW_2	19
II-1	Nominal 270 GeV μ^+ Beam Line Currents	25
II-2	Quadratic Fits to B(I) in 1E4	27
II-3	Some Proportional Chamber Information	29
II-4	z-Positions of all E319 Equipment	33
II-5	Calculation of Average Target Density and Radiation Length	38
II-6	Some WSC Information	42
II-7	Fits to Toroid Magnetic Fields	43
II-8	Quadrant Replacements for TBC and BV Alignment	50
II-9	Alignment Constants for TBC and BV Counters	51
II-10	Some Trigger Signal Definitions	58
II-11	CAMAC Scaler Contents	67
II-12	Visual Scaler Quantities	68
II-13	Contents of the Time-Digital-Converters	68
II-14	Primary Tape Event Block Structure	73
III-1	Acceptable Three-Point Line Types	80
III-2	Single View Line Cuts	80
III-3	Vertex Cuts	80

Table	Page
III-4	Track Quality Standards 81
III-5	MULTIMU Output Tape Format 83
III-6	GETP and GETP2 Output Tape Format 90
IV-1	Cross Section Corrections 105
IV-2	Fits to Ionization Loss 109
IV-3	Beam Tape Format 119
IV-4	Stepping Process Cuts 124
IV-5	Accepted Event Tape Format 125
IV-6	Generated Event Tape Format 126
IV-7	Smeared Event Tape Format 128
IV-8	Third Stage Program Cuts 128
V-1	Beam Distribution Limits 145
V-2	Ordered List of COMPARE Program Cuts . . . 148
V-3	Non-Kinematic Information COMPARE Output Tapes 151
V-4	COMPARE Analysis Tape Format 152
V-5	Bounds of Kinematic Planes Used for Analysis 156
V-6	Maintained Cell Information 156
V-7	Some Values of Resolution in Kinematic Variables 159
V-8	Results of Three Parameter QCD Fits . . . 163
V-9	Total Muon Yield in Monte Carlo Systematic Checks 183
V-10	Effect of Changing E' Resolution 190
V-11	Calculation of Average Nucleus, Nucleon Content 192
V-12	A List of All Examined Systematic Error Possibilities 194

Table		Page
C-1	F_2 in Parametric Q^2 Regions	209
C-2	F_2 in Parametric x Regions	215
D-1	E' Comparison	221
D-2	θ Comparison	224
D-3	Q^2 Comparison	226
D-4	x Comparison	228
D-5	W^2 Comparison	231
E-1	Integral Field Measurements in Spectrometer Magnets	237

LIST OF FIGURES

Figure	Page
I-1. Muon-Nucleon Scattering Feynman Diagram . . .	5
I-2. Early SLAC Scaling Data	10
I-3. FNAL Exp 26 Data/Monte Carlo Ratios	11
I-4 Sea and Valence Quark Distributions from QCD	20
II-1. N1 Beam Transport System	24
II-2. Experiment Apparatus	31
II-3. E398 Hodoscope Diagram	36
II-4. TBC Diagram	46
II-5. Trigger Bank Counter Overlap	47
II-6. Geometry of Displacement of Circle of Radius R	49
II-7. Halo Veto Diagram	54
II-8. Target Hodoscope Cross Section Diagram	55
II-9. Fast Logic Schematic	60
II-10. FNAL Timing Pulses	63
II-11. CAMAC and Computer Gating Schematic	64
II-12. CAMAC Crate Contents	66
II-13. DCR Bit Latch Contents	69
III-1. MULTIMU Program Organization	79
III-2. GETP and GETP2 Program Organization	89
III-3. Contour Plot of MULTIMU Inefficiency	96

Figure	Page
III-4. Raw Q^2 Data Distribution	97
III-5. Raw ω Data Distribution	98
III-6. Raw E' Data Distribution	99
III-7. Raw θ Data Distribution	100
III-8. Raw x Data Distribution	101
III-9. Raw W^2 Data Distribution	102
IV-1. Radiative Process Diagrams	113
IV-2. Triangular Region Contributing to Radiative Correction	113
IV-3. Contour Plot of Radiative Correction Weight Factor	114
IV-4. Contour Plot of Wide Angle Bremsstrahlung Background Factor	116
IV-5a. Data Beam Distribution and Comparison to Monte Carlo	120
IV-5b. Data Beam Distribution and Comparison to Monte Carlo	121
IV-6. Contour Plot of $1/E'$ Resolution (percent)	134
IV-7. Contour Plot of Theta Resolution (mrad)	135
IV-8. Contour Plot of Momentum Fit E' Shifts (GeV)	136
IV-9. Hardware Acceptance Contour Plot	137
IV-10. Software Acceptance Contour Plot	138
IV-11. Contours of Constant Q^2 Values	139
IV-12. Contours of Constant x Values	140
IV-13. Contours of Constant W^2 Values	141
V-1. FLUXSIM Program Results	144
V-2a. $F_2(\bar{x}, \bar{Q}'^2)$ in Parametric Q^2 Regions	165
V-2b. $F_2(\bar{x}, \bar{Q}'^2)$ in Parametric Q^2 Regions	166

Figure	Page
V-2c. $F_2(\bar{x}, \bar{Q}'^2)$ in Parametric Q^2 Regions . . .	167
V-2d. $F_2(\bar{x}, \bar{Q}'^2)$ in Parametric Q^2 Regions . . .	168
V-2e. $F_2(\bar{x}, \bar{Q}'^2)$ in Parametric Q^2 Regions . . .	169
V-2f. $F_2(\bar{x}, \bar{Q}'^2)$ in Parametric Q^2 Regions . . .	170
V-3a. $F_2(\bar{x}', \bar{Q}'^2)$ in Parametric x Regions . . .	171
V-3b. $F_2(\bar{x}', \bar{Q}'^2)$ in Parametric x Regions . . .	172
V-3c. $F_2(\bar{x}', \bar{Q}'^2)$ in Parametric x Regions . . .	173
V-3d. $F_2(\bar{x}', \bar{Q}'^2)$ in Parametric x Regions . . .	174
V-4. Ratio of Data/Monte Carlo vs Raw ω . . .	176
V-5. The Variation of F_2 with Target Mass Effects . . .	179
V-6. Effect of Variation of E_0 and Magnetic Field on E' . . .	184
V-7. Effect of Variation of E_0 and Magnetic Field on θ . . .	185
V-8. Effect of Variation of E_0 and Magnetic Field on Q^2 . . .	186
V-9. Effect of Variation of E_0 and Magnetic Field on x . . .	187
V-10. Effect of Variation of E_0 and Magnetic Field on W^2 . . .	188
VI-1. The Normalized Ratio Data/Monte Carlo vs W^2 .	198
VI-2. Illustration of Effects of Resolution on the Determined Value of F_2 . . .	199
VI-3. Correction of W^2 Ratio by "B High" Results .	200
E-1. $B(R)$ in Spectrometer Toroidal Magnets . . .	238

CHAPTER I

THEORETICAL BACKGROUND

A) Introduction: Historical Development

Lepton-nucleon scattering theory has evolved considerably over the last ten years. A chronological scan of the literature on the subject during this time would first claim⁽¹⁾ that the nucleon (proton or neutron) structure functions, the quantities describing the internal structure of the nucleon, scaled in terms of the variable ω (defined in Table I-1). Scaling means that as $\omega = \frac{2M\nu}{Q^2}$ increases beyond a given value, and in the limit that both $Q^2 \rightarrow \infty$ and $\nu \rightarrow \infty$, the structure functions assume constant values, and can be parametrized for smaller ω solely in terms of ω . Knowledge of ω then determines the value of the structure function independent of the specific value of Q^2 , the mass of the virtual photon exchanged in the interaction. Since as Q^2 increases the effective size of objects which can be probed decreases, an independence of Q^2 means all internal structure which is present has been probed. This feature of the data, with its lack of an obvious mass scale, became known as Bjorken scaling.⁽²⁾ Since the structure functions scaled, the photon was thought to be interacting with

Table I-1. Definitions of Kinematic Variables

$\mu = (E_0, 0, 0, k)$	Incident muon momentum in the Lab frame
$\mu' = (E', k' \sin \theta, 0, k' \cos \theta)$	Scattered muon momentum in a particular reference frame
$p = (M, 0, 0, 0)$	Nucleon momentum in the Lab frame
X	All interaction products other than μ'
$q = \mu - \mu'$	Momentum vector of the virtual photon
$\nu = \frac{p \cdot q}{M} = E_0 - E'$	Energy of the virtual photon in the Lab frame
$q^2 = -Q^2 = -4E_0 E' \sin^2 \frac{\theta}{2}$	
$x = \frac{1}{\omega} = \frac{Q^2}{2M\nu}$	
$y = \frac{\nu}{E_0} = 1 - \frac{E'}{E_0}$	
$W^2 = (p+q)^2 = 2M\nu + M^2 - Q^2$	The total mass squared of X. The missing mass squared

The metric used in this table is

$$g_{00} = -g_{11} = -g_{22} = -g_{33} = +1$$

$$g_{\mu\nu} = 0, \mu \neq \nu$$

essentially free quarks within the bounds of the nucleus,⁽³⁾ and additionally the quarks were deduced to be pointlike particles. Thus the model of a nucleus built entirely of point-like constituents came into wide acceptance. This model, known as the parton model, also contained the chargeless gluons which bound the whole nucleon together. The gluon presence is necessary because the total fractional momentum carried by quarks and anti-quarks in the nucleus is given by⁽⁴⁾

$$\int_0^1 F_2(x) dx = 0.507 \quad (1)$$

which is significantly less than the value of 1.0 which would have been found if the quarks and anti-quarks were the only particles present. Obviously then, upwards of 50% of the nucleon momentum must be carried by the chargeless gluons. ($F_2 = \nu W_2$ is defined by Eqn. I-6 below.)

As more data became available, scaling began to have problems; it began to appear that the data may not scale after all. At first attempts were made to save scaling; after all, simple theories with simple, easily tested predictions have wider appeal than esoteric, difficult to understand theories. Various new scaling variables, such as $\omega' = (2M\nu + M^2)/Q^2$, were tried and all were eventually discarded. Scaling was violated.⁽⁵⁻⁷⁾ Now attempts were made to parametrize structure functions in terms of two variables, e.g., q^2 and ν , or q^2 and ω , and the asymptotically free gauge theories (Q.C.D. = quantum-chromo-dynamics) began

to rise in popularity. These theories bypass nucleons and try to deal directly with interactions between the quarks constituting the nucleons, not just the three valence quarks, but also a "sea" of quark-anti-quark pairs and the gluon cloud keeping the whole nucleon together.

Today evidence is mounting in favor of these theories, of which there are presently several parameterizations.^(8,9) In this dissertation I will present measurements taken in the scattering of 270 GeV muons from an iron target, and compare these against the predictions of the QCD model of Buras and Gaemers.⁽⁹⁾

B) Early Theorems and the Deep Inelastic Cross Section

At the simplest level, deep inelastic muon-nucleon scattering can be represented (Fig. 1) by the exchange of a photon between the incident muon and one of the quarks constituting the nucleon. The photon is virtual and can therefore have a mass = Q^2 .

The photon-muon vertex is simply understood. All three particles are point-like and the matrix element squared is easily written from quantum electrodynamics (QED) as

$$|M_1|^2 = [(\bar{k}' \gamma_\nu k) * (\bar{k}' \gamma_\mu k)] \quad (2)$$

$$\sigma_{\mu\nu} = \frac{1}{2} m_\mu^2 \sum_{\text{spins}} |M_1|^2 .$$

This contribution to the cross section can be calculated exactly; however, the second vertex, where the interaction

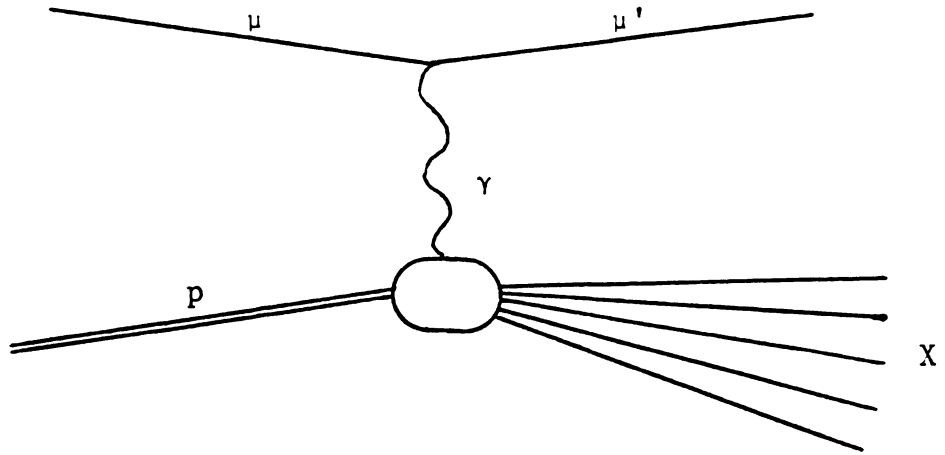


Figure I-1. Muon-Nucleon Scattering Feynman Diagram

is strong in character, is less well understood. In terms of the four-current J_μ , the matrix element describing this vertex is

$$|M_2|^2 \sim \sum_x \langle p | J_\nu | x \rangle \langle x | J_\mu | p \rangle \quad (3)$$

where the sum is over all possible intermediate states x . The matrix element as a whole results from combining Eqns. 2 and 3, and also contains a momentum conserving delta function and the photon propagator. It is then

$$M = k' \gamma_\mu k \frac{1}{q^2} \langle x | J_\mu^{\text{em}}(0) | p \rangle \delta^4(k+p-k'-x) . \quad (4)$$

The hadronic portion of the matrix element squared can be evaluated by defining the Lorentz invariant, covariant tensor $W_{\mu\nu}$ by

$$W_{\mu\nu}(p, q) = (2\pi)^3 \frac{E_p}{M} \sum_x \langle p | J_\nu^{\text{em}}(0) | x \rangle \langle x | J_\mu^{\text{em}}(0) | p \rangle \cdot \frac{\pi}{a} \frac{1}{(2\pi)^3} d^3 p_a \delta^4(p+q-x) . \quad (5)$$

$$q = k - k'$$

This tensor can be expanded in terms of all possible tensor contractions of p and q as

$$W_{\mu\nu}(p, q) = \left(\delta_{\mu\nu} - \frac{q_\mu q_\nu}{q^2} \right) W_1 + \frac{1}{M^2} \left(p_\mu - \frac{p \cdot q}{q^2} q_\mu \right) \cdot \left(p_\nu - \frac{p \cdot q}{q^2} q_\nu \right) W_2 \quad (6)$$

where W_1 and W_2 are the (unknown) nucleon structure functions and describe the combined effect of all the strong interaction vertex corrections. The total inclusive cross section can now be formed by inclusion of a particle flux factor $\left(\frac{|\vec{k}|}{E_0}\right)$, muon normalization factors $\left(\frac{m_\mu}{E_\mu}\right)$ and $\left(\frac{m'_\mu}{E'_\mu}\right)$, the electromagnetic coupling factors $((4\pi\alpha)^2)$, the final muon phase space $\left(\frac{d^3k'}{(2\pi)^3}\right)$ and the extra factor included in the definition of $W_{\mu\nu}\left(\frac{M}{E_p}\frac{1}{(2\pi)^3}\right)$. Combining these factors and Eqns. 2 - 6, it is then

$$d\sigma = \frac{4\alpha^2}{(q^2)^2} \frac{1}{E_0} \ell_{\mu\nu} W_{\mu\nu} \frac{d^3k'}{E'} \quad . \quad (7)$$

By a convenient choice of coordinate system and in the high E_0 limit, we can write

$$\ell_{\mu\nu} W_{\mu\nu} = (ME_0 xy W_1 + E_0^2(1-y)W_2) \cos^2\theta/2 \quad . \quad (8)$$

The cross section can then be written

$$\frac{\sigma^2}{dE'd\theta} = \frac{8\pi\alpha^2 E' \sin\theta}{(Q^2)^2 y} (\nu W_2) \left\{ (1-y) + \frac{MxW_1}{\nu W_2} y^2 \right\} \cos^2\theta/2 \quad (9)$$

or, in terms of the variables x and y

$$\frac{d^2\sigma}{dx dy} = \frac{8\pi\alpha^2}{4ME_0 x^2 y^2} \nu W_2 \left\{ (1-y) + \frac{MxW_1}{\nu W_2} y^2 \right\} \left\{ 1 - \frac{Mxy}{2E_0(1-y)} \right\} \quad (10)$$

The only remaining problem is to separate the contributions from W_1 and W_2 . Although W_1 will contribute most for

very inelastic scattering ($y \sim 1$) at large scattering angles (θ), it can possibly contribute in other kinematic regions as well. One method⁽²⁾ of separation is to consider the scattering of an imaginary photon of mass Q^2 and momentum k (in the nucleon rest frame) from the nucleon p . The total absorption cross section can be separated into two cases, one where the photon is polarized perpendicular (t) to q and p and one where it is longitudinal, or scalar (s). The two cross sections are

$$\begin{aligned}\sigma_t &= \frac{4\pi^2 e^2}{k} W_1 \\ \sigma_s &= \frac{4\pi^2 e^2}{k} \left[\left(1 + \frac{v^2}{Q^2}\right) W_2 - W_1 \right] .\end{aligned}\tag{11}$$

Then the ratio of magnetic to electric structure functions is

$$\frac{W_1}{W_2} = \left(1 + \frac{v^2}{Q^2}\right) \left(\frac{\sigma_t}{\sigma_s + \sigma_t}\right) .\tag{12}$$

Defining $R = \sigma_s/\sigma_t$, the ratio can be written

$$\frac{W_1}{W_2} = \frac{1 + v^2/Q^2}{1 + R} .\tag{13}$$

The differential cross section now becomes

$$\begin{aligned} \frac{d^2\sigma}{dE'd\theta} &= \frac{8\pi\alpha^2 E' \sin\theta \cos^2 \theta/2}{(Q^2)^2 y} \nu W_2 \left\{ 1-y + \frac{Mxy^2}{\nu} \left(\frac{1+\nu^2/Q^2}{1+R} \right) \right\} \\ &= \frac{8\pi\alpha^2 E' \sin\theta \cos^2 \theta/2}{(Q^2)^2 y} \nu W_2 \left\{ 1-y + \frac{1}{2} \frac{y^2}{1+R} \right\} . \end{aligned} \quad (14)$$

Despite several years of effort, too little information is available on the functional form of R . Although it seems that the general trend is for R to decrease as x or Q^2 increases, available data are also consistent with R being a constant⁽¹⁰⁾

$$R = 0.21 \pm 0.10 . \quad (15)$$

Constant values used in the past have ranged from 0.18⁽¹¹⁾ to 0.52.⁽¹²⁾ Also advocated⁽¹²⁾ is the form

$$R = \frac{R_0 \cdot (1-x)}{Q^2} \quad R_0 = 1.20 \begin{matrix} +0.43 \\ -0.36 \end{matrix} (\text{GeV}/c)^2 \quad (16)$$

It is this form which shall be used in the analysis presented in chapter five.

C) The Move Away from Scaling

Early data taken with an electron beam incident on hydrogen and deuterium targets⁽¹³⁾ supported the scaling picture, although to be sure the data did not extend to very high values of ω or Q^2 (Fig. I-2). However, as higher

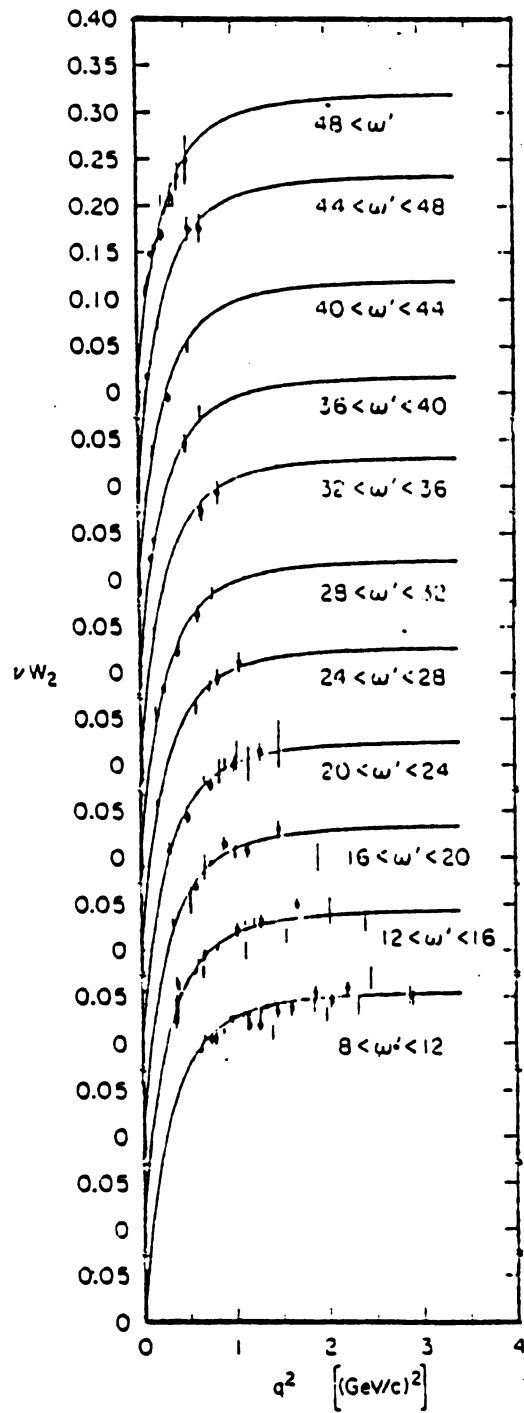


Figure I-2 Early SLAC Scaling Data

$\mu A \rightarrow \mu' + \text{Anything}$
150 GeV and 56 GeV

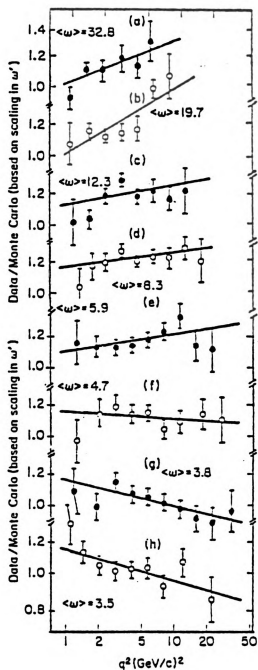


Figure I-3. FNAL Exp 26 Data/Monte Carlo Ratios

energy results began to appear, questions concerning the validity of scaling began to arise. The new data did not appear to be constant at higher values of ω , nor did it appear to be Q^2 independent. Variables such as $\omega' = \omega + \frac{M^2}{Q^2}$, M being the proton mass,⁽¹⁴⁾ were introduced which seemed to give better scaling fits,⁽¹⁵⁾ but doubt over the validity of scaling led to attempts to parameterize the degree of scaling violation in terms of a propagator form in Λ . The structure function would become⁽¹⁶⁾

$$F_2(x, q^2) = F_2(x) \cdot \left(\frac{1}{1 + Q^2/\Lambda^2} \right)^2 . \quad (17)$$

With the event rate expected for this experiment ($\sim 10^{11}$ incident muons), a value of Λ greater than 50 (GeV/c)^2 would have been consistent with scaling at a 70% confidence level level.⁽¹⁷⁾ Finally, μ -Fe data at incident energies of 156 GeV and 56 GeV⁽⁵⁾ were published which left little doubt that scaling was violated (Fig. I-3). Not only was the data Q^2 dependent when compared to a scaling model in the variable ω' ⁽¹⁸⁾, but the dependence changed with the value of ω . For $\omega < 5$, the ratio data events/monte carlo prediction decreased as Q^2 increased, and for $\omega > 5$, the opposite was true. Scaling had been laid to rest.

D) Asymptotically Free Gauge Theories

During this time the asymptotically free gauge theories (ASFT or QCD) were gaining in popularity. These non-abelian theories, when taken to the asymptotic limit ($Q^2 \rightarrow \infty$), approach the free field theories of which the parton models are representative, and could thus conceivably explain the apparent scaling of electro-production data.⁽¹⁹⁾ At first (1970), attempts were made to explain the data using abelian gauge theories, but these were not Ultra-Violet (UV) stable at the origin, so an approach using non-abelian theories was suggested, since these were UV stable. UV stability means the momentum dependent coupling constant, \bar{g} , for the scalar fields in the Lagrangian (e.g., g in $g\phi^4$ where $\bar{g}(g, t=0) = g$) approaches a constant value as $Q^2 (=t)$ approaches infinity, and is strictly increasing as Q^2 decreases from there. The origin refers to the approached constant value being zero.

In gauge theories, the symmetry is traditionally broken at this point, which is the device through which the introduced, vector meson propagators (gluons) would receive a mass. Introduction of Higgs bosons to break the symmetry does not work since either a satisfactory abelian sub-group arises, or the UV stability is lost by attempting the use of larger representations such as $SU(8)$.⁽¹⁹⁾ One possibility⁽²⁰⁾ is that the symmetry is not broken, but is exact, and that a "dynamical" reason exists which does not allow the collision of color singlet particles to produce unpaired color non-singlet particles such as quarks and gluons.

Thus the gluons may remain massless, yet unseen. This allows the use of models such as the $SU(3) \otimes SU(3)$ global symmetry model of Gell-Mann⁽²¹⁾ with three fermion triplets, and an $SU(3)$ color gauge group providing strong interactions.

E) A Particular QCD Model

The QCD model of Buras and Gaemers^(9,22) is just such a model as this. In this model, Q^2 independent quark and gluon density functions ($q(x, Q_0^2)$) are defined at a value Q_0^2 . These are then used as boundary conditions in renormalization group equations to find the functional dependence at any value of $Q^2 > Q_0^2$. The most natural functions arrived at by this approach are the moments

$$\langle q(Q^2) \rangle_n = \int_0^1 dx x^{n-1} q(x, Q^2) ; n \geq 2 \quad (18)$$

whereas experimentalists measure the structure functions. However, a complete knowledge of all moments will yield the structure functions, and vice versa (see Appendix A).

In general, the moments are quite complicated analytic functions, so Buras and Gaemers have used much simpler analytic functions as approximations. They are, however, accurate to within 2% for $x < 0.8$ and $\bar{s} < 1.4$, where

$$\bar{s} = \ln \left(\frac{\ln(Q^2/\Lambda^2)}{\ln(Q_0^2/\Lambda^2)} \right) . \quad (19)$$

The scale parameter Λ characterizes the strength of the scaling violation and is related to the effective gluon coupling constant $\alpha_s(Q^2)$ by

$$\alpha_s(Q^2) = \frac{\bar{g}^2(Q^2)}{4\pi} \frac{12\pi}{(33-2m)\ln(Q^2/\Lambda^2)} \quad (20)$$

m being the number of quark flavors. For $Q^2 \leq \Lambda^2$ this coupling becomes large, invalidating its perturbation theory basis. For this reason, the validity of this QCD formulation is limited to $Q^2 \geq Q_0^2$.

Buras and Gaemers start by defining quark distributions for the valence quarks

$$\begin{aligned} p(x, Q^2) &= p_v(x, Q^2) + \lambda(x, Q^2) \\ n(x, Q^2) &= n_v(x, Q^2) + \lambda(x, Q^2) \\ \bar{n}(x, Q^2) &= \bar{p}(x, Q^2) = \lambda(x, Q^2) = \bar{\lambda}(x, Q^2) \end{aligned} \quad (21)$$

for the SU(3) symmetric non-charmed sea

$$S(x, Q^2) = 6\lambda(x, Q^2) \quad (22)$$

and for the charmed sea

$$C(x, Q^2) = c(x, Q^2) + \bar{c}(x, Q^2) \quad (23)$$

where $\lambda(x, Q^2)$ represents the strange quark density function. Contributions from heavier quarks are assumed negligible, which means $m = 4$ in Eqn. 20 above. Gluons (G) are next

introduced along with the combinations

$$\begin{aligned}
 V_8(x, Q^2) &= p_V(x, Q^2) + n_V(x, Q^2) (=u_V + d_V) \\
 V_3(x, Q^2) &= p_V(x, Q^2) - n_V(x, Q^2) (=u_V - d_V)
 \end{aligned}
 \tag{24}$$

and then the analytic approximations at Q_0^2 are used by defining, at $Q^2 = Q_0^2$

$$\begin{aligned}
 xV_i(x) &= A_i x^{z_1^{(i)}} (1-x)^{z_2^{(i)}} ; i = 3, 8 \\
 xS(x) &= A_S (1-x)^{z_S} \\
 xG(x) &= A_G (1-x)^{z_G} \\
 xC(x) &= 0
 \end{aligned}
 \tag{25}$$

where all z and A are constant. ASFT effects then introduce a Q^2 dependence in the form of the variable \bar{s} defined in Eqn. 19, such that the z and A are now functions of \bar{s} which can be found from the theory.

For the valence quarks, a linear dependence of the z on \bar{s} is used,

$$z_i(\bar{s}) = z_i(0) + z_i' G' \bar{s} \tag{26}$$

where the $z_i(0)$ are evaluated at Q_0^2 using the moments $\langle V_i(Q_0^2) \rangle_n$. Then the slope parameters z_i' are fit to data with the help of the relation

$$\langle V_i(Q^2) \rangle_n = \langle V_i(Q_0^2) \rangle_n e^{-\bar{s} \gamma^n} \tag{27}$$

with γ^n constant and determined by the theory. The valence quark formulations for $Q^2 \geq Q_0^2$ are

$$xV_8(x, Q^2) = \frac{3}{B(z_1(\bar{s}), 1+z_2(\bar{s}))} \cdot x^{z_1(\bar{s})} \cdot (1-x)^{z_2(\bar{s})} \quad (28)$$

$$xV_3(x, Q^2) = xV_8(x, Q^2) - \frac{2}{B(z_3(\bar{s}), 1+z_4(\bar{s}))} \cdot x^{z_3(\bar{s})} \cdot (1-x)^{z_4(\bar{s})} .$$

G' is $\frac{4}{33-2m} = \frac{4}{25}$ which appears in Eqn. 20 for the strong coupling constant. $B(z_1(\bar{s}), 1+z_2(\bar{s}))$ is Euler's beta function, necessary to satisfy the known sum rules

$$\begin{aligned} \int_0^1 dx V_8 &= 3 = \text{total number of valence quarks} \\ &\quad \text{in the nucleon} \\ \int_0^1 dx V_3 &= 1 = \text{number of up quarks minus num-} \\ &\quad \text{ber of down quarks in the proton .} \end{aligned} \quad (29)$$

S , G , and C , describing the sea quark distributions, are strongly decreasing functions of x , becoming nearly insignificant beyond $x = 0.3$. The functions can thus be completely determined on the basis of their first two moments alone. From ASFT then,

$$\begin{aligned} xk(x, Q^2) &= A_k(\bar{s}) \cdot (1-x)^{z_k(\bar{s})} \\ A_k(\bar{s}) &= P_k \cdot \left(\frac{1}{\langle x \rangle_k} - 1 \right) \quad k = S, C, G \quad (30) \\ z_k(\bar{s}) &= \frac{1}{\langle x \rangle_k} - 2 \end{aligned}$$

where P_k is the second parton moment and

$$\langle x \rangle_k = \frac{3^{\text{rd}} \text{ k - moment}}{2^{\text{nd}} \text{ k - moment}} = \text{average } x \text{ for the distribution.}$$

The prescription for the moment evaluation is given in Appendix B. Table I-2 summarizes the values of all constants used along with the best fit values for the valence parameters z_i and for Q_0^2 , and Figure I-4 displays the sea and valence distributions which result.

F) The Structure Function for Iron

With the evaluation of the various parton densities, a value for the structure function F_2 can be calculated. Since iron is a complex nucleus, containing for Fe^{56} 26 protons and 30 neutrons, an average structure function is found. Weighting by the square of the charge of the quarks, we use the prescription for the proton (p) and neutron (n)

$$F_2^{\begin{pmatrix} p \\ n \end{pmatrix}}(x, Q^2) = x \left\{ \frac{5}{18} V_8(x, Q^2) \pm \frac{1}{6} V_3(x, Q^2) \right. \\ \left. + \frac{2}{9} S(x, Q^2) + \frac{4}{9} C(x, Q^2) \right\} \quad (31)$$

and then compute the average F_2

$$F_2(x, Q^2) = \frac{26 \cdot F_2^p(x, Q^2) + 30 \cdot F_2^n(x, Q^2)}{56} \quad (32)$$

Buras and Gaemers have tested their formulation on SLAC ep data⁽¹⁸⁾ and Fermilab μp data⁽²³⁾ for $x < 0.8$ and all $0 \leq \bar{s} \leq 1.4$ and found it to be satisfactorily accurate

Table I-2. Constants and Best Fit Parameter Used in the QCD Calculation of νW_2

Constants:

n	γ^n	γ_+^n	γ_-^n	α_n	β_n
2	0.427	0.747	0	0.429	0.429
3	0.667	1.386	0.609	0.925	0.288

Best Fit Parameters

$Q_0^2 = 2.00$	
$z_1 = 0.70$	$z'_1 = -1.1$
$z_2 = 2.60$	$z'_2 = 5.0$
$z_3 = 0.85$	$z'_3 = -1.5$
$z_4 = 3.35$	$z'_4 = 5.1$

Quantities Derived from Best Fit Parameters

$\langle S(Q_0^2) \rangle_2 = 0.111$	$\langle S(Q_0^2) \rangle_3 = 0.01111$
$\langle G(Q_0^2) \rangle_2 = 0.402$	$\langle G(Q_0^2) \rangle_3 = 0.05738$
$\langle V_8(Q_0^2) \rangle_2 = 0.488$	$\langle V_8(Q_0^2) \rangle_3 = 0.15700$

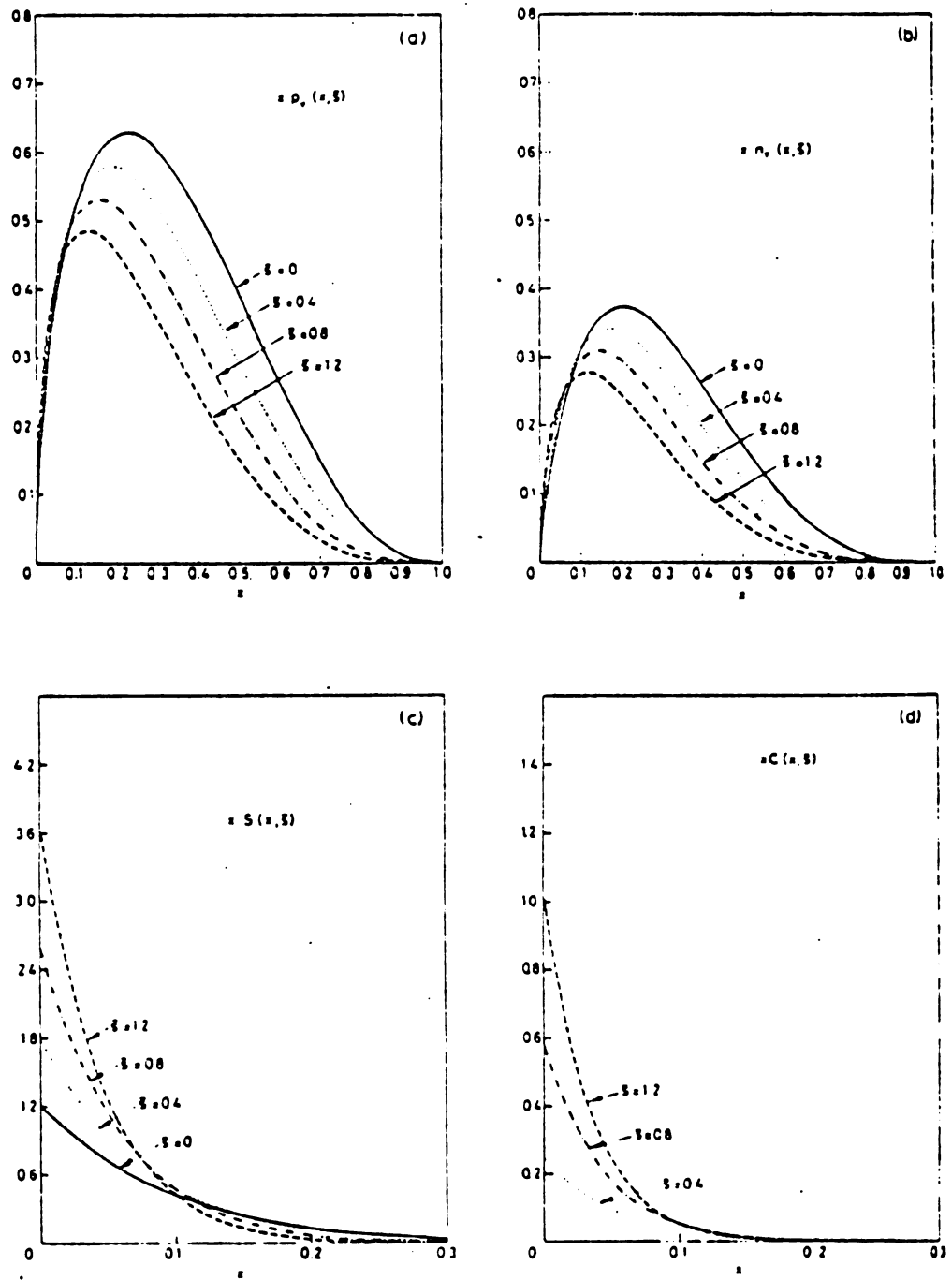


Figure I-4. Sea and Valence Quark Distributions from QCD

(<2% deviation). There is some difficulty for $0.6 < x < 0.75$ where their formulation seems to be flatter when plotted against the SLAC data⁽²⁴⁾ as a function of Q^2 . Speculation is that this is likely due to target mass effects, higher order corrections and higher twist contributions not treated in their analysis. With the parameterization thus completed, we can proceed to compare the model to the data of this experiment.

CHAPTER II

EXPERIMENTAL EQUIPMENT

A) Beam Transport

The muon beam we used was derived from a secondary proton beam at 400 GeV, slowly extracted from the main ring at Fermilab. These protons, approximately 10^{13} spaced in "buckets" over a 1.8 second period, were directed onto an aluminum oxide production target .75" in diameter and 12" long. This target and its associated focusing and bending magnets used to produce muon beams are known as the "triplet train." The name comes from the mounting of the equipment atop movable cars situated on tracks and the fact that, in this configuration, there are three extra sets of focusing quadrupole magnets. The "buckets" refer to the accelerating peaks of the RF of the main proton ring, 53.1 MHz. This gave a bucket spacing of 19 ns. Most buckets, obviously, were empty; however, when not empty, they usually contained only one muon. Exceptions to this rule which showed up in later analysis were thrown out of the data sample.

Preceding this 1.8 sec. "live" beam period were approximately 8 sec. of "dead" time during which protons were injected into the main ring and accelerated to their peak energy of 400 GeV. At this point the extraction began.

Protons not scattered from the production target were deposited in a beam dump, while the remainder of the charged particles (positive or negative, depending on the "train" magnet polarities) were steered into the beginning of the N1 beam line.

This first portion of the N1 line consisted of a "decay pipe," a 300 m. long region where the particles (mostly pions with about 10% kaons) could decay into the desired muons. Entering enclosure 100, the first of four momentum selections via dipole bending magnets was made. Only those particles with the desired 270 GeV/c momentum were transported. After a second bend, the beam was directed thru approximately 60 feet of polyethylene, which absorbed all but a minute fraction of the pions, kaons, and protons, all strongly interacting particles, which had contaminated the beam up to this point. The resultant beam had a μ/π ratio of 4×10^8 , and was only very slightly dispersed by its traversal of the polyethylene.

Two further bends and a bit of focusing brought the beam into the muon lab and to the experimental target. Of the 10^{13} protons which left the main ring, approximately 600,000 usable muons reached the target in what we defined as the beam.

We directly controlled the currents in many of the magnets in the transport system and on the triplet train thru a MAC computer connected to a CAMAC serial branch highway. Using this feature, several SWIC's (Single

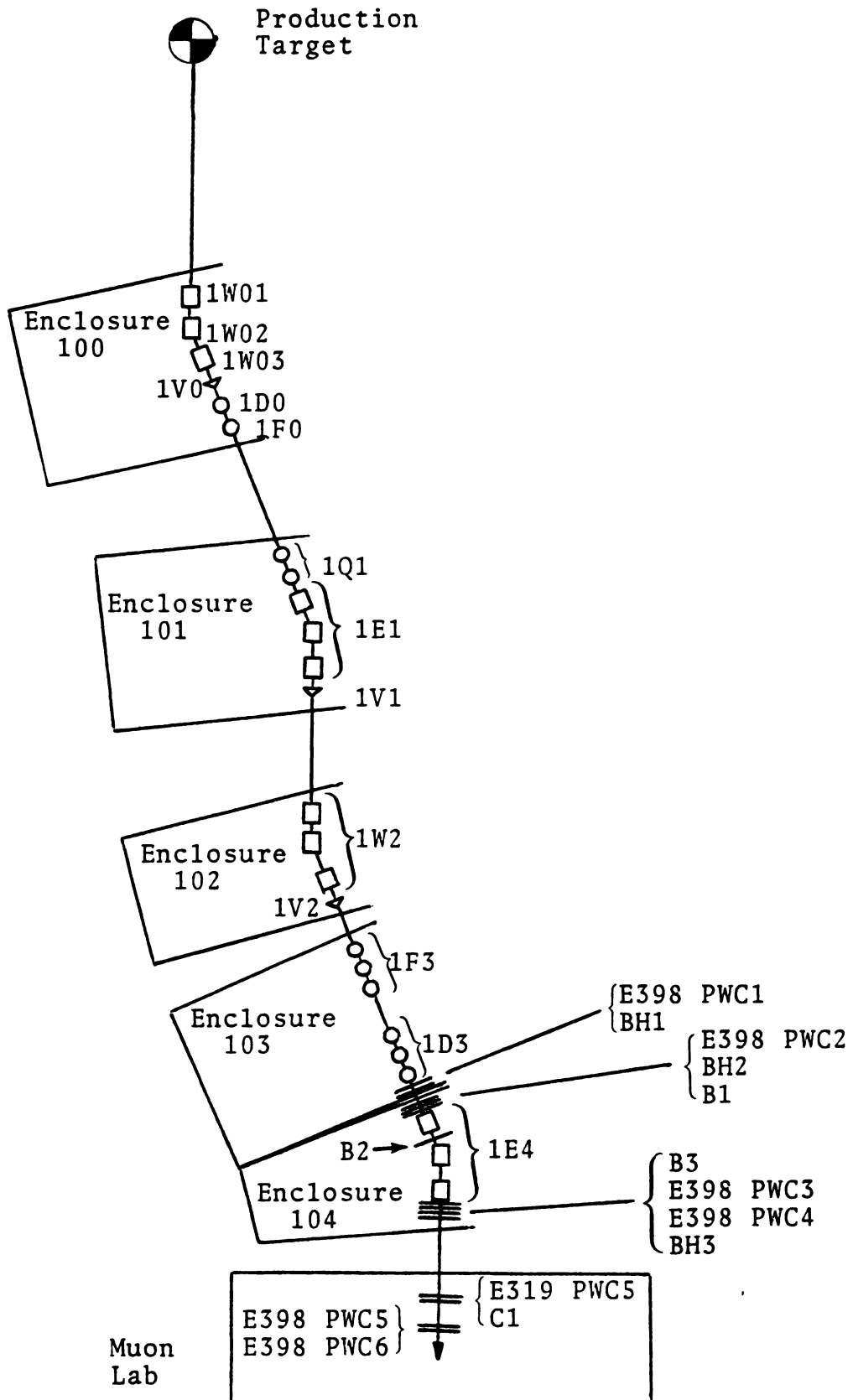


Figure II-1. N1 Beam Transport System

Table II-1. Nominal 270 GeV μ^+ Beam Line Currents

Magnet	Parity	Set Current	Actual Current (AMPS)
Triplet Train			
OUT	0	174.9990	173.0
OVT	0	32.0000	32.0
OHT	1	120.9990	117.5
OFT1	1	96.2248	92.6
OFT2	1	95.5998	92.5
ODT	0	3102.0200	2982.0
OPT	0	3077.0200	2955.0
OPT3	0	3227.0200	3110.0-3115.0
N1 Beam Line			
1W01	0	0.0000	4630.0
1W02	0	4332.0100	4180.0-4210.0
1W03	0	4832.0100	4630.0
1V0	0	25.0000	1.9375
1F0	1	370.0120	361.5
1D0	1	370.0120	354.0
1Q1	0	4174.9800	4010.0
1E1	0	3862.0200	3710.0-3720.0
1V1	1	119.9990	67.3-0068.0
1W2	0	3712.0200	3540.0-3550.0
1F3	0	969.9970	947.5
1D3	0	1019.9900	995.0
1E41	0	4319.9800	4237.48
1E42	0	0.0000	4224.0-4227.0

Measurements taken July 2, 1976

Wire Ionization Chambers) and scalers located in the beam, some tuning was available to increase the muon yield. These magnets and their nominal current settings are shown in Fig. II-1 and Table II-1.

In addition to minor adjustments, the complete N1 line could be "scaled" to use a different beam energy, e.g., calibration runs using beam energies as low as 25 GeV were performed. The magnet currents were "scaled" for lower energies than 270 GeV by a linear decrease from the values used at 270 GeV. Spatial smearing of the beam due to magnet saturation made energies higher than 270 GeV impractical.

All muons entering the muon lab in the beam passed thru a series of proportional wire chambers and scintillator hodoscopes (see below) on either side of the final bending magnet, 1E4. Using this counter information, if the $\int B \cdot dl$ for this magnet as a function of the current in the magnet were known, then the energy of each beam muon could be tagged to an accuracy of 0.1-0.8%, depending on precisely which chamber information was available.

Consequently, using a Hall probe with a DVM readout, the magnetic field as a function of depth in the magnet was measured at several current values. The "effective length" of the magnet was calculated on the basis of these measurements to be 18.64 m. This length multiplied by the plateau value of the magnetic field in 1E4 gives $\int B \cdot dl$.

A quadratic fit to the magnetic field as a function of current was used. Two fits were necessary since, after a

Table II-2. Quadratic Fits to B(I) in 1E4.

$$B = a \cdot I^2 + b \cdot I + c$$

I measured in Amps

B measured in Kilogauss

Coefficients prior to August 23, 1976

$$a = -0.5964 \times 10^{-8}$$

$$b = 0.3289 \times 10^{-2}$$

$$c = -0.03107$$

Coefficients after August 23, 1976

$$a = -0.1714 \times 10^{-7}$$

$$b = 0.3364 \times 10^{-2}$$

$$c = -0.03279$$

one month shutdown in July, the magnet had been slightly modified. The two fits were $B = a \cdot I^2 + b \cdot I + c$. The fit values are given in Table II-2.

Muons with insufficient information to determine their energy were assigned the value 270.00. This occurred on approximately 7% of the raw triggers before August 23, and on less than 1% after August 23. The difference is due to a PWC timing problem corrected during the one month shutdown.

The average energies determined by this method were 268.6 GeV for the μ^+ runs, and 267.6 GeV for the μ^- runs (those after August 23).

B) Proportional-Wire Chambers (PWC)

Two different sets of PWC's were used in this experiment, each with one bit/one wire read-out. The first, designated E319 chambers, were on loan from Cornell University. Construction details can be found in the thesis of Y. Watanabe.⁽²⁵⁾ The gas mixture used in these chambers was Isobutane (20.0%)-Methylal (3.92%)-Freon 13B1 (0.263%)-Argon (balance), vented to the exterior of the Muon lab after circulation. Since no delay circuitry was used for the signals, a fast-logic pre-trigger was used to initiate the recording, in 16 bit CAMAC latches, of the wire information. Two signals were involved; the first, called P.C. Reset, cleared previous information from the latches, the second, called P.C. Enable, enabled them to receive new information during the length of the signal. Three of these

Table II-3. Some Proportional Chamber Information

PWC	Location (cm)	No. of Planes	Orientation*	Size of Planes Edge to Edge (cm)
-----	---------------	---------------	--------------	----------------------------------

A) E319 Proportional-Wire-Chamber (PWC)

5	-3685.54	2	-X, -Y	19.2
4	-517.76	3	X, V', W'	19.2
3	-235.35	3	-Y, V, W	19.2
2	625.32	2	-U, V	32.0
1	649.77	2	-X, Y	38.4

*Sign indicates direction in which the numbered wires increase. Also see Fig. II-2.

Wire Spacing = 2.0 mm

Reset Pulse Width = 15 ns

Enable Pulse Width: PWC1,2,3,4 (X,V') = 120 ns
PWC4W' = 86 ns
PWC5 = 80 ns

B) E398 PWC's

1	-15512.95		Y	20.3
2	-8512.30		Y	20.3
3	-6393.49		Y	20.3
4	-6393.49		X	20.3
5	-3294.28		Y	20.3
6	-3294.28		X	20.3

Wire Spacing = 2.12 mm

Reset Pulse width = 20 ns

Enable Pulse Width = 98 ns

chambers were used upstream of the target to record beam information (x-y position and angles and incident energy) and two were downstream, the hadron PWC's, to aid in vertex location and track reconstruction. More information is contained in Table II-3A.

The second set of chambers, designated E398 PWC's, were on loan from the University of Chicago. There were six planes, four measuring horizontal and two vertical displacements, all situated in the beam line. These were used only in determining the beam energy. Readout was identical to that for the E319 chambers.

The E398 chambers were placed precisely on the Fermilab beam line (Fig. II-1), which bends thru an angle of 28.68 mR at beam magnet 1E4. Alignment of the two E398 horizontal chambers downstream of 1E4 with the three E319 beam chambers thus aligned our spectrometer with this assumed axis.

The gas mixture in these chambers was different than that used in our own. It was gas mixture LK152287 supplied by Union Carbide-Linde Division, and consisted of 24.3% CO₂, 0.37% of gas 13B1, with the balance being Argon.

C) Beam-Line Scintillation Counters

Three distinct sets of scintillator counters were used in the muon beam line. The first set were called, "E398 hodoscopes" since they were on loan from the E398, University of Chicago people. There were three sets of these

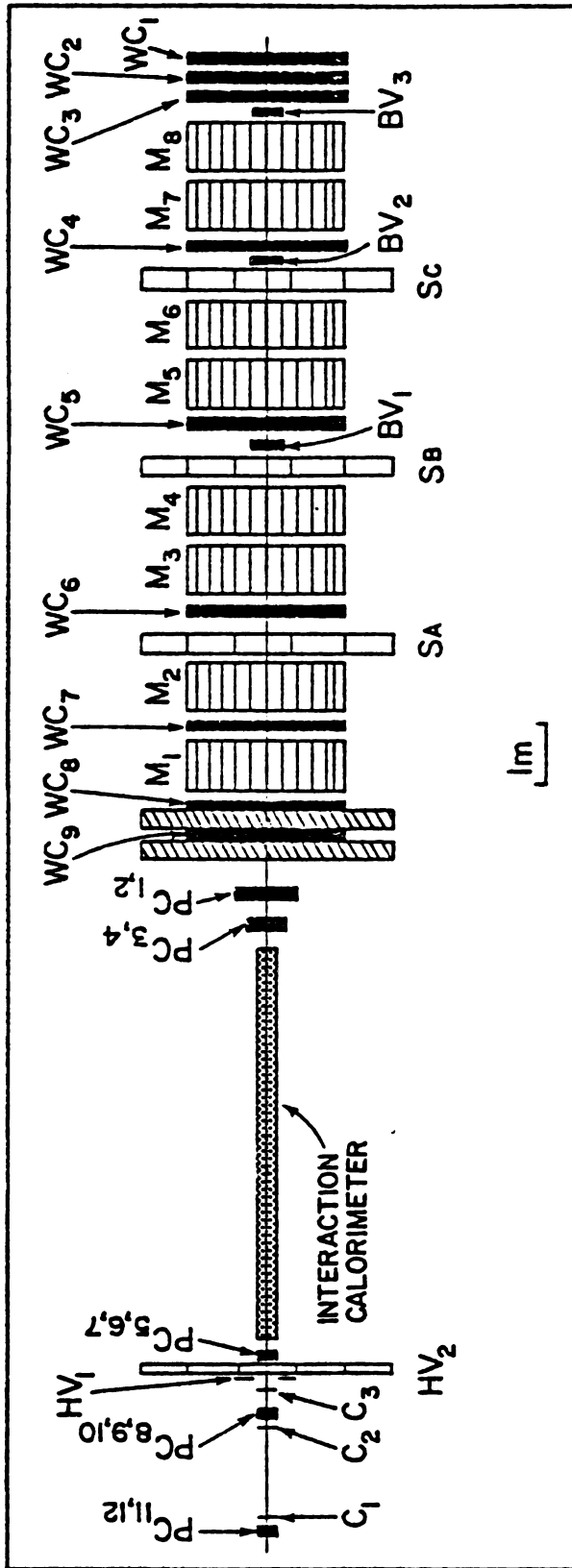


Figure II-2. Experiment Apparatus

Figure II-2. (continued)

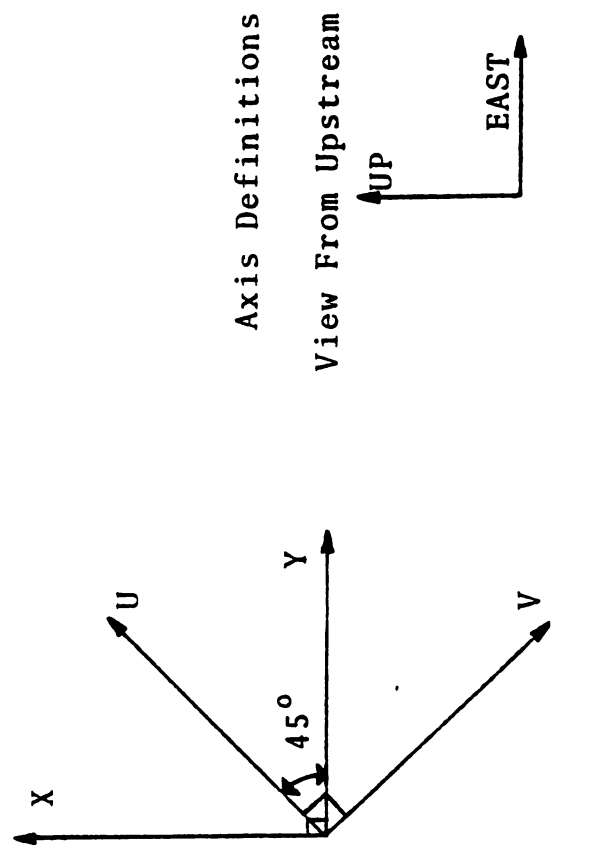
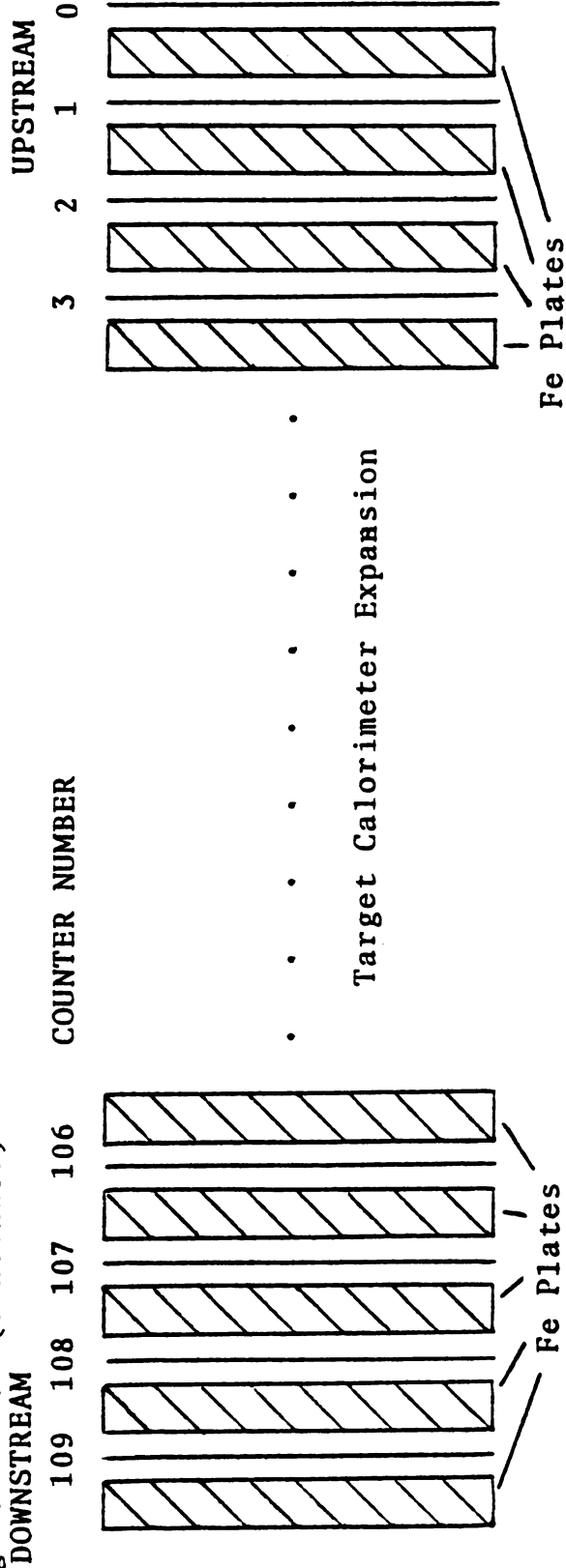


Table II-4. z-Positions of all E319 Equipment (cm)

Equipment		Position
E398	PWC1	-15512.95
	BH1	-15486.28
E398	PWC2	-8512.30
	BH2	-8485.63
	B1	-8450.00
	B2	-7800.00
	B3	-6460.00
E398	PWC3	-6393.49
E398	PWC4	-6393.49
	BH3	-6366.82
E319	PWC5	-3685.54
	C1	-3630.00
E398	PWC5	-3294.28
E398	PWC6	-3294.28
	C2	-525.00
E319	PWC4	-517.76
	C3	-490.00
	HV1	-480.00
	HV2	-400.00
E319	PWC3	-235.35
Target - Calorimeter		-165.74 to 574.14
E319	PWC2	625.32
E319	PWC1	649.77
Hadron - Shield I		736.76 to 798.51
	WSC9	848.68
Hadron - Shield II		869.63 to 902.65
	WSC8	922.02
	M1*	978.54 (79.70)
	WSC7	1035.37
	M2*	1092.68 (79.85)
	SA	1148.87
	SA'	1170.70
	WSC6	1201.42
	M3*	1282.70 (79.06)
	M4*	1370.33 (79.86)
	SB	1427.80
	SB'	1449.87

Table II-4. Continued

Equipment		Position
BV1	WSC5	1464.79
		1478.92
	M5*	1565.59 (79.46)
		M6*
	SC	1710.53
		SC'
BV2		1747.20
BV3	WSC4	1761.49
		M7*
	M8*	1911.19 (79.93)
		1960.36
	WSC3	1988.03
	WSC2	2086.29
	WSC1	2190.43

*Values are center (length)

Key: PWC = Proportional-Wire-Chamber

BH = Beam Hodoscope

B = Beam Telescope B

C = Beam Telescope C

HV = Halo Veto Counters

WSC = Wire-Spark-Chamber

M = Magnet

BV = Beam Veto Counters

S = V Trigger Bank Hodoscopes

S' = H Trigger Bank Hodoscopes

To convert to FNAL coordinates, the Chicago Cyclotron Magnet Center in the MSU coordinate system is $-920.125'' = -2337.12$ cm
 FNAL System = 106523.83'

hodoscope, labeled BH1-BH3, one in enclosure 103, one in enclosure 104, and one in the upstream end of the muon lab (see Fig. II-1). They were used, in conjunction with the E398 PWC's, solely for incident momentum (E_0) determination. Each hodoscope contained eight individual scintillator counters, numbered sequentially from the east starting with one (Fig. II-3). Counter #1 was one-inch wide, while counters 2 thru 8 were 3/4" wide. The alignment of these counters with the rest of the equipment was accomplished by finding the muon track "shadow" of individual counters in the hodoscope on the E398 PWC closest to it (~30 cm). The average beam muon energy determined on the basis of beam hodoscope information only, differs from that determined from the proportional chambers by 0.3 GeV, or 0.1%.

The second set of counters, designated B1-B3 (Fig. II-1), were small scintillator counters (2 1/2" high x 3 1/2" wide) which formed a narrow "telescope" for the incoming muons to enter. Following the "B" counters were the third scintillator counter set, C1-C3. These were somewhat larger than the "B" set (~6" diameter) which allowed the beam to spread spatially as distance from the last beam transport magnet increased. Coincidence of signals from all six of these counters was required for a trigger to be recorded (see II-K).

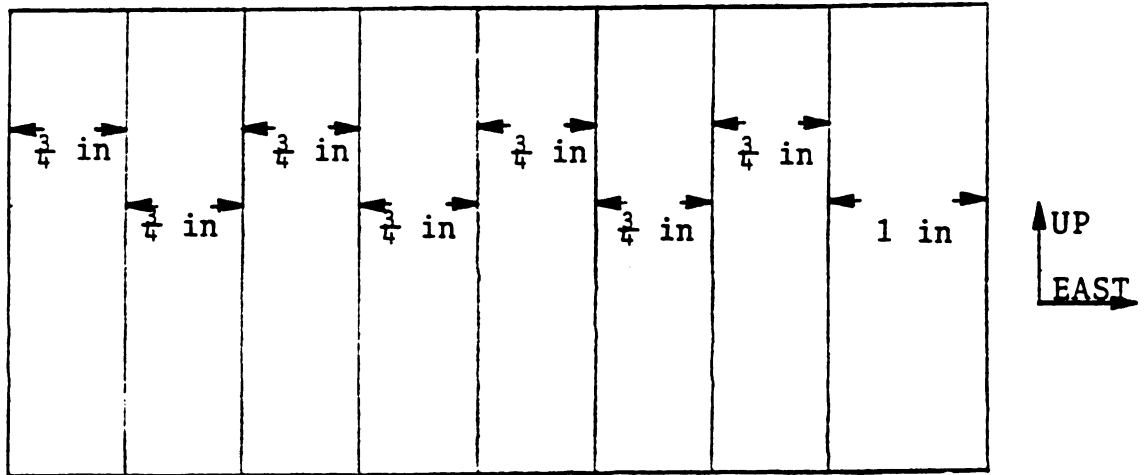


Figure II-3. E398 Hodoscope Diagram

D) The Target

The experimental target, along with most of the remainder of the spectrometer still to be discussed, was mounted on rails for ease of movement. 110--2" x 20" x 20" steel plates sandwiched with scintillator counters and placed on top of two target carts made up the target-calorimeter. The total length of all material in the beam path was 739.6 cm with an average density of 5.741 g/cm³. (Table II-5)

In a deep-inelastic scatter, some of the energy, the "missing mass," goes into the creation of a "shower" of hadrons from the interaction vertex. The calorimeter was designed to measure the energy in this shower, thereby giving an independent measurement of $\nu = E_{inc} - E_{scat} = E_{shower}$. Interactions occurring at the downstream end of the target would occasionally have their showers leave the end of the target. To keep these particles from washing out the spark chamber information with too many sparks or possibly vetoing the event (see Beam Vetoes), the hadron shields were set in place behind the target. This one meter total thickness of steel absorbed the shower's energy before it could reach the spectrometer.

The signals from the calorimeter counters photo tubes, RCA 4340's, were split and read into 220 LRS 2249A, Analog-Digital Converter channels. One of the split signals was monitored directly by the ADC's while the second "hi gain" channel was amplified for better resolution of small signals,

Table II-5. Calculation of Average Target Density and Radiation Length

Material in Each Target Segment			
Material	Thickness t(cm)	Density ρ (g/cm ³)	L _{RAD} (cm)
Fe	1 7/8" = 4.7625	7.870000	1.76
Scintillator	3/8" = 0.9525	1.032000	42.90
Vinyl	2x.015" = 0.0762	1.390000	28.70
Al foil	4x.001" = 0.1016	2.700000	8.90
Air*	.363" = 0.9223	0.001205	30050.00

Total target thickness = 110 segments x 6.7237 cm/segment
= 739.6 cm

*Air gap in each segment varies--it has been adjusted here for agreement with the total measured target length.

$$\langle \rho \rangle = \frac{\sum_i t_i \rho_i}{\sum_j t_j} = 5.741 \text{ g/cm}^3 = 4246 \text{ g/cm}^2$$

$$\langle L_{\text{RAD}} \rangle = \frac{\sum_j t_j}{\left(\sum_i t_i / L_{\text{RAD}_i} \right)} = 2.46 \text{ cm} = 14.1 \text{ g/cm}^2$$

corresponding to few charged particles passing thru this counter. Using these signal pulse heights, the energy of the hadron shower in the inelastic scattering event could be measured directly once suitable calibration measurements were taken.

E) Wire Spark Chambers (WSC)

The primary devices used to record tracks for scattered muons were magneto-strictive wire-spark chambers. There were 36 planes of these chambers interspersed with toroidal magnets in the spectrometer proper (Fig. II-2), 4 planes making up one chamber.

Each chamber was actually made up of two modules, each module containing two planes of wires at 90° to each other. The modules were oriented at 45° with respect to each other in a common aluminum frame, thus giving x, y, u and v planes corresponding to the main spectrometer axes as defined in Fig. II-2.

An event trigger would cause a breakdown in a brass sparkgap at each chamber which would cause a chamber breakdown along the ion trail of a charged particle which had passed thru the chamber. The chamber wire nearest the ion trail would carry the current to one edge of the chamber where it would intersect an orthogonal magnetostrictive wire encased in a plastic catheter. The presence of the current would induce an acoustic pulse in this wire, which, traveling to the wire end, would be picked up, amplified, and sent on to

the CAMAC equipment as a -24 V signal pulse. Two acoustic pulses due to fiducial wires which always carried a current were the first and last pulses on the wand, the name for the assembly containing the magnetostrictive wire and its amplifier. Eight sparks per plane were recordable in this manner. Systematic uncertainties due to changing acoustic pulse propagation velocities, dependent on temperature and state of magnetization of the wand, were minimized by monitoring the fiducial wire locations on a run to run basis and reversing the wand orientations from chamber to chamber. For more information on chamber construction see the Ph.D. thesis of C. Chang.⁽²⁶⁾

The spark chambers were aligned⁽²⁷⁾ by first de-Gaussing⁽²⁸⁾ the toroids and then iteratively fitting sets of straight-thru muon tracks until a change of less than .001 cm was found. Once the relative alignment was set, the toroids were turned back on, and muon tracks of known momentum were fit, iteratively shifting the spectrometer axis and overall orientation until the mean of the χ^2 distribution of the fit was minimized, and the mean momentum of tracks in each spectrometer quadrant agreed within statistical errors.

The first four spark chambers and proportional chambers 1-4 were aligned together using one set of straight thru muons from run 130. The final five spark chambers could not be aligned in this manner because of central dead regions in these chambers 30 cm in diameter. These five chambers were

aligned using muons in runs 113-120 where the beam was purposely defocused. Lines in the front were extrapolated to find sparks in the back five chambers, and hence a new alignment constant. This was iterated until chamber movement became less than .001 cm.

One further problem remained in the relative alignment; x, y, u and v relative orientations were now correct, but the match distributions, defined as⁽²⁷⁾

$$\begin{aligned} \Delta x_{\text{match}} &= \frac{u-v}{\sqrt{2}} - x & \Delta u_{\text{match}} &= \frac{x+y}{\sqrt{2}} - u \\ \Delta y_{\text{match}} &= \frac{u+v}{\sqrt{2}} - y & \Delta v_{\text{match}} &= \frac{y-x}{\sqrt{2}} - v \end{aligned} \quad (1)$$

should have a zero mean, but as it turned out, did not. This was solved by offsetting x and y views in a linear fashion by minimizing the expression

$$\begin{aligned} \text{WSC} &= \sum_{z=1}^9 (\Delta y_{\text{match}})^2 + (\Delta x_{\text{match}})^2 \\ &+ (\Delta u_{\text{match}} + \frac{az+b+cz+d}{\sqrt{2}})^2 \\ &+ (\Delta v_{\text{match}} + \frac{az+b-cz-d}{\sqrt{2}})^2 \end{aligned} \quad (2)$$

where z is the chamber longitudinal position, and $y_{\text{shift}} = az+b$, $x_{\text{shift}} = cz+d$ are the chamber offsets necessitated by the minimization.

Table II-6. Some WSC Information

Active area 73" x 73"

Be-Cu wire 0.005" diameter spaced 0.7 mm apart

Fiducial wire separation 184.15 cm in WSC1-5
182.88 cm in WSC6-9

Gas mixture Ne-He 78-80%
Ar 2-3%
Alcohol 0.7 SCFH @80°F

Wand catheters contain Ar

Spark gaps contain N₂

Time from trigger signal to spark gap breakdown 220 ns

Wand Reversal* and Chamber High Voltage

Chamber	Reversal	H.V.	Chamber	Reversal	H.V.
1X	+		6X	-	
1Y	+	8.6 kV	6Y	-	8.6 kV
1U	-		6U	+	
1V	-		6V	+	
2X	-		7X	+	
2Y	-	8.4 kV	7Y	+	7.6 kV
2U	+		7U	-	
2V	+		7V	-	
3X	+		8X	-	
3Y	+	8.4 kV	8Y	-	7.8 kV
3U	-		8U	+	
3V	-		8V	+	
4X	-		9X	+	
4Y	-	7.6 kV	9Y	+	7.4 kV
4U	+		9U	-	
4V	+		9V	-	
5X	+				
5Y	+	7.2 kV			
5U	-				
5V	-				

* + means increasing time counted with increasing displacement

- means decreasing time count with increasing displacement

Table II-7. Fits to Toroid Magnetic Fields

Coefficients	a	c	d	f
M1,M3,M5,M7	12.20	19.92	-0.08357	0.0004346
M2,M4,M6,M8	12.07	19.71	-0.08270	0.0004301

Current = 35 Amps

Average Field = 17.09 kG M1,M3,M5,M7
 17.27 kG M2,M4,M6,M8

$$B(r) = a/r + c + dr + fr^2$$

B in kG

r in cm

As it turned out, there was one problem missed before all the data tapes were momentum analyzed; systematic, linear offset between fit tracks and actual sparks in the y direction for the last six spark chambers were discovered to exist. Refitting all the data would have been exorbitantly expensive, so this shift was simulated in fitting Monte Carlo tracks and determining the final resolution (Sec. IV-I).

F) Magnets

The momentum analyzing magnets in the spectrometer, eight numbered from upstream to downstream and denoted M1-M8, were wire wound iron toroids operating at saturation current levels (~35 A). The toroids were ~80 cm long with an inner diameter of 30.5 cm and an outer diameter of 172.7 cm. Lead loaded concrete filled the inner hole volume not occupied by the wiring.

The radial field dependence was known to within 1% and fit by a polynomial in r, the radial coordinate (Table II-7). Two power supplies were used, one for even, the other odd numbered magnets, necessitating two sets of fit coefficients. For construction and field measurement details, see the Ph.D. thesis of S. Herb ⁽²⁸⁾ and Appendix E.

G) Trigger Banks Counters (TBC)

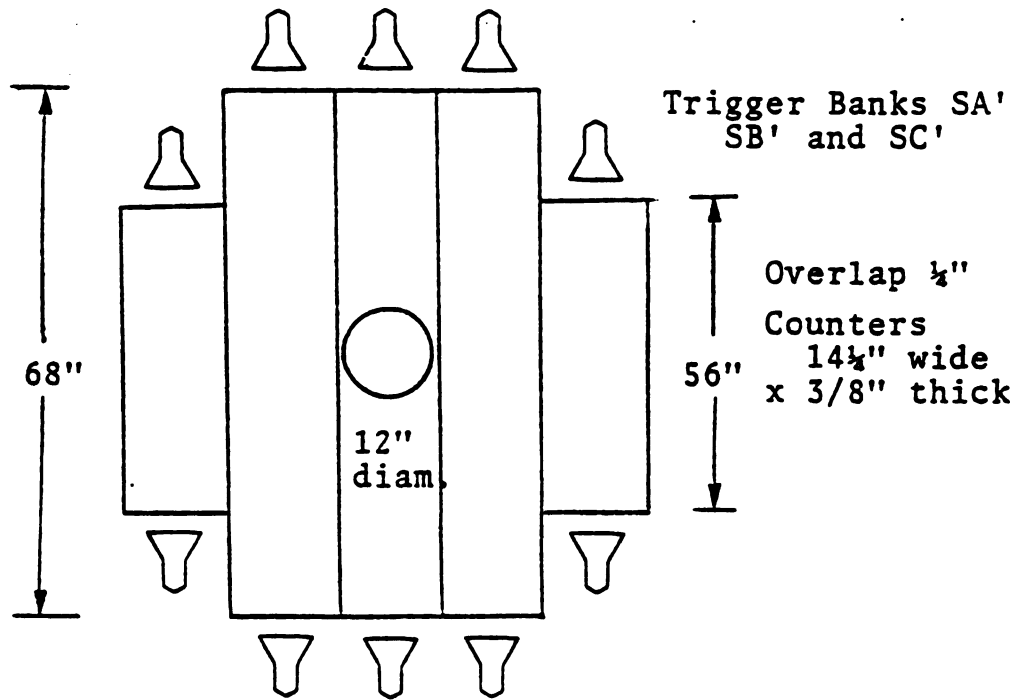
The trigger banks were hodoscopes of scintillation counters roughly circular in shape with a diameter of 180 cm. They were three in number, positioned in the spectrometer

behind magnets M2, M4 and M5, and were centered on the spectrometer axis. The primary function of the trigger banks was their contribution to the hardware trigger; coincident signals from all three banks were required to form "S" in $B \cdot S \cdot \overline{BV}$ (Sec. II-K).

The three banks were designated SA, SB and SC, and consisted of two planes of hodoscopes, one oriented vertically with phototubes at the top and bottom of each counter and designated with a superscript (e.g., SA'), the second oriented horizontally with phototubes at either end and designated with no superscript (e.g., SA). The latter were also known as SAV, SBV and SCV because of their vertical displacement measurements. The primed TBC's were also known as SAH, SBH and SCH because of their horizontal displacement measurements. They were constructed specifically for this experiment. Spatially, the H TBC's were always upstream from the V TBC's.

The V trigger banks contained eight separate scintillators, six of which gave the bank its roughly circular shape, but left a 14" square hole in the center, and two which corrected the center to a circular shape with a 13 1/2" diameter. (Fig. II-4)

The H trigger banks contained only six scintillators since the two center counters were designed to give a central hole diameter of 12". In addition all counters were rectangular in shape so that the primed banks were not circular in cross-section. (Fig. II-4)



All phototubes are Amperex 56AVP

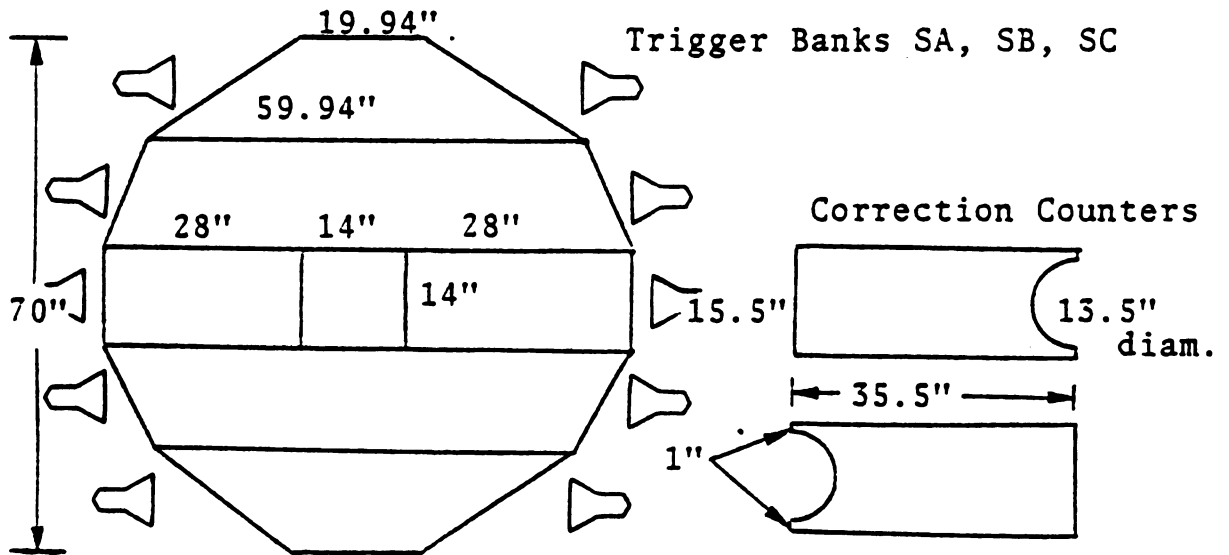


Figure II-4. TBC Diagram

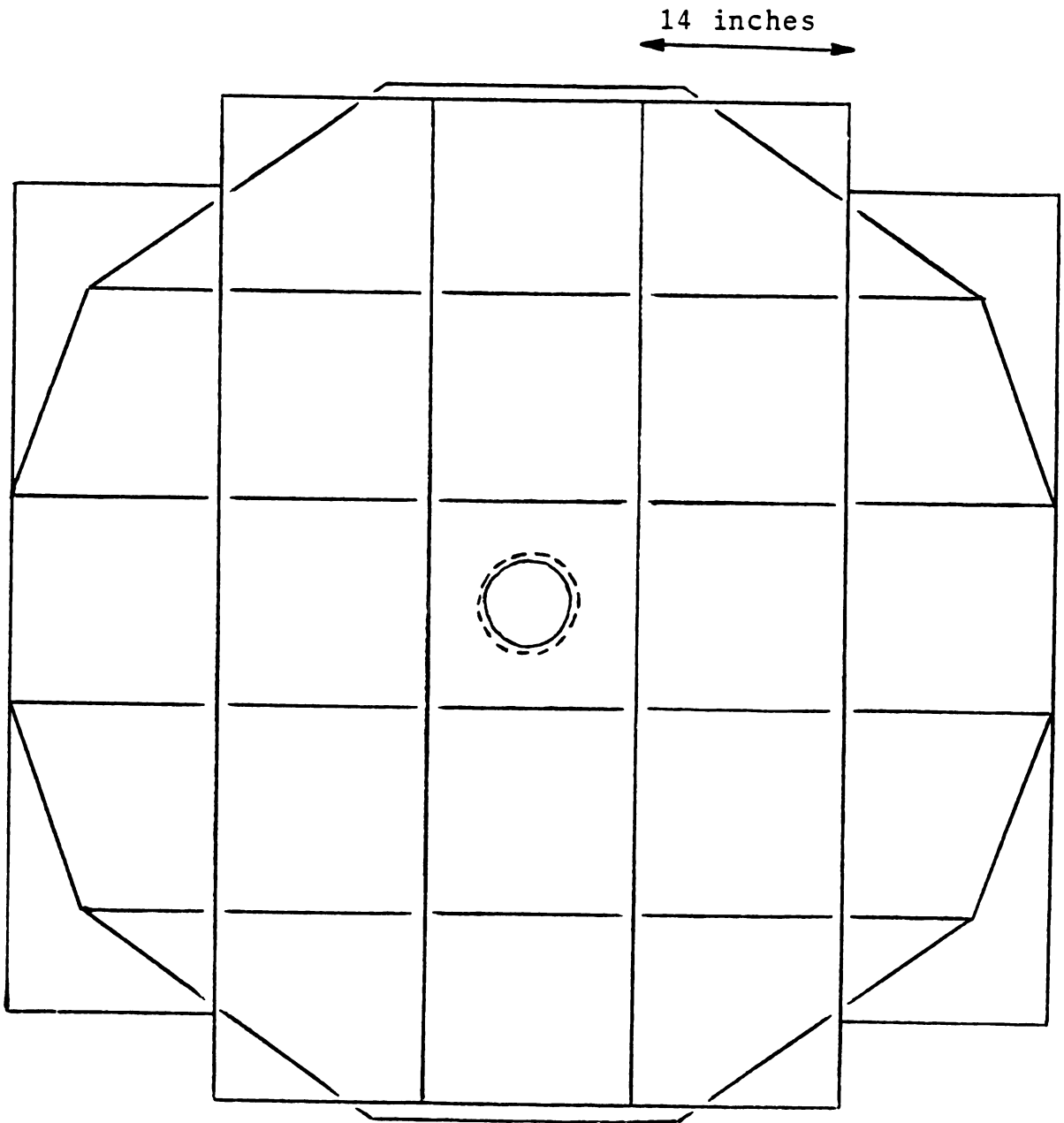


Figure II-5. Trigger Bank Counter Overlap

The software (on-line and off-line) and hardware (after the initial discriminators) treated each bank (primed and un-primed) as if it were only five counters, numbered either from top to bottom, or east to west. Individual phototubes were numbered from 1 to 5 (east and bottom) then from 6 to 10 (west and top) for each bank. The two correction tubes on the center section of the V banks were numbered 11 and 12. The holes in the trigger banks were present so that non-deep-inelastically scattered muons traveling down the spectrometer axis would not trigger the apparatus.

Since the trigger banks were placed on the rails with no special attempt to center them, it was necessary to determine their positions relative to the axis with some alignment procedure. The procedure settled upon was as follows (Fig. II-6): the spectrometer was divided into four quadrants with the intention of measuring the circular coordinates of point B, the trigger bank center, with respect to point A, the spectrometer axis. If a counter in a quadrant recorded a hit, the track radius at the nearest spark chamber to the counter struck was entered in a histogram for that counter/quadrant. The counter position would thus be "shadowed" in the histogram, and the minimum radius in the distribution would correspond to the length of the rays d_1 thru d_4 .

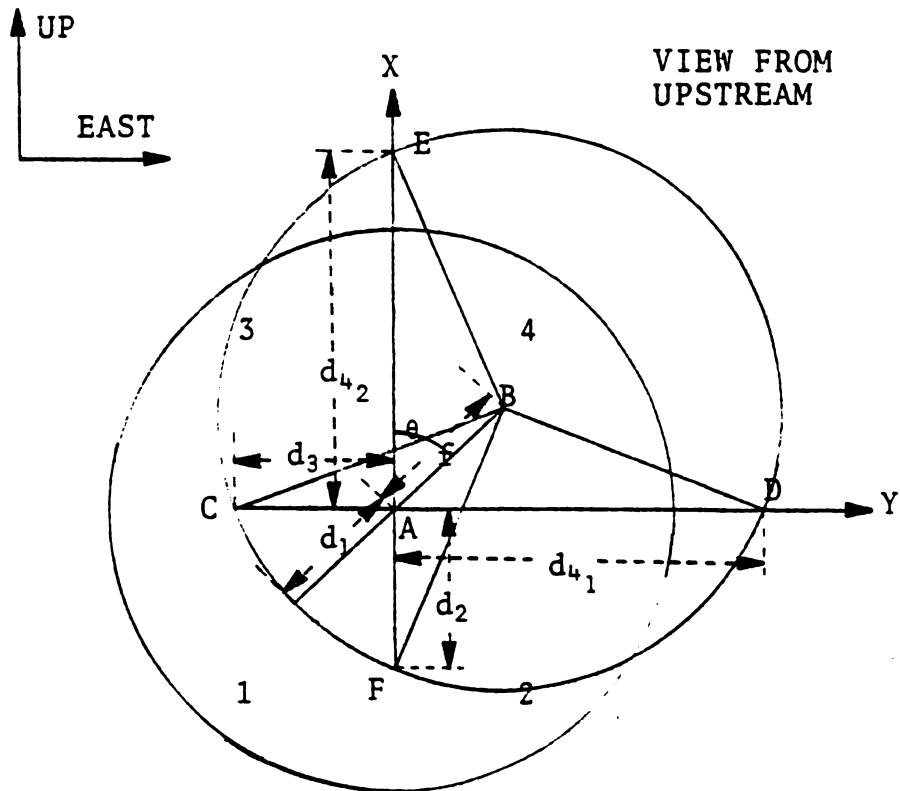


Figure II-6. Geometry of Displacement of Circle of Radius R

Table II-8. Quadrant Replacements for TBC and BV Alignment
 (for quadrants other than four in Equations
 II3-5, the measurements $d_1 \rightarrow d_4$ and θ should
 be replaced as follows):

Quadrant	Replace	With	
		$\theta < 45$	$\theta > 45$
		(measured from c.c.w. quadrant boundary axis)	
2	d_1	d_3	d_3
	d_2 (unused)	d_1 (unused)	d_4 (unused)
	d_3	d_4	d_1
	d_4	d_2	d_2
	θ	$90 + \theta$	$90 + \theta$

3	d_1	d_2	d_2
	d_2 (unused)	d_4 (unused)	d_1 (unused)
	d_3	d_1	d_4
	d_4	d_3	d_3
	θ	$180 + \theta$	$180 + \theta$

1	d_1	d_4	d_4
	d_2 (unused)	d_3 (unused)	d_2 (unused)
	d_3	d_2	d_3
	d_4	d_1	d_1
	θ	$270 + \theta$	$270 + \theta$

Table II-9. Alignment Constants for TBC and BV Counters
1/30/79

Counter	Displacement f(cm)	Angle °,rad.	X,Y (cm)
SA3	0.53	180, π	-0.53,0
SA2,4	0.44	180, π	-0.44,-
SA'3	1.03	0,0	1.03,0
SA'2,4	--	--	--
SB3	1.10	10.1,0.176	1.08,0.19
SB2,4	0.65	0,0	0.65,-
SB'3	2.13	3.5,0.061	2.13,0.13
SB'2,4	0.38	90, $\pi/2$	-,0.38
BV1	1.16	18.5,0.324	1.10,0.37
SC3	0.72	-24.5,-0.428	0.66,-0.30
SC2,4	0.69	0,0	0.69,-
SC'3	2.20	4.96,0.087	2.19,0.19
SC'2,4	0.41	90, $\pi/2$	-,0.41
BV2	1.58	12.3,0.214	1.54,0.34
BV3	0.31	15.2,0.266	0.30,0.08

Measurement error is 2.5 mm

From the law of cosines, for $\theta < 45^\circ$,

$$R^2 = f^2 + d_3^2 - 2fd_3 \cos(90+\theta) \quad (3)$$

and

$$R^2 = f^2 + d_4^2 - 2fd_4 \cos(90-\theta) \quad (4)$$

Eliminate R from the equations using $R = f + d_1$ and it is found that, purely in terms of the measured quantities,

$\theta < 45^\circ$

$$f = \frac{d_4^2 d_3 + d_4 d_3^2}{2d_1(d_4 + d_3)} - \frac{d_1}{2} \quad (5)$$

$$\sin\theta = \frac{d_1^2 + 2fd_1 - d_3^2}{2fd_3} \quad .$$

For $\theta > 45^\circ$

$$f = \frac{d_4^2 d_2 + d_4 d_2^2}{2d_1(d_4 + d_2)} - \frac{d_1}{2} \quad (6)$$

$$\cos\theta = \frac{d_1^2 + 2fd_1 - d_2^2}{2fd_2} \quad .$$

The center displacement for the non-circular counters, which is also a measure of the T.B. displacement, is easily determined. For the V trigger banks

$$x_{\text{Disp}} = \frac{d_3 + d_4 - d_1 - d_2}{4} \quad (7)$$

and for the H trigger banks

$$y_{\text{Disp}} = \frac{d_4 + d_2 - d_1 - d_3}{4} \quad . \quad (8)$$

Theta can not be determined.

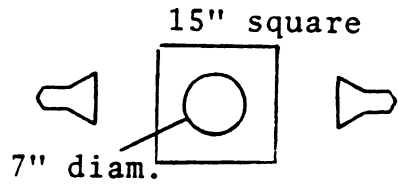
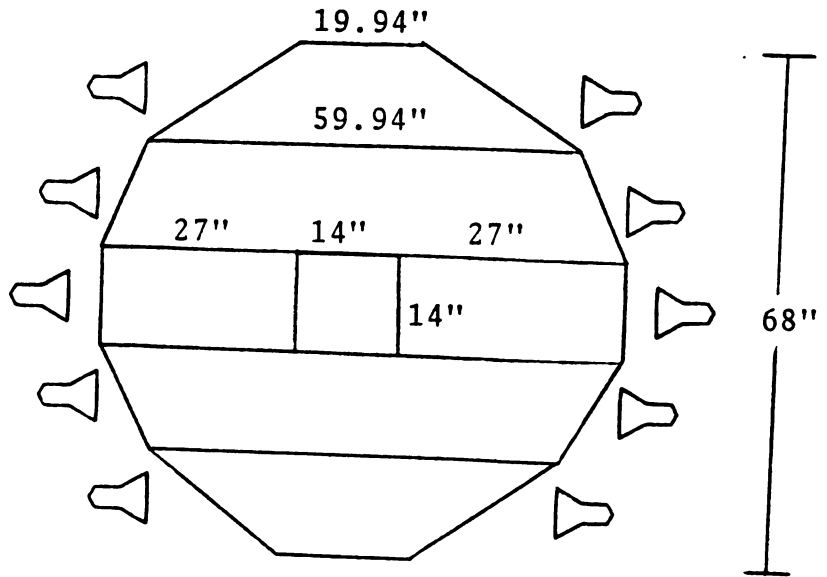
Table II-8 summarizes the variable replacements in the equations for quadrants other than no. 4, and Table II-9 summarizes the displacement determined in this way.

H) Halo Vetoes (HV)

Located between E319 PWC3 and 4 was a bank of scintillator counters equipped with Amperex 56 AVP phototubes known as the Halo Vetoes. Halo, muons outside of the useful beam muon area and extending over the entire cross section of the spectrometer, could fake the hardware into believing a deep inelastic trigger had occurred. Consequently, this bank was installed to introduce a 20 ns dead time for coincidence in the "B" telescope whenever a halo muon was detected by the bank. Muons passing thru the 7" diameter central hole in the bank were considered to be beam muon candidates and were not vetoed in this manner. (Fig. II-7).

I) Beam Vetoes (BV)

Situated on the spectrometer axis behind Magnets M4, M6, and M8 were three 12 1/2" diameter scintillator counters equipped with 56 AVP phototubes known as the Beam Veto counters (BVI-BVIII). These counters were designed to



CORRECTION COUNTERS

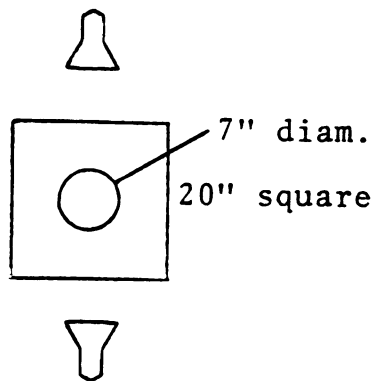


Figure II-7. Halo Veto Diagram

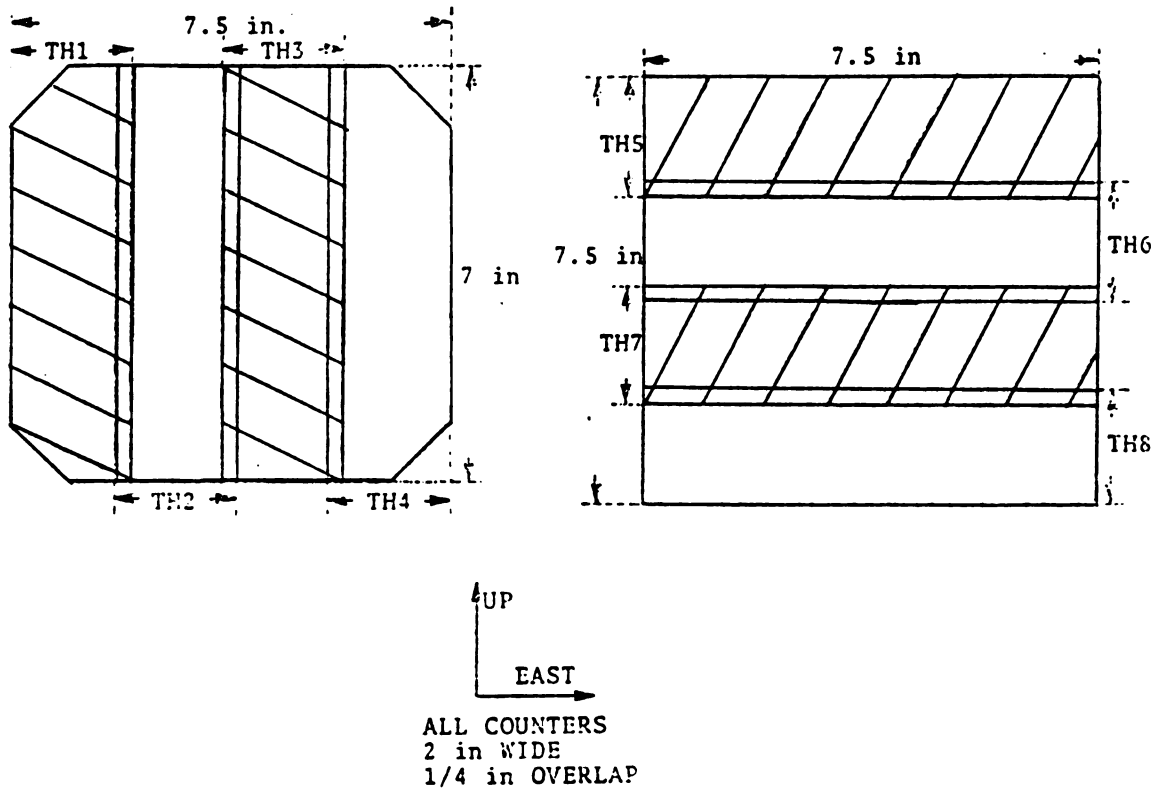


Figure II-8. Target Hodoscope Cross Section Diagram

prevent a trigger from muons which merely went straight down the spectrometer axis. A coincidence between BVIII, the furthest downstream, and either of BVI or BVII was sufficient to set this veto in motion. To prevent accidental vetoes due to shower pions striking the vetoes, the hadron shields were set behind the target and surrounding WSC9, and the toroid holes were filled with lead loaded concrete. The hadron shields also served to protect the front spark chamber information from being washed out by too many sparks.

Since the placement of these counters was done visually, they were aligned in the same manner as the trigger banks were aligned, except that histogram entries were made if the counter did not show a hit.

J) Target Hodoscope

The target hodoscope is the second piece of equipment from which information was never utilized. The hodoscope consisted of eight ~2" scintillator counters, four horizontally and four vertically oriented, overlapping each other by upto half their width (Fig. II-8). The counters could have been used, for example, to eliminate extra beam tracks when more than one beam track was present.

K) Fast Trigger Circuitry

With the target hodoscope, the summary of the data measuring equipment is complete. This equipment would be useless, though, without fast-logic hardware to trigger the

measurement procedure and a means to collect the measurements.

The trigger procedure was accomplished with several racks of NIM-standard electronics located next to the spectrometer itself. Using various "AND" and "OR" logic modules, several signals were defined. (Table II-10). From these signals the primary single-muon trigger, $B \cdot S \cdot \overline{BV}$, was formed. This trigger meant a beam muon was present along with a spectrometer track, but nothing was detected in the toroid hole region. Once formed the trigger signal started the spark-chamber firing sequence, closed the event gate (see below) and scaler gates, and signaled the CAMAC electronics to begin processing.

In addition to this primary trigger, two other triggers were used. The first of these was $B \cdot SD \cdot \overline{BV}$, a multi-track trigger. This trigger required the appearance of more than one track with penetration necessary only as far as the second trigger bank. This trigger did not work well. See the theses of D. Bauer⁽²⁹⁾ and J. Kiley⁽³⁰⁾ (both to be published) for details. The second additional trigger was used for random beam sampling, defined as $B \cdot (P\theta SA)$. This random beam sample was later used as input to the Monte Carlo programs, because the accepted sample of scattered deep-inelastic events depends on the beam distribution used. These three triggers were treated identically in all respects.

Two further triggers were hardware defined, but not used to trigger the data-collection procedure. These were

Table II-10. Some Trigger Signal Definitions

HV	--the logical "OR" of the twelve halo vetoes [HV1@HV2@...@HV12]
C	--the logical "AND" of the telescope counters C1, C2 and C3 [C1.C2.C3]
B104	--the "AND" of the telescope B1, B2 and B3 [B1.B2.B3]
B	--B104.C.HV; if B is present, then a beam muon is entering the target.
BV	--BVIII.(BVI@BVII); the beam veto signal, if present, indicated a muon traveling down the spectrometer axis.
P	--the output of a square wave signal pulser
SA	--the "OR" of the signals from the ten segments of trigger bank A.
SB,SC	--defined similarly to SA.
SAH	--the "AND" of any two segments of the V SA counters.
SAV	--the "AND" of any two segments of the H SA counters
SBH,SBV	--defined similarly to SAH,SAV.
SLH	--SC2@SC3@SC4; a low angle trigger indicator from V trigger bank C
SLV	--SC'2@SC'3@SC'4; a low angle trigger indicator from H trigger bank C
SCH	--SC1@SC5@SC'1@SC'5 a high angle trigger indicator
S	--SA.SB.SC; presence of this signal means a muon has penetrated all three trigger banks; self- vetoing for 200 ns after firing
SL	--SA.SB.SLH.SLV; the low angle signal, indicated the muon trajectory was near the spectrometer axis; also self vetoing for 200 ns.

-continued on next page-

Table II-10 continued

SH--SA·SB·SCH; the high angle signal, indicated the muon trajectory was near the outer edge of the spectrometer.

SD--(SAH⊕SAV)·(SBH⊕SBV); the multi-track signal, indicating simultaneous firing of several counters in trigger banks A and B

PCS--C·(P⊕SA); the fast pre-trigger for collecting P.W.C. information

⊕ is the logical "OR"

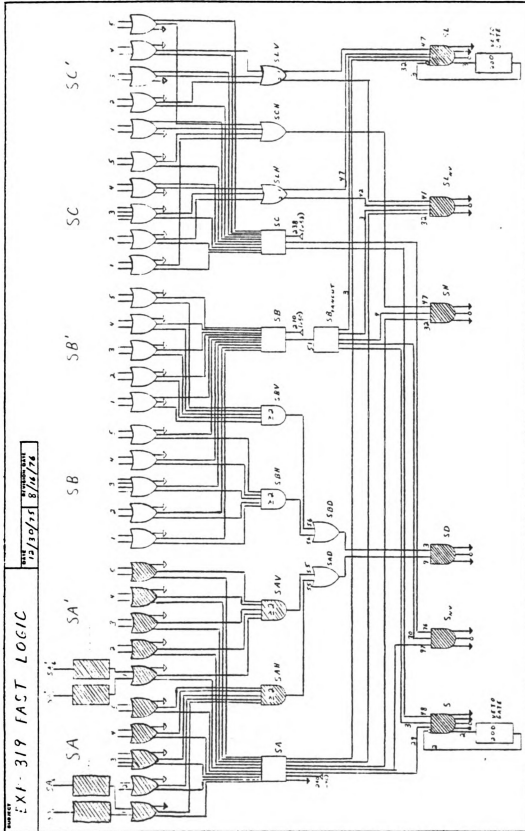
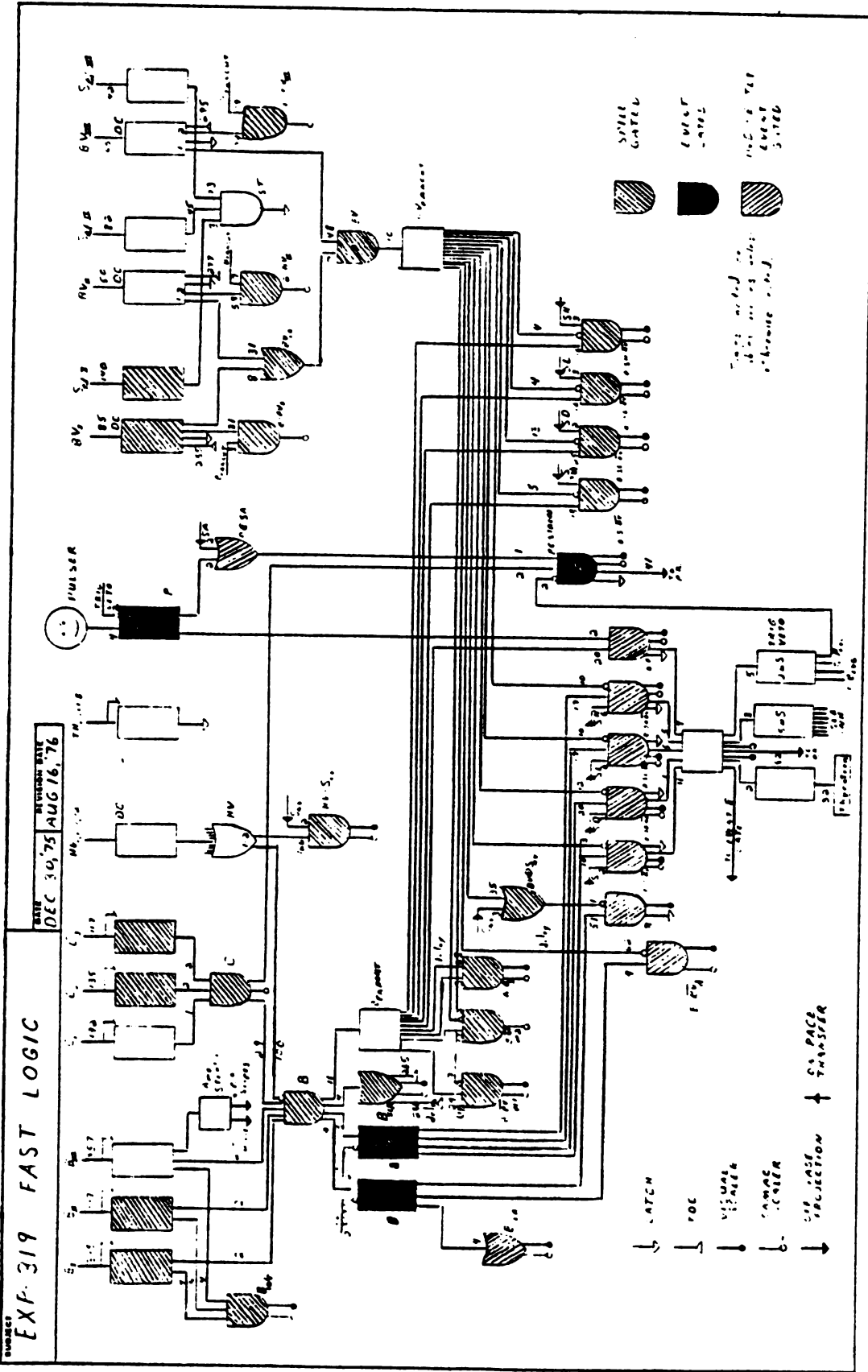


Figure II-9. Fast Logic Schematic

Figure II-9. (continued)



$B \cdot SL \cdot \overline{BV}$, a low- q^2 trigger, and $B \cdot SH \cdot \overline{BV}$, a high- q^2 trigger. These triggers were scaled, and, if in coincidence with one of the active triggers, entered into a CAMAC bit latch (see below).

The electronics were gated on/off (active/inactive) in several different ways. The major gate, called the spill gate, was activated by the Fermilab timing signal T2 (Fig. II-10). This gate which activated all electronics, came on then just before the muon spill was due in the muon lab, and stayed on until just after the muon spill had ended. The remainder of the gates were active only within the time range supplied by the spill gate.

Logical signals S and SL initiated their own 200 ns veto gates. These gates kept the logic from overloading with too high of a signal rate.

In addition to setting the spark-chamber firing sequence in motion, the trigger signal also set up three gates, the scaler inhibit, the event gate, and a trigger veto gate. The scaler inhibit shut down all scalars, CAMAC and NIM, for a period of 5 μ s, thus preventing spark chamber noise from disturbing them. The trigger veto gate prevented a second trigger signal from being formed for a period of 2 μ s, until the event gate was fully closed. The event gate was a 42 ms gate which closed down only trigger-related electronics after a trigger signal was sent out. This dead time allowed the spark chamber capacitors to recharge in preparation for a new trigger.

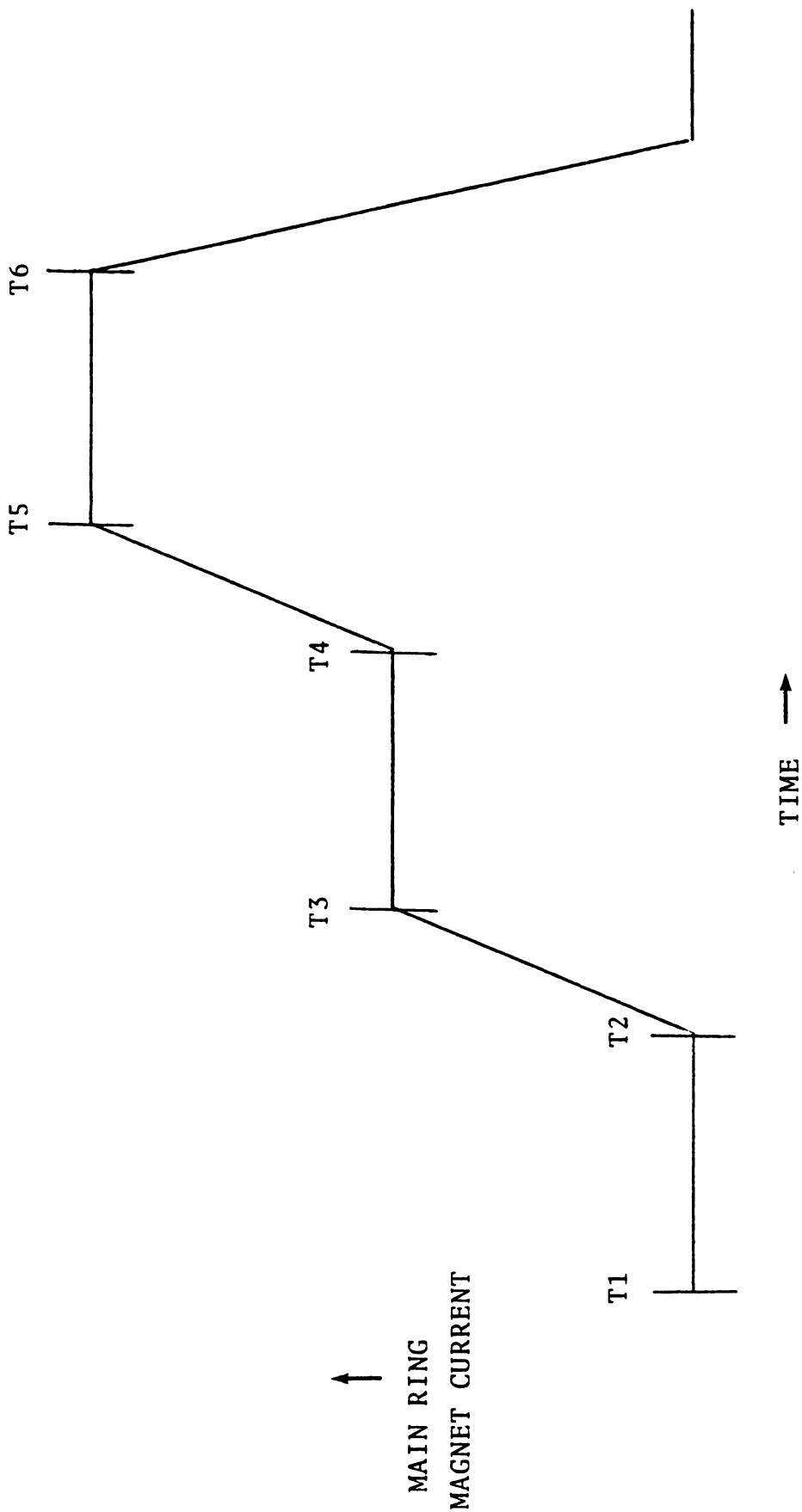


Figure II-10. FNAL Timing Pulses

The final gate used was the pinger-veto gate. Often during bubble-chamber running, pulses of neutrinos (pings) were directed at the bubble chamber. Accompanying these pings was a shower of other particles, which could greatly disturb our equipment, so using Fermilab supplied signals our spill gate was shut off for the duration of the ping, a period of about 1.6 μ s.

L) The CAMAC Equipment

One of the trigger module outputs was routed into the experiment's porta-camp outside of the muon lab where the CAMAC equipment was kept. This signal was used to send "open gate" signals to the various CAMAC data collection modules which were used. These gates are detailed in Fig. II-11. In addition, the signal was used to "veto" later trigger signals from interfering for a period of 5 μ s.

A second signal received in the porta-camp was the PCS signal used to reset and enable the PWC bit latches. This has been detailed above (Fig. II-11).

The third and final signal received in the porta-camp was an output of the event gate module. This signal was received by the gate control module and passed to the spark chamber time-digitizer control module (see below) as a signal to begin counting.

The CAMAC equipment itself consisted of several different kinds of data collection modules, all contained in six CAMAC crates (see Fig. II-12) and controlled by an EG&G

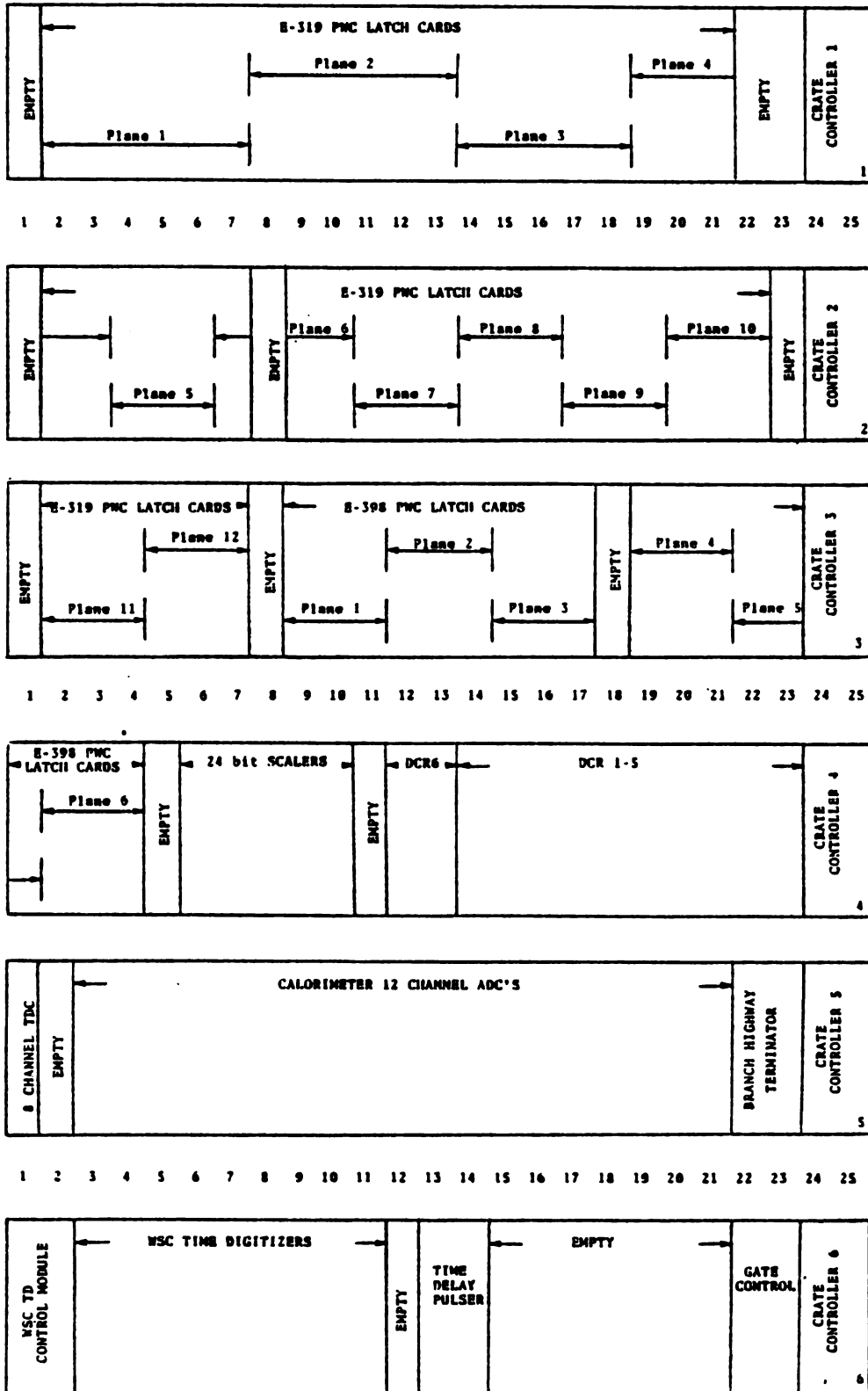


Figure II-12. CAMAC Crate Contents

Table II-11. CAMAC Scaler Contents

Scaler No.	Scaled Quantity	Scaler No.	Scaled Quantity
1	$B \cdot BV1$	19	--
2	$B \cdot BV2$	20	$B \cdot P$ (EVG)
3	$B \cdot BV3$	21	S (SPG)
4	$B \cdot \overline{BV}$ (EVG)	22	SD (SPG)
5	B (SPG)	23	SL (SPG)
6	$B \cdot \overline{BV}$ (SPG)	24	SH (SPG)
7	B (EVG)	25	SL (SPG, NV)
8	$B \cdot \overline{BV} \cdot SA$ (EVG)	26	S (SPG, NV)
9	$B \cdot S \cdot \overline{BV}$ (EVG)	27	SEM
10	$B \cdot SD \cdot \overline{BV}$ (EVG)	28	SPIILLS
11	$B \cdot SL \cdot \overline{BV}$ (EVG)	29	B104
12	$B \cdot SH \cdot \overline{BV}$ (EVG)	30	C
13	$B \cdot S \cdot \overline{BV}$ (SPG)	31	$B \cdot B_d$
14	$B \cdot SD \cdot \overline{BV}$ (SPG)	32	PCS
15	$B \cdot SL \cdot \overline{BV}$ (SPG)	33	HV · S
16	$B \cdot SH \cdot \overline{BV}$ (SPG)	34	TOTAL TRIGGERS
17	$B \cdot \overline{BV}_d$ (EVG)	35	A.D.C. GATES
18	--	36	P.C. RESETS

EVG = GATED BY EVENT GATE

SPG = GATED BY SPILL GATE

SEM = PROTONS DIRECTED ON PRODUCTION TARGET

NV = NOT SELF VETOED

d = 60 ns Delay in Signal

Table II-12. Visual Scaler Quantities

Quantities	
Triggers	$B \cdot \overline{BV}_d$ (EVG)
PCS	SEM
$B \cdot S \cdot \overline{BV}$ (EVG)	B104 (SPG)
$B \cdot S \cdot \overline{BV}$ (SPG)	B (SPG)
$B \cdot SD \cdot \overline{BV}$ (EVG)	B (EVG)
$B \cdot SD \cdot \overline{BV}$ (SPG)	$B \cdot B_d$
$B \cdot P$	HV $\cdot S$ (NV)
$B \cdot \overline{BV}$ (SPG)	S
$B \cdot SL \cdot \overline{BV}$ (EVG)	$B \cdot SH \cdot \overline{BV}$ (EVG)
$B \cdot SL \cdot \overline{BV}$ (SPG)	$B \cdot SH \cdot \overline{BV}$ (SPG)

d = 60 ns cable delay

Table II-13. Contents of the Time-Digital-Converters (TDC)

TDC No.	Timed Counter
1	B_d
2	SA
3	SB
4	SC
5	BV1
6	BV2
7	BV3
8	-

d = 60 ns cable delay

BIT	LATCH
1	SAV-1
2	SAV-2
3	SAV-3
4	SAV-4
5	SAV-5
6	SBV-1
7	SBV-2
8	SBV-3
9	SBV-4
10	SBV-5
11	SCV-1
12	SCV-2
13	SCV-3
14	SCV-4
15	SCV-5
16	---

DCR1

BIT	LATCH
1	SAH-1
2	SAH-2
3	SAH-3
4	SAH-4
5	SAH-5
6	SBH-1
7	SBH-2
8	SBH-3
9	SBH-4
10	SBH-5
11	SCH-1
12	SCH-2
13	SCH-3
14	SCH-4
15	SCH-5
16	---

DCR2

BIT	LATCH
1	B·P ^{evg}
2	B·S· \overline{EV} ^{evg}
3	B·SD ^{evg}
4	B·SI· \overline{EV} ^{evg}
5	B·SH· \overline{EV} ^{evg}
6	\overline{EV} ^{evg}
7	---
:	:
14	P.C. RESET
15	---
16	---

DCR3

BIT	LATCH
1	BH 21
2	BH 22
3	BH 23
4	BH 24
5	BH 25
6	BH 26
7	BH 27
8	BH 28
9	BH 31
10	BH 32
11	BH 33
12	BH 34
13	BH 35
14	BH 36
15	BH 37
16	BH 38

DCR4

BIT	LATCH
1	BH 41
2	BH 42
3	BH 43
4	BH 44
5	BH 45
6	BH 46
7	BH 47
8	BH 48
9	---
:	:
16	---

DCR5

BIT	LATCH
1	P.C. STROBE
2	TH 1
3	TH 2
4	TH 3
5	TH 4
6	TH 5
7	TH 6
8	TH 7
9	TH 8
10	---
11	---
12	S TELESCOPE
13	BV I
14	BV II
15	BV III
16	---

DCR6

Figure II-13. DCR Bit Latch Contents

BD011 branch driver interface. Thirty-six channels of scalers (SLR) kept count of various important quantities during the course of a run. These scaled quantities are tabulated in Table II-11. Many of these same quantities were also tabulated on visual scalers in the muon lab, along with other less important quantities. (Table II-12). Six discriminator coincidence register (DCR) bit latches maintained information on counters struck and logic signals formed during the event, e.g., which counters in new Trigger Bank A (SA') were struck was recorded in DCR number two (Fig. II-13). Eight channels of time of flight information were recorded in a time-to-digital converter (TDC) (Table II-13). This TDC information, due to unfortunate gating problems, has never been used. Information about the calorimeter counter signal sizes was recorded in 19 LRS 2249A 12-channel Analog-to-Digital Converters (ADC). All of these modules were commercially available equipment.

The remaining modules, the PWC bit latches and spark chamber time digitizers, were "home-made" equipment. The PWC latches handled 32 wires each, one latch per wire. The total of 2,048 wires was thus handled in 64 cards. The spark chamber time digitizers (TD) were controlled by the time digitizer control module located in the same CAMAC crate and communicated with it using the crate's bussed signal lines. The control module contained a 20 MHz clock and issued signals clearing the old TD information and initiating a new counting sequence. There was one TD per

four spark chamber wands, nine in all. As each TD received a pulse from its wand, a word was stored with the clock count corresponding to receipt of the signal. Information for the first eight sparks on the wand was recorded in this way. The rest of the spark pulses were ignored. If less than eight pulses were received, the remaining words were zero filled. Upon readout, an extra "ID" word was put out by each TD, identifying itself and telling which wands had overflowed the maximum of eight sparks.

At the end of the spark digitizing, the slowest CAMAC crate process, the time digitizer control passed the start it had received from the gate control to the BD011 as signal to interrupt the on-line computer.

M) On-Line Computing

The computer used for on-line data collection and analysis was a PDP 11/45 with 32K of core memory, an RK11 disk pack with 1.2 million words of storage, and a TU10 nine-track tape drive. The operating system when not in on-line mode was DOS-9, a non-real-time system. The on-line program was really three related programs originally written for E26, and later modified for use for both E382 and E319, this experiment. The first two program parts built, modified, and initialized a disk resident library of programs which could be scheduled and run under the third program, the actual on-line program. This third program was a stand-alone program, not dependent on the DOS operating system in

any way. Originally called⁽³¹⁾ DROS 11 for Disk Based Real Time Operating System for the PDP 11, it replaced the DOS monitor and peripheral drivers with its own versions, setting up its own interrupt priority system. Routines on the disk library available for execution were written using "stack" and disk storage only, so that program swapping wasn't necessary. When a higher priority program needed to be run, the location of the routines personal "stack" was stored and the core the program had occupied was made available to be overwritten. The highest priority of the program was recognizing the BD011 interrupt to read out the CAMAC crates and then, at a slightly lower priority, writing this information to tape.

Information from an event was recorded in a 768 word (12PRU) block, and tapes (called primary tapes) were written with four events per record. These tapes were only read once, and that was to copy them on an IBM 360/50 computer as two events/record tapes. These primary tape copies were used in all later analysis which was performed on CDC 6000 series computers. See Table II-14 for the details of the event block structure.

From information received during the course of various branch driver interrupts, the on-line could detect the end of the beam spill, and schedule routines for running which would sample the data event blocks collected during the preceding spill. These diagnostic routines could collect information dealing with any of the data stored in the event block, e.g., the distribution of wires struck in a

Table II-14. Primary Tape Event Block Structure

A) Overview

Words	Content
1-15	I.D. block
16-87	Scalers
88-179	E319 PWC's
180-215	E398 PWC's
216-220	DCR's 1-5
221-228	TDC's
229-456	ADC's
457	DCR 6
458-464	Not used
465-761	TD's
762-768	Not used

B) Detail--I.D. Block

Word	Content
1	Operator name
2	Run number
3	Event number
4	Date = $1000 \cdot (\text{YR}-1970) + \text{Day}$
5	Time--high order 16 bits
6	Time--low order 16 bits
	Time = $((60 \cdot \text{HR}) + \text{MIN}) \cdot 7200$
7	Tape number
8	Beam energy
9	Unused
10	Type of target
11	Unused
12	Beam spill number
13-15	CAMAC error flags

C) Detail--Scalers

Word	Content
16	High order 8 bits, scaler 1
17	Low order 16 bits, scaler 1
⋮	
86	High order 8 bits, scaler 36
87	Low order 16 bits, scaler 36

Table II-14. Continued

D) Detail--E319 PWC's

Words	Chamber- Module	Physical Location of Wire, Lowest Numbered Word, Bit 1
88-99	1-1	West-most
100-111	1-2	Top-most
112-121	2-3	West-most
122-131	2-4	West-most
132-137	3-5	East-most
138-143	3-6	West-most
144-149	3-7	West-most
150-155	4-8	Bottom-most
156-161	4-9	East-most
162-167	4-10	West-most
168-173	5-11	Top-most
174-179	5-12	East-most

E) Detail--E398 PWC's

Words	Chamber
180-185	1
186-191	2
192-197	3
198-203	4
204-209	5
210-215	6

proportional chamber. Other programs could then be run which would display the information for the operators' perusal, either at the line printer or on a CRT display. These programs were scheduled by setting in the computer display register an identifying octal code unique to the program, output device instructions, and an optional seven bits of information for the program itself. Depressing a panic button would signal an interrupt to the computer via the BD011, and the on-line would then read the display register and act to schedule the correct routine for earliest possible running. The availability of these programs aided considerably in the early detection and correction of hardware breakdowns.

Data collection was classified by runs; a run was maximum of one tape in length, or about 10,000 triggers. A sequence of operator commands would initialize a tape at the beginning of a run, clear all histogram storage, and enable the event trigger, while at the end of a run, another sequence of commands would disable the event trigger, write all events onto tape, close the tape, and print selected accumulation areas to the line printer. Additional accumulations could be printed at the operators request. At this point the tape could be changed (or left mounted for more events from a new run) and a new run begun, or the normal DOS-9 monitor could be entered and initialized.

There were some difficulties with the on-line monitor. Occasionally, usually with high trigger rates, the system

would lock up, crashing the computer and losing the accumulated run information. However, the data tape was safe at times such as this, so only events not yet written out to tape (never more than a few) were lost.

A second problem was extraneous bits appearing in the scalers. The CAMAC scalers could hold 24-bits of information, or a maximum of $2^{23} - 1 = 8,388,607$ after which they reset to zero. The accumulation program could occasionally be fooled by the extra bit into totalling in extraneous values of 8,388,607, resulting in outrageous quantities at runs end, such as 16 million triggers found. The source of this problem was never found, but no other equipment used the data lines 17-24 where the problem was isolated, so no other equipment was affected.

A final problem never has been completely resolved. It turned out that the ADC supplied to us by LeCroy (the LRS 2249A) did not have a sufficiently isolated gate, so that spark chamber noise (from the 8 KV discharge) could feed along the input cables from the counters in the calorimeter and reopen the gate. Any noise then on the input cables was digitized right in with the actual counter signal. As a result, information from the calorimeter outside of the shower region is nearly unusable. Additionally, some channels would not respond to CAMAC enquiry and as a result higher numbered channels of the twelve in that ADC were ignored by the branch driver/crate controller read out. Since the spark chamber time digitizers were immediately

behind the ADC's in the crate addressing system, on-line this error showed up as a "time-digitizer block transfer error." The ADC read command, in order to satisfy its word count, would take information from the TD's. When it came time for the normal TD readout, the information wasn't available since these modules could only be read once before they were cleared and redigitized. These were the last modules in the crates, so a crate readout failure resulted. This problem increased with increasing data collection rates, and disappeared completely at lower rates. A correction to the incident flux total (sec. V-A) was used to account for events missed in this way.

CHAPTER III

DATA EVENT RECONSTRUCTION

A) Track Finding

Once tapes were written by the on-line computer, it was necessary to read these tapes and extract the information necessary to determine if a scattered muon was present, and if so, what were the kinematics. The computer program MULTIMU, written at MSU by Daniel Bauer,⁽²⁹⁾ performed the first of these functions. The program used information from the upstream spark chambers (WSC7-WSC9) and the hadron proportional chambers (PWC1-PWC2) to find muon tracks originating in the target, then traced these the full length of the spectrometer. Figure III-1 displays the program organization, while Tables III-1 to III-4 show restrictions imposed on acceptable track candidates by the program.

Using information from the above listed four spark and proportional chambers, the program formed all likely three point lines in all four available views (x,y,u,v, defined in Fig. II-2). This allowed one chamber in each view to have no correctly positioned sparks. Looping over all four views, the program then matched these lines to form possible scattered muon tracks in three dimensions. These track candidates

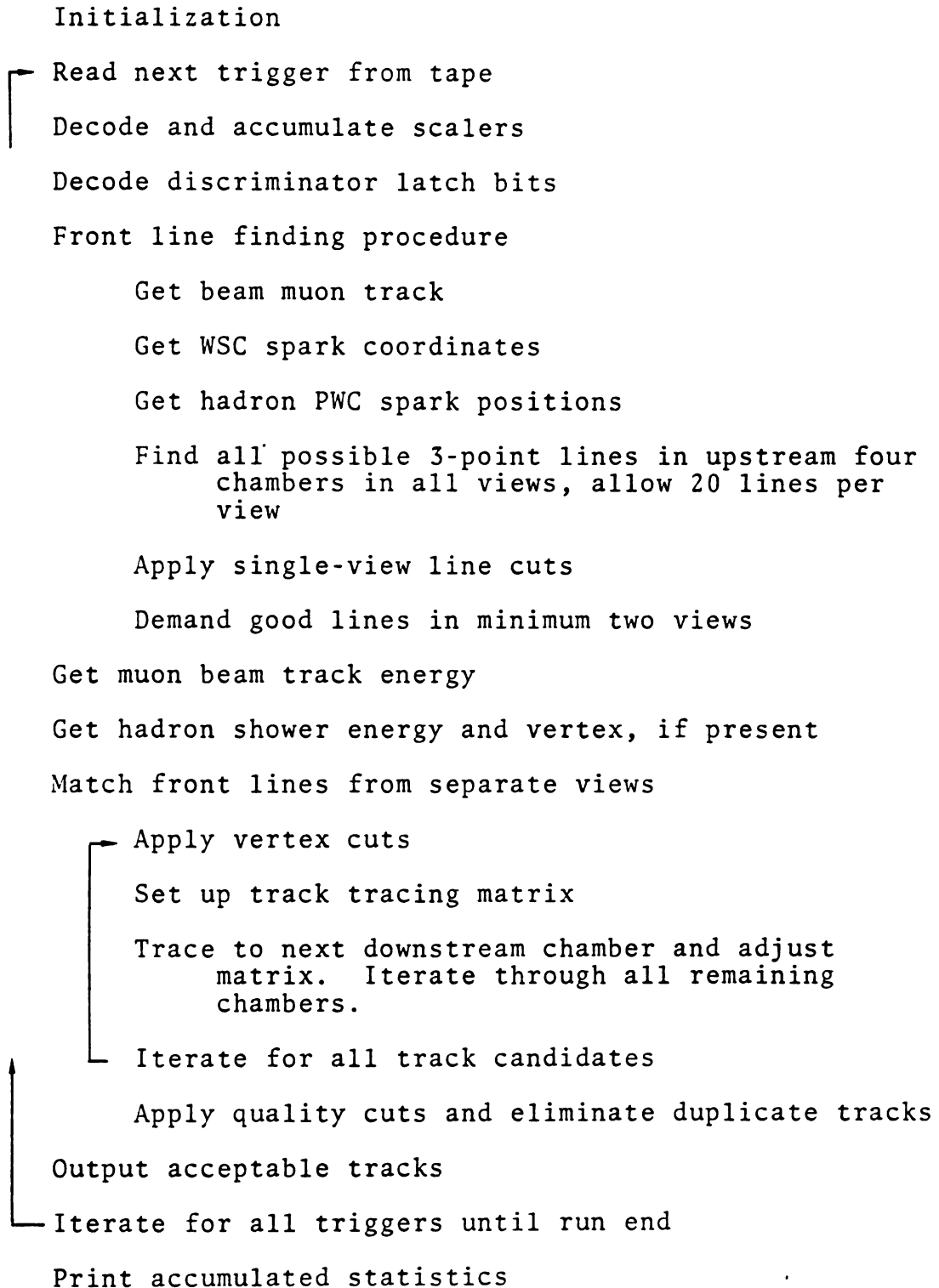


Figure III-1. MULTIMU Program Organization

Table III-1. Acceptable Three-Point Line Types

Type	Included Chambers
1	HPC, WSC9, WSC7
2	WSC9, WSC8, WSC7
3	HPC, WSC8, WSC7
4	HPC, WSC9, WSC8

HPC = Hadron Proportional Wire Chamber

Table III-2. Single-View Line Cuts

Cut	Description
1	Line slope less than 234 mRad
2	Extrapolated line within target bounds at one of upstream edge, middle, or downstream edge
3	Intersection with beam track line (projected) within $-2500 \text{ cm} < z < 2500 \text{ cm}$

Table III-3. Vertex Cuts

Cut	Description
1	Z position of minimum separation from beam track (ZMIN) within $-250 < z < 600 \text{ cm}$
2	Minimum separation from beam track (DMIN) less than $0.15 \cdot R + 2.0$; R is track radius at WSC8
3	ZADC = z-position of hadron shower $ ZADC - ZMIN < 400 \text{ cm}$ (when shower present)

Table III-4. Track Quality Standards

Standard	Description
1	Average chamber match code* greater than 2.80
2	Track outside of toroid hole region at a minimum of one chamber
3	One parameter+ χ^2 /degree of freedom less than 10.0

+This is a primitive χ^2 fit to 1/E' based on equal weights for all chambers.

*Each chamber is assigned a match code on the basis of which module views contribute to the spark position for the track. The match codes are summed and divided by the number of contributing chambers to get the average for the track. Match codes are assigned as follows:

Contributing Chambers	Match Code	Contributing Chambers	Match Code
XYUV	4.0	XY	2.5
XY V	3.8	X U	2.4
XYU	3.6	YU	2.3
YUV	3.4	X V	2.2
X UV	3.2	Y V	2.1
		UV	2.0

were then traced chamber-by-chamber through the remaining six spark chambers to form completed tracks. A maximum of ten track candidates were allowed. At each chamber downstream from the first four, a window was set up, inside of which the program would look for spark positions. The window was set up by estimating the muon momentum the track supposedly corresponded to, and extrapolating this track with any magnet induced bend to the next nearest spark chamber. The program then searched within a circle centered on this extrapolated position, the radius of which consisted of the multiple scattering expected and the chamber measurement error summed in quadrature. If a spark was found by this process, its position was used in estimations for the next downstream chamber. Complete tracks, when found, were written onto an output tape (Table III-5), again with up to ten tracks per trigger read. A new trigger was then read, and the process was iterated until the end of the run was reached.

Several types of trigger were automatically rejected by the program. If any of the CAMAC error flags were set (Table II-14), the trigger was deemed unreliable and skipped. The incident flux was corrected for this eventuality. Similarly, if the spark chambers were off for some reason as indicated in the time digitizer ID words, the trigger was skipped and the flux corrected. The same is true for events where no beam track or more than one beam track was found. Events where the pulser trigger bit in DCR3 was set were skipped, but the flux was not corrected. See chapter five

Table III-5. MULTIMU Output Tape Format

150 Words/Track	
Words	Content
1	100,000•Run# + Event# (I)
2	Track# (1 to 10) (I)
3	Value of scaler $B \cdot \overline{BV}_d$ (EVG) (I)
4	Found x-coord. PWC5
5	Found x-coord. PWC4
6	Found x-coord. PWC3
7	0.0
8	Found x-coord. HPC
9	Found x-coord. WSC9
:	:
17	Found x-coord. WSC1
18	Same as words 4-17, except for y-coords.
:	:
31	
32	Match Code PWC5
33	Match Code PWC4
34	Match Code PWC3
35	0.0
36	Match Code HPC
37	Match Code WSC9
:	:
45	Match Code WSC1
46	0.0
:	:
53	0.0
54	X-component of beam momentum E_0
55	Y-component of beam momentum E_0
56	Z-component of beam momentum E_0
57	Extrapolated x-position of beam track at $z = 0$
58	Extrapolated y-position of beam track at $z = 0$

Table III-5. Continued

Word	Content
59	x-component scattered muon momentum guess (E')
60	y-component scattered muon momentum guess (E')
61	z-component scattered muon momentum guess (E')
62	Extrapolated x-position of scattered muon track at $z = 0$
63	Extrapolated y-position of scattered muon track at $z = 0$
64	One parameter χ^2
65	Degrees of freedom
66	ZADC
67	Shower energy
Words 68 - 71 measured at WSC8	
68	Angle from z-axis in x-z plane
69	Angle from z-axis in y-z plane
70	x-position
71	y-position
72	E' guess
73	θ guess
74	Packed word with number of HPC wires hit in each plane (I)
75	Packed word with total number of WSC sparks for each chamber (I)
76	Packed word with truncated match codes from PWC's 5-3 and HPC (I)
77	Number of spectrometer tracks this event (I)
78	Number of beam muon tracks (I)
79	DCR1 contents (I)
80	DCR2 contents (I)
81	DCR3 contents (I)
82	DCR4 contents (I)
83	DCR6 contents (I)

Table III-5. Continued

Word	Content
84	Average Match Code
85	DMIN guess
86	ZMIN guess
87	Packed number of accepted lines/view (I)
88	Packed number of found lines/view (I)
89	8 - J or 0 [Track leaves spectrometer at WSCJ] (I)
90	Packed, truncated match codes from WSC1-9 (I)
91-150	Packed ADC counts (I)

(I) Indicates integer value; otherwise stored as floating point value.

for a further discussion of these flux corrections.

B) Program Initialization

Several files of information pertinent to the run under consideration were read into the program at initialization time. The first of these contained information on the spark chamber fiducials. Since the acoustic pulse propagation velocity (Sec. II-E) depended on several externally imposed factors, the time count digitized for a given position in the chamber varied from run to run. The two fiducial wires, one at either end of all 36 chamber modules, were fired on all triggers, so the average position of these wires as indicated by the time counts was recorded for all runs and read in when that run was reconstructed. Digitized time counts for all triggers in the run could thus be properly interpreted in terms of physical location in the chamber.

The second file contained information on the ADC pedestal values. In the calorimeter, independent of whether there was a particle traversing a particular counter, the ADC would accumulate a small amount of charge, typically on the order of two pico-coulombs (6-10 counts). To evaluate the shower energy, this value was subtracted from the count digitized by the ADC on the trigger being considered. The pedestals varied slowly in time, so any one of several files were read, depending only on the run number.

The third file contained the ADC counter gains, and the fourth contained the single-particle peaks. For the high

gain ADC's, a single particle traversing a counter leaves a clearly defined peak in the count minus pedestal distribution after many events. This information then calibrates the counter to give the number of particles traversing it. Using the counter gain, this information can also be retrieved from the low gain ADC. With the total number of particles thus found for a shower, and with the results of several calibration, pion beam runs at known energies, the shower energy can be determined. See the Ph.D. thesis of D.Bauer⁽²⁹⁾ for more information on this procedure.

The fifth file contained the z positions of all steel plates in the target. During the course of all running for the experiment, several different target configurations were used. Reading the plate positions allowed the program the versatility necessary to reconstruct triggers from any of these configurations. Additionally, the plate positioning was not perfectly regular, so reading the positions would determine ZADC (defined in Table III-3) more accurately than interpolation along the length of the target.

Finally, an input file containing many of the constants discussed above was read into the program. These constants were established as optimal values during the debugging of the program, but left to be input in this manner for use in other program applications (e.g., see Sec. III-D). The current in the bending-momentum selecting magnet 1E4 was also input in this manner along with the nominal momentum it corresponded to.

C) The Momentum Fitting

The output tape from MULTIMU contained the reconstructed muon tracks plus some other information, but did not contain an accurate determination of the muon kinematics. This job was left for the fitting programs GETP and GETP2. These programs performed a five parameter fit on the spark positions contained in the MULTIMU output tape, iterating the fit procedure until the change in momentum (p) determined by the fit was less than 1%. The five parameters varied were the momentum p , and four quantities defined at WSC8, the positions x and y in the x - z and y - z planes, and the angles θ_x and θ_y from the z axis in these same two planes. The complete procedure is illustrated in Fig. III-2.

These two programs also performed a second service, the removal of bad sparks from the set output by MULTIMU. Since MULTIMU was a search program, it would occasionally stray and pick bad spark positions from the spark chambers, usually when the correct spark was missing. If the $\chi^2/\text{degree of freedom}$ found by GETP was greater than 5.0, the program assumed a spark was bad. Since no better procedure was determined, it then pulled the sparks of one chamber after another from the fit, determining which chamber, if pulled, would give the greatest improvement in the $\chi^2/\text{degree of freedom}$. The sparks from this chamber were then permanently removed from the event. GETP2 performed the same function, removing a second chamber's sparks if necessary. The output block of words from these programs is shown in Table III-6.

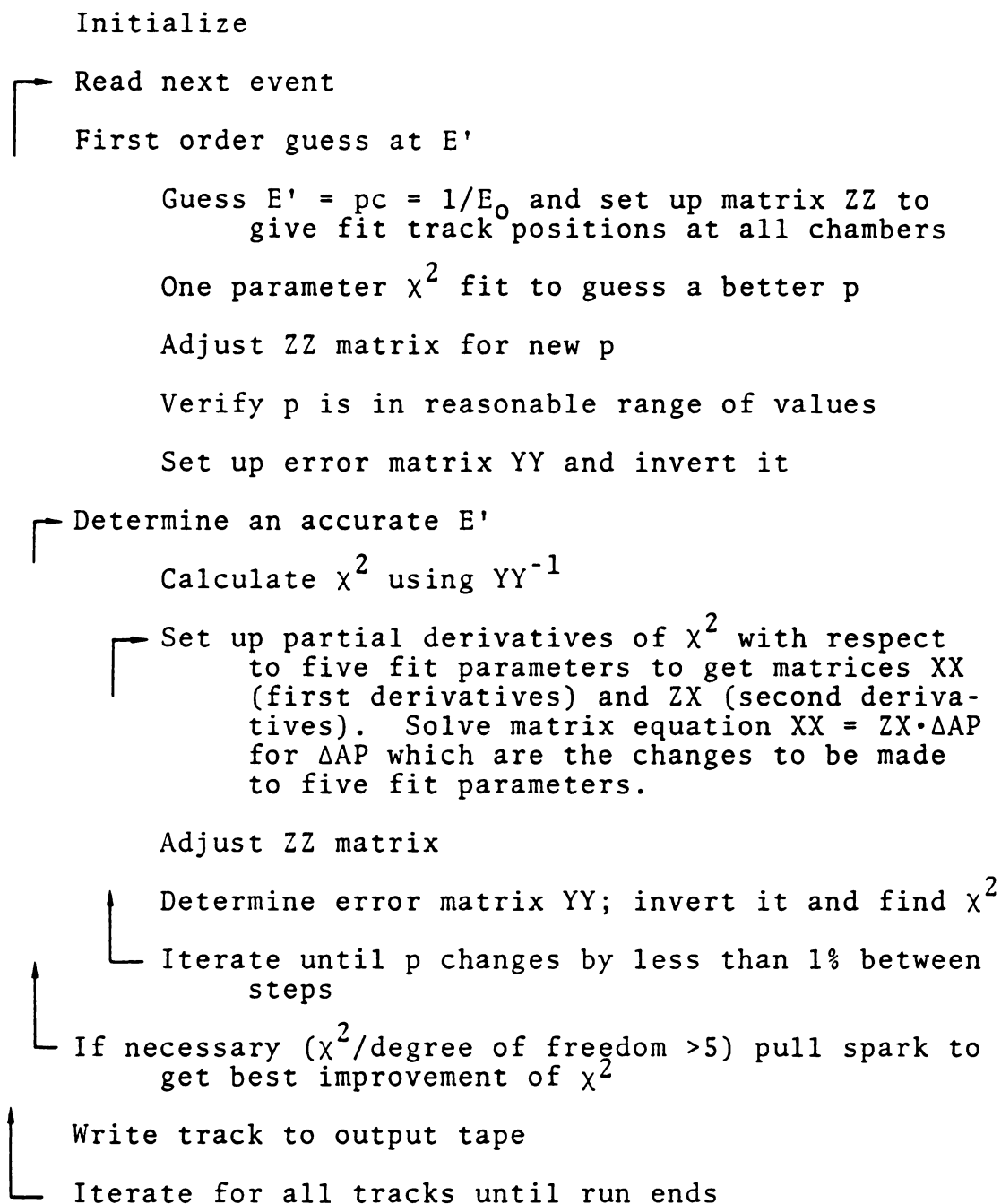


Figure III-2. GETP and GETP2 Program Organization

Table III-6. GETP and GETP2 Output Tape Format

150 Words/Track	
Words	Content
1	Same as for MULTIMU
:	:
31	
32	0.0
33	Fitted x-coordinate HPC
34	Fitted x-coord. WSC9
:	:
42	Fitted x-coord. WSC1
43	Same as words 32-42 for y coords.
:	:
53	Word 46 set = -1024.0 if track is not fit
54	Same as for MULTIMU
:	:
58	
59	x-component of scattered muon momentum E' from the fit
60	y-component of E'
61	z-component of E'
62	Extrapolated x-position of scattered muon track at z = 0
63	Extrapolated y-position of scattered muon track at z = 0
64	χ^2 of the momentum fit
65	Degrees of freedom
66	ZADC
67	Shower Energy
68	θ_x , angle of scattered muon track from z-axis in x-z plane
69	θ_y , same as word 68 for y-z plane
70	Same as word 62
71	Same as word 63

Table III-6. Continued

Words	Content
72	Chamber shut off by GETP2 or zero
73	Chamber shut off by GETP or zero
Value in words 72 and 73 is 16-J where WSCJ or HPC (J=10) is turned off	
74	Same as for MULTIMU
⋮	⋮
150	⋮

It is similar to the output tape from MULTIMU in many respects, but also contains the information from the fitting procedure.

D) Program Cross Checks

The reconstruction of tracks would have been worthless without verification that it was being done correctly. This confirmation was done in four ways. The first was performed during the debugging of the program. Extensive computer dumps of information on many triggers were taken to verify the program was choosing the correct lines to start with, and then following them correctly to the downstream end of the spectrometer. Finding the correct front lines was no easy task. The hadron shields protected the front chambers to quite an extent, but often there were still many possible lines which could be formed through the many existing spark positions. In addition, there was no shield other than the target itself to protect the hadron proportional chambers. There will be more on this problem shortly.

The second verification was obtained through comparison with results of a program called VOREP used earlier in this experiment⁽²⁷⁾. This program began with lines found at the downstream spectrometer end, and worked upstream searching for more track indicating sparks. Event tracks found by the two programs were passed through a filter program described in chapter five. On an event by event basis then, these resultant tracks were examined and differences determined.

Two regions in particular were examined, $Q^2 > 40$ (GeV/c)² and $Q^2 < 8$ (GeV/c)². The large Q^2 region was found to be inefficient by $9 \pm 4\%$ while the small Q^2 region was approximately 1.5% inefficient when compared to the combined event sample of the two programs. These results will be summarised at the end of this section when the final check is discussed.

The comparison with VOREP still left a class of events not found by either program. This class was determined by visually scanning events randomly chosen from the data tapes. From a subset of tapes scattered over nearly the full range of μ^+ data taking, 50 triggers per tape were checked for program efficiency. A total of 2298 triggers were checked in this way. The triggers were checked against the fitting program results; if the fit seemed reasonable, no further checks on the trigger were performed. If the fit results were poor (e.g., χ^2/DOF too large), or the track was not fit or even found, then the trigger was flagged for visual display using a program which would display a pictorial view of the entire target-spectrometer system in any of the four X,Y,U,V views. These could then be checked to see if a track was actually present. In this way, 1251 triggers were visually scanned, of which 117 seemed to contain good muon tracks. This good category did not include very low energy, high angle tracks or very low angle tracks which the filter program would not pass. For these triggers the VOREP reconstruction was tried, and if this failed,

sparks were chosen from those available and manually inserted into a MULTIMU type output file for fitting. When finally filtered, 49 events were found to have been missed. This corresponds to an overall inefficiency of $11.5 \pm 1.9\%$. In addition, there seemed to be a Q^2 dependence to the inefficiency; it was higher ($\sim 20\%$) at higher values of Q^2 , although 49 total events did not allow an accurate determination in this kinematically unfavorable region.

With these results in hand, all the checks performed were reexamined. It was determined that the inefficiency, for the most part, stemmed from the demand for the presence of three of the front four chambers in any one view to find a line candidate (sec. III-A). Since the hadron PWC's, the most efficient chamber used (99.5%), were only 40 cm across as opposed to 190 cm for the spark chambers, large radius tracks would miss them completely, thereby demanding all of chambers WSC7,8,9 to be present. Chamber WSC8 was the most inefficient chamber used (efficiency 81%), so for these large radius tracks, real problems in reconstruction existed. This was also true for triggers in which the maximum allowable number of hadron PWC sparks was found, in which case the information contained by them was not used at all. In this case it was as if the chamber was missed completely. These large radius tracks were primarily low to middle E' tracks at large angles, which means that large Q^2 tracks were preferentially excluded by the reconstruction.

To solve this a special version of MULTIMU was used which required only two point lines be found and allowed information from saturated hadron PWC planes to be considered. This obviously meant more line possibilities, but also an increase of execution time and core storage by the program. The program was therefore restricted to triggers from which tracks were not previously found. Additionally, triggers cut by the filter program's cuts on beam track distribution (sec. V-B) were ignored. In this way, 28 data tapes representing 21% of the 270 GeV μ^+ data sample were reconstructed. Events successfully passed through the filter program were weighted by this fraction and the result was applied as a weight factor to all events from the original MULTIMU which passed the filter program cuts. This weight factor is shown in Fig. III-3 as a function of the reconstructed variables Q^2 and x .

E) Raw Kinematic Distribution

With this weight factor the reconstruction of the data is complete. The modified version of MULTIMU was able to find nearly all of the 49 trigger tracks found in the visual tape scan. The remaining events are assumed to be uniformly distributed kinematically, and as such can be treated as an overall normalization factor of 1.019. Some of the raw kinematic distributions of events are shown in Figures III-4 thru III-9. These distributions reflect the true cross section for deep inelastic scattering of muons modified by

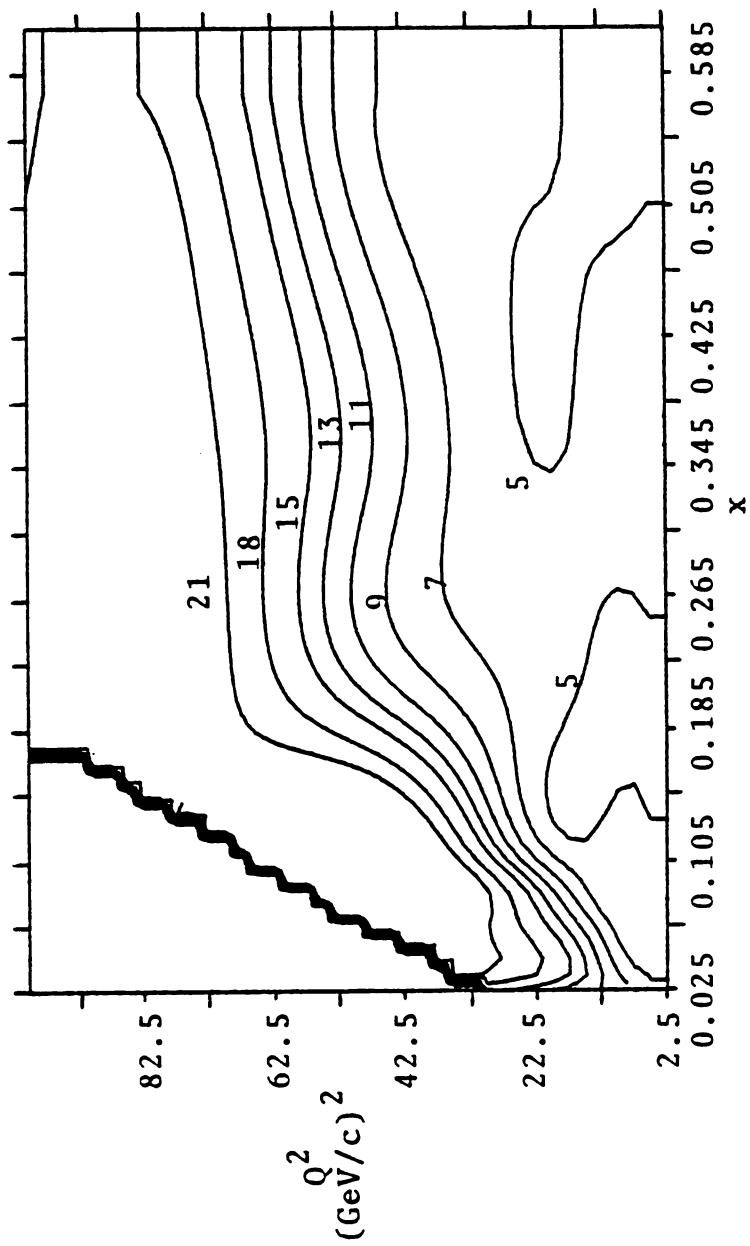


Figure III-3. Contour Plot of MULTIMU Inefficiency (percent)

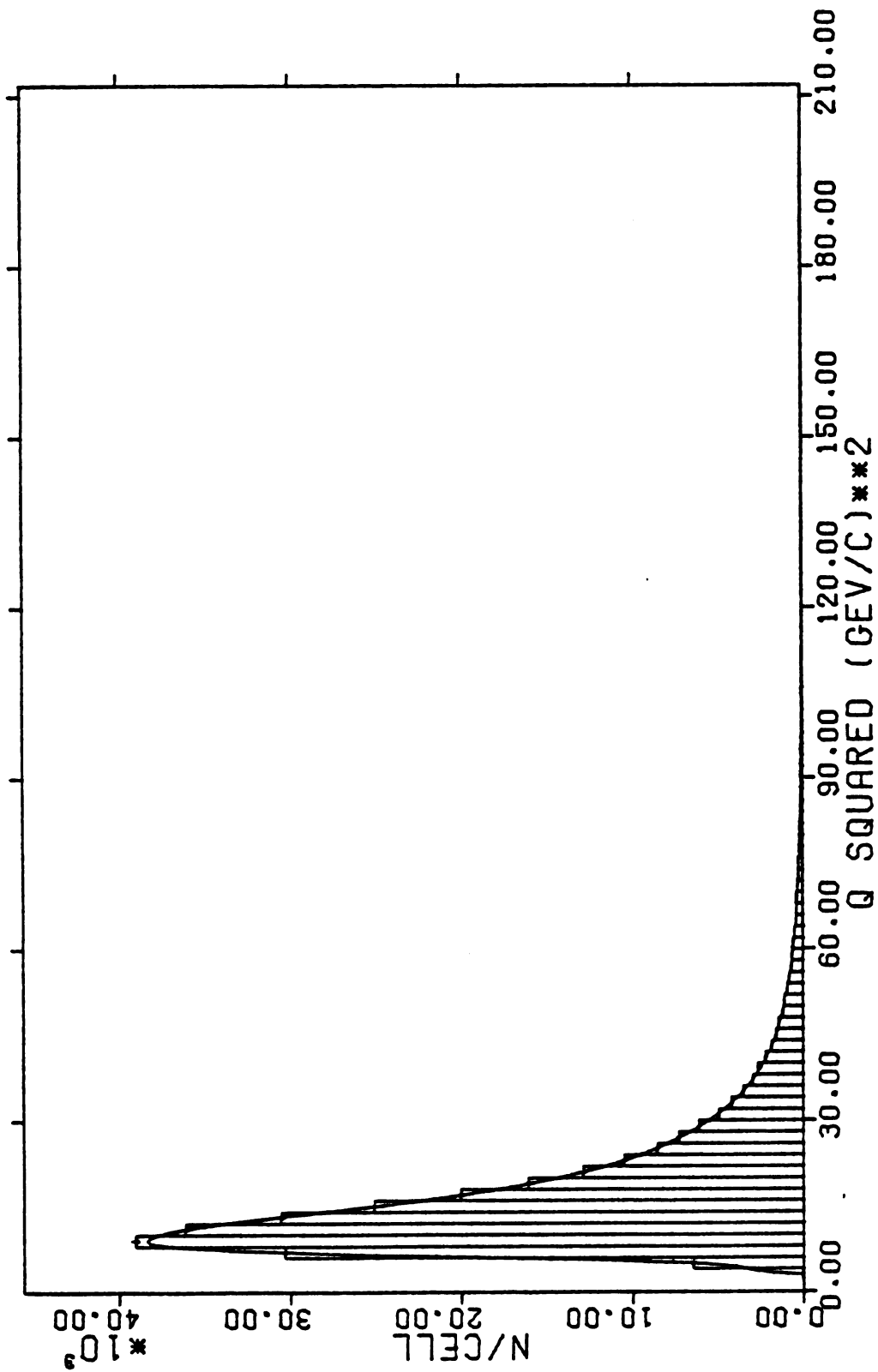
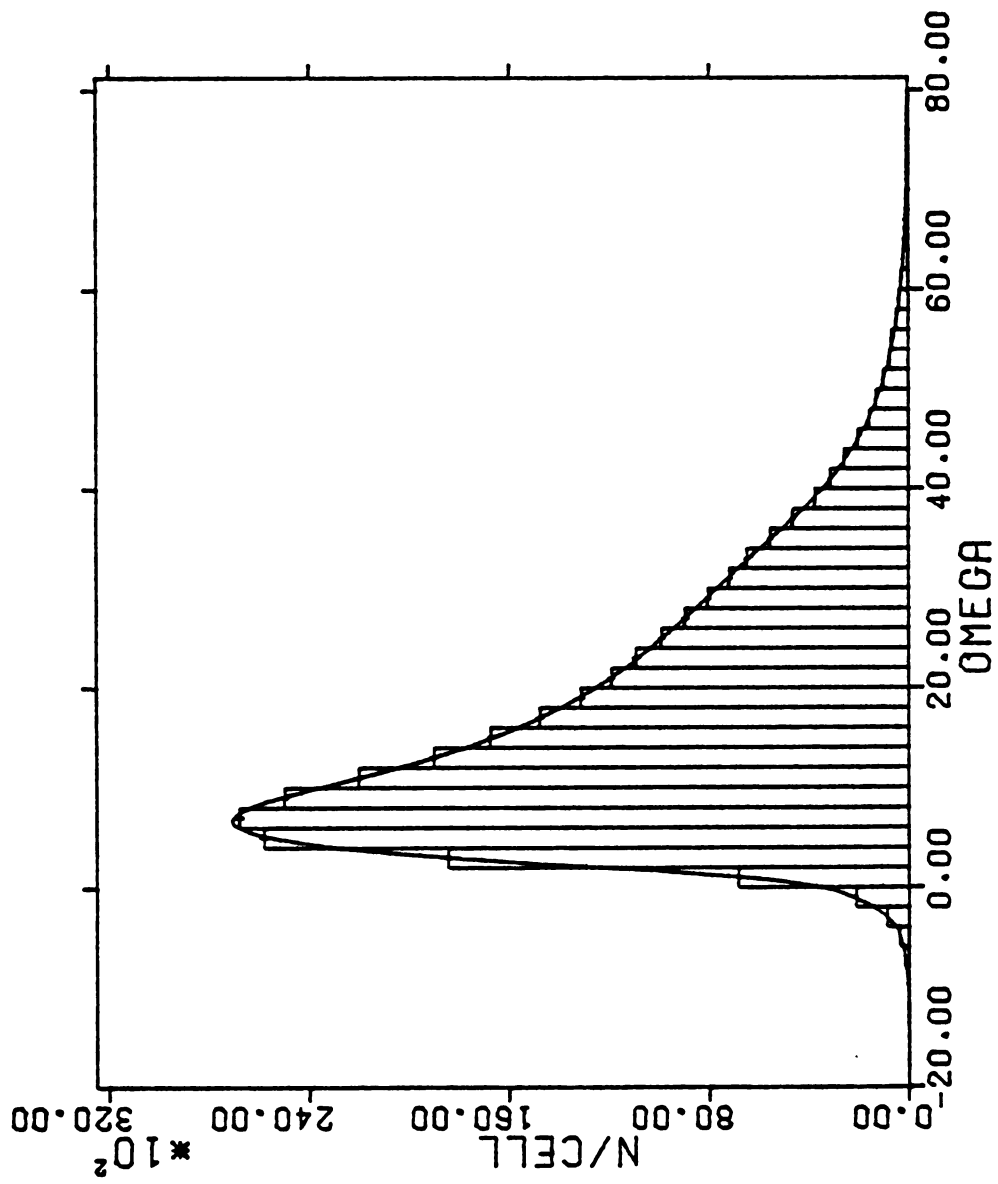


Figure III-4. Raw Q^2 Data Distribution

Figure III-5 Raw ω Data Distribution

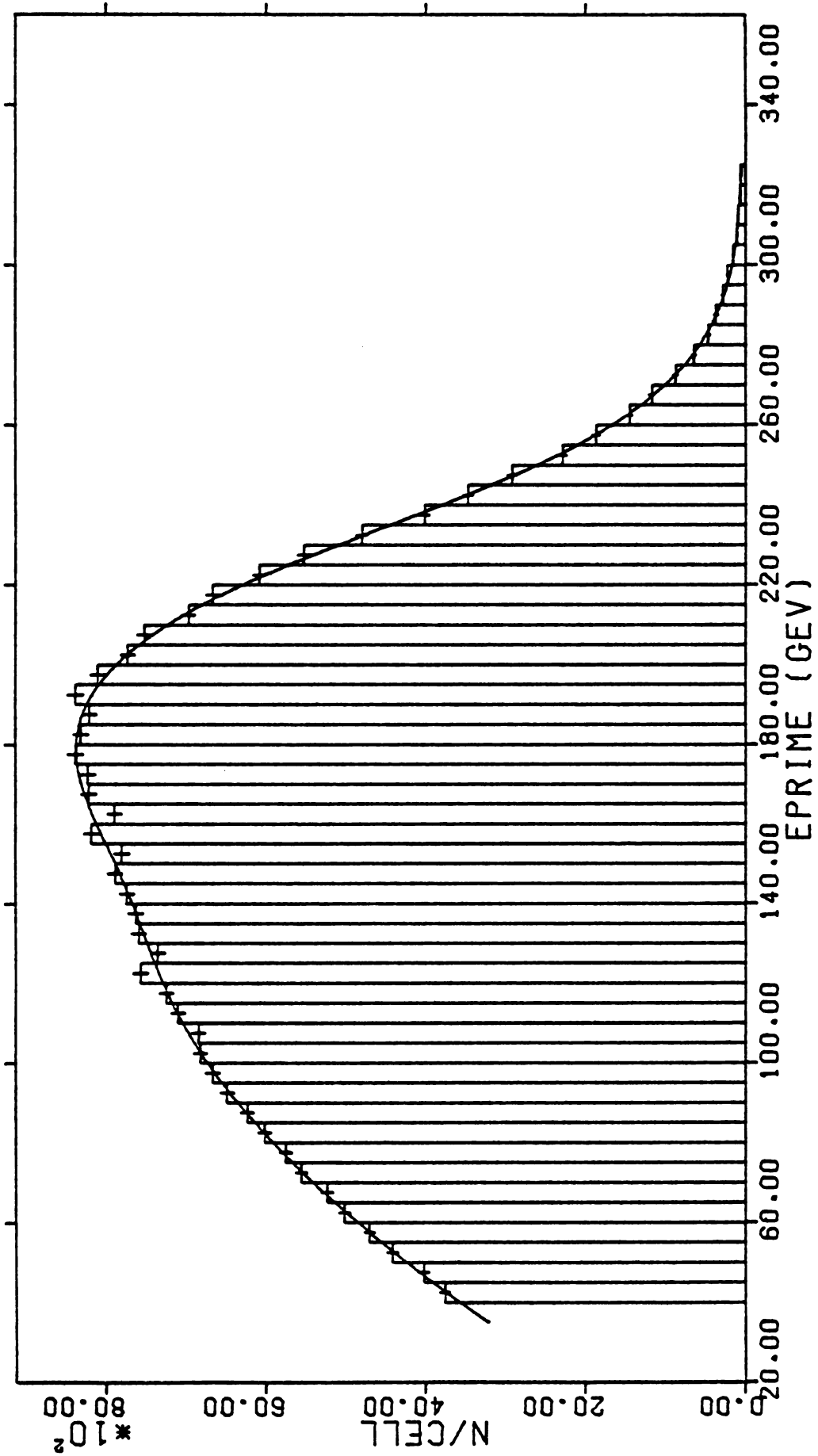
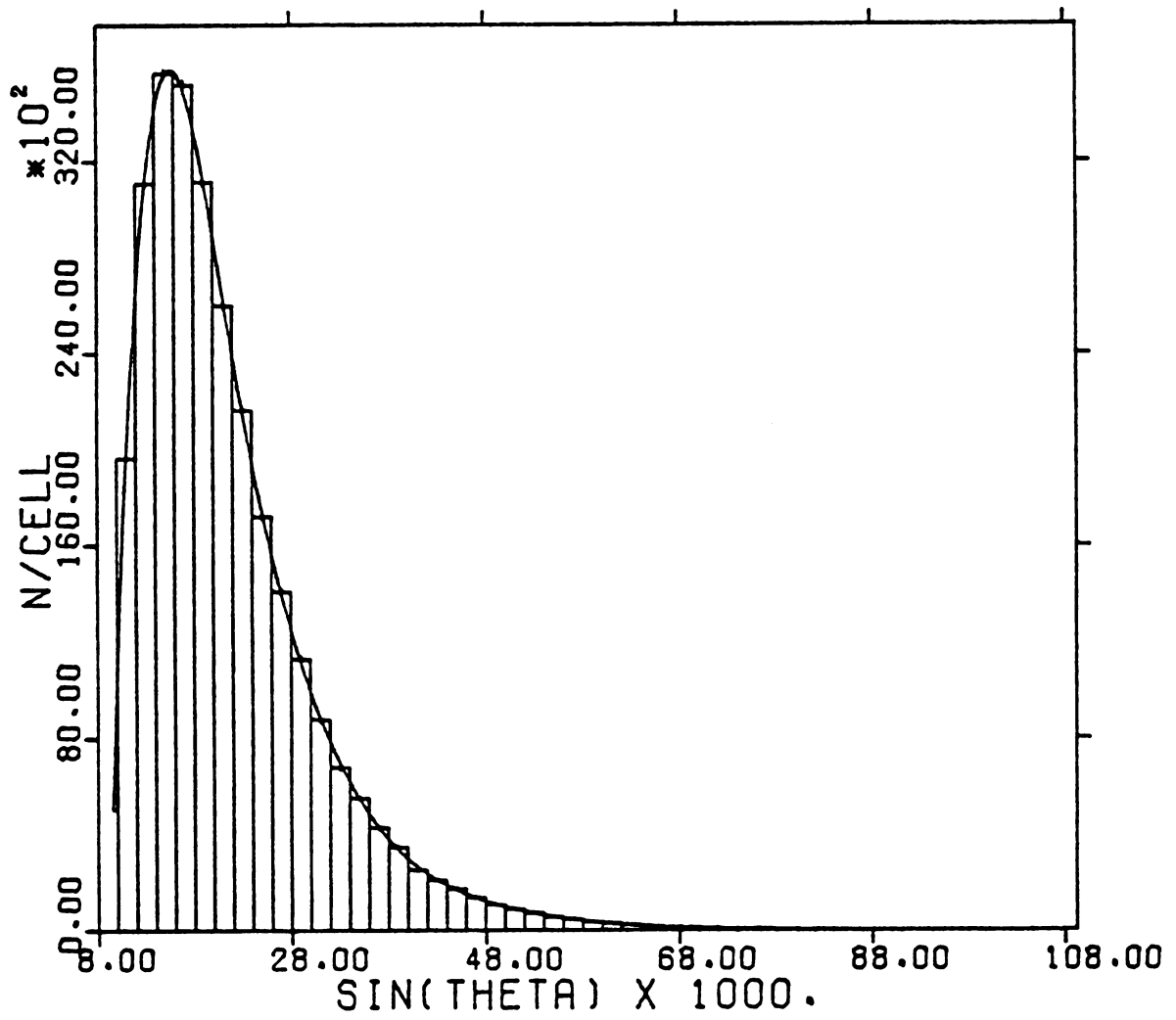


Figure III-6. Raw E' Data Distribution

Figure III-7. Raw $\text{SIN}(\theta)$ Data Distribution

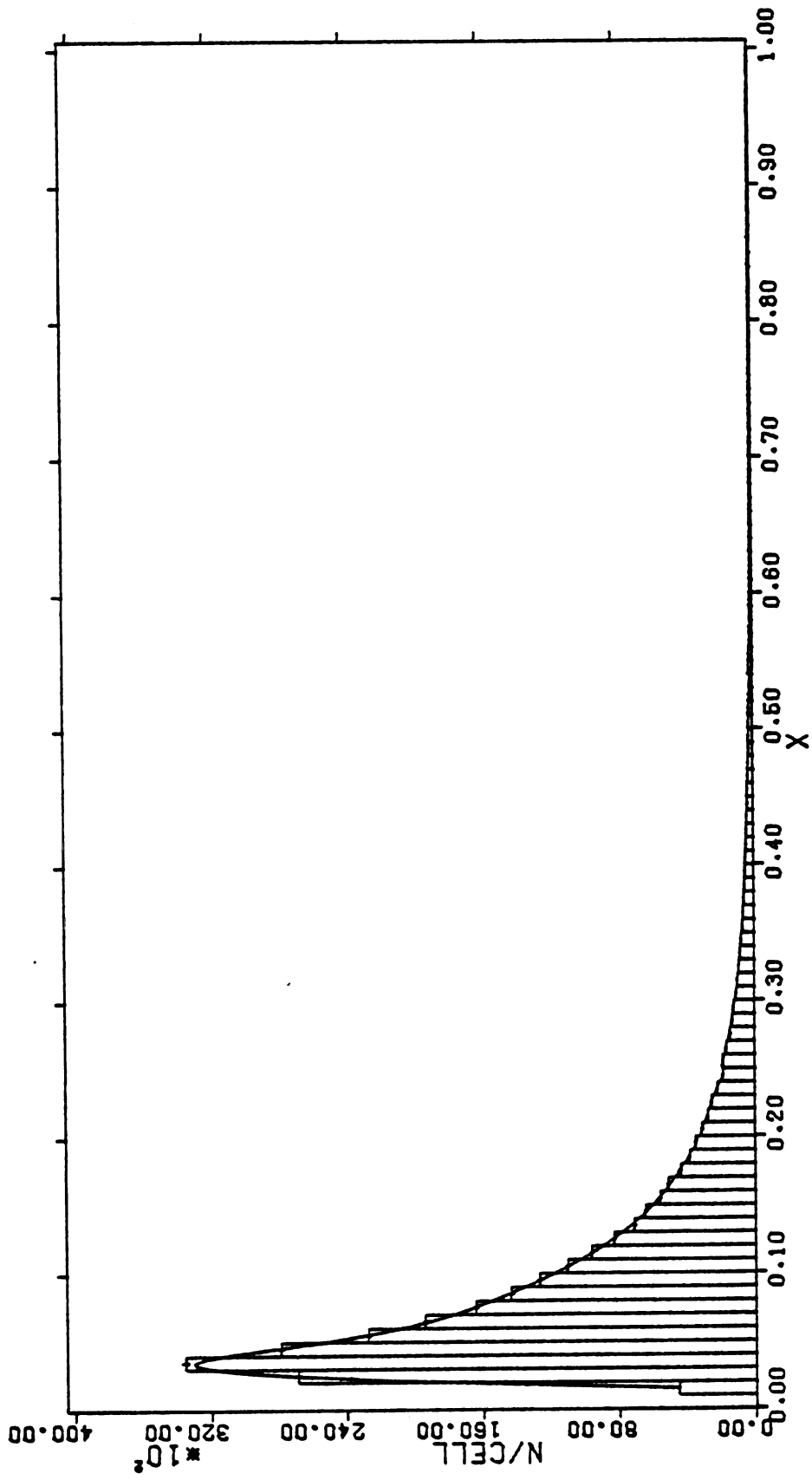


Figure III-8. Raw x Data Distribution

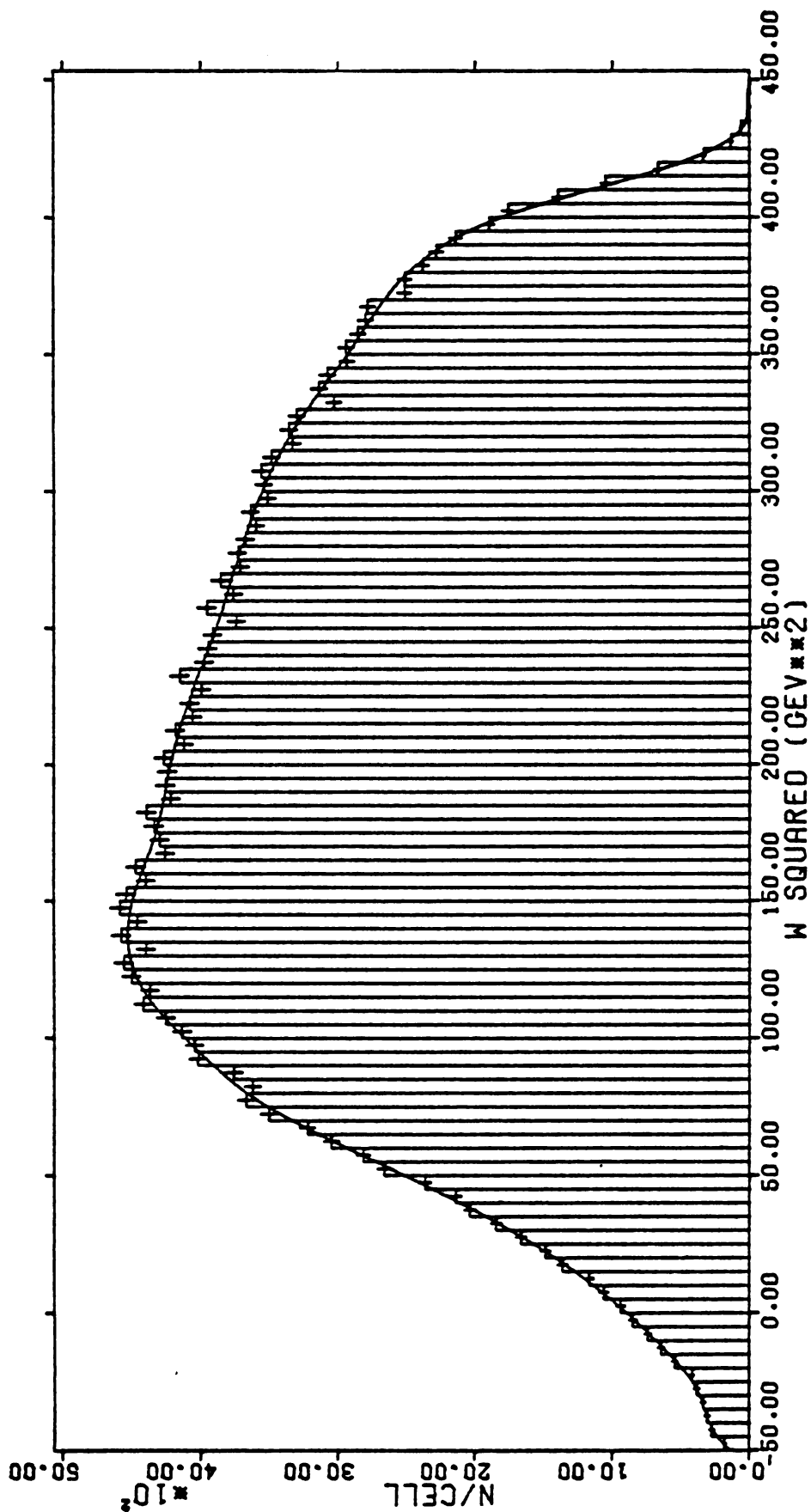


Figure III-9 Raw W^2 Data Distribution

both acceptance and resolution effects. To deduce the actual cross section, or alternatively the structure functions, the acceptance and resolution effects must be precisely determined. The monte carlo program discussed next was designed for this purpose.

CHAPTER IV

THE MONTE CARLO

A) Modeling the Data

The spectrometer used in the experiment, unfortunately, did not have 4π steradian acceptance. Therefore a means of modeling the expected kinematic distributions was needed. The monte carlo program MUDD, originally written at Fermilab by A. Van Ginnekan to model $D\bar{D}$ production, fulfilled the required acceptance and resolution modeling.

Our analysis would have been easier if Eqn.(I-9) developed in chapter I for the differential cross section was the only contribution to events measured. Corrections were necessary though, and the ones eventually applied to the cross section are listed in Table IV-1. Conveniently for the user, the program was structured in such a way that these corrections could be applied as easily after the program was run as during the actual running.

B) Multiple Coulomb Scattering and Energy Loss

As a muon traverses the length of a dense substance, there is a large probability that it will be deflected by the concentrated charge of a nucleus without undergoing a deep-inelastic scatter. This type of scattering, called

Table IV-1. Cross Section Corrections

-
-
- 1) Wide Angle Bremsstrahlung background
 - 2) Radiative Corrections
 - 3) Fermi Motion effective nucleon mass
-
-

multiple scattering, results in an angular scatter⁽³²⁾ which is approximately gaussian with standard deviation $\theta_{\text{plane}}^{\text{rms}}$ for angles $\theta_{\text{ms}} < \theta_{\text{plane}}^{\text{rms}}$ and falls as a power for $\theta_{\text{ms}} > \theta_{\text{plane}}^{\text{rms}}$, where $\theta_{\text{plane}}^{\text{rms}}$ is defined by⁽¹²⁾

$$\theta_{\text{plane}}^{\text{rms}} = z_{\text{proj}} \frac{.015 \text{ GeV}/c}{p\beta} \sqrt{\delta_x/L_R} \text{ radians} \quad (1)$$

and describes the net distribution of scattering angles projected onto any plane. δ_x is the thickness of the medium, L_R is the radiation length of the medium, p is the projectile momentum, z is the projectile charge and βc is its velocity. The non-projected angle is distributed with $\theta^{\text{rms}} = \sqrt{2} \theta_{\text{plane}}^{\text{rms}}$. The formula is accurate to within 10%.

This distribution was simulated in the monte carlo by the equation

$$\theta_{\text{ms}} = (-\ln(R_V) \frac{0.00045 \cdot \delta_x}{p^2 \beta^2 L_R})^{1/2} \quad (2)$$

where R_V is a uniformly-distributed random number in the interval $[0,1]$. A broad, single-scattering tail on the distribution was ignored since, in the region where the tail could begin to be important, it is damped out by the nuclear form factor.⁽²⁵⁾

As the muon traversed the target and spectrometer it was also losing energy thru various processes. Energy loss⁽³⁴⁾ for three of these processes, ionization (or collision), brem strahlung, and pair production, was modeled in

the monte carlo. A fourth process, energy loss due to nuclear interactions, is much smaller than these three processes and was ignored.

The ionization loss is due to the interaction of the muon with atomic electrons. For particles heavier than electrons, the average energy loss is given by the Bethe-Bloch equation,

$$-\frac{dE}{dx} = \frac{2\pi n z^2 e^4}{m v^2} \left[\ln \left(\frac{2 m v^2 W_{\max}}{I^2 (1 - \beta^2)} \right) - 2\beta^2 - \delta - u \right] \quad (3)$$

where n is the material electron number density, I the material ionization potential, W_{\max} the maximum energy transfer to the electrons, u a screening function for inner shells important at low energies, and δ a density function due to polarization of the material by the passage of charged particles. For passage thru a material of finite thickness, a broad distribution of energy loss is formed, known as straggling. This distribution is shown in Figs. 2.71 and 2.72 of Rossi.⁽³⁵⁾ Following Rossi's prescription and using the values of Sternheimer⁽³⁶⁾ and Joseph⁽³⁷⁾ a most probable energy loss ϵ_p was thrown:

$$\epsilon_p = \frac{A t \rho}{\beta^2} \left[B + 1.06 + 2 \ln \frac{p}{m_\mu} + \ln \frac{A t \rho}{\beta^2} - \beta^2 - \delta + S \right]$$

$$A = \frac{2\pi N_0 e^4 \beta^2}{m_e v^2 \rho} = 7.15 \times 10^{-5} \frac{\text{GeV}}{\text{g/cm}^2} \quad [\text{for iron}] \quad (4)$$

$$B = \ln \frac{m_e}{I} = 15.64$$

$$\delta = \begin{cases} 0.0443 \beta^2 \left(\frac{E}{m_\mu}\right)^{1.73} & ; \frac{E}{m_\mu} < 4 \\ 10 [0.043 - 0.730(x-1) - 0.188(x-1)^2] \\ \quad + 2 \ln \frac{E}{m_\mu} - 4.3 & ; 4 < \frac{E}{m_\mu} < 100 \quad (5) \\ 2 \ln \frac{E}{m_\mu} - 4.3 + (3.8 + 3.33 \times 10^{-4} \left(\frac{E}{m_\mu}\right)^2)^{-1} & ; \frac{E}{m_\mu} > 100 \end{cases}$$

$$x = \log_{10} \frac{E}{m_\mu}$$

$$b = \lambda = 1.48$$

$$S = \frac{1}{4} \frac{W^2}{E_\mu^2}$$

$$W = \frac{E_\mu^2}{m_\mu} / \left(\frac{2m_\mu}{m_e} + \frac{E_\mu}{m_\mu} \right) \quad (6)$$

$$\Delta_o = \frac{0.3Zm_e b t \rho}{A \beta^2} .$$

Fits to the distribution in Rossi in four regions in terms of the variable $x = \frac{\epsilon_p - E}{\Delta_o}$ (Table IV-2) have been made and the integral probability in the regions computed. Based on these normalized integrals the region in which an energy loss would be made was chosen (randomly) and the ionization energy loss for the desired material thickness was computed.

Table IV-2. Fits to Ionization Loss

Region 1: Probability fraction 0.094

$$f(x) = 0.4662 e^{(x+1.878 \cdot 10^{-4})} \cdot 0.4662$$

$$-4.0 \leq x < -0.75$$

Region 2: Probability fraction 0.378

$$f(x) = \frac{1}{(2\pi)^{\frac{1}{2}}} e^{\left(\frac{-x^2}{2 \cdot 0.9705^2}\right)}$$

$$-0.75 \leq x \leq 0.75$$

Region 3: Probability fraction 0.453

$$f(x) = 0.003672 \cdot x - 0.08318 + 0.61186/x - 0.25295/x^2$$

$$0.75 < x \leq 9.0$$

Region 4: Probability fraction 0.075

$$f(x) = \frac{1}{x^2}$$

$$9 < x < \frac{E_0 - \epsilon_p - m_\mu}{\Delta_0}$$

$$x = \frac{E - \epsilon_p}{\Delta_0} \quad \epsilon_p \text{ and } \Delta_0 \text{ defined in the text}$$

The energy loss due to muon bremsstrahlung, the radiation of a real photon by the muon, was modeled after the work of Tsai.⁽³⁸⁾ The probability of a bremsstrahlung is a function of the muon energy, given by the equation

$$P(E) = \frac{N_A}{A} \rho t \sigma_B \quad (7)$$

where

$$\sigma_B = \int \frac{d\sigma_B}{dy} dy = \frac{\alpha^3}{m_\mu^2} \int \frac{1}{y} F(y) dy$$

$$F(y) = \left(\frac{4}{3} - \frac{4}{3}y + y^2\right) \left(z^2(\phi_1 - \frac{4}{3} \ln z - 4f(z)) + z(\psi_1 - \frac{8}{3} \ln z)\right) \quad (8)$$

$$f(z) = 1.202\left(\frac{z}{137}\right)^2 - 1.0369\left(\frac{z}{137}\right)^4 + \frac{1.008\left(\frac{z}{137}\right)^6}{\left(1 + \left(\frac{z}{137}\right)^2\right)}$$

$$y = \frac{\text{photon energy}}{\text{muon energy}} .$$

ϕ_1 and ψ_1 are Bethe-Heitler screening functions. To shorten computing time, a fit to $P(E)$, which is accurate to within 1.2%, was used rather than this exact expression. If a thrown random number was greater than this probability, no bremsstrahlung loss was calculated. Otherwise a photon energy in the distribution $\frac{1}{y}F(y)$ was chosen. This energy loss occurred about 2-3% of the time.

Pair production of electrons by the incident muon was calculated on an average basis only since straggling is

highly suppressed ($\sim v^{-3}$) and what is known about the straggling is only approximate.⁽³⁹⁾ This contribution to energy loss is always present and is

$$\frac{dE}{dx} = \frac{N}{A} \frac{m_e}{m_\mu} \frac{(\alpha z r_e)^2}{\pi} E_o \left(19.3 \ln \frac{E_o}{m_\mu} - 53.7 f \right)$$

; $E_o < 20 \text{ GeV}$

(9)

$$f = \left(\frac{16}{9} \ln \frac{183}{z^{1/3}} + 1 \right) / \left(\frac{16}{9} \ln \frac{E_o}{m_\mu} - \frac{14}{9} + \ln 2 \right)$$

; $E_o > 20 \text{ GeV}$

where f is due to screening by atomic electrons. The total energy lost by the muon in traversing a thickness t of material was the sum of the contributions from these three processes.

Multiple scattering and the muon energy loss were computed together for a given step thru the target or spectrometer. Before the interaction point, the muon was straggled, then multiple scattered and straggled again over the course of a full step. After the interaction point it was multiple scattered and then straggled for the first and only time for each step. Both these methods gave the same distributions of multiple scattering and energy loss for traced muons.

C) Radiative Corrections

Several higher order corrections to the measured cross section must be performed in order to arrive at the final parametrization of F_2 . These processes, the most important of which are shown in Fig. IV-1, disguise themselves as an interaction at given E_0 or E' , when in reality they may have been a lower E_0 or higher E' process associated by the emission of a photon away from the virtual photon-muon vertex of the primary deep inelastic scatter. Collectively, the corrections to the measured cross section due to these processes and necessary to arrive at the true deep inelastic cross section are known as radiative corrections.

If the cross section is measured at a point A in Fig. IV-2, the value measured will be larger than the true cross section because of radiative contributions from events in the shaded triangle ABC.⁽⁴⁰⁾ The region is bounded by the lines $\cos \theta_\gamma = \pm 1$ and the elastic scattering peak, where θ_γ is the angle, in the scattered muon-virtual photon plane, of the emitted photon with respect to the virtual photon.

Rather than calculate the exact correction^(41,42) for every simulated muon, the value of the radiative correction on a $30 \times 30 \times 10$ grid in E' , θ and E_0 respectively, was calculated by the effective radiator method⁽⁴¹⁾ and then linearly interpolated to the specific values needed for a given muon. This method was compared to the exact method of Mo and Tsai⁽⁴¹⁾ and the ratio was found to be accurate to one or two percent with deviations becoming larger for very low E' .⁽⁴³⁾

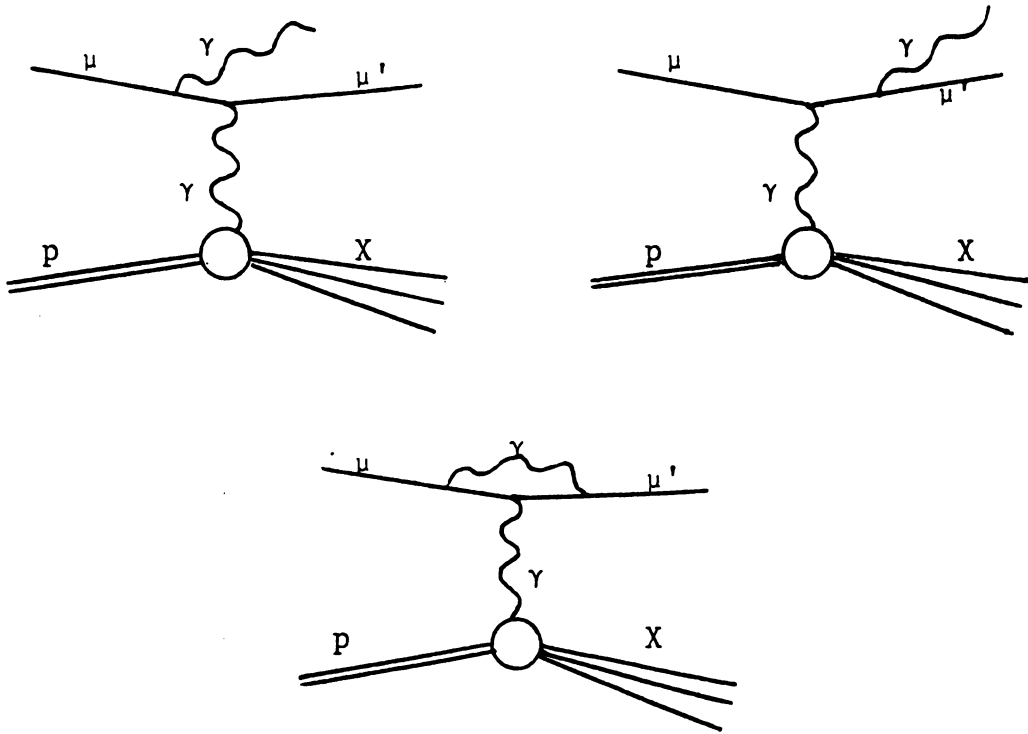


Figure IV-1. Radiative Process Diagrams

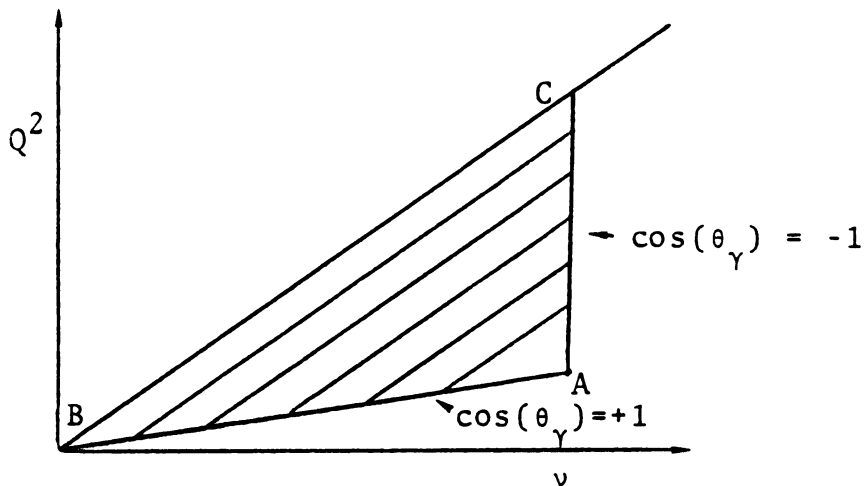


Figure IV-2. Triangular Region Contributing to Radiative Correction

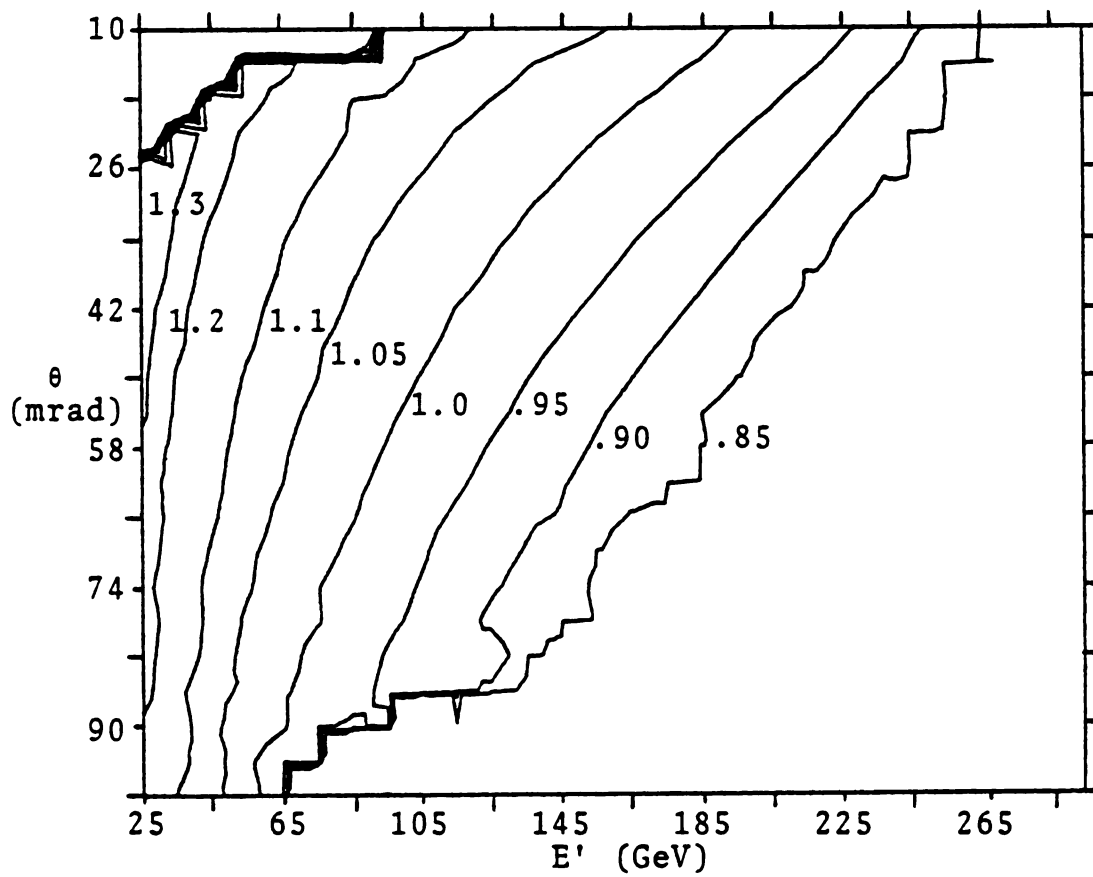


Figure IV-3. Contour Plot of Radiative Correction Weight Factor

The value of the radiative correction was

$$R = \frac{\left(\frac{d^2\sigma}{dE d\Omega}\right)_{el} + \left(\frac{d^2\sigma}{dE' d\Omega}\right)_{inel}}{\left(\frac{d^2\sigma}{dE' d}\right)_{QCD}} \quad (10)$$

where the subscripts el, inel and QCD imply the elastic peak and inelastic radiative contributions and the Buras QCD⁽⁹⁾ parametrization of the cross section, respectively. The event weight was multiplied by this factor to get the corrected weight. Fig. IV-3 shows the value of R as it contributes to the Monte Carlo event weight, as a function of E' and θ .

D) Wide Angle Bremsstrahlung (WAB) Background

D. Yennie⁽⁴⁴⁾ pointed out that wide angle bremsstrahlung can be an important background process in deep-inelastic lepton scattering. In this process a bremsstrahlung photon is emitted at a larger angle than usually considered ($t \gg m_\mu^2 E_\gamma / (E_0 - E')$). Momentum conservation requires the muon to also undergo an angular deflection which can then be misinterpreted as a deep-inelastic scattering.

The ratio of the cross section for WAB to the deep-inelastic (DI) cross section can be written⁽⁴⁵⁾ as,

$$\frac{d\sigma^{WAB}}{d\sigma^{DI}} \approx \frac{z^2 \alpha}{\pi A} \frac{y^2}{1-y} \frac{G(Q_{11}^2)}{v W_2^2} \frac{(1-y + \frac{1}{2} y^2)}{(1-y + \frac{1}{2} \frac{y^2}{1+R})} \quad (11)$$

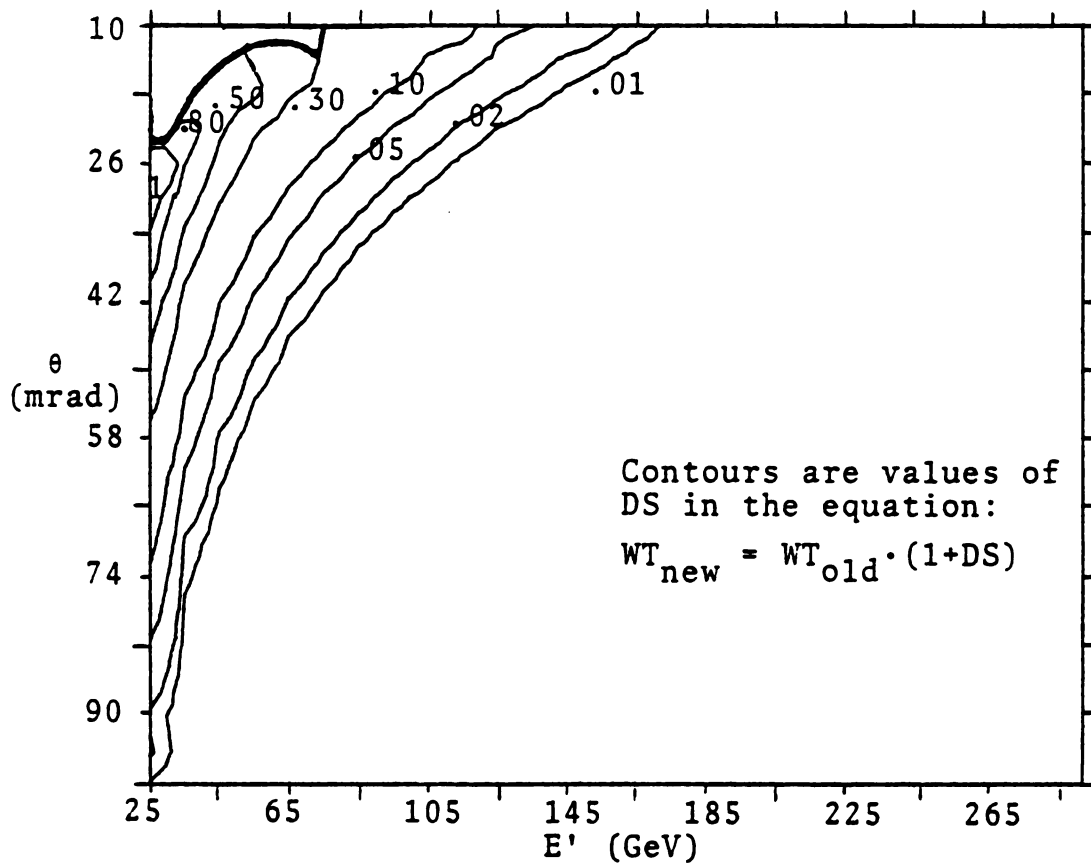


Figure IV-4. Contour Plot of Wide Angle Bremsstrahlung Background Factor

where

$$G(Q_{\perp}^2) = \int_0^{\infty} \frac{dQ_{\perp}^2 Q_{\perp}^2 F^2(Q_{\perp}^2 + Q_{\parallel}^2)}{(Q_{\perp}^2 + Q_{\parallel}^2)^2} \quad (12)$$

F^2 is the nuclear form factor and directions are defined with respect to the beam direction. The nuclear form factor integral was approximated by the fit

$$G(Q_{\perp}^2) = e^{\left(\frac{-68.062}{\omega^2} - \frac{29.107}{\omega} + .70671 + .011969\omega - .49948 \cdot 10^{-4} \omega^2 \right)} \quad (13)$$

which is accurate to less than 1% for omega between 5 and 100. The effect of this background correction is shown in Fig. IV-4.

E) Nuclear Fermi Motion

Since the target iron nuclei are not at rest in the lab frame, but the cross section is calculated in an assumed nucleon rest frame (NRF), the effect of the nuclear motion on the measured cross section must be considered. This was done by allowing the nucleon a Fermi gas motion described by the probability distribution

$$W(P) = \frac{p^2}{1 + e^{((P^2 - P_F^2)/2MkT)}} \quad (14)$$

where $kT = 0.492/56$ GeV, $P_F = 0.259$ GeV and M is the proton mass. The spatial orientation of this Fermi momentum was randomly applied, and the momentum range was limited to $|P| \leq 2 \cdot P_F$.

Once the transformation to the nucleon's rest frame had been performed, the cross section could be calculated. This was done using an effective nucleon mass of 0.9086 GeV which was used to determine the energy at which the interaction occurs

$$E = E_{inc} \cdot \frac{M_{eff}}{M_p} \quad (15)$$

This effective nucleon mass conserves the atomic weight of iron for this Fermi momentum distribution. (28)

F) The Incident Beam

Because of the holes in the toroidal magnets, the spectrometer acceptance depended on where the beam entered the target. To best simulate the data then, a beam representative of that actually entering the target was used in the monte carlo. The pulser trigger information helped to accomplish this. These triggers, collected from the data tapes and merged into three beam tapes (Table IV-3), were input to the MUDD program at event generation time.

Study of the beam distributions from data events and monte carlo events showed that for beam track radii less than 8 cm, angles less than 2 mR, and extrapolated positions at BVIII less than 10.5 cm in radius the beam distributions

Table IV-3. Beam Tape Format.

Total Record Length	100 words
Words Written/Event	10 words
Events on Each Record	10 events

Breakdown of 10 words

- 1) Data run number
 - 2) Data event number
 - 3) Track slope in x-z plane
 - 4) Track slope in y-z plane
 - 5) Track x-position at upstream target edge
 - 6) Track y-position at upstream target edge
 - 7) χ^2 for fit in x-view
 - 8) χ^2 for fit in y-view
 - 9) Contents of data event DCR #3
 - 10) Beam track energy
-
-

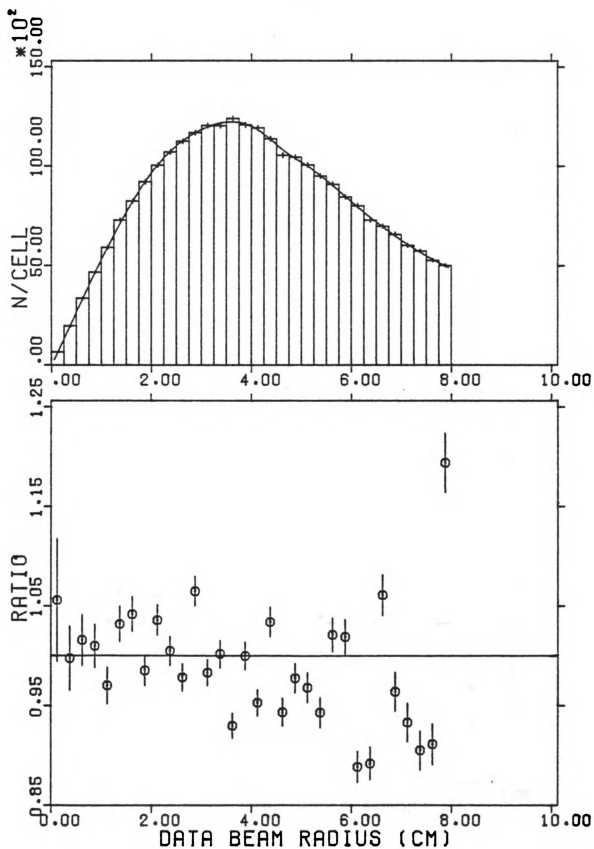


Figure IV-5a. Data Beam Distribution and Comparison to Monte Carlo

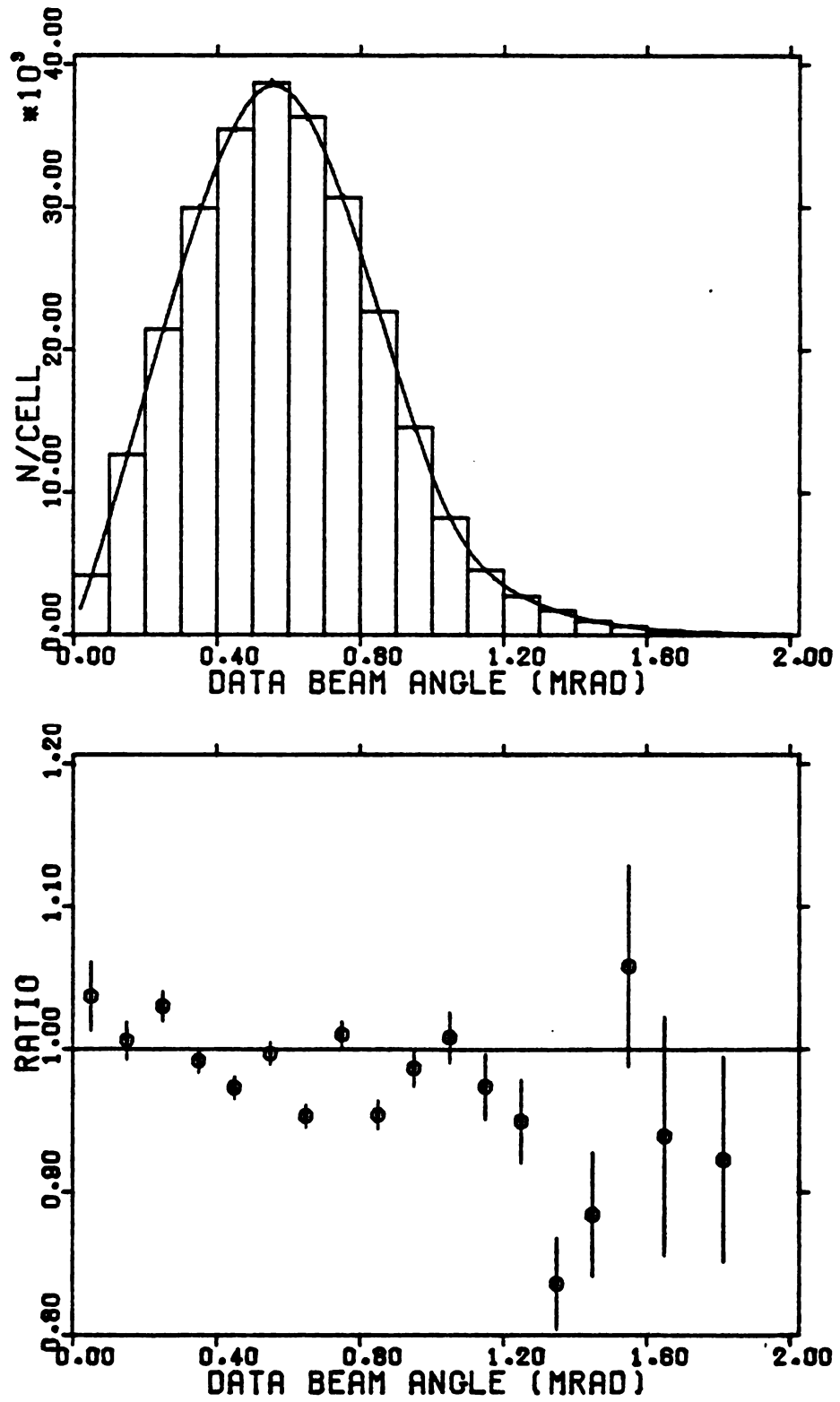


Figure IV-5b. Data Beam Distribution and Comparison to Monte Carlo

agree with each other (Fig. IV-5a-b). Events with beam tracks outside of this acceptable region were rejected and the incident fluxes for both data and monte carlo were corrected.

G) Computer Program Description

The program itself was run in three stages. The first stage used as input the target density, length, and radiation length as well as the position and composition of all spectrometer elements. A beam tape containing information from the experiment's beam sampling pulser trigger was read to determine where an incident muon would enter the target. A random number was thrown to determine where in the target this muon would undergo a deep-inelastic scatter. The muon was then traced to this z-position in a maximum of ten steps, each of a minimum length of 5 cm. While stepping to this point, and during all later target stepping, the muon would undergo simulated multiple scattering and energy loss (section IV-B). If at any time the muon lost all its energy, it was deemed to have failed a hardware cut and rejected.

At the interaction point, a Fermi-momentum vector (section IV-E) was determined, and quantities were relativistically transformed into a reference frame where the interacting nucleon was at rest. In this frame, an energy and an angle for the scattered muon were chosen (section IV-H), the currently favored weights were applied, and a transformation back to the lab frame was performed.

With the event fully generated the beam cuts could be performed. These cuts, also performed on the data, ensured that the beam distributions (angles from the axial direction, energy and position) of the accepted events were identical. Deviations between MUDD and MULTIMU beams would result in a systematic deviation of the determined structure function from the true value. The total weight of events cut in this manner was used to correct the usable flux by the equation

$$\text{usable flux} = \text{thrown flux} \times \left(1 - \frac{W_{\text{CUT}}}{W_{\text{TOT}}}\right) \quad (16)$$

where W_{CUT} = sum of beam cut event weights and W_{TOT} = sum of all thrown event weights. Events with an acceptable beam were then passed to further tracing.

From interaction to the face of the first spectrometer magnet, 5 cm steps were used, while for the remainder of the spectrometer, a new step size was calculated. A check of the muon energy was made to determine if a smaller step was necessary, since low energy, large bend tracks need to be stepped more carefully to avoid a systematic positional deviation which would increase with distance into the spectrometer. For this purpose the E-26 monte carlo criterion was used which determined a step small enough that a 5 GeV muon in the Fermilab E-26 spectrometer configuration⁽⁵⁾ no longer deviated in position when it reached the downstream spectrometer end, yet large enough that computation time was not excessive. A step determined by this method which was

Table IV-4. Stepping Process Cuts

A. Hardware Flagged Cuts

- 1) Not all three trigger banks struck
- 2) μ stops or leaves spectrometer before SC trigger bank
- 3) BV3 and either of BV1 or BV2 struck

B. Software Flagged Cuts

- 1) Scattered μ energy less than 10 GeV at hadron shield
- 2) $Z_{MIN} < Z_{abs} = -250.0$ cm
- 3) $Z_{MIN} > Z_{abs} = 600.0$ cm
- 4) $DMIN =$ distance of closest approach of incident and scattered (smeared) muon track
 $DMIN > MINIMUM (2.0+15 \cdot R8, 10.0$ cm)
 $R8 =$ track radius at WSC8
 $R =$ track radius at a given point (z)
- 5) $R < 16.8$ cm at SA'
- 6) $R < 17.9$ cm at SB'
- 7) $R < 18.0$ cm at SC'
- 8) $R < 17.5$ cm at BV1 and $R < 16.7$ cm at BV3
- 9) $R < 18.0$ cm at BV2 and $R < 16.7$ cm at BV3
- 10) Muon crosses spectrometer axis between SA' and BV3--
check for change to 180° opposite quadrant as compared to that at SA'

C. Beam Cuts

- 1) Track radius < 10.0 cm ($z = 0$)
 - 2) Track radius < 10.5 cm ($z = BVIII$)
 - 3) Track angle < 0.002 Radians
 - 4) $|E_0 - 270.0| \leq 27.0$ GeV
-
-

Table IV-5. Accepted Event Tape Format

Total Record Length	510 words
Words Written/Event	17 words
Events on Each Record	30 events

Breakdown of 17 Words

- 1) Event weight
 - 2) Beam track x-position at $z = 0$
 - 3) Beam track y-position at $z = 0$
 - 4) Beam track angle, x-projection
 - 5) Beam track angle, y-projection
 - 6) Incident muon energy at upstream target edge (E_0)
 - 7) ZMIN--z position of closest approach of incident and scattered (smeared) muon tracks
 - 8) Angle scattered muon makes r.e. incident muon, measured at the hadron shield
 - 9) E of scattered muon measured at the hadron shield
 - 10) Energy of incident muon in the target nucleons rest frame ($E_0(\text{NRF})$)
 - 11) Angle of scatter in the NRF ($\theta(\text{NRF})$)
 - 12) Energy of scattered muon in the NRF ($E'(\text{NRF})$)
 - 13) Radiative correction weight factor
 - 14) Run x 100000 + event from which beam track came
 - 15) $F_2 = vW_2$ used in the event generation
 - 16) Incident muon energy in the lab frame at the interaction point ($E_0(\text{LAB})$)
 - 17) Scattered muon energy in the lab frame at the interaction point ($E'(\text{LAB})$)
-
-

Table IV-6. Generated Event Tape Format

Total Record Length	17 words
Words Written/Event	17 words

Word Breakdown

- 1) Event weight
- 2) Beam track x-position at $z = 0$
- 3) Beam track y-position at $z = 0$
- 4) Beam track angle, x-projection
- 5) Beam track angle, y-projection
- 6) Incident muon energy at upstream target edge
- 7) *Scattered muon energy at the hadron shield
- 8) *Angle scattered muon makes r.e. incident muon, measured at the hadron shield
- 9) Thrown interaction position, z-direction
- 10) E_0 (NRF)
- 11) E' (NRF)
- 12) θ (NRF)
- 13) Radiative Correction weight factor
- 14) E_0 (LAB)
- 15) E' (LAB)
- 16) Logical variable, FALSE, unless muon cut on a hardware cut
- 17) Integer flag indicating cut classification
 - 1 = accepted
 - 2 = software cut
 - 5 = hardware or energy of μ too low

*Variable set to zero for a beam cut event

smaller than 5 cm was used instead of the previous 5 cm stepping which was otherwise retained. Cuts applied during the stepping process are listed in Table IV-4.

Events which were not cut were sent back to the main program and pertinent information was written onto an output tape, as shown in Table IV-5. In addition another output tape was maintained containing information from all events generated, including those cut because of their beam track. This tape format is shown in Table IV-6. The whole process was now repeated for a new muon until the maximum specified at the program beginning was reached, whereupon this first program stage terminated.

The second program stage calculated the radiative correction to the event weight (section IV-C), filled in the appropriate word for either the generated event tape or the accepted event tape, and wrote the block out to a new tape. The method used was a three-dimensional (E_0 , E' , θ) linear interpolation of a table previously written for this purpose. The table contained the radiative correction value at specific values of the variables E_0 , E' and θ , measured in the rest frame of the target nucleon. If values were returned with the radiative event weight correction less than 0.84, then the correction was calculated by the same method used to generate the table, since for these events the interpolation was not accurate.

The third program stage performed the requested resolution smearing on the accepted events, applied kinematic cuts,

Table IV-7. Smearred Event Tape Format

Total Record Length	459 words
Words Written/Event	153 words
Events/Record	3 events

Breakdown of 153 Words

- 1) F_2
 - 2) E_0 (NRF)
 - 3) E' (NRF)
 - 4) θ (NRF)
 - 5) E' (LAB)
 - 6) E_0 (LAB)
 - 7) ZMIN
 - 8) E_0
 - 9) Number of resolution smears (max 36) this event
 - 10) E' at hadron shield, first smear
 - 11) $\sin(\theta)$ at hadron shield, first smear
 - 12) $x = Q^2/2Mv$ for first smear
 - 13) WEIGHT for first smear
 - ⋮
 - 150) E' at hadron shield, 36th smear
 - 151) $\sin(\theta)$ at hadron shield, 36th smear
 - 152) x for 36th smear
 - 153) WEIGHT for 36th smear
-
-

Table IV-8. Third Stage Program Cuts

-
-
- 1) $40 < E' < 325$ GeV
 - 2) $0.010 < \theta$ Radians
 - 3) $1 < Q^2 < 500$ (GeV/c)²
 - 4) Beam Track Radius < 8.0 cm
-
-

and wrote an output tape in preparation for comparison to the data. At this stage reweighting the events could be performed, if desired, or additional cuts applied. The output tape here was similar in structure to the final data event output tape, but contained additional information on the actual kinematic variables of the deep-inelastic scatter (Table IV-7).

Using this procedure a total of 450,000 muon paths were traced, of which 206,900 passed the tracing cuts of Table IV-2. The resolution smearing and other third stage cuts (Table IV-8) allowed a final total of 200,150 events with up to 36 smears each to be written to output tapes. The analysis used in chapter five is based upon these tapes.

H) Event Weighting

There are two basic methods of simulating a distribution such as that of a cross section. The first is to actually select events in proportion to the cross section. For example, if one wishes to throw an exponentially decaying distribution, one normalizes the kinematically accessible region of the exponential by the maximum ordinate value it attains in this region, then for a given value of the abscissa, which is randomly selected, a second random variable is thrown. If the height of the normalized curve exceeds the random value [range 0 to 1] then the event is deemed acceptable and the track tracing can proceed. Otherwise, a new abscissa value is chosen and the process is repeated.

This method, used by the E-26 monte carlo program, results in all scattered muons having a unit weight just as for the data, since the rate of occurrence of these simulated muons is exactly proportional to the cross section.

The second method, which was used by MUDD, is to randomly throw kinematic variables, and then to weight the event by the probability of its occurrence (the cross section). In this way there was no iterative repetition in search of acceptable values of E' and θ . To aid statistical stability, speed execution time, and approximate the kinematic acceptance, the scattering angle was not thrown uniformly over the experiment's usable kinematic range. It was instead thrown uniformly from 8 mR to 20 mR and then as a falling distribution from 20 mR to 150 mR. This approximated the cross section somewhat which falls as θ^{-3} . The procedure was to throw one random number to determine which angular region will be used. A value less than 0.409092 meant the low angle region would be used, a higher value chose the large angle region. For the low angle region, a second random number was thrown (V_{RAN}) and the angle used was

$$\theta = 0.008 + V_{\text{RAN}} 0.012 \quad . \quad (17)$$

Since any value of theta in this region had the same probability of occurrence as any other, all such events were assigned a weight factor (W_{θ}) of 0.0293333. For the high

angle region a second random number was again thrown, but the assigned angle was

$$\theta = \frac{1.0}{\frac{1.0}{0.020} - V_{\text{RAN}} \left(\frac{1.0}{0.020} - \frac{1.0}{0.150} \right)} \quad . \quad (18)$$

The weight factor for such an event was

$$W_{\theta} = 73.3332 \cdot \theta^2 \quad . \quad (19)$$

The weight factor in either case was the inverse of the probability of occurrence of the chosen value of θ so that the total probability of choosing some angle to scatter thru was exactly 100%.

The scattered muon's energy (E') was thrown as a uniform distribution between 20 GeV and the energy of the incident muon (E_0). A weight factor ($W_{E'} = E_0 - 20.0$) was then assigned such that probability was again conserved, i.e., there was a 100% probability of throwing some value of E' .

The form of the cross section used was a variation of Eqn.(I-14) of chapter I which took into account the average density and total length of the target ($\bar{\rho}$ and L) and the total flux of muons the program was expected to simulate (F). This cross section formula was (N_0 is Avogadro's number)

$$\frac{d^2\sigma}{dE'd\theta} = \sigma_{\text{THROWN}} = 8\pi F \alpha^2 \bar{\rho} L N_0 \cdot (\hbar c)^2 \cdot \left(\frac{E' \cdot \sin(\theta)}{y \cdot (q^2)^2} \right) \cdot v W_2 \cdot \left(1 - y + \frac{1}{2} \frac{y^2}{(1+R)} \right) \quad . \quad (20)$$

The final event weight used, at this stage of the program, was just $WEIGHT = W_{E'} \cdot W_{\theta} \cdot \sigma_{THROWN}$. This weight, modified by the wide angle bremsstrahlung correction (section IV-D) was the weight written out on the first stage output tape. Since by this formulation each thrown event was weighted as if it were the only scattered muon to result from the total input flux, a normalization factor equal to the total number of interactions thrown must be applied to the results.

I) Geometric Acceptance and Resolution

Previously, monte carlo events were tracked thru the spectrometer, recording spark positions at all spark chambers. These sparks were then smeared by a spark resolution function, and then turned off or left on depending on the comparison of a random number to the measured efficiency of the chamber module. Sparks appearing in regions where the reconstruction program would not look, such as the toroid hole region in the back five spark chambers, were also discarded. The remaining sparks were then fit as if this were a real data event.

The MUDD program does not fit events, but rather takes an event which has passed all geometry cuts and then smears this event in E' and θ using a gaussian function. Using the E-26 monte carlo, suitably modified, events were started thru the spectrometer with specific values of E' and θ as measured at the hadron shield. These tracks were fit using the standard event fitting program and the resulting

distributions in $1000/E'_{FIT}$ and θ were fit to gaussian forms. This procedure was followed for $E' - \theta$ pairs on a rectangular grid for $8 < \theta < 100$ mR and $20 < E' < 300$ GeV.

Four values were extracted for each grid point by this procedure, the mean of the fit gaussians, the width of the θ distribution in mRad and σ/μ in percent for the $1000/E'$ distribution. These values were entered into four grid surfaces which were then parametrized using a two-dimensional B-spline representation.⁽⁴⁶⁾ Using this representation the values of any of the above four parameters could be found at any $E' - \theta$ pair within the limits of the grid.

These four surface representations were input to the third stage, resolution program and used to smear accepted events. Figures IV-6 thru IV-8 show three surfaces evaluated in this manner. Also shown in Figs. IV-9 and IV-10 are the spectrometer acceptance found in the same way.

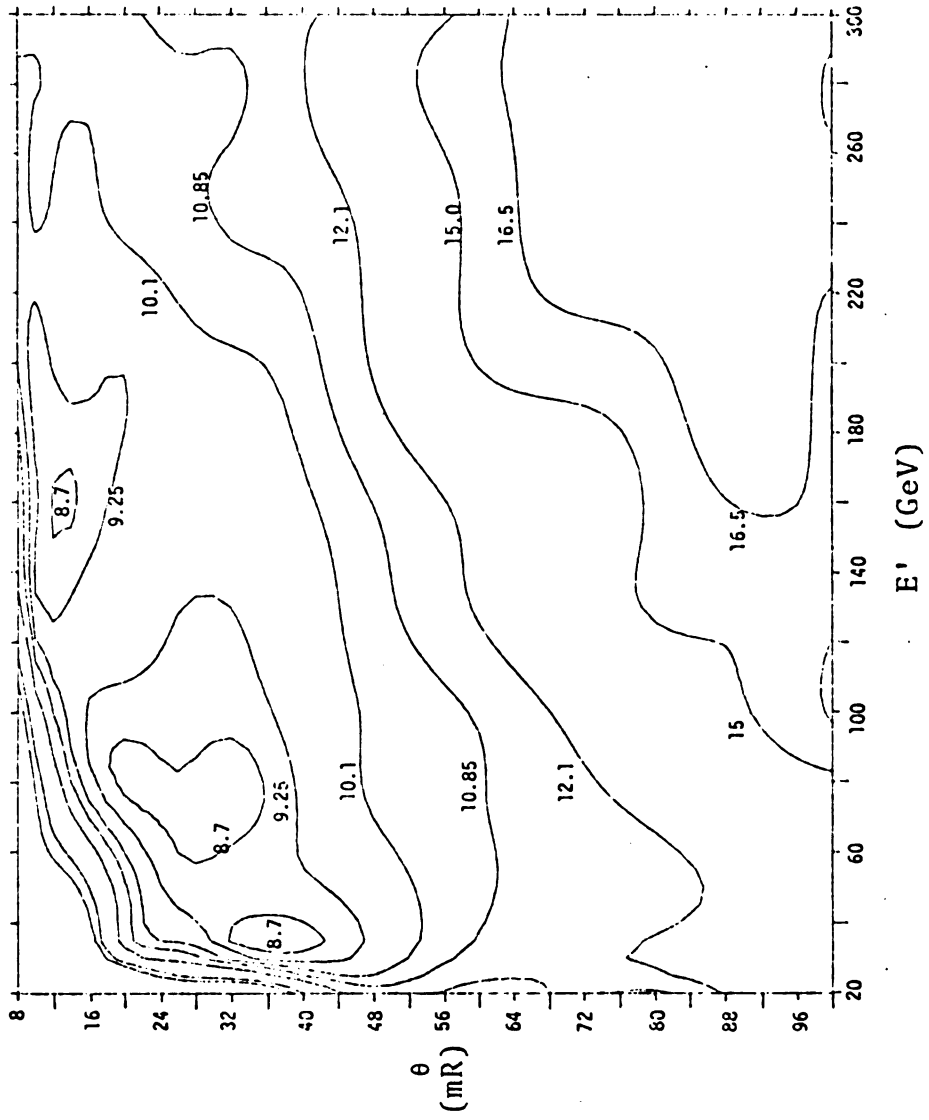


Figure IV-6. Contour Plot of $1/E'$ Resolution (percent)

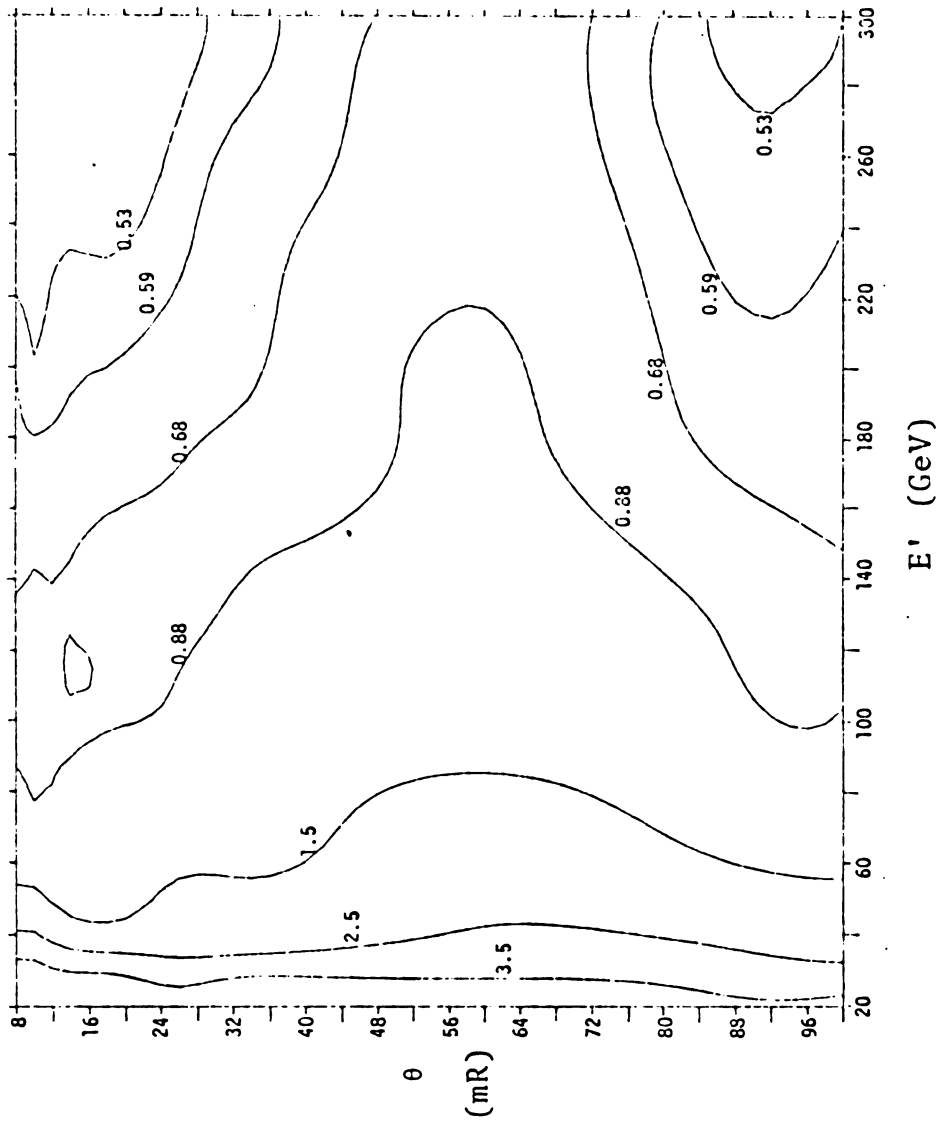


Figure IV-7. Contour Plot of Theta Resolution (mR)

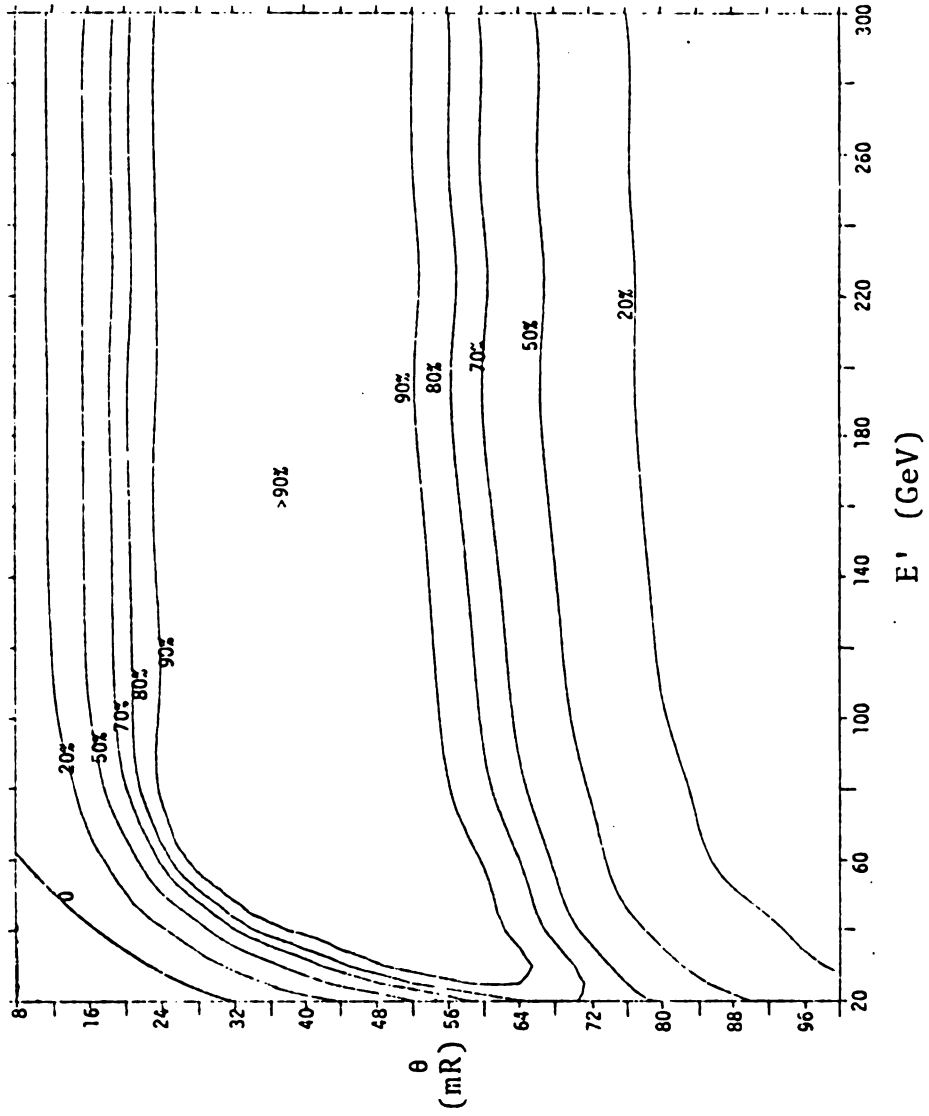


Figure IV-9. Hardware Acceptance Contour Plot

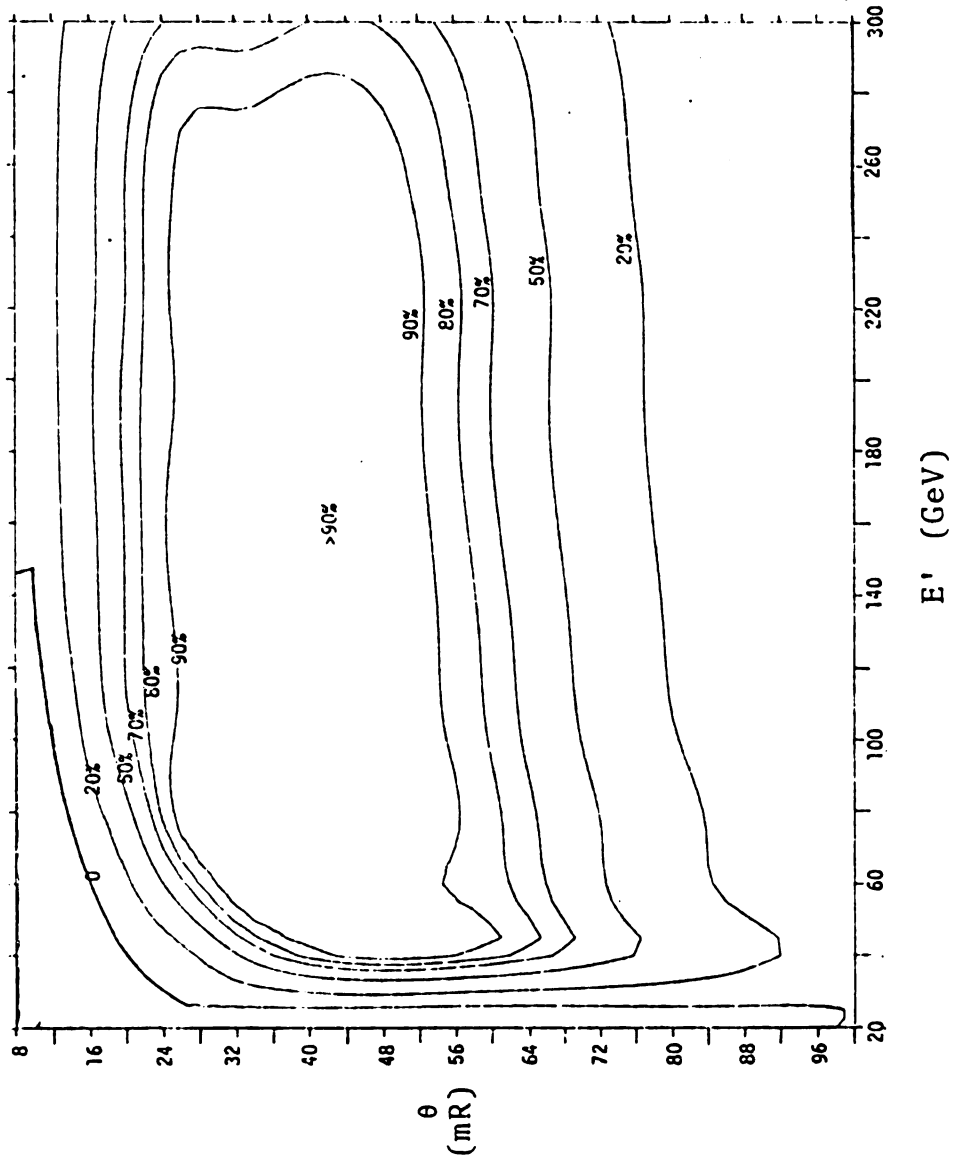
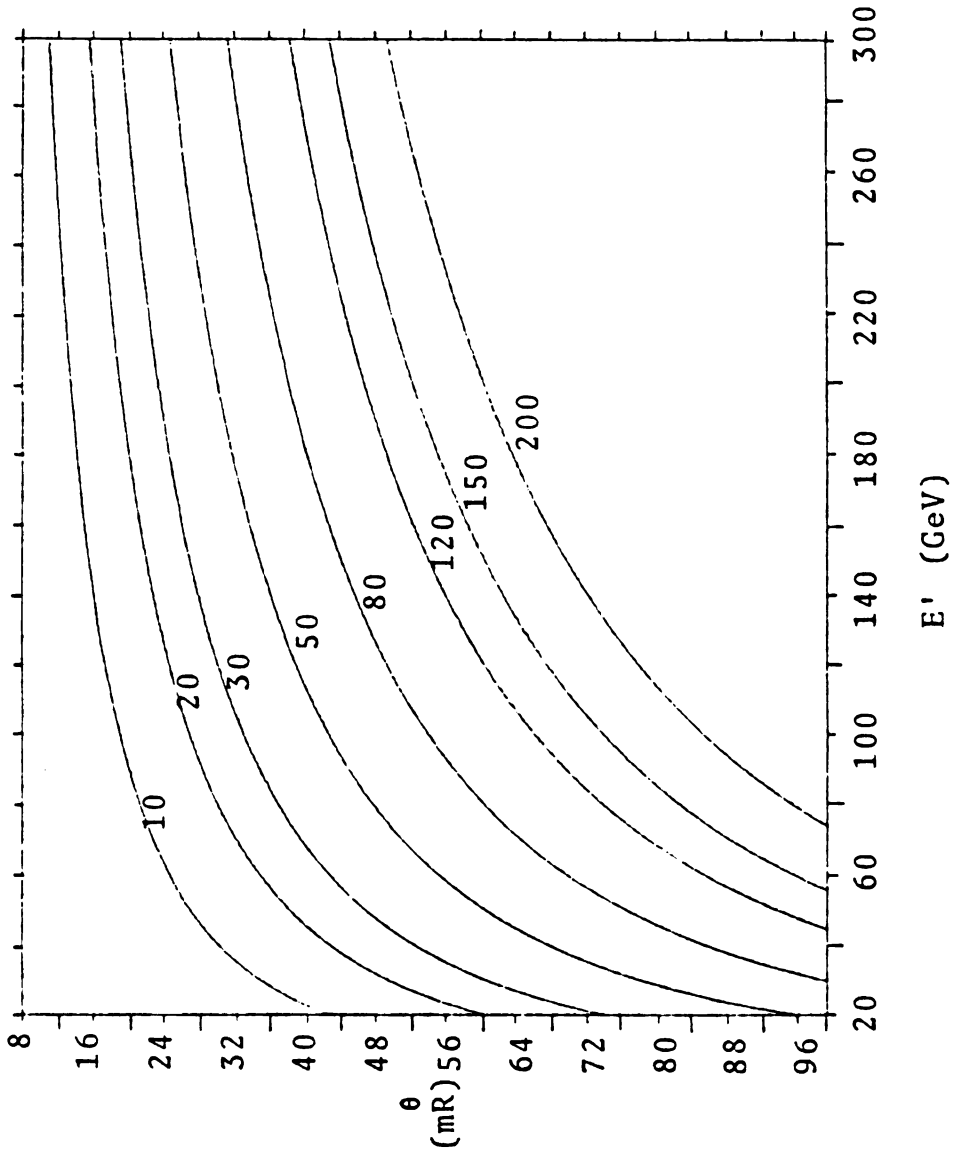
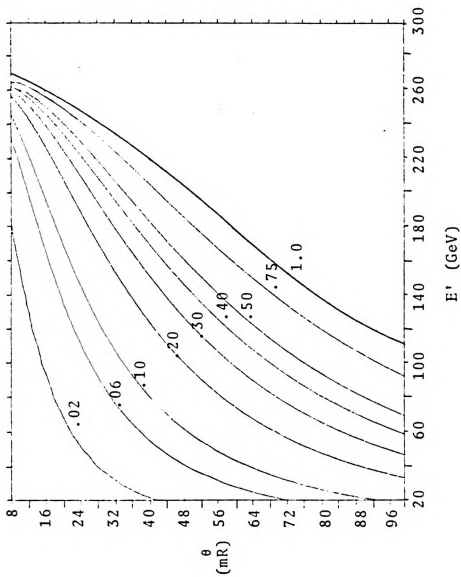


Figure IV-10. Software Acceptance Contour Plot

Figure IV-11. Contours of Constant Q^2 Values

Figure IV-12. Contours of Constant x Values

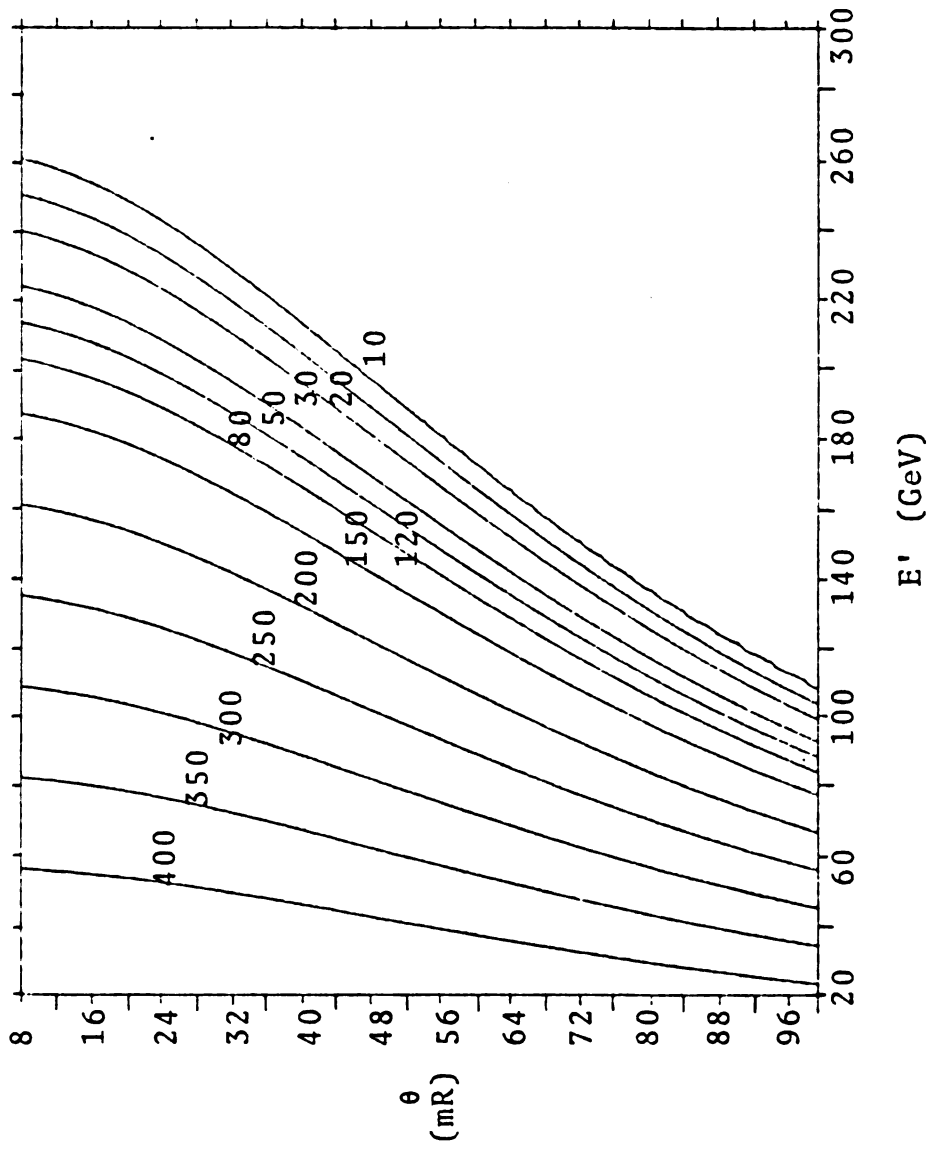


Figure IV-13. Contours of Constant W^2 Values

CHAPTER V

ANALYSIS PROCEDURE

A) Normalization by Flux

As was noted previously, the number of deep-inelastic interactions which can be expected to occur is dependent on the flux of muons onto the experimental target, i.e. on the total number of muons transported to our target during the entire course of the data taking. This quantity, labelled B_{EVG} , was counted continuously by a scaler during the experiment, and updated on the data tape as each event was written onto it. The value in this scaler was too large, since it did not allow for the incidence of two muons in the same r.f. bucket (sec. II-A), one of which scatters, the other not, nor did it allow for the non-zero accidental rate⁽²⁷⁾ of the beam veto (a BV signal when BV should not really be present). Either of these conditions would veto a good deep-inelastic interaction, preventing it from being recorded. For this reason, the quantity $B \cdot \overline{BV}_{\text{d,EVG}}$ was used as the flux. The BV signal was delayed (d) 60 ns, equivalent to three r.f. buckets. If this signal was not present when a muon next set B_{EVG} , then the muon was also counted in the flux. The delayed BV

signal was used since any bucket had the same probability of containing a muon, and it could therefore simulate the two occurrences listed above while avoiding problems with hardware dead time. The scaler was gated live by the event gate since deep-inelastic interactions could only be successfully recorded when the event gate was live. For the 135 runs considered here, the total quantity of muons scaled was 1.2859×10^{10} .

Two types of hardware failure were not detected in the same on-line manner as the B_{EVG} correction, but were accounted later. These were complete failures of the spark chambers and the so-called branch diver CAMAC errors (BDERR) discussed in section II-M. These types of errors completely invalidated the trigger on which they occurred, so the flux was corrected downwards by the rate of their occurrence. This 1.51% correction changed the flux to 1.2665×10^{10} incident muons.

Three types of error other than these have been categorized, but there is no correction to the flux for their occurrence. The three types are pulser triggers ($B \cdot P_{EVG}$), triggers due to random electronic noise, and a category including triggers via halo muons and interactions outside of the target bounds. These types can be ascertained to be uninteresting, and a monte carlo simulation has shown that the occurrence of such triggers does not affect the total number of good deep-inelastic interactions when normalized by the computed value of the muon flux.

$\nabla = 22,000 \mu/\text{sec.}$ $\blacktriangle = 367,000 \mu/\text{sec.}$ $\nabla = 2,200,000 \mu/\text{sec}$
 $\circ = 110,000 \mu/\text{sec.}$ $\blacktriangle = 550,000 \mu/\text{sec.}$

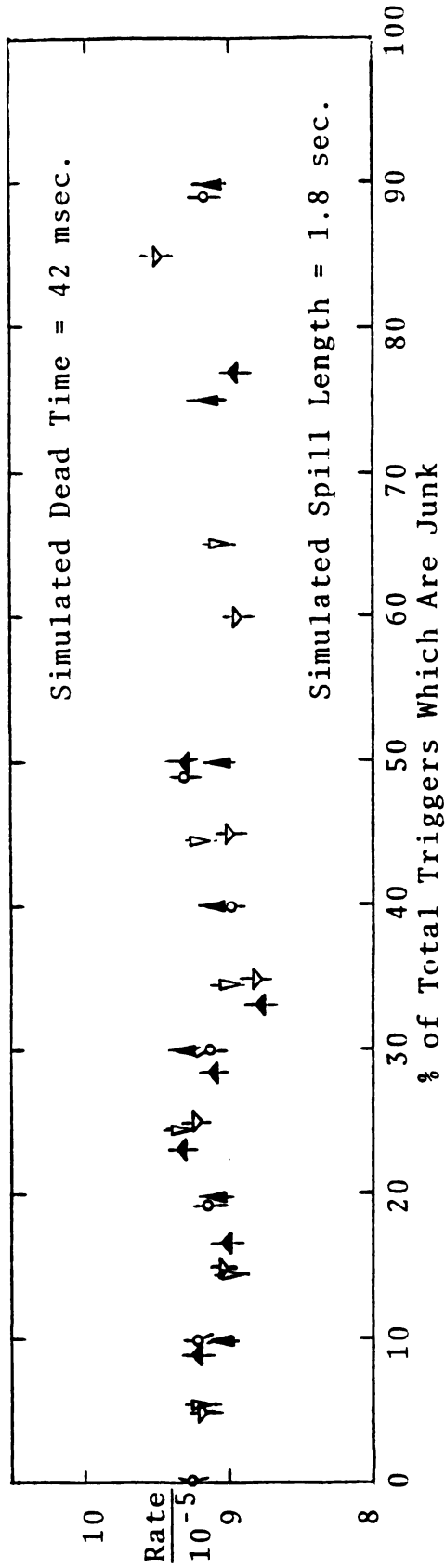


Figure V-1. FLUXSIM Program Results

Table V-1. Beam Distribution Limits

Limit	Description
1	Angle from axial less than 0.002 Radians
2	Extrapolated track radius from axis, measured at target center, less than 8 cm
3	$243 \text{ GeV} < E_0 < 297 \text{ GeV}$ (10% deviation from nominal value)
4	Extrapolated track radius from axis, measured at position of BV3, less than 10.5 cm

The reason is that such triggers close the event gate, and so do their own correction of the incident flux.

Two final types of occurrence also resulted in corrections to the flux. The first was a category of triggers where the incident muon track did not satisfy the criteria listed in Table V-1. The second was that class of triggers where zero or more than one beam muon track was found. Both these categories contain events wherein a portion of beam muons was rejected as unsuitable for use, and so the incident flux was corrected for that fraction rejected. These two brought the flux down to the value finally used, 9.186×10^9 incident muons.

For the monte carlo program MUDD, several of these corrections were unnecessary. Pulser triggers with bad incident energy or without just one beam track were not written onto the pulser trigger tapes, and the triggers with hardware failures were always ignored. The only flux correction necessary then was due to the same cuts on the beam track muon listed in Table V-1 for data events. These tracks, in order to simulate the effects of the chamber measurement error on their characteristic angles, positions, and energy, were smeared by gaussian functions for each monte carlo event. The angles were smeared 0.01 mrad, the x and y positions by 0.01 cm, and the energy by 0.3 GeV unless the energy was exactly 270 GeV. In this case only positions and angles were smeared since it was assumed this was a trigger where the energy was assigned to 270 GeV, the real energy

being unavailable. Since the monte carlo was assigned to generate a number of scattered muons equivalent to 1.0×10^{10} incident muons, the beam cut correction of 6.2% corrected this to 9.380×10^9 incident muons.

B) The Filter Program COMPARE

With the reconstructed and momentum-fit data events in hand, the task of comparison to the monte carlo predictions could begin. To do this, it was first necessary to eliminate from the event sample (a total of 860,037 events of the 1,364,000 taped triggers) those triggers in unstable geometric and kinematic regions. For example, scattered muon tracks which were too near the toroid holes were eliminated because the positions of the trigger bank counters SA, SB, SC, and the beam veto counters BV were uncertain by 1/4 cm. For safety then, circular cuts on the track radius were applied which radii were at a minimum 1/2 cm removed from the counter edges. Additionally, the number of triggers cut because of their beam track was tallied. All applied cuts are listed in Table V-2.

The order in which the cuts were applied is important. Triggers were first checked for proper beam distributions. These cuts were applied first since, in the cut accumulation, once a trigger failed, higher numbered cuts were not considered; the program simply skipped to the next trigger. To then get an accurate determination of the amount of beam lost in this way, these cuts must be applied first. This

Table V-2. Ordered List of COMPARE Program Cuts

Cut	Description	Triggers Cut
1		6,037
2	Cuts as listed in Table V-1	163,767
3		683
4		1,452
5	Junk Triggers*	34,358
6	Z-position (fit) of interaction (Z_{MIN}) within range $-250 \text{ cm} < Z < 600 \text{ cm}$	10,797
7	Minimum distance of approach of incident and scattered muon tracks (D_{MIN}) less than 5 cm	9,832
8	$\chi^2/\text{degree of freedom} < 10$	2,689
9	Track radius at trigger banks less than 16.8 cm (SA), 17.9 cm (SB), 18 cm (SC). Cut applied to fit muon track radius at nearest spark chamber to trigger bank (WSC 6-4 respectively).	334,647
10	Track may not cross axis into opposite spectrometer quadrant between WSC6 and WSC3	7,408
11	Scattering angle > 0.01 Radians	6,639
12	Energy of scattered muon in the range $40 \text{ GeV} < E' < 325 \text{ GeV}$	20,988
13	$Q^2 > 1 \text{ (GeV/c)}^2$	0
Total Reconstructed Trigger Sample		860,037
Total Triggers Cut		599,297
Total Accepted Events		260,740

*A junk trigger is one which could not be successfully fit, or which had fewer than one degree of freedom.

was also true in the monte carlo generation, where, once it had been determined that a beam track was in an unacceptable region, no further tracing thru the spectrometer occurred.

Geometric cuts were next applied. This corresponded to the monte carlo where, as muons were traced, information was accumulated on the track position at the various points in the spectrometer where cuts were applied to the data triggers. Failure to pass the cuts resulted in the monte carlo event rejection at this stage.

The final cuts applied were those on the track kinematics. In the monte carlo, the third stage, resolution program was where the simulation of the GETP track fitting was performed. This assignment of energy and scattering angle to the muon occurred after the monte carlo performed all other cuts, and this order was preserved in filtering the data triggers.

The order in which the geometric and kinematic cuts were applied was not important as far as the final data to monte carlo comparison was concerned. It did make the comparison easier to perform, and allowed optimal cut values to be determined without undue delay, for instance, due to a necessity to rewrite monte carlo output tapes, a tedious process.

One obvious difference between these two approaches is in how the cuts are applied. In the monte carlo, the exact position of the muon was always known, and was the quantity used in the position dependent cuts. For data triggers, the

most reliable quantity was the predicted track position from the momentum fit, since the muon position was not always known at every chamber. These two quantities are obviously not identical. A given track may pass a set of criteria based on the fit position, but fail on actual position, or vice versa. For a large number of scattered muons though, this difference minimizes, leaving no detectable trace in a comparison between the two methods. This is a result of the careful alignment of the spectrometer in which the distributions of actual minus fit spark positions were adjusted at all chambers to give mean values as close as possible to zero. The deviations from a mean of zero discovered for y-positions in the downstream--most six spark chambers (section II-E) were simulated in monte carlo runs so that no systematic error would be introduced.

Once a trigger was past the set of cuts, it was considered to be a good deep-inelastic event and its kinematic content could be accumulated. Three output tapes were maintained for this purpose. The first tape was merely a list containing the run and event numbers unique to each event. It was written in a computer output format, 13I10, which is thirteen run-event pairs per line written, 10 columns per pair, right justified in the field. Each pair was one number, equal to the run number multiplied by 100000 then added to the event number.

The second tape contained various non-kinematic bits of information on the event which were not really pertinent

Table V-3. Non-Kinematic Information, COMPARE Output Tape

Word	Information
1	E_0 , measured at upstream target face
2	Z_{MIN} (cm)
3	D_{MIN} (cm)
4	χ^2 /degree of freedom
5	Extrapolated beam track position at target center, x-z plane (cm)
6	Extrapolated beam track position at target center, y-z plane (cm)
7	Extrapolated beam track radius at target center (cm)
8	Projected beam track angle, x-z plane (mrad)
9	Projected beam track angle, y-z plane (mrad)
10	Axial angle of beam track (mrad)
11	E'_R , if event is in SLAC data region. This region is defined as
	$Q^2 < 15 \text{ (GeV/c)}^2$
	$\omega < 9$
	$Q^2 \cdot (\omega + 0.5) < 29.1$

Table V-4. COMPARE Analysis Tape Format

Record Length	500 words
Event per record	100 events
Words per event	5 words
Details for a Single Record	
Word	Content
1	E_0 , 1 st event, measured at upstream target face
2	E' , 1 st event, measured at the hadron shield
3	$\text{SIN}(\theta)$, 1 st event
4	x , 1 st event
5	Z_{int} , 1 st event
.	.
.	.
496	E_0 , 100 th event
497	E' , 100 th event
498	$\text{SIN}(\theta)$, 100 th event
499	x , 100 th event
500	Z_{int} , 100 th event

to the determination of the structure function. These data are listed in Table V-3. This output tape was rewound and compacted by a separate program at the termination of COMPARE, and then released.

The third tape written was the basis for all subsequent analysis. For each event, four words of kinematic information and one word of non-kinematic information were packed into a 500 word buffer and written onto the tape when the buffer filled. The tape format is shown in Table V-4. With the information included, any other kinematic variable desired could be calculated. In this way, accepted event information from 135 data tapes was packed into 45 files and written onto one, 2400 foot magnetic tape, ready for the next stage of analysis.

C) The Comparison of Data to Monte Carlo

To compare the 45 files of data events to the monte carlo distributions in a meaningful way, the difference between real and reconstructed kinematic variables must be understood. The reconstructed variables for the data events are those assigned through the GETP fitting process, wherein the value of scattered muon momentum was assigned which minimized a calculated χ^2 . The spectrometer E' resolution was about 10%, so there was a 70% probability that this assigned momentum was within 10% of the value which the muon actually scattered with. Only this reconstructed momentum, and similarly, the scattering angle, could be known for the data events.

For monte carlo events, the actual momentum was known at every point in its trajectory, thus, the real value of E_0 and E' , the incident and scattered muon energies, and θ , the angle through which the muon scattered, could be known, and were in fact retained in the information recorded for the muon. On the basis of the values of E' and θ , measured at the hadron shield, reconstructed values (E'_R and θ_R) for both variables were assigned using the known resolution functions. These resolution smeared values corresponded to the fit values determined for data events, without undergoing the time consuming fit procedure. For the monte carlo events then, both the reconstructed and real kinematic variables were known.

In the ideal situation, the momentum fitting procedure would determine values of momentum and angle which distributions would be centered at the actual values of these variables. An attempt was made to do this, but the shifts in mean induced by the fit were complicated functions of muon energy and angle. Consequently, this effort fell short of its goal of zero shifts in the means of the distributions.

For purposes of comparison between the samples of data and monte carlo, the only variables in common were the reconstructed energy and angle of the scattered muon, E'_R and θ_R , and the energy of the incident muon at the upstream face of the target, E_0 . In addition, other variables such as Q_R^2 and x_R could be constructed using these values. It was decided, then, to group events into cells in a kinematic

plane which axes were Q_R^2 and x_R . The size of the cells depended on the production rate of data events in that region of the plane. Generally, as many as a thousand events per cell were obtained in high yield portions of the plane, without exceeding a maximum memory storage requirement imposed on the complete program. Other regions were maintained with up to several hundred events per cell. A summary of the six kinematic planes used is given in Table V-5.

For these planes to be useful, it was necessary to accumulate many pieces of information for each cell. In addition to the total event weight for both data and monte carlo, the information necessary to compute the average values of several real kinematic variables in the cell was maintained for each cell. This information is summarized in Table V-6. It is these accumulated monte carlo predictions of real kinematic variables against which all data will be plotted.

To bin the data for plotting, a program was told what the parametric variable for the plot would be, e.g. Q^2 between 10 and 15 $(\text{GeV}/c)^2$, and then which variable against which to plot, for example x . A sequence of input lines would then give minimum and maximum value pairs of this variable for a given data point. The program searched all cells of all six planes for averages in the correct range, printing the list of cells for later use. In an attempt to optimize the data presentation, this process became an

Table V-5. Bounds of Kinematic Planes Used for Analysis

Plane	x_{\min}	x_{\max}	Δx	Q_{\min}^2 (GeV/c) ²	Q_{\max}^2 (GeV/c) ²	ΔQ^2 (GeV/c) ²
1	0	0.06	0.003	0	30.0	1.0
2	0.06	0.14	0.005	0	70.0	1.0
3	0.14	0.20	0.010	0	90.0	2.0
4	0.20	0.30	0.010	0	112.0	4.0
5	0.30	0.60	0.020	0	152.0	4.0
6	0.60	1.00	0.100	0	136.0	4.0

Table V-6. Maintained Cell Information

Word	Information
1	Σ Data Event Weights
2	Integer number of data entries
3	Σ Monte Carlo Event Weights
4	Σ Monte Carlo Weight $\cdot Q^2$
5	Σ Monte Carlo Weight $\cdot x$
6	Σ Monte Carlo Weight $\cdot W^2$
7	Σ Monte Carlo Weight $\cdot (Q_R^2 - Q^2)$
8	Σ Monte Carlo Weight $\cdot (x_R - x)$
9	Σ Monte Carlo Weight $\cdot (W_R^2 - W^2)$
10	Σ Monte Carlo Weight $\cdot (Q_R^2 - Q^2)^2$
11	Σ Monte Carlo Weight $\cdot (x_R - x)^2$
12	Σ Monte Carlo Weight $\cdot (W_R^2 - W^2)^2$

iterative one. Parametric variable ranges were used which approximated, or were larger than, the resolution in that variable at the center of the parametric range. Sizes of the dependent variable range were adjusted to give approximately 3% statistical error to the data/monte carlo ratios determined by this approach.

To determine the ratios, a two step process was used. In the first step, the monte carlo was broken into fifteen pieces, each of equal size, and the list of cells was read and the total event weight for each data point accumulated separately for each piece. All of the data events were treated together as a sixteenth piece. The second step read all sixteen pieces and computed the flux normalized ratios of data event weight divided by monte carlo weight,

$$\text{Ratio} = \frac{\text{Data Weight/Data Flux}}{\text{Monte Carlo Wt./Monte Carlo Flux}} \quad . \quad (1)$$

The error in this ratio was the standard method of errors in quadrature,

$$\frac{\Delta R}{R} = \left[\left(\frac{\Delta D}{D} \right)^2 + \left(\frac{\Delta M}{M} \right)^2 \right]^{1/2} \quad (2)$$

D = Data Weight

M = Monte Carlo Weight

R = Determined Ratio .

For data events, normally distributed errors were assumed, which gave the error as

$$\frac{\Delta D}{D} = 1/\sqrt{D_N} \quad (3)$$

D_N = integer number of data entries.

For the monte carlo events, this was not true. Each monte carlo muon was weighted by the total cross section for that muons E_0 , E' , and θ , making this a bias-type calculation as opposed to the real data above, which is an analog calculation. It is for this reason that the monte carlo was broken into fifteen pieces.⁽⁴⁷⁾ Each piece then gave an independent prediction of the muon yield in the various cells. These predictions were normally distributed, so the error in the mean value of the fifteen predictions could be computed as

$$\left(\frac{\Delta M}{M}\right)^2 = \frac{\left(\sum_{i=1}^N a_i^2 - N \bar{a}^2\right)}{\bar{a}^2 N(N-1)} \quad (4)$$

\bar{a} = average of the predictions a_i

with $N = 15$. This N was chosen as convenient because the monte carlo was written on fifteen output tapes.

Associated with each of these ratios, the average values of the real variables \bar{Q}^2 , \bar{x} , and \bar{W}^2 were calculated. These values were put into a common file together with the ratios and statistical errors, while at the same time computing the model dependent $F_2(\bar{x}, \bar{Q}^2)$ (see section V-D). In addition

Table V-7. Some Values of Resolution in Kinematic Variables

Q^2 (GeV/c) ²	x	$\sigma(Q^2)$ (GeV/c) ²	$\sigma(W^2)$ (GeV) ²	$\sigma(x)$
11.5	0.04	3.7	62	0.05
12.0	0.10	2.6	37	0.06
11.8	0.20	2.3	33	0.12
21.8	0.10	4.1	38	0.05
22.4	0.20	3.6	36	0.09
22.1	0.30	3.2	30	0.13
33.0	0.10	7.8	53	0.04
33.5	0.20	5.1	34	0.06
34.5	0.29	4.7	33	0.11
34.6	0.40	4.3	29	0.14
45.1	0.15	9.1	49	0.05
45.3	0.24	6.6	35	0.07
44.9	0.33	5.7	32	0.10
44.5	0.44	5.0	29	0.15
59.5	0.19	11.4	46	0.05
62.3	0.29	9.0	35	0.07
61.3	0.40	7.5	33	0.11
87.9	0.30	13.7	39	0.06
93.1	0.40	12.5	37	0.09
97.0	0.54	11.4	39	0.15
124.0	0.38	19.0	41	0.08
129.0	0.54	16.0	40	0.12

to the average values, the shift in the means of these variables due to the fit process could be determined, along with the associated resolution in the variable. Table V-7 shows some values of the resolution calculated in this way. The non-zero shifts in means which were found indicate that the raw distributions shown in chapter III, which are plotted as functions of variables assigned through the fitting process, cannot be directly used to obtain structure functions or cross sections.

D) The Construction of $F_2(x, Q^2)$

With the determination of the data to monte carlo, flux normalized ratios and associated errors, the next step was to determine structure functions. This was done using the Buras-Gaemers prescription detailed in chapter I. The values of Q^2 and x were those average real values computed using the accumulated quantities of Table V-6. The structure functions and associated errors, then, were just these QCD values multiplied by the data/monte carlo ratios,

$$F_2(\bar{x}, \bar{Q}^2) = R(\bar{x}, \bar{Q}^2) \cdot F_{2\text{QCD}}(\bar{x}, \bar{Q}^2) \quad (5)$$

$$\Delta F_2(\bar{x}, \bar{Q}^2) = \Delta R(\bar{x}, \bar{Q}^2) \cdot F_{2\text{QCD}}(\bar{x}, \bar{Q}^2) \quad .$$

The Euler Beta function used in F_2 was calculated using the gamma function MGAMMA on the IMSL library of programs, ⁽⁴⁸⁾ so that ⁽⁴⁹⁾

$$B(z_1, z_2) = \frac{\Gamma(z_1)\Gamma(z_2)}{\Gamma(z_1 + z_2)} \quad . \quad (6)$$

The data points determined in this way could next be manipulated in various fashions. The method chosen here was to do a least squares minimization fit to three parameters using the program⁽⁵⁰⁾ KINFIT4. The three free parameters were Λ , Q_0^2 , and an overall normalization factor N. For each parametric $Q^2(x)$ region, the structure functions could then be shifted to the central value of $Q^2(x)$, while still being plotted at the same values of $x(Q^2)$. The prescription used for the shift was

$$F_2(\bar{x}, \bar{Q}'^2) = F_2(\bar{x}, \bar{Q}^2) \cdot \frac{F_2(\bar{x}, \bar{Q}'^2)_B}{F_2(\bar{x}, \bar{Q}^2)_B}$$

or

$$F_2(\bar{x}', \bar{Q}^2) = F_2(\bar{x}, \bar{Q}^2) \cdot \frac{F_2(\bar{x}', \bar{Q}^2)_B}{F_2(\bar{x}, \bar{Q}^2)_B} \quad (7)$$

where \bar{x} and \bar{Q}^2 were those accumulated, average kinematic values found above, \bar{x}' and \bar{Q}'^2 were the central values to which the shift was being performed, and the subscript B indicates the best fit values of Λ and Q_0^2 were used in the evaluation. Lack of the subscript B implies the same values of Λ and Q_0^2 (0.5 and 2.0) were used as in the monte carlo. The values of the structure function found in this way are shown in Figures V-2 and V-3, while the data point values are tabulated in appendix C.

Table V-8. Results of Three Parameter QCD Fits

The fit is $F_2(x, Q^2) = N \cdot F_2^{QCD}(x, Q^2; \wedge, Q_0^2)$

Fit	Restrictions [†]	*R= σ_L/σ_T	Data Points	Fit Parameters		
				\wedge	Q_0^2	N
1	pxc	1	139	0.38±0.11	1.56±0.47	0.989±0.008
2	pQc	1	168	0.61±0.13	2.64±0.59	0.990±0.007
3	pxc (or pQc)	2	139 (168)	0.42±0.13	1.66±0.53	1.016±0.008
4	$Q^2 < 20$ pxc	1	55	0.28±0.15	1.17±0.60	0.973±0.006
5	$10 < Q^2 < 20$ pQc	1	68	1.27±0.21	5.00±0.78	0.978±0.005
6	$10 < Q^2 < 20$ pxc	1	39	0.86±0.29	3.44±1.12	0.976±0.006
7	$Q^2 < 20$ pxc	2	55	0.56±0.16	2.10±0.59	0.990±0.006
8	$10 < Q^2 < 20$ pQc	2	68	1.40±0.20	5.27±0.74	0.996±0.005
9	$Q^2 > 10$ pxc	1	123	0.60±0.16	2.57±0.74	0.993±0.008
10	$Q^2 > 20$ pxc	1	84	0.61±0.36	2.45±1.70	1.020±0.015

Table V-8. Continued

Fit	Restrictions [†]	*R= σ_L/σ_T	Data Points	Fit Parameters		
				Λ	Q_0^2	N
11	$Q^2 > 20$ pQc	1	100	0.63 ± 0.33	2.56 ± 1.61	1.018 ± 0.014
12	$Q^2 > 20$ pxc	2	84	2.01 ± 0.26	0.56 ± 0.88	1.074 ± 0.017
13	$Q^2 > 20$ pQc	2	100		Non-Convergent	
14	$Q^2 > 30$ pxc	1	54	0.03 ± 0.14	0.03 ± 0.17	1.167 ± 0.052
15	$Q^2 > 30$ pQc	1	60	0.22 ± 0.44	0.51 ± 1.38	1.099 ± 0.038
16	$Q^2 > 30$	2			Non-Convergent	
17	$10 < Q^2 < 30$ $Q^2 > 50$ pQc	1	135	0.56 ± 0.13	2.42 ± 0.55	0.985 ± 0.006
Fits 18-21 use 1.9% uniform inefficiency in data reconstruction						
18	$10 < Q^2 < 30$ $Q^2 > 50$ pQc	1	135	0.67 ± 0.12	2.89 ± 0.54	0.985 ± 0.006

Table V-8. Continued

Fit	Restrictions ⁺	*R= σ_L/σ_T	Data Points	Fit Parameters		
				$\hat{\Lambda}$	Q_0^2	N
19	$Q^2 > 10$ pQc	1	168	0.68±0.13	2.95±0.61	0.985±0.006
20	$Q^2 > 20$ pQc	1	100	0.90±0.34	3.99±1.76	1.007±0.013
21	$Q^2 > 30$ pQc	1	60	0.55±0.62	1.83±2.73	1.063±0.036

*form 1 is $R = 1.2 \cdot (1-x)/Q^2$

⁺ pxc = parametric x cells

form 2 is $R = 0.25$

pQc = parametric Q^2 cells

- - $\rightarrow \Lambda=0.3, Q_0^2=1.8$
 — $\rightarrow \Lambda=0.60, Q_0^2=2.53, N=1.0$
 $\circ \rightarrow R=1.2 \cdot (1-x)/Q^2$
 * $\rightarrow R=0.25$
 $\Delta \rightarrow \text{SLAC } F_2^D/2 \text{ (ref 24)}$

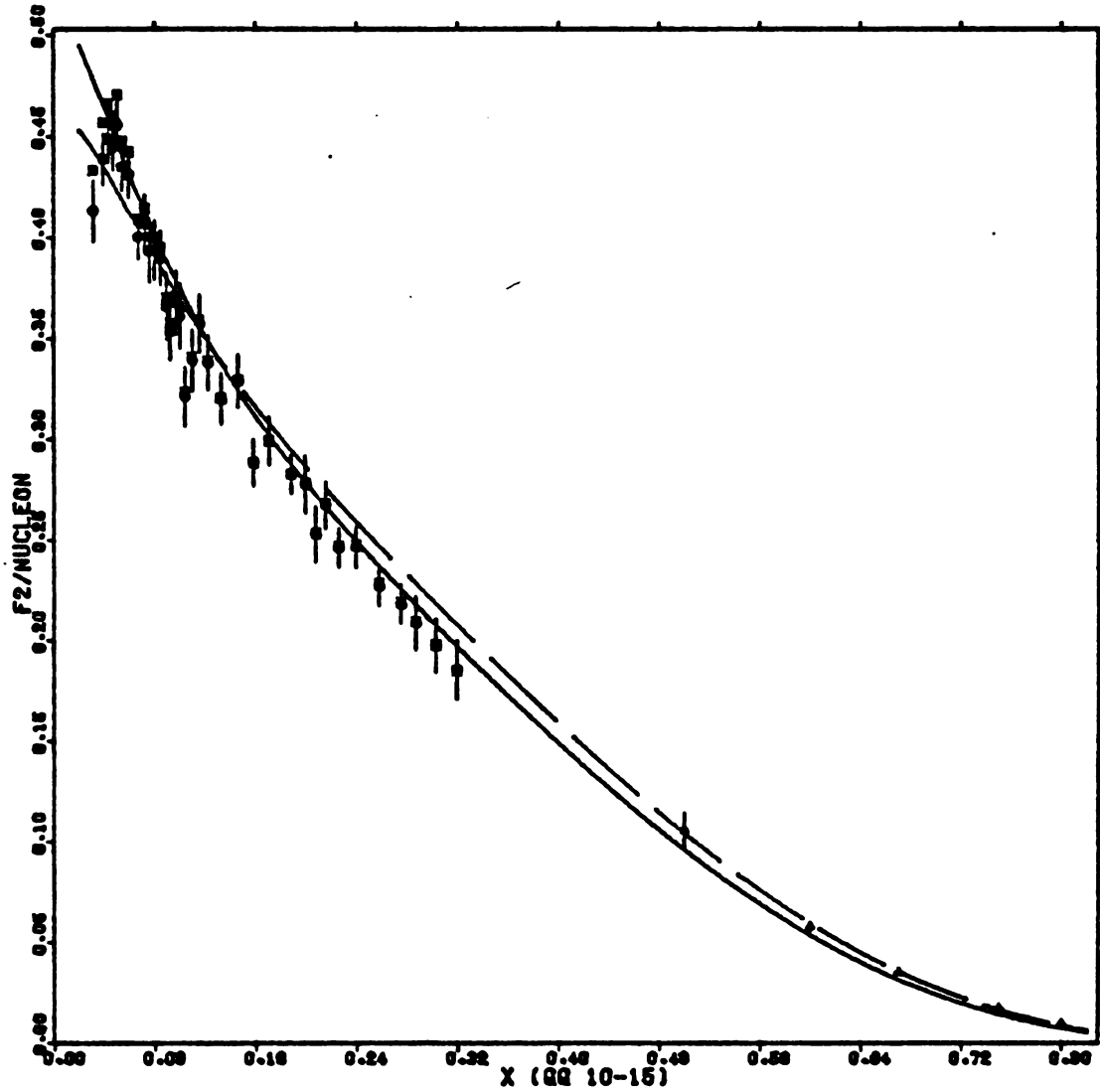


Figure V-2a. $F_2(x, Q^2)$ in Parametric Q^2 Regions

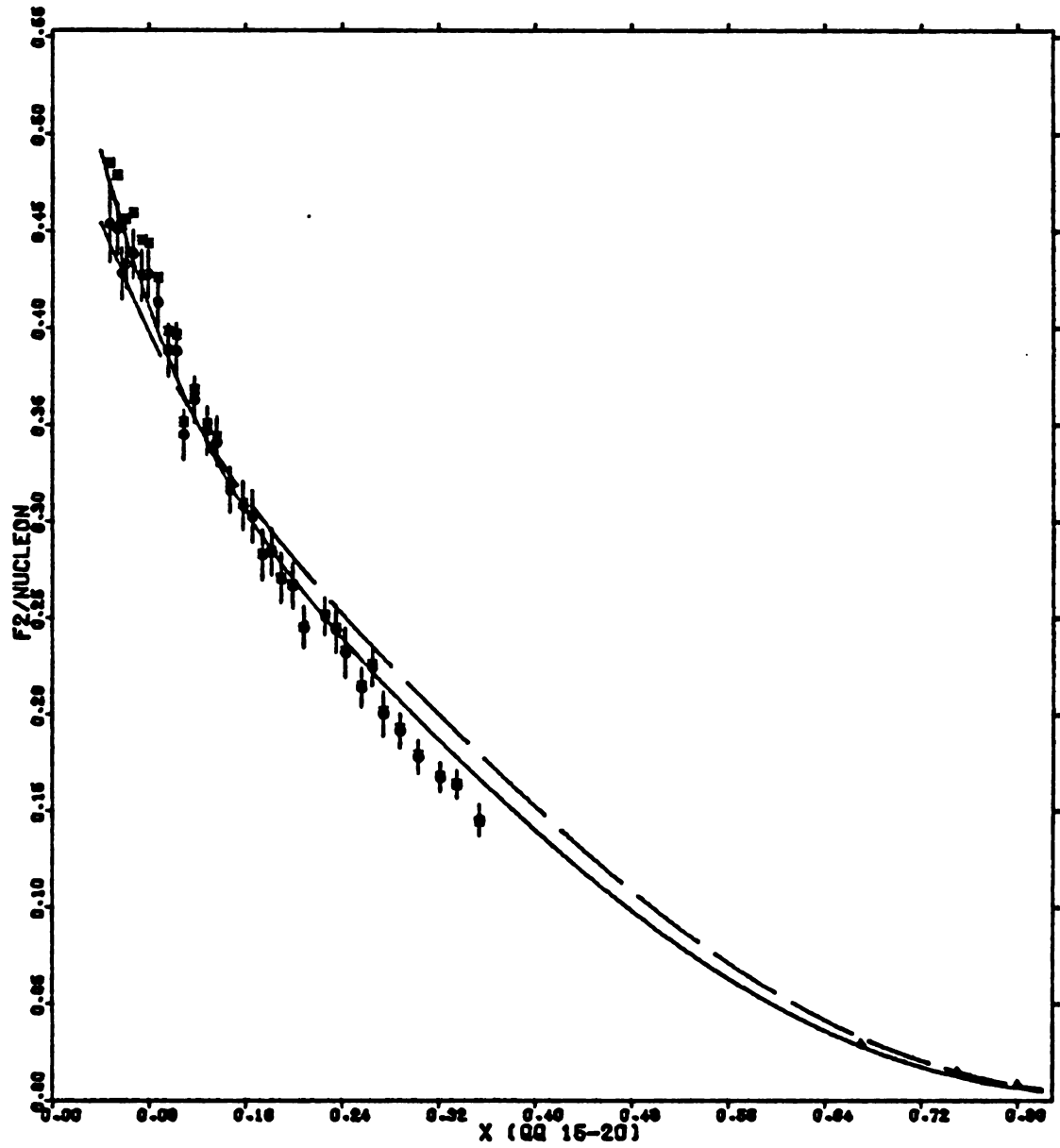


Figure V-2b. $F_2(x, Q^2)$ in Parametric Q^2 Regions

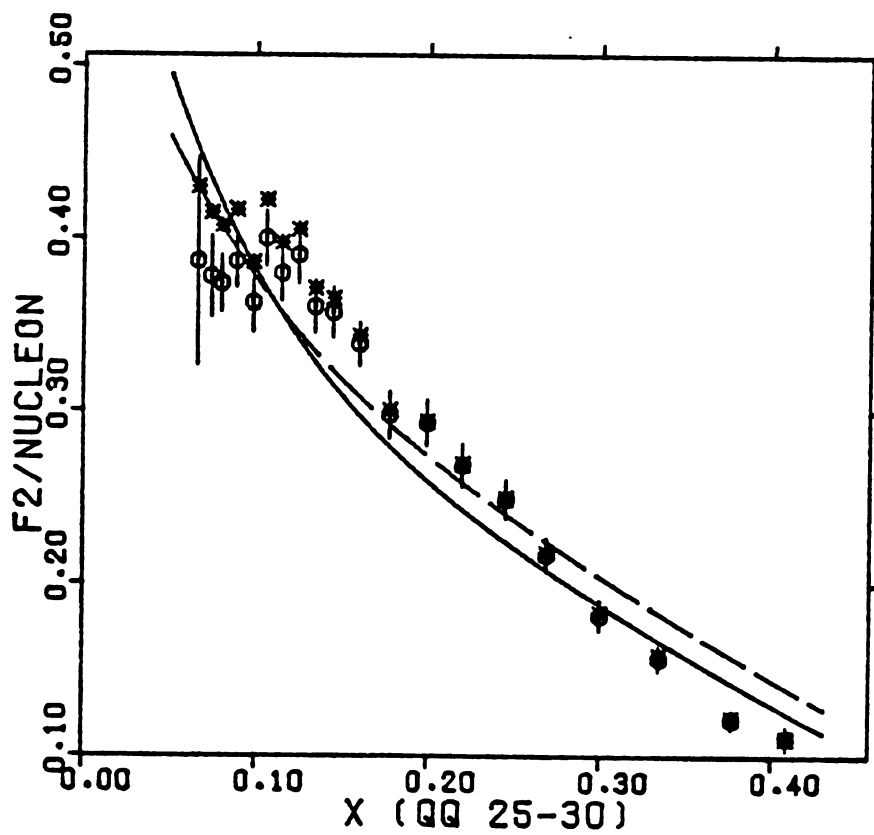
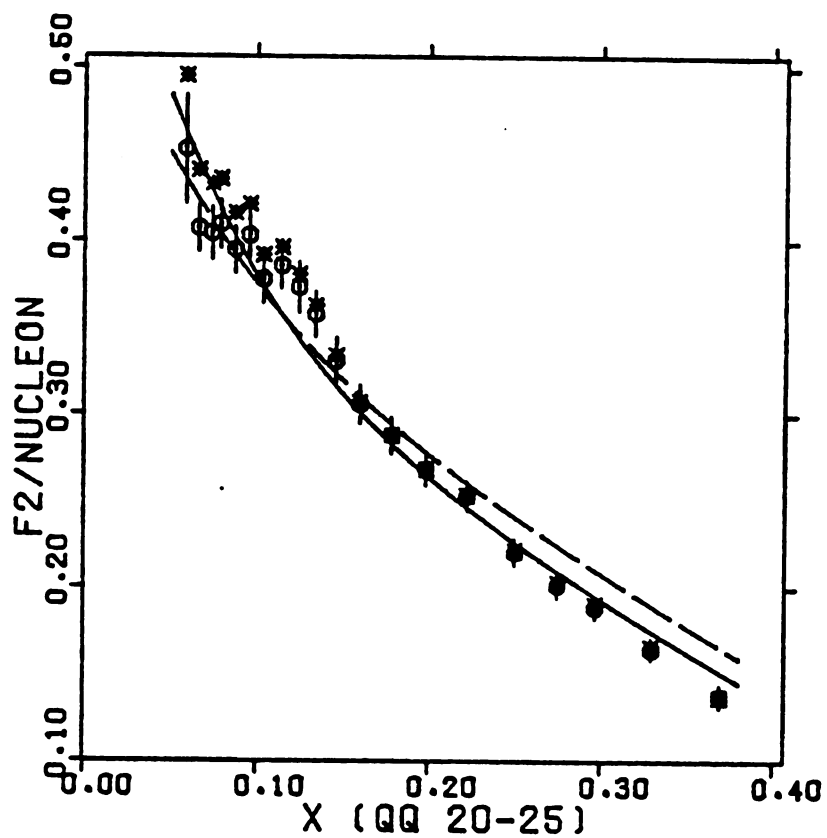


Figure V-2c. $F_2(x, Q^2)$ in Parametric Q^2 Regions

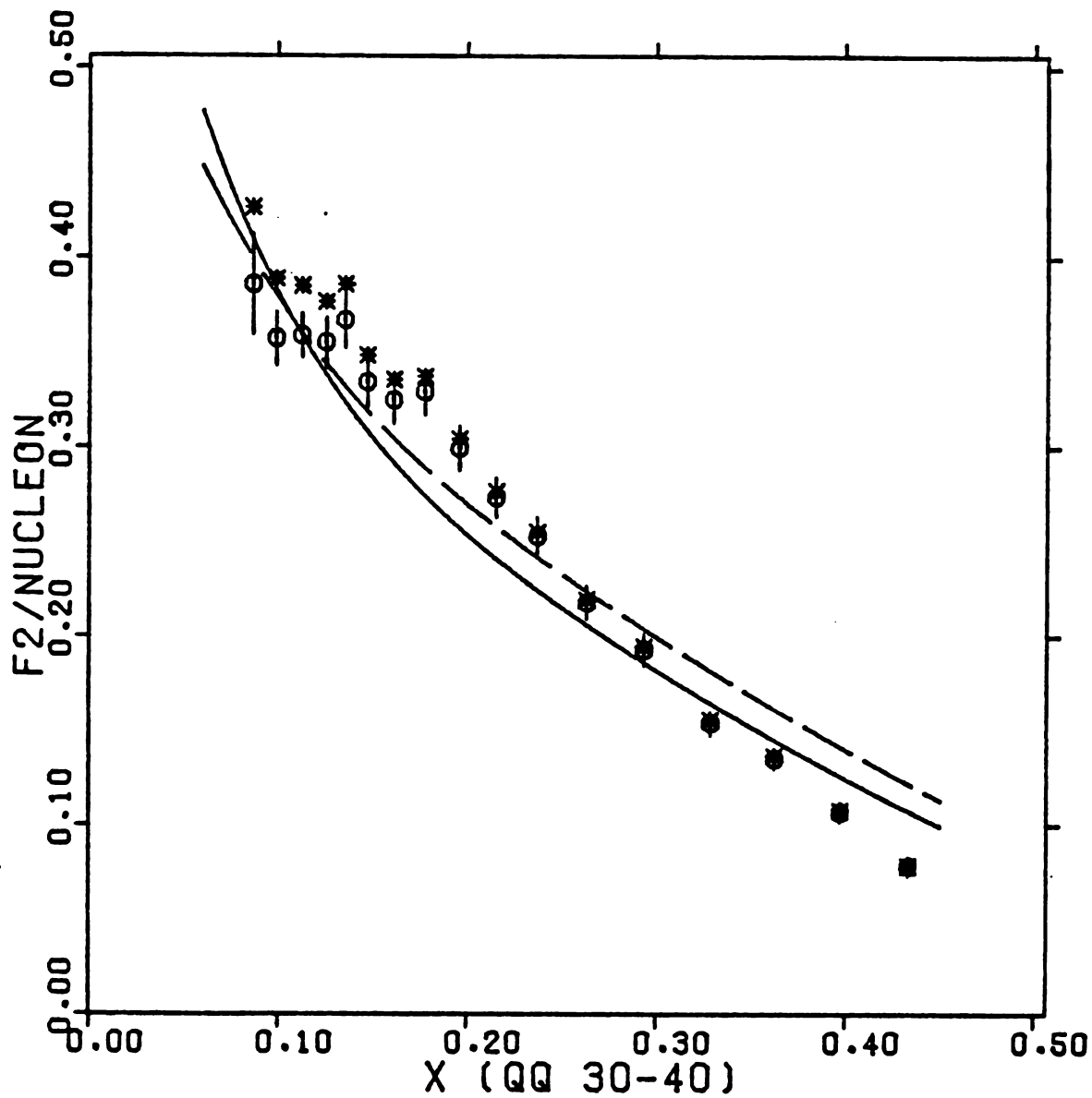


Figure V-2d. $F_2(x, Q^2)$ in Parametric Q^2 Regions

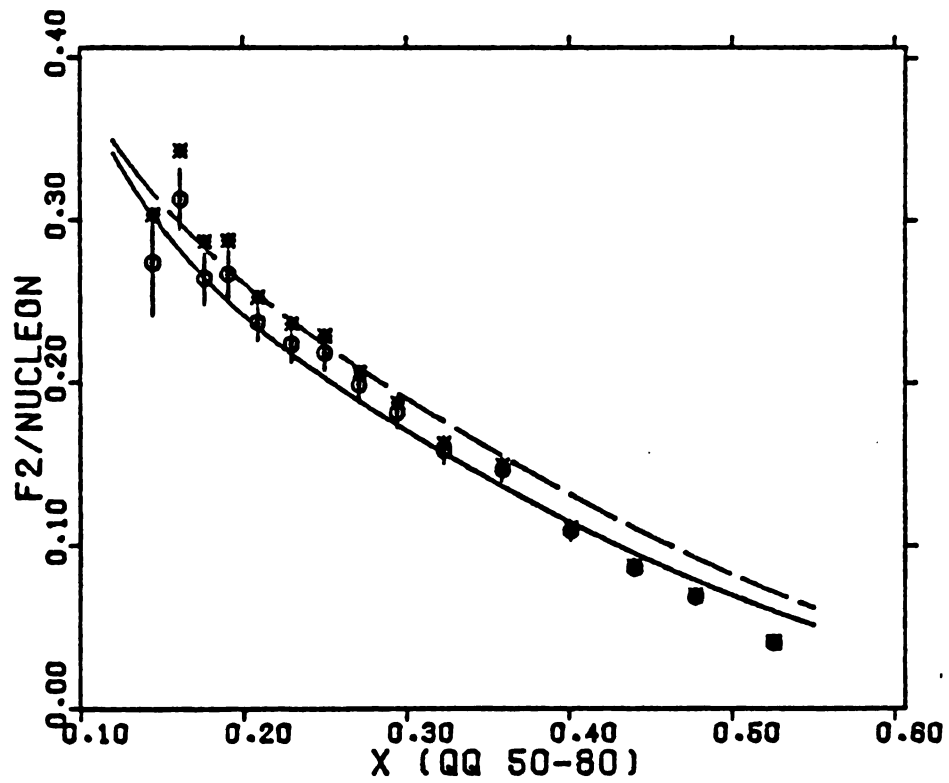
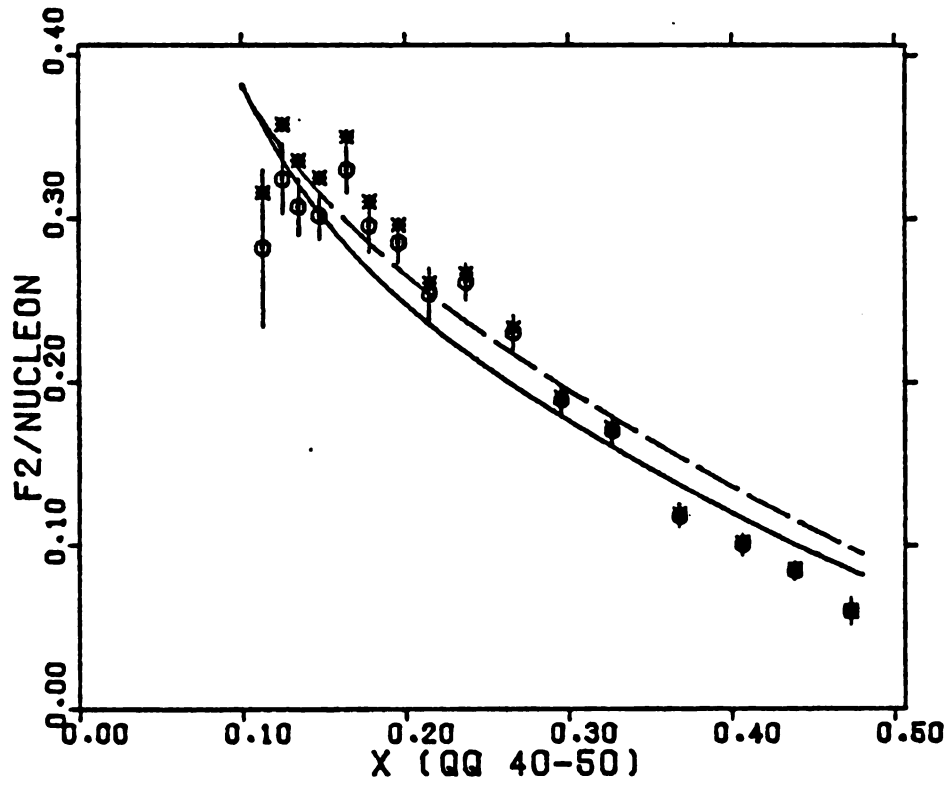


Figure V-2e. $F_2(x, Q^2)$ in Parametric Q^2 Regions

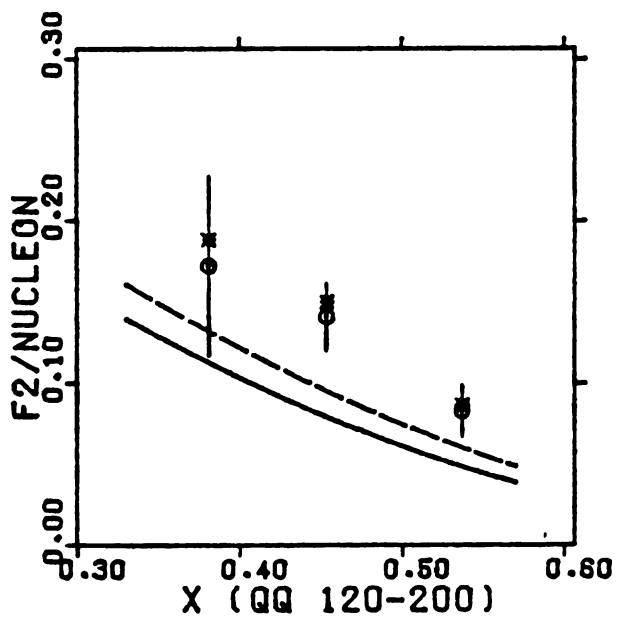
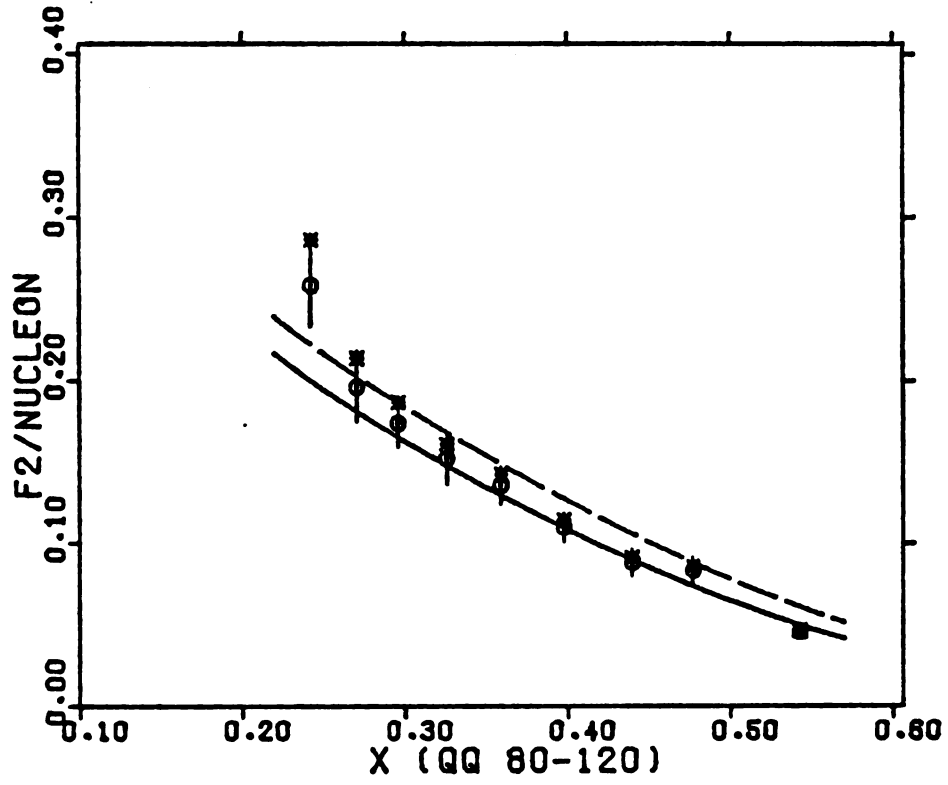
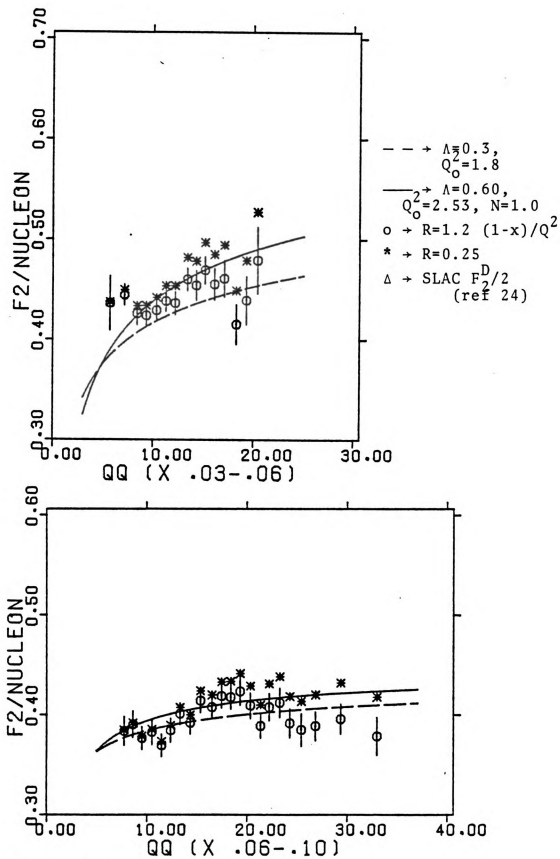


Figure V-2f. $F_2(x, Q^2)$ in Parametric Q^2 Regions

Figure V-3a. $F_2(x, Q^2)$ in Parametric x Regions

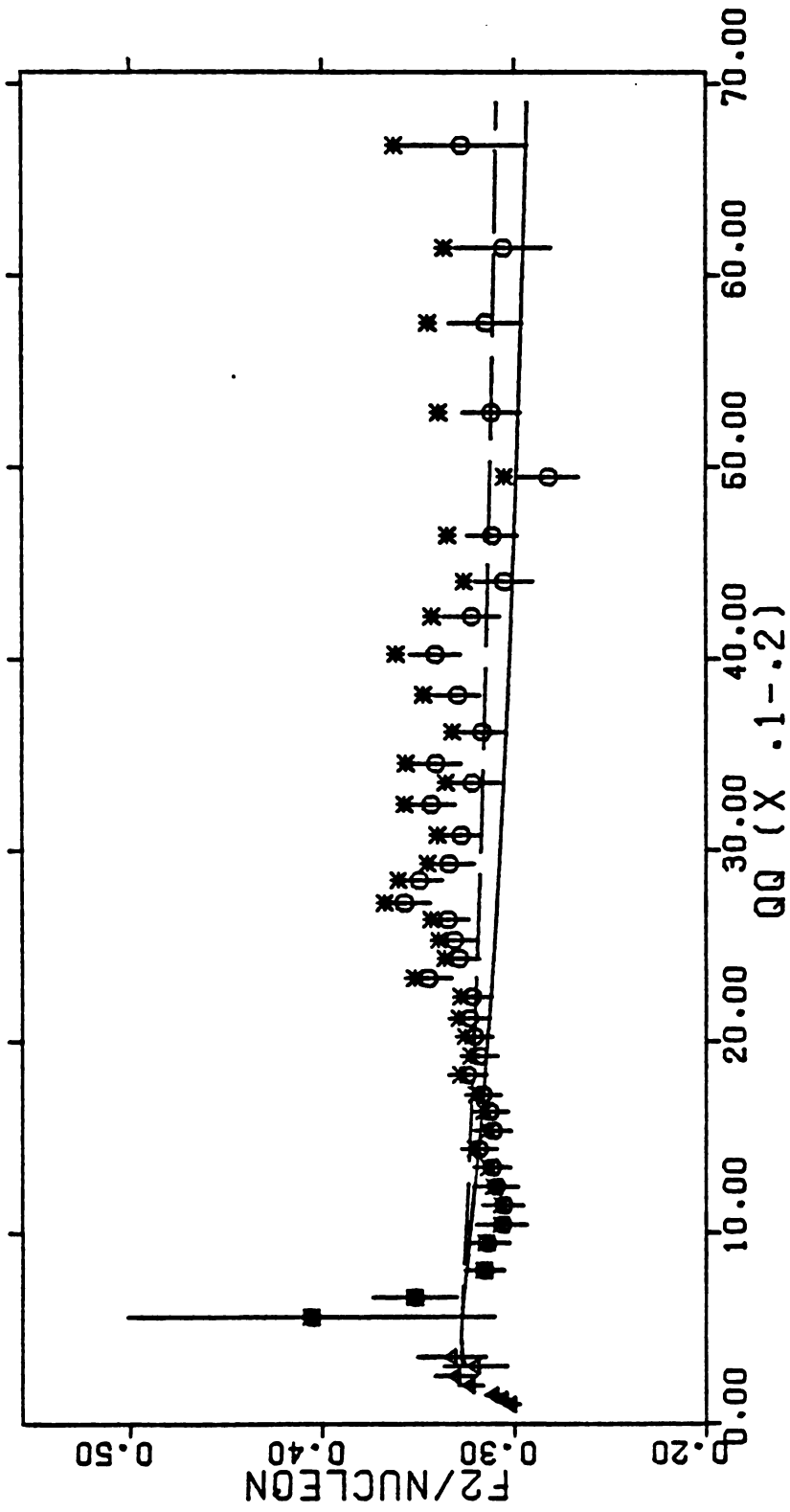


Figure V-3b. $F_2(x, Q^2)$ in Parametric x Regions

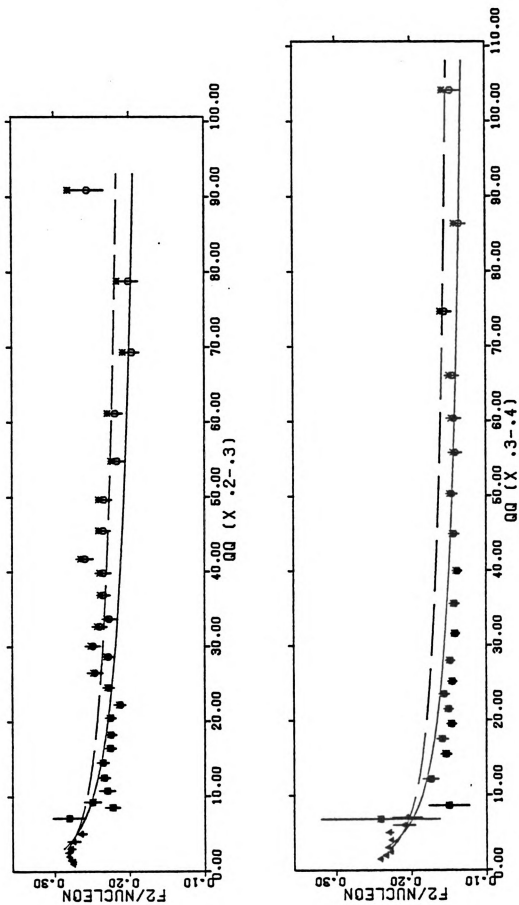


Figure V-3c. $F_2(x, Q^2)$ in Parametric x Regions

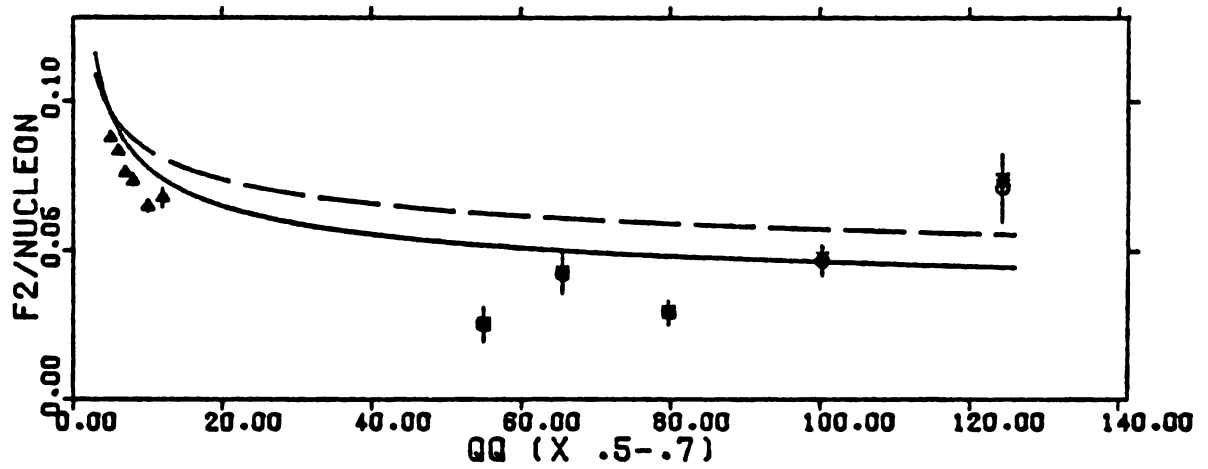
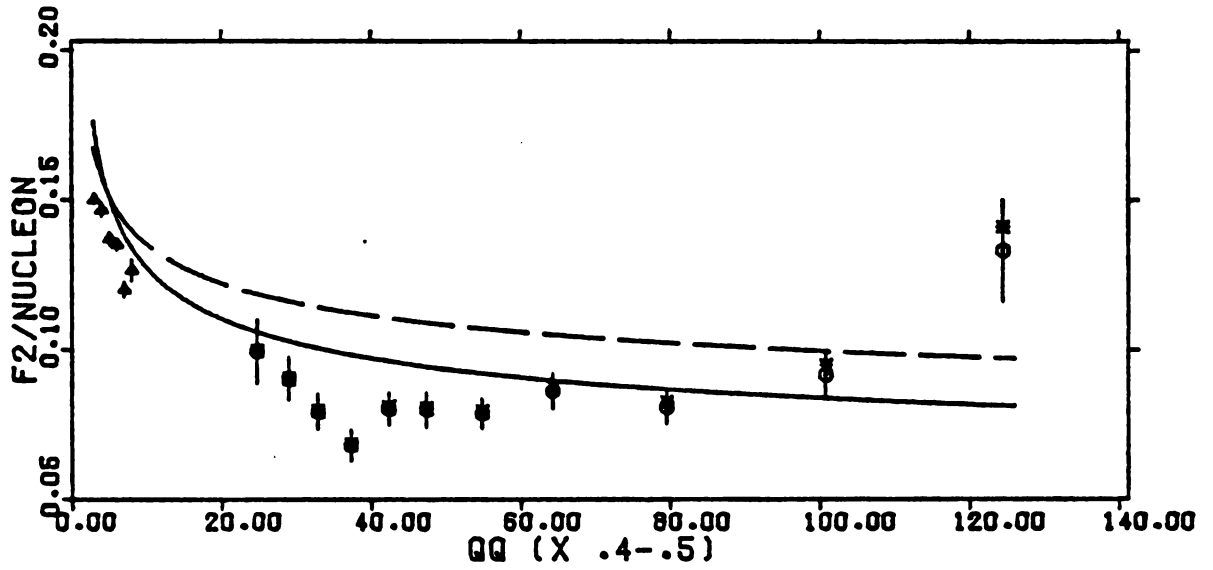


Figure V-3d. $F_2(x, Q^2)$ in Parametric x Regions

This fitting process has revealed several problems. First of all, the values of the fit parameters Λ and Q_0^2 are dependent on the kinematic region of the data which is being considered. Consistent results of Λ , $Q_0^2 = 0.60, 2.5$ are found with the restrictions $Q^2 > 10$ or $Q^2 > 20$ $(\text{GeV}/c)^2$ applied, but when lower Q^2 data are added to these sets, or the restriction $Q^2 > 30$ is used, Λ and Q_0^2 each undergo a substantial decrease in value. Additionally, the $Q^2 > 30$ fit finds a 10% rise ($N = 1.1$) in the data over the model prediction.

A second problem is the dependence of the results of the fit on the form of $R = \sigma_L/\sigma_T$ which is used. When a constant⁽²⁷⁾ $R = 0.25$ is used, the fits do not exhibit the consistency of results found previously for fits which include the $10 < Q^2 < 30$ data, and in fact the fit is non-convergent in a few instances. This constant R does not seem to be consistent with most recent experimental results, although it cannot be ruled out with certainty. Structure functions with this value of R are therefore also plotted in Figures V-2 and V-3, although the associated error bars are left off.

Data at low x are difficult to interpret. The possibility of the suppression of the cross section due to nuclear shadowing effects has been neglected, since it appeared to be a less than 5% effect⁽⁵¹⁾ applicable only for $x < 0.1$. A clear fall in the data/monte carlo ratio in the raw ω distribution for large ω can be seen, though

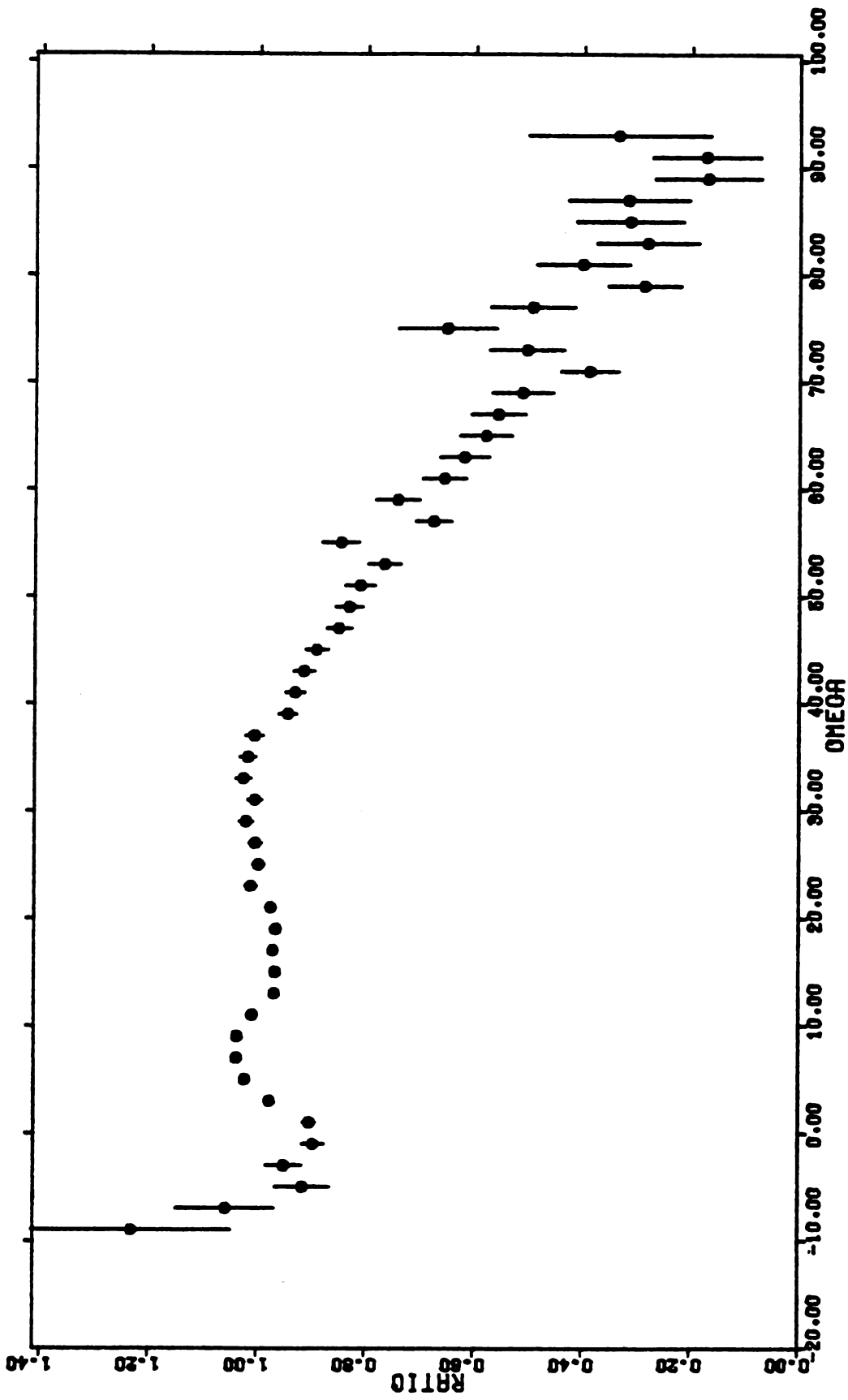


Figure V-4. Ratio of Data/Monte Carlo vs Raw ω

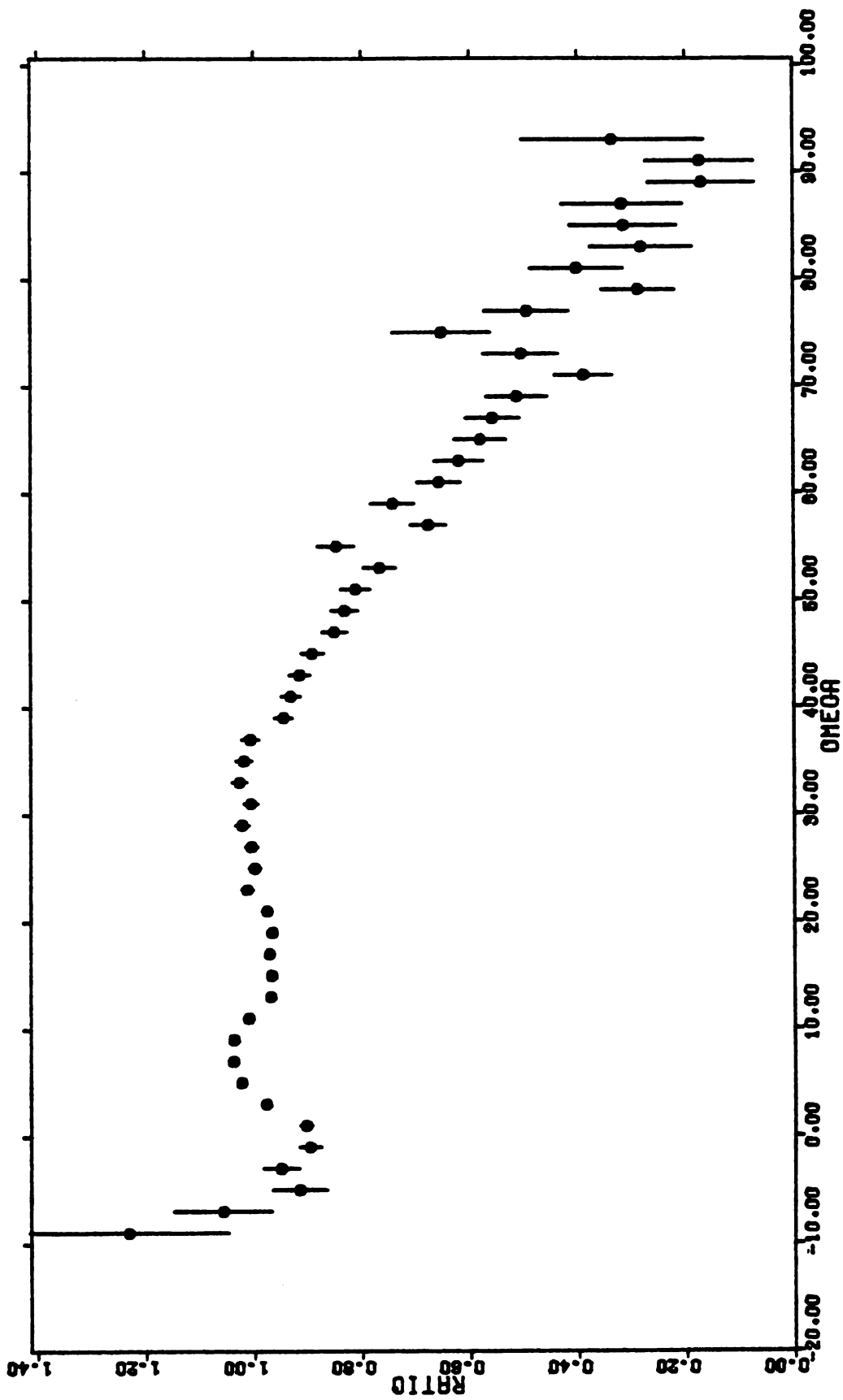


Figure V-4. Ratio of Data/Monte Carlo vs Raw ω

(Fig. V-4). This may be due to shadowing, but a definitive statement would require data on targets with several values of atomic weight. It does place low x (<0.1) data in poor light, though. Resolution at $x = 0.05$ can throw such events as high as $x = 0.15$ ($0.05+2\sigma$) and at $x = 0.10$, $x = 0.15$ is only removed by one standard deviation. From the $0.03 < x < 0.06$ data, this would imply that data with Q^2 as high as $30(\text{GeV}/c)^2$ in neighboring, small x regions should be viewed with suspicion.

Similarly, data points with $Q^2 < 10(\text{GeV}/c)^2$ should be viewed with suspicion. These data are in a region of rapidly changing acceptance for the most part and even a small miscalculation here could throw the results off significantly. Exceptions are those muons which suffer large energy losses before the deep-inelastic interaction, resulting in an E_0 at the interaction point $\ll 270$ GeV, and a significantly smaller Q^2 than would otherwise be construed. This is not a highly probable circumstance though ($<2\%$), and these events cannot be separated from the rest of the sample.

With these points in mind, the values of Λ and Q_0^2 equal to 0.60 and 2.53 respectively have been chosen as most representative of the data sample with a data normalization factor (N) of 0.992. These values have been used in equation V-7 to arrive at the shifted data tabulated in appendix C. The results of all of the fits have been summarized in Table V-8.

E) Systematic Errors

Besides the statistical errors resulting from the finite number of scattered muons, there were many possible sources of systematic errors which contributed to inaccuracies in the determination of $F_2(x, Q^2)$. In this section, several of the most important will be discussed along with their effects on F_2 .

First of all, strictly speaking, Q_0^2 should not be allowed to vary without also changing the values of the z_i and z'_i used in the evaluation of the valence quark density functions. This cannot be done using this data, because there are no events at the low values of Q^2 which are necessary ($1 < Q^2 < 5$), and nearby regions are unreliable as has been noted above. J.G.H. de Groot et al.⁽⁵²⁾ have performed a fit with $Q_0^2 = 5.0(\text{GeV}/c)^2$ and found values for z_1 , z_2 , z'_1 , and z'_2 which are within quoted errors of the values used by Buras and Gaemers. For these reasons, Q_0^2 has been allowed to vary while retaining the same values for all z_i .

Scrutiny of the high x regions (0.4-0.5 in particular) of Figure V-3 show that the model prediction of F_2 is approximately constant, while the data start below the curve and rise above it as Q^2 increases beyond $\sim 80(\text{GeV}/c)^2$. This is likely a consequence⁽⁵³⁾ of target mass effects on the structure function, at least where the data are below the curve at lower Q^2 values. These low points are seemingly an extrapolation of the SLAC data of reference 24 at high x and low $Q^2 (< 20(\text{GeV}/c)^2)$. Figure V-5 illustrates the way in

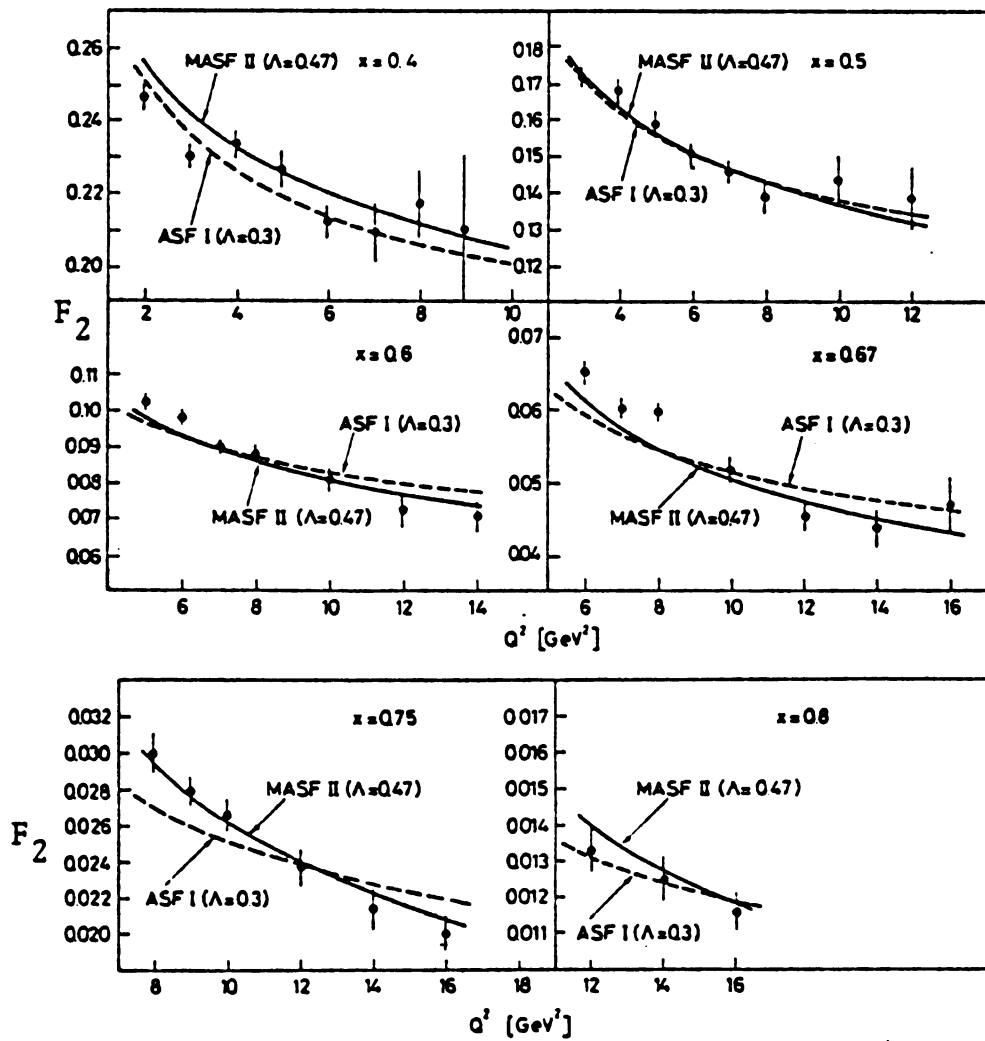


Figure V-5. The Variation of F_2 With Target Mass Effects

which these mass effects can modify F_2 . The curve labeled ASF I is the parametrization used here, except with $\Lambda = 0.3$, and the curve labeled MASF II illustrates the change in F_2 as the target mass effects are included. Q_0^2 is $1.8(\text{GeV}/c)^2$. The target mass effect is primarily a high x phenomenon, and should have little effect for $x < 0.4$. This has not been checked with this data set because of the difficulty in calculating the required single and double integrals in the formula,

$$\begin{aligned}
 F_2(x, Q^2) &= K^3 \frac{x^2}{\xi^2} F_2(\xi, Q^2) \\
 &+ 6 \frac{M^2}{Q^2} K^4 x^3 \int_{\xi}^1 d\xi' \frac{F_2(\xi', Q^2)}{\xi'^2} \\
 &+ 12 \frac{M^4}{Q^4} K^5 x^4 \int_{\xi}^1 d\xi' \int_{\xi'}^1 d\xi'' \frac{F_2(\xi'', Q^2)}{\xi''^2}
 \end{aligned} \tag{8}$$

where

$$\begin{aligned}
 K &= \frac{1}{(1 + 4x^2 M^2/Q^2)^{1/2}} \\
 \xi &= \frac{1}{1 + K^{-1}}
 \end{aligned} \tag{9}$$

$M = \text{nucleon mass}$.

Two sources of systematic error are unavoidable. The first is the fact that the analytic forms used by Buras and Gaemers are only accurate at a 1-2% level. The second is that the radiative correction weight factor

is accurate only to 1%. These two sources of error will be added in quadrature with another source to determine universally applicable systematic error. This third source is the PASSOUT correction for the MULTIMU reconstruction inefficiency. This correction is applied as a function of the reconstructed values Q_R^2 and x_R which are found. When it is applied to the data events of MULTIMU, a comparison of the corrected sample to the uncorrected sample should appear exactly as does the comparison of PASSOUT events to the uncorrected sample, since this is the comparison it is designed to mimic. It is not perfect though, suffering from deviations as large as 2% in such integrated distributions as Q_R^2 or E'_R . Consequently, a 2% systematic error should be added to the quadrature summation. These three error sources, when added, give a 3% total contribution due to systematic errors which would be added in quadrature to the statistical error bars. These error sources are applicable in all kinematic regions, as opposed to those still to be considered, which apply only in limited kinematic regions. Because of this, they have been totalled separately. It is to coincide with this 3% error that statistical errors of ~3% were used as a criterion to bin the data.

A problem related to the MULTIMU inefficiency is the inefficiency of PASSOUT itself. The overall efficiency of MULTIMU-PASSOUT is 98.1%, leaving 1.9% of events unreconstructed. Three possibilities exist: one, this 1.9% is kinematically similar to the PASSOUT plus MULTIMU event

sample, or two, the 1.9% is kinematically similar to the PASSOUT sample, or three, it is dissimilar to everything previously found. One and two are most likely, but the few events available cannot distinguish between them. All analysis performed here is presented with the use of possibility two, that the 1.9% is kinematically similar to the class of events already found by PASSOUT. The change in F_2 expected if case one is the truth is shown in appendix C, but not included amongst the quadratically summed error sources.

Samples of monte carlo have been run to test three possibilities, E_0 is 1% too low, the toroid magnetic field is 1% too low, and the toroid magnetic field is 1% too high. The first is important because an independent measurement of E_0 using, say, the University of Chicago Cyclotron Magnet in the muon lab, was never performed. The second two are important because the magnetic field measurements performed are acknowledged as accurate to only 1%. The integrated effect of these corrections on the scattered muon yield is shown in Table V-9, while the ratio of resultant distributions from these runs to the full monte carlo sample is shown in Figures V-6 to V-10. None of these ratios appears exactly as does the corresponding data/monte carlo ratio, although some features of the Q^2 and W^2 distribution in the \bar{B} too low runs show similarities to it, such as the slow rise to a plateau as Q^2 increases. This similarity could imply that the computed value of \bar{B} in the toroids is too small,

Table V-9. Total Muon Yield in Monte Carlo Systematic Checks

Run	Scattered Muons*
Reference (full Monte Carlo sample)	295,290 [±] 860
Raise \bar{B} field by 1% (\bar{B} High)	294,650
Lower \bar{B} field by 1% (\bar{B} Low)	296,660
Raise E_0 by 1% (E_0 High)	287,311

*Based on flux of 9.4×10^9 incident beam muons.

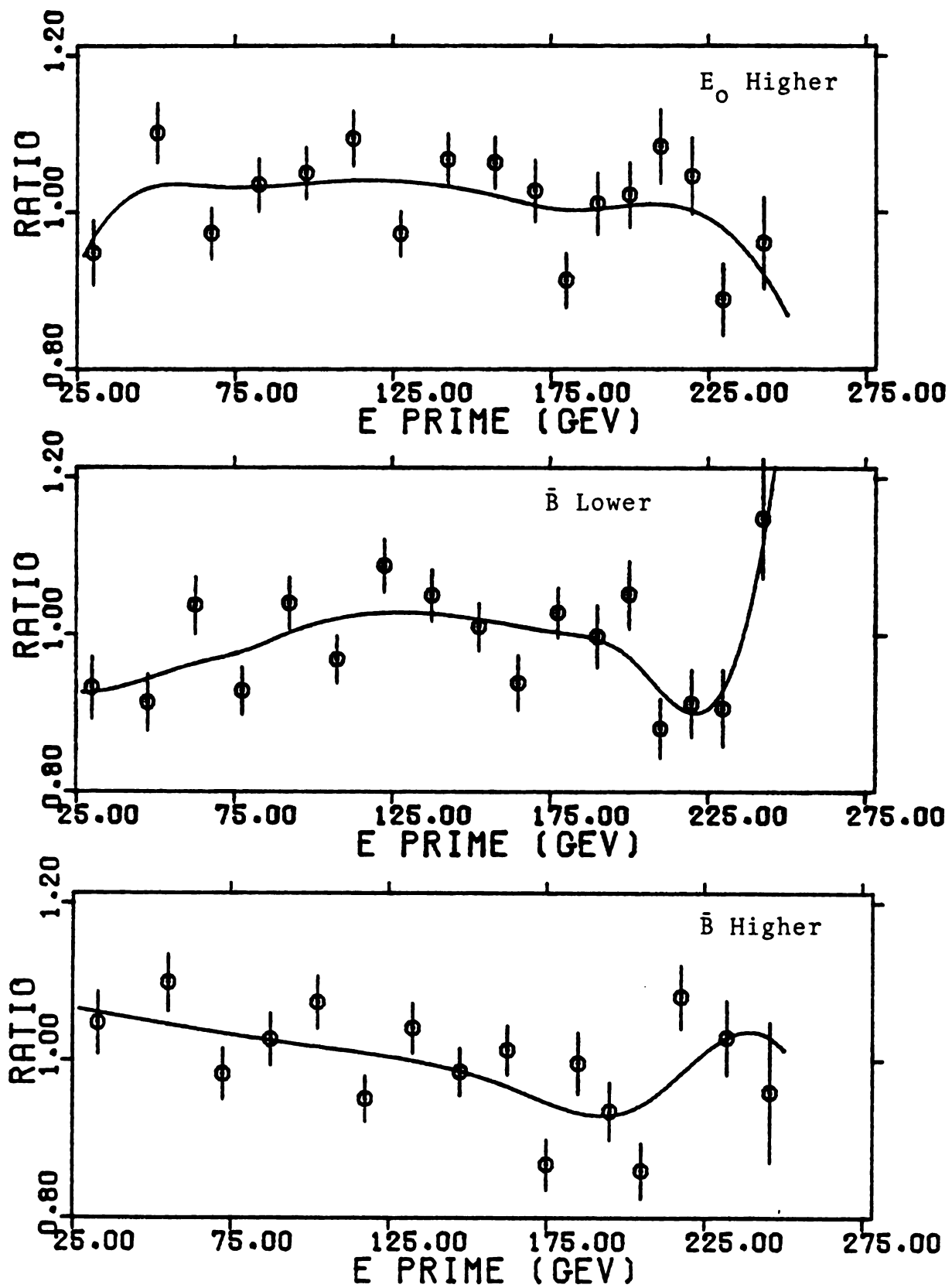


Figure V-6. Effect of Variation of E_0 and Magnetic Field on E'

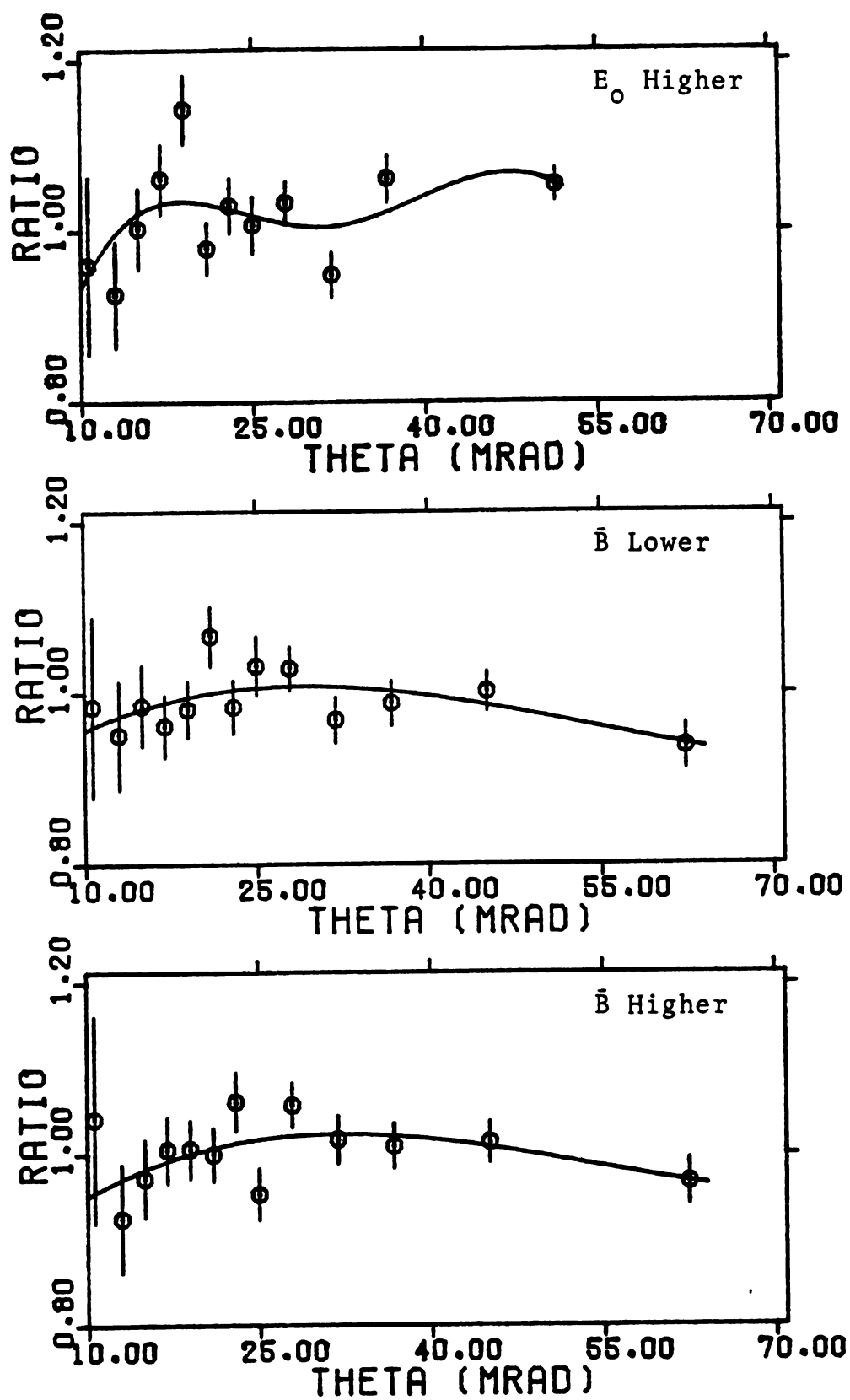


Figure V-7. Effect of Variation of E_0 and Magnetic Field on θ

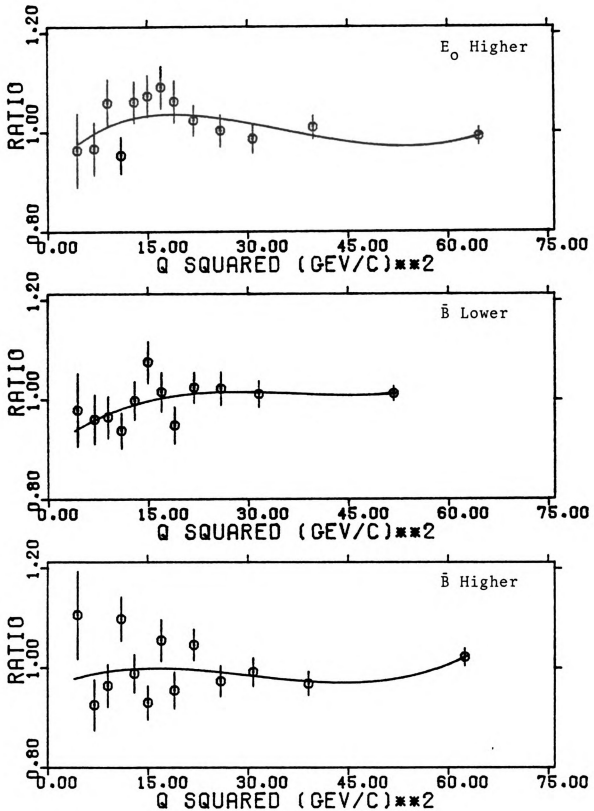


Figure V-8. Effect of Variation of E_0 and Magnetic Field on Q^2

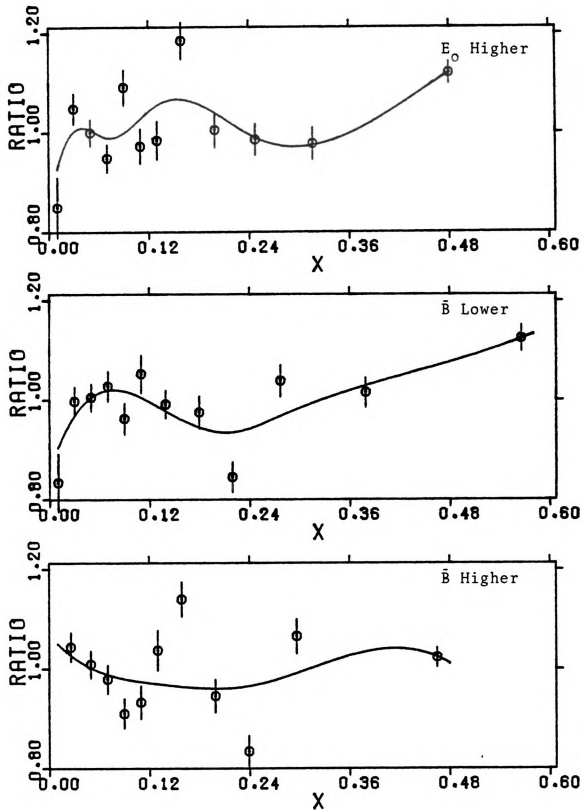


Figure V-9. Effect of Variation of E_0 and Magnetic Field on x

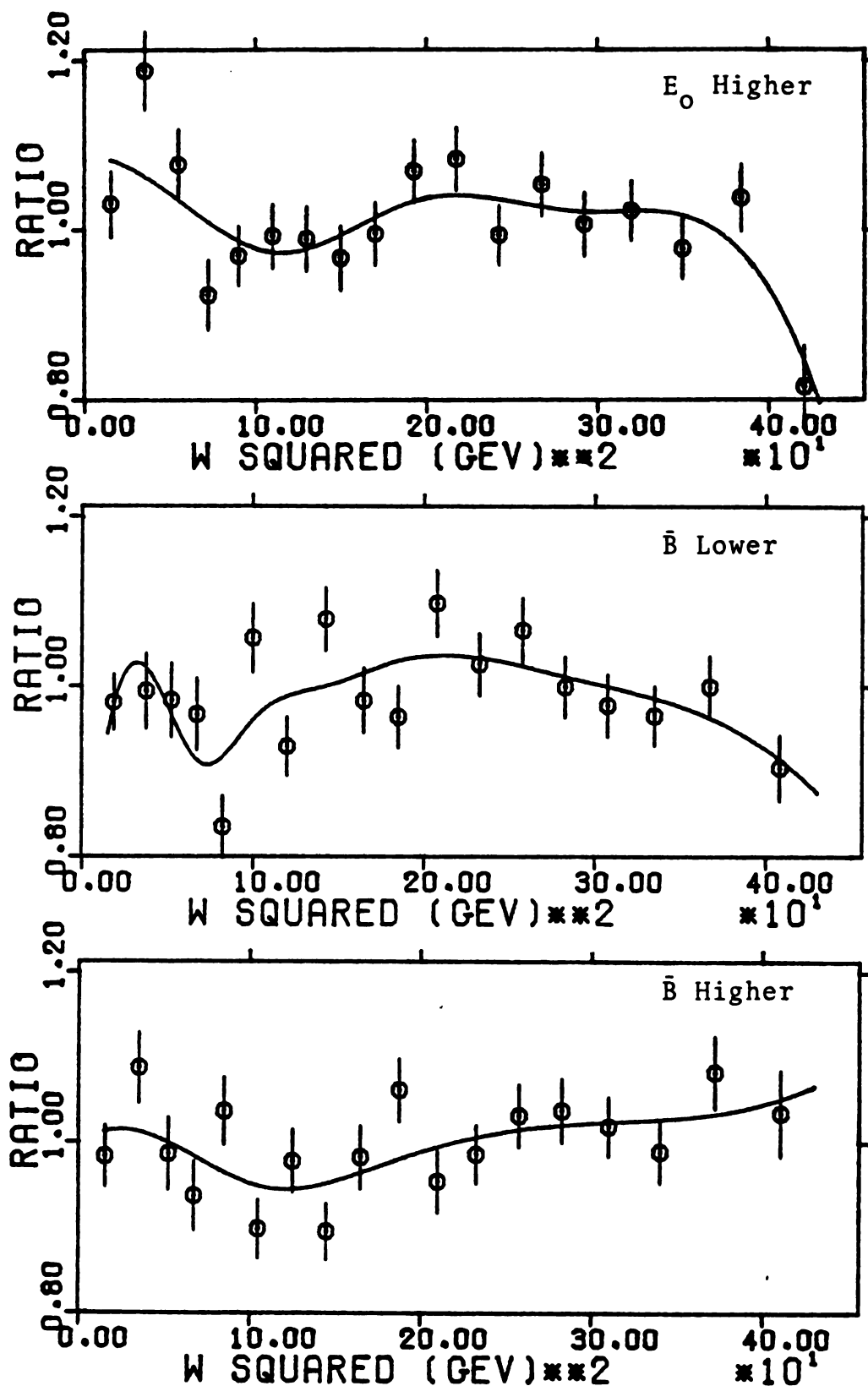


Figure V-10. Effect of Variation of E_0 and Magnetic Field on W^2

but there is no independent evidence such as improved toroid measurements to support this.

The background curves in these ratios are B-spline approximations⁽⁵⁴⁾ of the trends of the measured points, and are intended not only as a guide for the eye, but also to get an approximation for the value of the systematic deviation which these changes would induce. Consequently, both the values of the ratio and the approximation of the spline have been tabulated in appendix D for all five plots.

To check the resolution in E' , new monte carlo calculations were not run, but a sample of the full monte carlo was used with different resolution algorithms. This required only the third program stage to be rerun. The two algorithm changes used were to raise the E' resolution everywhere by the addition of one percent, and similarly with the subtraction of one percent (e.g., 9% became 10% or 8%). These re-smearred runs were then compared to the sample of events which had undergone the usual smearing process.

Raising the resolution 1% should smear more events out of the kinematically acceptable regions, and thereby would raise the overall data/monte carlo ratio. The total rise is quite small though, only 0.05%. When a comparison of W^2 distributions is performed, the rise is seen to be restricted primarily to lower values of W^2 , rising a maximum of 1.8% at $W^2 = 30 \text{ GeV}^2$. Similarly the net effect of lowering the resolution is to lower the overall normalization by 0.03%. In W^2 , the region near 250 GeV^2 is essentially unchanged,

Table V-10. Effect of Changing E' Resolution

The Ratio column represents how the Data/Monte Carlo Ratio would change given the resolution change

Q^2	Raise 1% Ratio	1% Error	Lower 1% Ratio	1% Error
$x = 0.045$				
5.7	0.957	0.127	1.035	0.137
7.2	0.994	0.028	1.007	0.028
8.4	1.004	0.028	1.006	0.028
9.3	1.002	0.026	0.998	0.026
10.4	1.003	0.024	0.994	0.023
11.3	1.009	0.022	0.997	0.022
12.2	1.001	0.025	1.006	0.025
13.4	1.003	0.024	0.990	0.023
14.3	1.046	0.039	0.998	0.037
15.2	1.012	0.033	1.021	0.033
16.1	0.973	0.041	0.994	0.042
17.1	1.013	0.050	0.987	0.047
18.3	1.005	0.054	1.011	0.055
19.3	1.014	0.064	0.967	0.059
20.4	1.024	0.088	1.077	0.094
$x = 0.25$				
7.1	0.797	0.174	0.823	0.174
8.5	1.039	0.119	0.896	0.103
9.3	0.990	0.136	1.095	0.154
10.8	1.034	0.086	0.948	0.076
12.5	1.042	0.058	1.014	0.055
14.5	1.003	0.057	0.949	0.053
16.5	1.044	0.047	0.997	0.044
18.2	1.015	0.044	0.961	0.041
20.5	1.014	0.039	0.985	0.037
22.2	1.019	0.047	1.009	0.046
24.5	1.001	0.034	0.952	0.032
26.5	1.021	0.050	0.989	0.048
28.7	1.014	0.034	0.981	0.033
30.1	1.018	0.042	0.956	0.039
32.7	1.031	0.041	1.044	0.041
33.7	1.001	0.038	0.958	0.036
36.9	1.009	0.032	1.003	0.032
39.9	0.977	0.037	0.986	0.037
41.7	1.008	0.036	1.012	0.036
45.5	1.017	0.031	0.997	0.030
49.6	0.982	0.030	1.012	0.031
54.8	0.998	0.028	1.007	0.028

Table V-10. Continued

Q ²	Raise 1%		Lower 1%	
	Ratio	Error	Ratio	Error
61.2	1.019	0.028	0.993	0.027
69.3	0.989	0.025	0.986	0.025
78.8	0.996	0.033	0.992	0.033
90.9	1.018	0.051	1.005	0.050
x = 0.45				
24.7	1.042	0.142	1.073	0.138
29.0	0.849	0.067	1.243	0.100
32.9	0.908	0.054	1.125	0.071
37.3	0.960	0.050	1.052	0.055
42.4	0.948	0.044	1.075	0.052
47.4	0.970	0.041	1.005	0.043
54.9	1.016	0.035	1.035	0.035
64.3	0.985	0.033	0.994	0.033
79.6	1.009	0.029	1.000	0.028
100.8	1.004	0.033	1.013	0.033
124.5	0.959	0.052	1.000	0.054

Table V-11. Calculation of Average Nucleus, Nucleon Content

Material	Z	N	ρ (g/cm ³)
Fe	26.0	29.85	7.87
(CH) [$\frac{H}{C} \approx 1.10$]	7.1	6.02	1.032
Vinyl = Mylar (C ₅ H ₄ O ₂)	50.0	46.09	1.39
Al	13.0	13.98	2.70
Air (N ₂)	14.0	14.02	<u>0.001205</u>
			12.993205

$$\bar{Z} = \frac{\sum \rho_i Z_i}{\sum \rho_i} = 24.36$$

$$\bar{N} = \frac{\sum \rho_i N_i}{\sum \rho_i} = 26.40$$

$$\rightarrow \bar{A} = 50.76$$

$$\frac{\bar{Z}}{\bar{A}} = 0.4799$$

$$\frac{26}{56} = \frac{Z_{Fe}}{A_{Fe}} = 0.4643$$

while for $W^2 = 30 \text{ GeV}^2$, the change again maximizes, the ratio falling by 2.2%.

When the effects of these resolution changes on F_2 are examined as functions of Q^2 and x , more detail can be seen than from the integrated W^2 distribution. Specifically, low x regions (<0.2) are nearly unaffected except at values of $Q^2 < 7 \text{ (GeV/c)}^2$. As x increases, the perturbations in the comparison increase, affecting larger values of Q^2 , until for the highest x region, all values of Q^2 are affected. These effects in some representative regions are shown in Table V-10. Neither raising nor lowering the E' resolution has any effect on the regions near Q^2 of 40 (GeV/c)^2 and x of 0.2 where the data seem to be higher than the monte carlo prediction.

A final possibility considered is that the use of a nucleus with 26 protons and 30 neutrons as representative of our target in obtaining structure functions, will result in the wrong relative mixture of neutron and proton in computing F_2 per nucleon. To check this, an exercise is performed (Table V-11) in which \bar{z} and \bar{n} , respectively, the average proton and neutron content in the nucleus, are calculated. When these averages are used, structure function values are returned which differ at most by 0.6% from those obtained with the original Fe values.

In summary then, the systematic effects listed in Table V-12 have been examined to determine their effects on the data. Several (3,4,5) were assumed as universally

Table V-12. A List of All Examined Systematic Error Possibilities

-
-
- 1) Variance of Q_0^2
 - 2) Target Mass Effects on F_2
 - 3) Analytic Approximations from QCD
 - 4) Accuracy of Radiative Corrections
 - 5) Reconstruction Efficiency
 - 6) Inefficiency of Reconstruction Efficiency Correction
 - 7) E_0 Assumed 1% Higher
 - 8) Toroid Magnetic Field Assumed 1% High
 - 9) Toroid Magnetic Field Assumed 1% Low
 - 10) E' Resolution 1% High
 - 11) E' Resolution 1% Low
 - 12) Effect of $R = \sigma_L/\sigma_T$
 - 13) Calculations Using an Average Nucleus, not Iron
-
-

applicable, and result in an overall variance of $\pm 3\%$ in the structure functions. Three (7,8,9) were determined to be highly probable, and their individual and summed contributions to the systematic error were tabulated in Appendix D. Two (6,12) were tabulated with the determined structure functions in Appendix C, and two (1,13) were rejected. Two (10,11) were determined to be unlikely, but within the realm of possibility, and the last one (2) affects primarily regions with $x > 0.4$, although resolution spreads this to slightly lower values of x .

CHAPTER VI

CONCLUSIONS

How accurate, then, is the QCD model of Buras and Gaemers in describing this set of data? It is clear that lower Q^2 data ($Q^2 < 20 \text{ (GeV/c)}^2$) can be accurately described by this model. However, an increase to the Q^2 region 20-25 finds the data beginning to rise above the model prediction for $x < 0.15$. Further increasing Q^2 to the region 25-30 $(\text{GeV/c})^2$ finds this excess beginning at $x \approx 0.27$ and lasting as low as $x \approx 0.12$. This high region persists to values as large as $Q^2 = 50 \text{ (GeV/c)}^2$, above which it is not in evidence. These statements apply to the model predictions using Λ and Q_0^2 equal to 0.60 and 2.53 respectively. The values originally found by Buras and Gaemers for Λ and Q_0^2 (0.3 and 1.8 respectively) do not describe this data very well even at low values for Q^2 , close to those which were originally used by Buras and Gaemers.

One explanation⁽⁵⁵⁾ which has been suggested is that this excess above monte carlo represents a threshold of production in the variable W^2 , starting at the value $W^2 = 80 \text{ GeV}^2$. These data do not support this contention. The regions of excess mentioned above correspond to minimum

W^2 values between 85 and 130 GeV^2 , depending on the Q^2 region, but the excess ends at values of W^2 between 180 and 300 GeV^2 , again depending on the Q^2 region. This can be seen more clearly in Figure VI-1 where the data/monte carlo ratio with Λ , $Q_0^2 = 0.60, 2.53$ is plotted. This shows that the ratio is plateaued at 95% at low W^2 , rising to a high of 105% around W^2 of 180 GeV^2 . The ratio then drops back to approximately 92%, belying any possibility of a threshold.

These low values for the ratio below $W^2 \sim 90 \text{ GeV}^2$ correspond to the low data points at higher values of x in Figures V-2. These data, as was discussed in chapter five, are likely low because of the failure to include target mass effects in the calculation of F_2 . Consequently, the appearance of a threshold in the ratio may be artificial. The values plotted for F_2 are correct, though. The reason is that small changes in the model, especially in a region where F_2 is not rapidly changing, have a negligible effect on the determined value of the structure function which is

$$F_2(Q^2, x) = \left(\frac{\text{Data}}{\text{M.C.}} \right) \cdot F_2^m(Q^2, x) \quad (1)$$

where F_2^m is the model prediction. The monte carlo weight (M.C.) is linearly dependent on this F_2 , so except for resolution effects, the determined F_2 is independent of the model used. If F_2 is rapidly changing, the resolution will smear more events away from peak regions in F_2 than are smeared in from nearby regions. This means the convenient

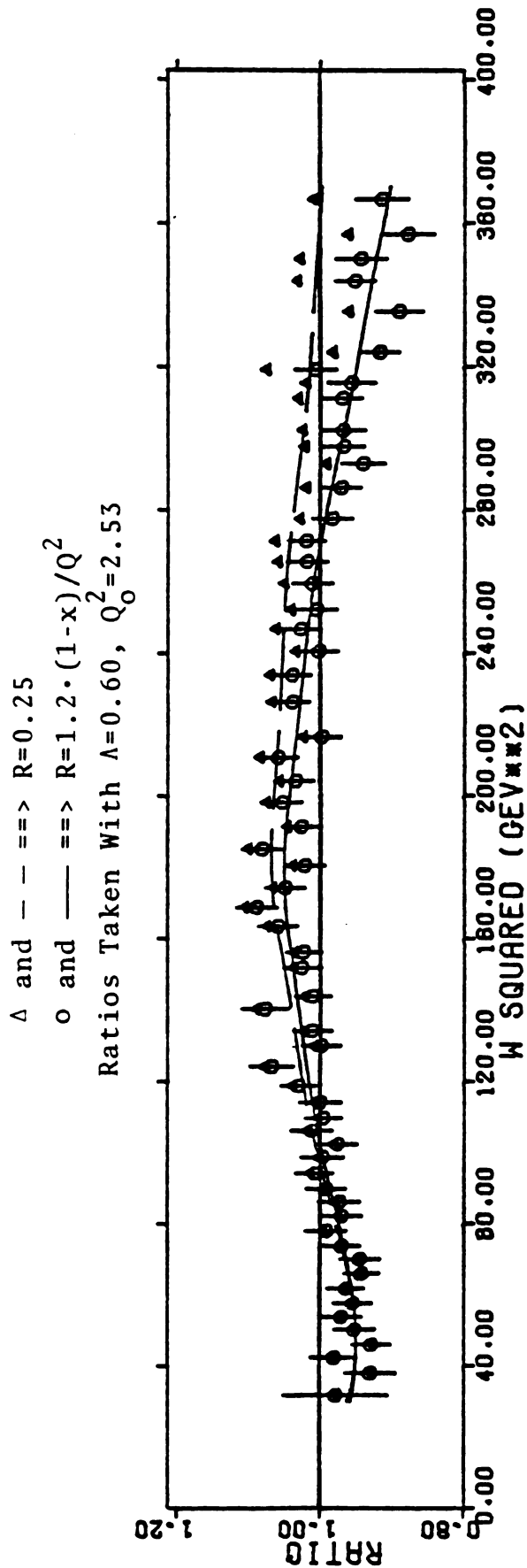


Figure VI-1. The Normalized Ratio Data/Monte Carlo vs. W^2

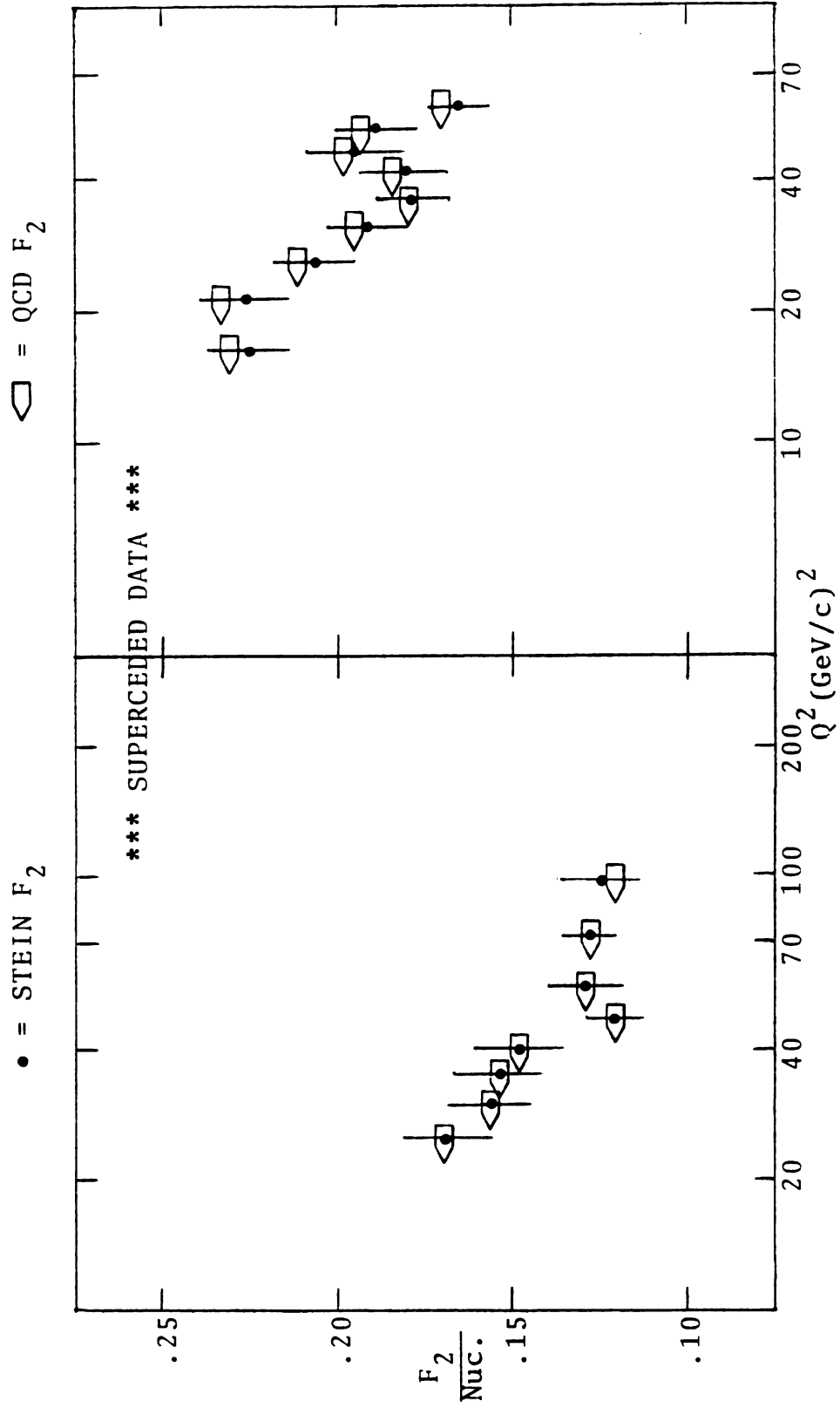


Figure VI-2. Illustration of Effects of Resolution on the Determined Value of F_2

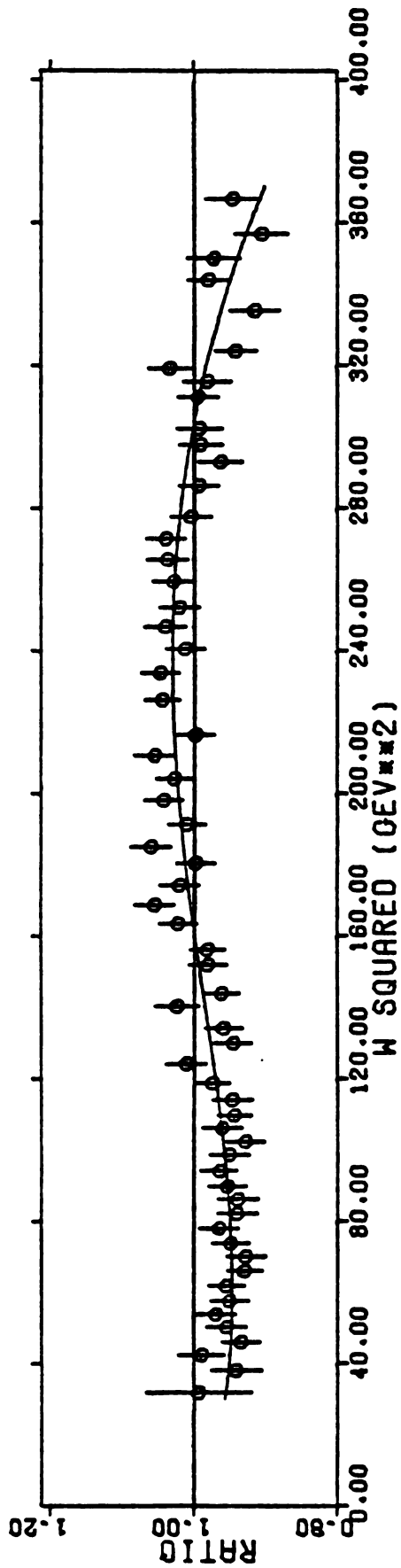


Figure VI-3. Correction of W^2 Ratio by "B-High" Results

cancellation of F_2^m in Eqn. 1 will not give the same determined results for F_2 when F_2^m is changed by more than a small amount. Figure VI-2 shows some very early results of this experiment where F_2^m was changed from the Stein model⁽¹⁸⁾ to the model of Buras and Gaemers, resulting in a shift of the determined F_2 due to resolution.

Of the systematic effects considered in chapter five, only raising the magnetic field by 1% gave results which could simulate this rise in W^2 . The values tabulated in Appendix D reflect the manner in which the ratio would change given the indicated monte carlo change. Multiplying these values by the determined W^2 ratios of Figure VI-1 will then simulate this monte carlo change. The result, plotted in Figure VI-3, gives ratios consistently closer to unity than in Figure VI-1. This cannot be done for the data regions of Figures V-2 and V-3 because of insufficient statistics, but it casts significant doubt on this high ratio region of W^2 .

One serious problem is the indeterminate status of $R = \sigma_L/\sigma_T$. For high values of x , this causes little problem for the two models attempted here, $R = 1.2 \cdot (1-x)/Q^2$ and $R = 0.25$ (plotted without error bars in Figures V-2 and V-3). However, for $x < 0.2$, serious disagreement occurs, particularly with increasing Q^2 . Changes in F_2 as large as 12% occur solely due to this change in R . Although, as was shown, the fitting process does not always converge using $R = 0.25$, this cannot be used as a criterion for rejecting

this form of R . Only better experimental results can be used for this purpose, and these do not currently exist. Systematically accurate results at higher Q^2 values, particularly at low x , await this occurrence.

In conclusion, with the form of R assumed here, the parameters $\Lambda = 0.60$ and $Q_0^2 = 2.53 \text{ (GeV/c)}^2$ most accurately describe the data. Values of F_2 for Q^2 between 25 and 50 (GeV/c)^2 seem to be higher than these parameter values allow, but as has been noted, this corresponding region in W^2 can be lowered to a tolerable level by a one percent rise in the assumed value of the toroid magnetic field. Higher values of x , where the data are too low r.e. this prediction, are likely explained by the target mass effect, which is not calculated here. Therefore, this model of F_2 would seem to give a satisfactory explanation for the trend of the values of F_2 measured here, but does not seem to adequately predict the observed details.

APPENDIX A

APPENDIX A

PROOF OF EQUIVALENCE OF THE STRUCTURE FUNCTION F_2 AND ITS MOMENTS

Problem: Define a function $f(x)$ in terms of its moments.

$\{P_i\}$ is a set of orthogonal functions such that

$$\int P_i(x)P_j(x)dx = \delta_{ij} \quad . \quad (\text{A-1})$$

We can make the expansions:

$$f(x) = \sum_{i=0}^{\infty} a_i P_i(x) \quad (\text{A-2})$$

$$x^k = \sum_{\ell=0}^k b_{\ell k} P_{\ell}(x) \quad . \quad (\text{A-3})$$

From equation A-3 then,

$$b_{\ell k} = \int x^k P_{\ell}(x) dx \quad (\text{A-4})$$

Now let us experimentally measure the moments C_j , defined as

$$C_0 = \int f(x) dx \quad (\text{A-5})$$

$$C_1 = \int x f(x) dx \quad (\text{A-6})$$

$$C_2 = \int x^2 f(x) dx \quad (\text{A-7})$$

⋮

Substitution of A-2 into A-5 gives

$$\begin{aligned} C_0 &= \int \sum_{i=0}^{\infty} a_i P_i(x) dx = \sum_{i=0}^{\infty} a_i \int P_i(x) dx \\ &= \sum_{i=0}^{\infty} a_i \delta_{i0} = a_0 . \end{aligned} \quad (\text{A-8})$$

Similarly, from A-2, A-3, and A-6,

$$\begin{aligned} C_1 &= \int \left(\sum_{i=0}^{\infty} a_i P_i(x) \right) \left(\sum_{\ell=0}^1 b_{\ell 1} P_{\ell}(x) \right) dx \\ &= a_0 b_{01} \int P_0(x) P_0(x) dx + a_1 b_{11} \int P_1(x) P_1(x) dx \\ &= a_0 b_{01} + a_1 b_{11} \\ &\rightarrow a_1 = \frac{C_1 - a_0 b_{01}}{b_{11}} \end{aligned} \quad (\text{A-9})$$

⋮

In this way, a matrix equation is established,

$$BA = C$$

or

$$\begin{pmatrix} b_{00} & 0 & 0 & 0 & \dots & 0 \\ b_{01} & b_{11} & 0 & 0 & \dots & 0 \\ b_{02} & b_{12} & b_{22} & 0 & \dots & 0 \\ \vdots & \vdots & \vdots & \cdot & & \vdots \\ b_{0n} & b_{1n} & b_{2n} & \dots & \cdot & b_{nn} \end{pmatrix} \begin{pmatrix} a_0 \\ a_1 \\ a_2 \\ \vdots \\ a_n \end{pmatrix} = \begin{pmatrix} C_0 \\ C_1 \\ C_2 \\ \vdots \\ C_n \end{pmatrix}$$

and so the a_i are uniquely determined. Knowledge of the moments C_i is then sufficient to determine the function $f(x)$.

APPENDIX B

APPENDIX B

PRESCRIPTION FOR S AND C MOMENT EVALUATIONS

To evaluate the moments $\langle q(Q^2) \rangle_n$ where $q = S, C, G$, and $n = 2, 3$, the following procedure is followed.

Define:

$$D_1^{(n)}(Q^2) \equiv \langle S(Q_0^2) \rangle_n e^{-\gamma_-^n \bar{s}} \quad (\text{B-1})$$

$$\begin{aligned} D_2^{(n)}(Q^2) \equiv & \{ (1-\alpha_n) \langle q^S(Q_0^2) \rangle_n - \beta_n \langle G(Q_0^2) \rangle_n \} e^{-\gamma_+^n \bar{s}} \\ & + \{ \alpha_n \langle q^S(Q_0^2) \rangle_n + \beta_n \langle G(Q_0^2) \rangle_n \} e^{-\gamma_-^n \bar{s}} \\ & - \langle V_8(Q_0^2) \rangle_n e^{-\gamma_-^n \bar{s}} \end{aligned} \quad (\text{B-2})$$

where

$$\langle q^S(Q_0^2) \rangle_n \equiv \langle S(Q_0^2) \rangle_n + \langle V_8(Q_0^2) \rangle_n \quad (\text{B-3})$$

and the parameters α_n , β_n , γ_{\pm}^n and γ_n and moments evaluated at Q_0^2 are given in Table I-2. In SU(3) gauge theory with four flavors then

$$\langle S(Q^2) \rangle_n = \frac{3}{4} D_2^{(n)}(Q^2) + \frac{1}{4} D_1^{(n)}(Q^2)$$

$$\langle C(Q^2) \rangle_n = \frac{1}{4} (D_2^{(n)}(Q^2) - D_1^{(n)}(Q^2))$$

(B-4)

$$\begin{aligned} \langle G(Q^2) \rangle_n &= \{ \alpha_n \langle G(Q_0^2) \rangle_n - \frac{(1-\alpha_n)\alpha_n}{\beta_n} \langle q^S(Q_0^2) \rangle_n \} e^{-\gamma_+^{n\bar{s}}} \\ &+ \{ (1-\alpha_n) \langle G(Q_0^2) \rangle_n + \frac{(1-\alpha_n)\alpha_n}{\beta_n} \langle q^S(Q_0^2) \rangle_n \} e^{-\gamma_-^{n\bar{s}}} \end{aligned}$$

APPENDIX C

APPENDIX C

SUMMARY OF DETERMINED STRUCTURE FUNCTION VALUES

This appendix contains lists of all the structure function values which have been determined. There are two sections, one for data binned (parametric) in Q^2 regions, and one for data binned in x regions.

The first three columns contain the average Q^2 , x , and W^2 values determined for the data point, while columns four and five are the determined value of F_2 and its error at this point. Column six is the central value of Q^2 (or x) to which the point has been shifted, as explained in Chapter five; columns seven to twelve refer to this shifted value. Columns seven and eight are the resultant, shifted F_2 and its error, while columns nine and ten are the obtained results if $R=0.25$ is used instead of $R=1.2 \cdot (1-x)/Q^2$. Columns eleven and twelve use the latter form of R , but the 1.9% inefficiency correction has been applied uniformly instead of in the manner decided upon in chapter five.

Table C-1. F_2 in PARAMETRIC Q^2 REGIONS

Q^2	x	W^2	Plotted			Shifted Values			
			F_2	$\sigma(F_2)$	Q^2	F_2	$\sigma(F_2)$	F_2	$\sigma(F_2)$
10.4	0.031	360.1	.3976	.0147	12.5	.4134	.0153	.4123	.0153
11.1	0.039	336.3	.4297	.0126	12.5	.4389	.0129	.4374	.0129
11.5	0.043	306.7	.4427	.0120	12.5	.4490	.0122	.4476	.0122
11.7	0.046	281.3	.4398	.0110	12.5	.4445	.0111	.4431	.0111
12.1	0.050	269.5	.4540	.0118	12.5	.4559	.0118	.4540	.0118
12.9	0.054	261.2	.4368	.0117	12.5	.4348	.0116	.4330	.0111
12.2	0.059	212.2	.4300	.0114	12.5	.4312	.0114	.4307	.0114
12.2	0.067	188.2	.3995	.0110	12.5	.4004	.0110	.4004	.0110
12.2	0.072	172.7	.4060	.0146	12.5	.4068	.0146	.4073	.0146
12.9	0.075	173.1	.3948	.0157	12.5	.3936	.0157	.3936	.0157
12.3	0.080	158.8	.3935	.0146	12.5	.3939	.0146	.3947	.0146
12.9	0.085	155.1	.3907	.0136	12.5	.3898	.0136	.3902	.0136
11.4	0.089	133.6	.3640	.0164	12.5	.3659	.0165	.3675	.0165
12.8	0.092	141.4	.3542	.0143	12.5	.3538	.0143	.3550	.0143
12.9	0.097	136.4	.3682	.0160	12.5	.3677	.0160	.3688	.0160
12.1	0.100	127.2	.3608	.0158	12.5	.3612	.0158	.3631	.0158
12.3	0.104	123.1	.3214	.0145	12.5	.3215	.0145	.3230	.0148
13.3	0.110	124.4	.3397	.0153	12.5	.3393	.0153	.3412	.0157
12.0	0.116	109.4	.3574	.0143	12.5	.3575	.0143	.3600	.0143
12.3	0.122	106.7	.3382	.0136	12.5	.3382	.0136	.3403	.0139
12.2	0.133	98.1	.3205	.0128	12.5	.3204	.0128	.3227	.0128
12.5	0.146	91.8	.3293	.0132	12.5	.3294	.0132	.3316	.0132
12.1	0.158	82.7	.2891	.0115	12.5	.2887	.0115	.2905	.0115
12.2	0.171	76.6	.2998	.0120	12.5	.2995	.0120	.3016	.0123
12.3	0.188	69.5	.2831	.0097	12.5	.2828	.0097	.2848	.0097
11.7	0.199	64.3	.2793	.0144	12.5	.2779	.0143	.2801	.0143
11.9	0.207	61.6	.2543	.0138	12.5	.2532	.0137	.2553	.0137
13.3	0.216	63.6	.2658	.0115	12.5	.2676	.0116	.2702	.0119
11.8	0.226	55.1	.2479	.0095	12.5	.2465	.0094	.2487	.0094

Table C-1. (continued)

Q ²	x	W ²	F ₂	σ(F ₂)	Q ²	Plotted		Shifted Values		N=1.019	
						F ₂	σ(F ₂)	F ₂	σ(F ₂)		
12.3	0.240	52.9	.2472	.0103	12.5	.2469	.0103	.2478	.0103	.2492	.0106
12.9	0.258	50.0	.2265	.0098	12.5	.2274	.0098	.2283	.0098	.2293	.0098
12.5	0.275	44.7	.2182	.0093	12.5	.2184	.0093	.2193	.0093	.2201	.0093
12.2	0.287	41.5	.2096	.0133	12.5	.2090	.0133	.2097	.0133	.2107	.0135
12.0	0.303	37.9	.1987	.0131	12.5	.1977	.0130	.1980	.0130	.1992	.0132
12.8	0.320	37.4	.1850	.0147	12.5	.1857	.0148	.1853	.0148	.1873	.0150
II) 15<Q ² <20											
16.2	0.047	355.2	.4488	.0195	17.5	.4536	.0197	.4849	.0210	.4493	.0197
15.9	0.054	325.3	.4458	.0129	17.5	.4509	.0130	.4787	.0139	.4466	.0130
16.8	0.057	311.7	.4262	.0132	17.5	.4281	.0133	.4528	.0141	.4240	.0133
17.1	0.061	299.4	.4320	.0126	17.5	.4329	.0126	.4561	.0133	.4288	.0126
17.0	0.067	258.9	.4368	.0127	17.5	.4379	.0127	.4591	.0133	.4344	.0127
17.0	0.074	232.4	.4262	.0131	17.5	.4271	.0131	.4451	.0137	.4242	.0131
17.4	0.079	218.7	.4274	.0124	17.5	.4275	.0124	.4435	.0129	.4250	.0124
16.8	0.087	190.4	.4124	.0128	17.5	.4132	.0128	.4262	.0132	.4116	.0128
17.0	0.096	175.8	.3881	.0135	17.5	.3884	.0135	.3984	.0138	.3876	.0135
17.4	0.103	166.8	.3880	.0143	17.5	.3880	.0143	.3965	.0146	.3877	.0143
17.4	0.109	156.6	.3449	.0128	17.5	.3449	.0128	.3514	.0130	.3453	.0128
17.7	0.118	146.5	.3630	.0120	17.5	.3630	.0120	.3682	.0122	.3634	.0120
16.7	0.128	129.5	.3473	.0126	17.5	.3470	.0126	.3506	.0127	.3484	.0126
17.0	0.136	123.2	.3415	.0129	17.5	.3412	.0129	.3439	.0130	.3428	.0129
17.3	0.147	115.8	.3166	.0117	17.5	.3165	.0117	.3181	.0118	.3184	.0117
16.8	0.158	105.4	.3090	.0126	17.5	.3084	.0126	.3094	.0126	.3105	.0126
17.6	0.166	104.4	.3024	.0134	17.5	.3026	.0134	.3032	.0134	.3050	.0137
16.9	0.174	95.8	.2835	.0131	17.5	.2829	.0131	.2833	.0131	.2855	.0131
17.1	0.182	92.9	.2847	.0122	17.5	.2843	.0122	.2845	.0122	.2871	.0122
16.7	0.190	87.5	.2715	.0130	17.5	.2706	.0130	.2708	.0130	.2733	.0133
16.3	0.199	80.7	.2687	.0119	17.5	.2670	.0118	.2672	.0118	.2697	.0120
17.5	0.208	81.3	.2454	.0107	17.5	.2454	.0107	.2456	.0107	.2478	.0107
17.7	0.226	74.7	.2509	.0096	17.5	.2512	.0096	.2517	.0096	.2537	.0099
17.2	0.235	69.4	.2447	.0123	17.5	.2443	.0123	.2449	.0123	.2464	.0125

Table C-1. (continued)

Q ²	x	W ²	Shifted Values								
			F ₂	σ(F ₂)	Q ²	Plotted F ₂ σ(F ₂)	F ₂	σ(F ₂)	F ₂	σ(F ₂)	
16.1	0.243	63.4	.2342	.0128	17.5	.2321	.0127	.2329	.0127	.2340	.0127
17.3	0.256	63.4	.2145	.0104	17.5	.2143	.0104	.2152	.0104	.2161	.0106
17.5	0.265	61.5	.2247	.0097	17.5	.2248	.0097	.2259	.0097	.2263	.0097
16.6	0.275	55.7	.2019	.0118	17.5	.2006	.0117	.2017	.0118	.2021	.0119
16.2	0.288	50.8	.1937	.0089	17.5	.1918	.0088	.1929	.0088	.1932	.0088
17.4	0.303	50.6	.1783	.0086	17.5	.1782	.0086	.1791	.0086	.1794	.0088
16.0	0.322	43.5	.1696	.0078	17.5	.1674	.0077	.1680	.0077	.1687	.0077
18.5	0.335	46.3	.1624	.0073	17.5	.1638	.0074	.1640	.0074	.1652	.0074
18.6	0.354	43.0	.1438	.0083	17.5	.1453	.0084	.1448	.0084	.1465	.0086
III) 20 < Q ² < 25											
20.3	0.059	362.7	.4486	.0310	22.5	.4530	.0313	.4954	.0342	.4464	.0308
21.5	0.066	331.8	.4058	.0134	22.5	.4073	.0134	.4406	.0146	.4015	.0134
21.7	0.074	297.8	.4035	.0151	22.5	.4044	.0151	.4329	.0162	.3992	.0151
22.1	0.078	280.9	.4093	.0139	22.5	.4096	.0139	.4357	.0148	.4046	.0139
22.2	0.087	249.8	.3947	.0133	22.5	.3949	.0133	.4160	.0140	.3904	.0133
22.5	0.096	228.5	.4032	.0136	22.5	.4032	.0136	.4211	.0142	.3989	.0136
21.7	0.104	202.2	.3780	.0138	22.5	.3781	.0138	.3919	.0143	.3755	.0138
22.3	0.114	186.6	.3859	.0132	22.5	.3859	.0132	.3965	.0136	.3837	.0132
21.7	0.124	165.3	.3736	.0148	22.5	.3733	.0148	.3809	.0151	.3730	.0148
22.4	0.134	156.9	.3578	.0132	22.5	.3578	.0132	.3631	.0134	.3581	.0132
22.1	0.146	141.9	.3313	.0136	22.5	.3311	.0136	.3341	.0137	.3323	.0136
22.2	0.160	129.4	.3062	.0111	22.5	.3060	.0111	.3073	.0111	.3074	.0111
22.0	0.178	115.6	.2885	.0104	22.5	.2881	.0104	.2883	.0104	.2898	.0104
22.4	0.198	104.4	.2689	.0097	22.5	.2688	.0097	.2687	.0097	.2704	.0097
22.1	0.222	91.3	.2538	.0086	22.5	.2534	.0086	.2536	.0086	.2549	.0088
22.4	0.250	80.9	.2206	.0076	22.5	.2206	.0076	.2216	.0076	.2219	.0076
22.0	0.275	70.6	.2022	.0075	22.5	.2017	.0075	.2033	.0076	.2029	.0075
22.0	0.297	63.8	.1895	.0066	22.5	.1890	.0066	.1909	.0067	.1902	.0068
23.1	0.329	57.8	.1641	.0065	22.5	.1648	.0065	.1663	.0066	.1660	.0065
22.3	0.369	47.2	.1378	.0070	22.5	.1377	.0070	.1374	.0070	.1388	.0070

Table C-1 (continued)

Q ²	x	W ²	F ₂	σ(F ₂)	Q ²	Plotted		Shifted Values		N=1.019	
						F ₂	σ(F ₂)	F ₂	σ(F ₂)		F ₂
IV)	25 < Q ² < 30										
26.3	0.066	377.1	.3858	.0603	27.5	.3870	.0605	.4298	.0672	.3802	.0596
26.1	0.074	348.9	.3770	.0235	27.5	.3781	.0236	.4151	.0259	.3715	.0236
27.5	0.080	333.1	.3743	.0165	27.5	.3742	.0165	.4075	.0180	.3675	.0161
26.7	0.088	296.5	.3868	.0153	27.5	.3871	.0153	.4168	.0165	.3802	.0149
27.2	0.098	275.1	.3631	.0173	27.5	.3631	.0173	.3865	.0184	.3565	.0169
26.7	0.106	243.0	.4002	.0163	27.5	.4002	.0163	.4225	.0172	.3947	.0160
27.1	0.115	224.7	.3801	.0157	27.5	.3800	.0157	.3977	.0164	.3754	.0157
27.6	0.124	207.9	.3906	.0164	27.5	.3906	.0164	.4053	.0170	.3869	.0164
27.2	0.134	186.8	.3609	.0154	27.5	.3608	.0154	.3716	.0159	.3591	.0151
27.0	0.145	170.7	.3577	.0148	27.5	.3574	.0148	.3656	.0151	.3565	.0148
27.3	0.160	154.6	.3391	.0130	27.5	.3390	.0130	.3440	.0132	.3387	.0130
27.2	0.178	137.4	.2983	.0136	27.5	.2981	.0136	.3006	.0137	.2984	.0136
27.9	0.199	123.9	.2929	.0134	27.5	.2933	.0134	.2944	.0134	.2936	.0134
27.1	0.220	108.8	.2692	.0126	27.5	.2688	.0126	.2693	.0126	.2695	.0126
27.3	0.246	96.7	.2491	.0113	27.5	.2490	.0113	.2497	.0113	.2499	.0116
28.9	0.269	90.8	.2156	.0100	27.5	.2169	.0101	.2181	.0102	.2177	.0103
28.5	0.300	78.2	.1808	.0089	27.5	.1817	.0089	.1834	.0090	.1827	.0091
27.7	0.335	65.9	.1566	.0074	27.5	.1568	.0074	.1587	.0075	.1578	.0074
26.7	0.377	53.6	.1222	.0059	27.5	.1217	.0059	.1227	.0059	.1226	.0061
27.7	0.409	48.5	.1110	.0073	27.5	.1111	.0073	.1108	.0073	.1119	.0073
V)	30 < Q ² < 40										
31.3	0.087	346.3	.3848	.0266	35.0	.3859	.0267	.4264	.0295	.3773	.0259
33.0	0.099	319.4	.3572	.0142	35.0	.3573	.0142	.3890	.0155	.3481	.0138
34.2	0.113	285.9	.3590	.0118	35.0	.3589	.0118	.3851	.0127	.3503	.0115
35.0	0.125	258.7	.3553	.0135	35.0	.3553	.0135	.3767	.0143	.3479	.0132
34.3	0.135	231.9	.3674	.0149	35.0	.3671	.0149	.3860	.0157	.3606	.0146
34.2	0.147	208.5	.3348	.0135	35.0	.3344	.0135	.3485	.0141	.3298	.0135
34.9	0.161	191.9	.3249	.0128	35.0	.3249	.0128	.3356	.0132	.3208	.0125
33.9	0.178	167.3	.3301	.0121	35.0	.3293	.0121	.3373	.0124	.3266	.0121

Table C-1. (continued)

Q ²	x	W ²	F ₂	σ(F ₂)	Q ²	Plotted		Shifted Values		F ₂	σ(F ₂)	N=1.019
						F ₂	σ(F ₂)	F ₂	σ(F ₂)			
33.5	0.196	147.5	.3006	.0118	35.0	.2995	.0118	.3044	.0120	.2979	.0118	
34.9	0.215	137.4	.2735	.0105	35.0	.2735	.0105	.2766	.0106	.2725	.0105	
33.7	0.237	119.2	.2542	.0101	35.0	.2532	.0101	.2552	.0102	.2532	.0101	
34.4	0.263	107.4	.2183	.0090	35.0	.2179	.0090	.2193	.0091	.2181	.0090	
34.5	0.294	94.1	.1934	.0085	35.0	.1931	.0085	.1945	.0086	.1938	.0085	
34.9	0.329	81.8	.1544	.0061	35.0	.1543	.0061	.1557	.0062	.1549	.0061	
34.0	0.363	69.8	.1359	.0058	35.0	.1354	.0058	.1368	.0059	.1358	.0059	
34.5	0.397	61.7	.1073	.0055	35.0	.1071	.0055	.1080	.0055	.1074	.0055	
35.3	0.433	54.5	.0784	.0054	35.0	.0785	.0054	.0786	.0054	.0790	.0054	
VI) 40 < Q ² < 50												
42.4	0.113	351.1	.2822	.0479	45.0	.2819	.0478	.3161	.0536	.2723	.0460	
42.9	0.125	321.8	.3248	.0212	45.0	.3243	.0212	.3581	.0234	.3136	.0205	
44.0	0.135	298.8	.3076	.0170	45.0	.3073	.0170	.3356	.0186	.2977	.0164	
45.1	0.147	274.4	.3018	.0142	45.0	.3018	.0142	.3252	.0153	.2930	.0136	
44.6	0.164	237.7	.3301	.0144	45.0	.3299	.0144	.3501	.0153	.3222	.0141	
44.5	0.178	214.4	.2960	.0164	45.0	.2958	.0164	.3106	.0172	.2902	.0161	
44.5	0.196	191.6	.2859	.0123	45.0	.2856	.0123	.2964	.0128	.2813	.0121	
44.5	0.215	171.5	.2544	.0160	45.0	.2541	.0160	.2611	.0164	.2515	.0158	
45.2	0.237	154.6	.2613	.0109	45.0	.2615	.0109	.2665	.0111	.2598	.0109	
44.1	0.266	130.8	.2311	.0105	45.0	.2306	.0105	.2335	.0106	.2300	.0105	
44.2	0.295	114.7	.1896	.0089	45.0	.1892	.0089	.1910	.0090	.1890	.0089	
44.8	0.327	101.5	.1704	.0093	45.0	.1703	.0093	.1719	.0094	.1700	.0093	
45.1	0.368	86.8	.1178	.0070	45.0	.1179	.0070	.1192	.0071	.1175	.0070	
44.7	0.406	73.6	.1007	.0066	45.0	.1006	.0066	.1018	.0067	.1004	.0066	
44.5	0.438	64.9	.0846	.0060	45.0	.0845	.0060	.0852	.0061	.0846	.0060	
45.6	0.473	58.1	.0596	.0083	45.0	.0597	.0083	.0598	.0083	.0596	.0083	
VII) 50 < Q ² < 80												
51.5	0.145	318.1	.2761	.0329	60.0	.2738	.0326	.3036	.0362	.2645	.0314	
53.7	0.161	294.4	.3152	.0187	60.0	.3129	.0186	.3429	.0203	.3033	.0180	

Table C-1. (continued)

Q ²	x	W ²	F ₂	σ(F ₂)	Q ²	Plotted		Shifted Values		N=1.019		
						F ₂	σ(F ₂)	F ₂	σ(F ₂)			
56.5	0.176	276.6	.2654	.0159	60.0	.2642	.0158	.2869	.0172	F ₂	.2570	.0153
59.5	0.191	262.5	.2672	.0145	60.0	.2670	.0145	.2876	.0156	F ₂	.2607	.0142
60.6	0.209	237.7	.2367	.0110	60.0	.2369	.0110	.2527	.0117	F ₂	.2324	.0107
60.9	0.230	212.5	.2236	.0113	60.0	.2240	.0113	.2366	.0119	F ₂	.2203	.0111
62.8	0.250	195.8	.2176	.0111	60.0	.2186	.0112	.2291	.0117	F ₂	.2154	.0110
63.7	0.271	178.8	.1975	.0112	60.0	.1988	.0113	.2068	.0117	F ₂	.1956	.0111
62.3	0.295	156.8	.1811	.0092	60.0	.1819	.0092	.1878	.0095	F ₂	.1793	.0090
62.7	0.323	139.1	.1577	.0082	60.0	.1586	.0082	.1626	.0084	F ₂	.1560	.0081
61.5	0.359	118.1	.1463	.0067	60.0	.1468	.0067	.1496	.0068	F ₂	.1445	.0065
61.2	0.401	99.5	.1091	.0060	60.0	.1094	.0060	.1110	.0061	F ₂	.1076	.0059
62.8	0.440	87.8	.0858	.0056	60.0	.0864	.0056	.0874	.0057	F ₂	.0849	.0055
62.5	0.477	75.7	.0682	.0048	60.0	.0687	.0048	.0694	.0049	F ₂	.0677	.0048
66.5	0.526	66.6	.0396	.0044	60.0	.0404	.0045	.0408	.0045	F ₂	.0398	.0044
VIII) 80 < Q ² < 120												
84.4	0.243	271.5	.2602	.0254	90.0	.2586	.0252	.2864	.0279	F ₂	.2517	.0245
85.2	0.271	236.7	.1977	.0220	90.0	.1966	.0219	.2139	.0238	F ₂	.1913	.0214
87.9	0.296	216.1	.1744	.0153	90.0	.1740	.0153	.1867	.0164	F ₂	.1692	.0148
92.6	0.326	198.1	.1515	.0155	90.0	.1520	.0156	.1612	.0165	F ₂	.1478	.0151
92.7	0.359	172.4	.1353	.0117	90.0	.1358	.0117	.1425	.0123	F ₂	.1319	.0114
93.0	0.398	147.9	.1095	.0088	90.0	.1100	.0088	.1144	.0092	F ₂	.1070	.0086
95.1	0.440	128.1	.0876	.0086	90.0	.0883	.0087	.0914	.0090	F ₂	.0861	.0086
95.1	0.477	110.9	.0826	.0083	90.0	.0833	.0084	.0858	.0086	F ₂	.0813	.0081
96.9	0.543	88.4	.0448	.0042	90.0	.0454	.0043	.0463	.0044	F ₂	.0444	.0042
IX) 120 < Q ² < 200												
124.1	0.381	208.3	.1732	.0560	130.0	.1722	.0557	.1886	.0609	F ₂	.1676	.0542
127.7	0.453	160.7	.1412	.0210	130.0	.1408	.0209	.1500	.0223	F ₂	.1373	.0204
128.5	0.537	117.3	.0831	.0162	130.0	.0829	.0162	.0864	.0169	F ₂	.0812	.0158

Table C-2. F_2 in PARAMETRIC x REGIONS

I) $0.03 < x < 0.06$		Shifted Values									
Q^2	x	W^2	F_2	$\sigma(F_2)$	Plotted		R=0.25		N=1.019		
					x	F_2	$\sigma(F_2)$	F_2	$\sigma(F_2)$	F_2	$\sigma(F_2)$
5.7	0.041	155.6	.4385	.0273	0.045	.4366	.0272	.4375	.0273	.4382	.0272
7.2	0.042	233.2	.4472	.0107	0.045	.4448	.0106	.4497	.0107	.4452	.0106
8.4	0.043	255.1	.4277	.0114	0.045	.4259	.0114	.4337	.0116	.4264	.0114
9.3	0.046	257.9	.4230	.0106	0.045	.4240	.0106	.4339	.0109	.4240	.0106
10.4	0.044	274.3	.4306	.0104	0.045	.4293	.0104	.4420	.0107	.4289	.0104
11.3	0.046	284.7	.4366	.0105	0.045	.4385	.0105	.4538	.0109	.4376	.0105
12.2	0.048	277.6	.4316	.0114	0.045	.4365	.0115	.4540	.0120	.4351	.0111
13.4	0.049	308.9	.4531	.0111	0.045	.4603	.0113	.4820	.0118	.4575	.0113
14.3	0.055	285.8	.4367	.0145	0.045	.4543	.0151	.4783	.0159	.4514	.0151
15.2	0.055	303.7	.4503	.0132	0.045	.4695	.0138	.4969	.0146	.4657	.0138
16.1	0.052	332.1	.4413	.0154	0.045	.4555	.0159	.4850	.0169	.4512	.0159
17.1	0.056	325.2	.4390	.0175	0.045	.4611	.0184	.4944	.0198	.4563	.0179
18.3	0.057	342.2	.3931	.0189	0.045	.4153	.0200	.4491	.0216	.4105	.0195
19.3	0.057	336.2	.4144	.0227	0.045	.4393	.0241	.4789	.0262	.4339	.0241
20.4	0.058	363.2	.4482	.0310	0.045	.4794	.0332	.5275	.0365	.4724	.0326
II) $0.06 < x < 0.10$											
7.7	0.076	118.1	.3874	.0146	0.080	.3838	.0145	.3849	.0145	.3857	.0145
8.6	0.078	128.2	.3925	.0135	0.080	.3906	.0134	.3921	.0135	.3926	.0134
9.5	0.077	136.9	.3798	.0116	0.080	.3768	.0115	.3788	.0116	.3788	.0115
10.5	0.079	143.9	.3839	.0128	0.080	.3827	.0128	.3855	.0129	.3843	.0128
11.5	0.077	154.4	.3724	.0114	0.080	.3695	.0113	.3731	.0114	.3704	.0113
12.4	0.078	164.8	.3862	.0122	0.080	.3846	.0121	.3895	.0123	.3855	.0121
13.3	0.074	186.3	.4086	.0112	0.080	.4011	.0110	.4074	.0112	.4007	.0110
14.3	0.075	194.8	.3987	.0121	0.080	.3922	.0119	.3999	.0121	.3914	.0119
15.4	0.077	203.4	.4188	.0120	0.080	.4141	.0119	.4240	.0122	.4130	.0119
16.5	0.073	239.9	.4184	.0118	0.080	.4078	.0115	.4197	.0118	.4054	.0111

Table C-2. (continued)

Q ²	x	W ²	Plotted		Shifted Values		N=1.019				
			F ₂	σ(F ₂)	F ₂	σ(F ₂)					
17.5	0.077	236.2	.4235	.0121	0.080	.4188	.0120	.4159	.0120		
18.4	0.079	238.9	.4195	.0121	0.080	.4176	.0120	.4143	.0120		
19.3	0.078	249.9	.4269	.0138	0.080	.4233	.0137	.4196	.0133		
20.3	0.075	280.3	.4185	.0132	0.080	.4092	.0129	.4046	.0125		
21.4	0.079	273.4	.3905	.0126	0.080	.3890	.0126	.3848	.0126		
22.2	0.080	279.3	.4064	.0138	0.080	.4076	.0138	.4025	.0133		
23.3	0.083	279.2	.4045	.0144	0.080	.4120	.0147	.4065	.0143		
24.3	0.081	300.7	.3892	.0146	0.080	.3915	.0147	.3856	.0143		
25.4	0.084	301.8	.3769	.0160	0.080	.3849	.0163	.3787	.0159		
26.8	0.085	311.3	.3791	.0144	0.080	.3887	.0148	.3819	.0144		
29.4	0.088	319.6	.3785	.0145	0.080	.3958	.0152	.3877	.0152		
33.0	0.093	337.2	.3518	.0177	0.080	.3786	.0191	.3688	.0186		
III) 0.10 < x < 0.20											
5.6	0.147	51.3	.4086	.0961	0.150	.4059	.0955	.4060	.0955	.4089	.0961
6.6	0.145	59.5	.3558	.0224	0.150	.3519	.0222	.3519	.0222	.3545	.0222
8.0	0.148	67.7	.3171	.0104	0.150	.3157	.0104	.3159	.0104	.3183	.0104
9.5	0.150	75.3	.3148	.0119	0.150	.3144	.0119	.3148	.0119	.3166	.0119
10.4	0.150	80.0	.3069	.0132	0.150	.3066	.0132	.3072	.0132	.3089	.0132
11.5	0.147	88.6	.3090	.0107	0.150	.3060	.0106	.3069	.0106	.3083	.0106
12.4	0.143	94.2	.3154	.0117	0.150	.3097	.0115	.3108	.0115	.3115	.0115
13.4	0.144	100.0	.3175	.0097	0.150	.3118	.0095	.3133	.0095	.3137	.0095
14.4	0.143	107.1	.3255	.0094	0.150	.3186	.0092	.3205	.0093	.3204	.0092
15.4	0.142	111.6	.3191	.0097	0.150	.3114	.0095	.3135	.0096	.3130	.0095
16.4	0.143	117.7	.3194	.0097	0.150	.3130	.0095	.3156	.0096	.3145	.0095
17.2	0.142	124.4	.3246	.0097	0.150	.3166	.0095	.3197	.0096	.3179	.0095
18.3	0.143	127.9	.3317	.0103	0.150	.3243	.0101	.3279	.0102	.3258	.0101
19.3	0.136	141.1	.3336	.0102	0.150	.3184	.0097	.3225	.0098	.3194	.0097
20.3	0.145	141.1	.3265	.0099	0.150	.3208	.0097	.3255	.0098	.3218	.0097
21.2	0.139	149.4	.3358	.0113	0.150	.3233	.0109	.3287	.0111	.3240	.0113
22.4	0.146	150.1	.3263	.0104	0.150	.3218	.0103	.3277	.0105	.3223	.0103
23.3	0.131	171.2	.3699	.0130	0.150	.3448	.0121	.3518	.0124	.3442	.0121

Table C-2. (continued)

Q ²	x	W ²	F ₂	σ(F ₂)	Plotted		Shifted Values		N=1.019 F ₂	σ(F ₂)
					F ₂	σ(F ₂)	F ₂	σ(F ₂)		
24.4	0.142	165.9	.3382	.0111	.3288	.0108	.3362	.0110	.3282	.0108
25.3	0.133	181.1	.3522	.0125	.3312	.0118	.3393	.0120	.3300	.0118
26.4	0.147	173.8	.3380	.0112	.3345	.0111	.3434	.0114	.3330	.0111
27.3	0.130	199.6	.3852	.0146	.3571	.0135	.3674	.0139	.3544	.0133
28.5	0.145	188.2	.3556	.0122	.3493	.0120	.3601	.0124	.3465	.0120
29.3	0.131	212.1	.3594	.0145	.3340	.0135	.3451	.0139	.3304	.0135
30.8	0.138	213.5	.3434	.0109	.3278	.0104	.3399	.0108	.3238	.0101
32.4	0.141	218.3	.3549	.0129	.3433	.0125	.3572	.0130	.3385	.0125
33.5	0.130	240.7	.3486	.0158	.3219	.0146	.3358	.0152	.3164	.0143
34.5	0.153	211.8	.3366	.0129	.3407	.0131	.3564	.0137	.3359	.0131
36.2	0.140	242.3	.3287	.0113	.3165	.0109	.3323	.0115	.3104	.0106
38.1	0.140	255.0	.3429	.0123	.3295	.0118	.3474	.0125	.3226	.0115
40.3	0.146	253.4	.3456	.0134	.3411	.0132	.3616	.0140	.3333	.0129
42.2	0.146	267.0	.3270	.0150	.3221	.0148	.3430	.0158	.3138	.0145
44.1	0.150	267.8	.3040	.0149	.3052	.0150	.3262	.0160	.2971	.0147
46.5	0.157	265.6	.3025	.0131	.3114	.0135	.3347	.0145	.3031	.0129
49.5	0.160	275.1	.2700	.0151	.2820	.0158	.3050	.0170	.2740	.0155
52.9	0.169	273.6	.2875	.0142	.3118	.0154	.3393	.0168	.3029	.0152
57.5	0.176	279.2	.2816	.0172	.3148	.0192	.3450	.0211	.3063	.0187
61.5	0.186	282.7	.2628	.0213	.3056	.0248	.3366	.0273	.2981	.0238
66.8	0.189	297.7	.2781	.0296	.3277	.0349	.3624	.0385	.3201	.0341
IV) 0.20 < x < 0.30										
7.1	0.234	36.1	.2917	.0228	.2808	.0219	.2810	.0219	.2828	.0221
8.5	0.239	40.3	.2290	.0100	.2228	.0097	.2230	.0097	.2245	.0100
9.3	0.252	40.6	.2482	.0113	.2498	.0114	.2500	.0114	.2517	.0114
10.8	0.228	51.4	.2438	.0113	.2302	.0107	.2304	.0107	.2322	.0107
12.5	0.253	50.1	.2317	.0078	.2341	.0079	.2343	.0079	.2360	.0081
14.5	0.230	63.0	.2493	.0085	.2357	.0080	.2361	.0080	.2381	.0080
16.5	0.256	61.1	.2219	.0073	.2259	.0074	.2263	.0074	.2277	.0074
18.2	0.237	72.7	.2335	.0074	.2249	.0071	.2255	.0071	.2268	.0071
20.5	0.259	72.3	.2194	.0068	.2256	.0070	.2264	.0070	.2271	.0070

Table C-2. (continued)

Q ²	x	w ²	F ₂	σ(F ₂)	x	Plotted		Shifted Values		F ₂	σ(F ₂)	N=1.019
						F ₂	σ(F ₂)	F ₂	σ(F ₂)			
22.2	0.227	89.6	.2283	.0084	0.250	.2131	.0078	.2140	.0078	.2145	.0078	.0796
24.5	0.248	88.4	.2290	.0076	0.250	.2280	.0076	.2293	.0076	.2292	.0076	.0271
26.5	0.231	100.9	.2607	.0112	0.250	.2463	.0106	.2479	.0107	.2472	.0106	.0104
28.7	0.256	96.6	.2241	.0081	0.250	.2286	.0083	.2305	.0084	.2293	.0083	.0071
30.1	0.233	111.5	.2625	.0108	0.250	.2491	.0102	.2514	.0103	.2494	.0102	.0076
32.7	0.245	114.2	.2440	.0103	0.250	.2402	.0101	.2430	.0102	.2402	.0101	.0068
33.7	0.248	114.2	.2288	.0095	0.250	.2273	.0094	.2301	.0095	.2273	.0094	.0063
36.9	0.257	118.5	.2294	.0089	0.250	.2347	.0091	.2384	.0092	.2345	.0091	.0060
39.9	0.237	140.8	.2456	.0110	0.250	.2348	.0105	.2393	.0107	.2338	.0105	.0058
41.7	0.244	140.4	.2648	.0118	0.250	.2595	.0116	.3649	.0118	.2584	.0116	.0096
45.5	0.243	153.3	.2402	.0098	0.250	.2348	.0096	.2407	.0098	.2331	.0096	.0248
49.6	0.241	167.1	.2404	.0106	0.250	.2338	.0103	.2409	.0106	.2317	.0101	.0092
54.8	0.247	177.1	.2181	.0095	0.250	.2163	.0094	.2245	.0098	.2140	.0092	.0091
61.2	0.236	206.8	.2288	.0106	0.250	.2187	.0101	.2290	.0106	.2151	.0101	.0122
69.3	0.245	225.9	.1998	.0096	0.250	.1963	.0094	.2083	.0100	.1921	.0091	.0218
78.8	0.260	234.0	.1937	.0120	0.250	.2008	.0124	.2164	.0134	.1957	.0122	.0060
90.9	0.271	252.0	.2372	.0209	0.250	.2561	.0226	.2817	.0248	.2491	.0218	.0060
V) 0.30 < x < 0.40												
6.8	0.337	23.3	.2508	.0821	0.350	.2413	.0790	.2413	.0790	.2432	.0796	.0796
8.6	0.318	27.3	.1655	.0297	0.350	.1501	.0269	.1501	.0269	.1513	.0271	.0271
12.2	0.308	37.3	.1991	.0119	0.350	.1739	.0104	.1741	.0104	.1756	.0104	.0104
15.5	0.323	42.0	.1683	.0078	0.350	.1539	.0071	.1541	.0071	.1551	.0071	.0071
17.5	0.328	45.4	.1707	.0081	0.350	.1587	.0075	.1590	.0075	.1600	.0076	.0076
19.5	0.328	49.9	.1578	.0065	0.350	.1466	.0060	.1469	.0060	.1478	.0060	.0060
21.5	0.345	50.6	.1533	.0064	0.350	.1506	.0063	.1510	.0063	.1516	.0063	.0063
23.5	0.331	57.8	.1670	.0072	0.350	.1564	.0067	.1569	.0067	.1577	.0068	.0068
25.2	0.339	60.0	.1515	.0062	0.350	.1456	.0060	.1461	.0060	.1464	.0060	.0060
28.0	0.335	66.6	.1566	.0061	0.350	.1483	.0058	.1489	.0058	.1492	.0058	.0058
31.6	0.346	70.6	.1436	.0056	0.350	.1415	.0055	.1422	.0055	.1423	.0057	.0057
35.6	0.350	76.3	.1420	.0063	0.350	.1424	.0063	.1433	.0063	.1428	.0063	.0063
40.0	0.352	83.7	.1374	.0059	0.350	.1387	.0060	.1398	.0060	.1389	.0060	.0060

Table C-2. (continued)

Q ²	x	W ²	F ₂	σ(F ₂)	Plotted		Shifted Values		N=1.019		
					x	F ₂	σ(F ₂)	F ₂		σ(F ₂)	
44.9	0.349	93.2	.1437	.0070	0.350	.1432	.0070	.1448	.0071	.1429	.0070
50.3	0.341	106.3	.1511	.0076	0.350	.1461	.0073	.1480	.0074	.1452	.0073
55.8	0.339	117.9	.1470	.0092	0.350	.1410	.0088	.1434	.0090	.1396	.0088
60.4	0.348	122.2	.1435	.0096	0.350	.1427	.0095	.1456	.0097	.1406	.0094
66.1	0.350	131.1	.1447	.0092	0.350	.1449	.0092	.1484	.0094	.1421	.0091
74.7	0.344	150.3	.1581	.0094	0.350	.1549	.0092	.1599	.0095	.1512	.0091
86.4	0.349	169.5	.1358	.0091	0.350	.1354	.0091	.1416	.0095	.1316	.0088
104.1	0.351	199.7	.1459	.0124	0.350	.1466	.0125	.1572	.0134	.1427	.0121
VI) 0.40 < x < 0.50											
24.7	0.403	45.1	.1223	.0131	0.450	.0995	.0107	.0998	.0107	.1004	.0107
29.0	0.411	49.9	.1076	.0087	0.450	.0904	.0073	.0906	.0073	.0911	.0073
32.9	0.421	53.8	.0906	.0067	0.450	.0793	.0059	.0796	.0059	.0799	.0060
37.3	0.426	58.7	.0761	.0059	0.450	.0681	.0053	.0685	.0053	.0684	.0053
42.4	0.432	63.8	.0875	.0060	0.450	.0804	.0055	.0809	.0055	.0805	.0055
47.4	0.431	70.7	.0877	.0063	0.450	.0800	.0057	.0806	.0057	.0797	.0057
54.9	0.444	76.7	.0809	.0051	0.450	.0787	.0050	.0795	.0050	.0780	.0050
64.3	0.447	87.6	.0876	.0060	0.450	.0863	.0059	.0874	.0060	.0848	.0058
79.6	0.445	106.8	.0827	.0056	0.450	.0809	.0055	.0825	.0056	.0789	.0054
100.8	0.447	131.9	.0931	.0078	0.450	.0917	.0077	.0950	.0080	.0894	.0076
124.5	0.451	158.0	.1320	.0169	0.450	.1330	.0170	.1412	.0180	.1297	.0166
VII) 0.50 < x < 0.70											
55.0	0.512	58.9	.0320	.0074	0.550	.0254	.0059	.0255	.0059	.0252	.0059
65.5	0.521	67.0	.0508	.0081	0.550	.0424	.0068	.0429	.0069	.0417	.0067
79.7	0.537	75.3	.0317	.0045	0.550	.0293	.0042	.0296	.0042	.0286	.0041
100.3	0.544	90.8	.0486	.0055	0.550	.0467	.0053	.0478	.0054	.0457	.0051
124.4	0.542	111.7	.0749	.0120	0.550	.0712	.0114	.0739	.0119	.0697	.0112

APPENDIX D

APPENDIX D

MAGNETIC FIELD AND INCIDENT ENERGY SYSTEMATICS

This appendix contains the summary of systematic shifts induced on integrated distributions through changes in incident muon energy (E_0) or toroid magnetic fields (\bar{B}). The three cases considered are underestimating E_0 by 1%, raising the monte carlo magnetic field by 1% (\bar{B} high), and lowering the monte carlo magnetic field by 1% (\bar{B} low). The actual point by point ratios for all three situations are first summarised, along with the B-spline⁽⁵⁴⁾ approximation of the ratios, and then the approximation is evaluated at regular intervals to find the maximum summed shifts away from $R=1.0$ in either direction. The ratios represent how the data/monte carlo ratios would change, given the indicated change in the monte carlo. The value of the smoothing parameter, S , used in the approximation is indicated for all sets of ratios. In situations where both \bar{B} high and \bar{B} low deviate in the same direction from 1.0, only the worst case (largest deviation) is summed.

Values in parentheses are continuations of the curves beyond the available data, or result from the use of such.

Table D-1. E' Comparison

A. E ₀ Higher 1% (S=31.58)			
E' (GeV)	Ratio	Error	Spline Approximation
30.12	.948	.041	.967
50.37	1.101	.038	1.033
67.57	.973	.033	1.033
82.57	1.035	.034	1.032
97.56	1.050	.033	1.037
112.50	1.094	.035	1.040
127.50	.973	.029	1.039
142.50	1.067	.033	1.032
157.40	1.063	.034	1.011
170.10	1.027	.040	1.009
180.00	.913	.035	1.003
190.00	1.011	.040	1.004
200.10	1.022	.042	1.008
209.90	1.084	.048	1.010
219.90	1.046	.049	1.002
229.70	.888	.046	.979
242.60	.961	.058	.920
B. Magnetic Field Higher 1% (S=35.80)			
32.88	1.048	.040	1.061
55.24	1.099	.037	1.046
72.51	.983	.032	1.035
87.60	1.027	.033	1.026
102.50	1.074	.034	1.017
117.60	.952	.029	1.009
132.60	1.041	.032	1.000
147.60	.985	.030	.986
162.60	1.013	.031	.967
175.00	.868	.032	.947
185.00	.997	.039	.934
195.00	.936	.037	.931
205.00	.860	.035	.943
217.60	1.081	.041	.983
232.10	1.029	.047	1.029
245.80	.960	.089	1.029

Table D-1. (continued)

E' (GeV)	Ratio	Error	Spline Approximation
C. Magnetic Field Lower 1% (S=25.75)			
30.02	.932	.040	.927
47.68	.914	.036	.944
62.66	1.037	.037	.963
77.59	.928	.030	.978
92.48	1.040	.034	1.002
107.60	.968	.030	1.020
122.50	1.088	.034	1.028
137.60	1.050	.033	1.027
152.50	1.010	.031	1.019
165.00	.939	.035	1.011
177.50	1.028	.032	1.003
190.00	.998	.040	.994
200.10	1.051	.044	.971
210.00	.881	.038	.929
219.90	.913	.043	.901
229.80	.906	.049	.929
242.40	1.148	.077	1.115

D. Individual and Summed Maximum Contributions

E' (GeV)	E ₀ High	B̄ High	B̄ Low	Maximum	
				Below	Above
				1.00(%)	
30.00	.97	1.06	.93	10	6
35.00	.99	1.06	.93	8	6
40.00	1.01	1.06	.93	7	7
45.00	1.03	1.05	.94	6	8
50.00	1.03	1.05	.95	5	8
55.00	1.04	1.05	.95	5	9
60.00	1.03	1.04	.96	4	7
65.00	1.03	1.04	.97	3	7
70.00	1.03	1.04	.97	3	7
75.00	1.03	1.03	.97	3	7
80.00	1.03	1.03	.98	2	6
85.00	1.03	1.03	.99	1	6
90.00	1.03	1.02	1.00	-	5
95.00	1.04	1.02	1.01	-	6
100.00	1.04	1.02	1.01	-	6
105.00	1.04	1.02	1.02	-	6
110.00	1.04	1.01	1.02	-	6

Table D-1. (continued)

E' (GeV)	E ₀ High	\bar{B} High	\bar{B} Low	Maximum Below Above 1.00(%)	
115.00	1.04	1.01	1.03	-	7
120.00	1.04	1.01	1.03	-	7
125.00	1.04	1.00	1.03	-	7
130.00	1.04	1.00	1.03	-	7
135.00	1.04	1.00	1.03	-	7
140.00	1.03	.99	1.03	1	6
145.00	1.03	.99	1.02	1	5
150.00	1.03	.98	1.02	2	5
155.00	1.02	.98	1.02	2	4
160.00	1.02	.97	1.01	3	3
165.00	1.01	.96	1.01	4	2
170.00	1.01	.95	1.01	5	2
175.00	1.01	.95	1.00	5	1
180.00	1.00	.94	1.00	6	-
185.00	1.00	.93	1.00	7	-
190.00	1.00	.93	.99	7	-
195.00	1.01	.93	.99	7	1
200.00	1.01	.93	.97	7	1
205.00	1.01	.94	.95	6	1
210.00	1.01	.96	.93	7	1
215.00	1.01	.97	.91	9	1
220.00	1.00	.99	.90	10	-
225.00	.99	1.01	.91	10	1
230.00	.98	1.02	.93	9	2
235.00	.96	1.03	.98	6	3
240.00	.93	1.04	1.06	7	6
245.00	(.93)	1.03	(1.06)	(7)	(6)

Table D-2. Theta Comparison

A. E_0 Higher 1% (S=19.35)

θ (mrad)	Ratio	Error	Spline Approximation
10.62	.960	.104	.950
13.00	.926	.062	.997
15.00	1.003	.048	1.021
17.00	1.061	.042	1.032
19.00	1.143	.040	1.035
21.00	.980	.031	1.032
23.00	1.030	.033	1.026
25.00	1.007	.033	1.018
27.89	1.033	.026	1.009
31.91	.949	.027	1.005
36.77	1.061	.028	1.022
51.41	1.054	.019	1.055

B. Magnetic Field Higher 1% (S=18.10)

10.62	1.041	.122	.956
13.00	.925	.064	.971
15.00	.972	.046	.982
17.00	1.005	.038	.992
19.00	1.006	.034	1.000
21.00	.999	.032	1.007
23.00	1.061	.034	1.013
25.00	.953	.030	1.017
27.90	1.057	.027	1.021
31.90	1.017	.028	1.023
36.75	1.009	.026	1.021
45.09	1.014	.024	1.008
62.47	.968	.027	.968

C. Magnetic Field Lower 1% (S=18.10)

10.69	.985	.105	.961
13.00	.951	.064	.973
15.00	.986	.047	.982
17.00	.962	.036	.989

Table D-2. (continued)

θ (mrad)	Ratio	Error	Spline Approximation
19.00	.981	.033	.995
21.00	1.067	.035	1.000
23.00	.984	.031	1.004
25.00	1.032	.035	1.006
27.90	1.029	.026	1.008
31.89	.969	.027	1.007
36.77	.988	.026	1.002
45.06	1.002	.024	.986
62.39	.938	.027	.940

D. Individual and Summed Maximum Contributions

θ (mrad)	E_0 High	\bar{B} High	\bar{B} Low	Maximum	
				Below 1.00(%)	Above
10.00	.93	.95	.96	12	-
12.00	.98	.96	.97	6	-
14.00	1.01	.98	.98	2	1
16.00	1.03	.99	.99	1	3
18.00	1.03	1.00	.99	1	3
20.00	1.03	1.00	1.00	-	3
22.00	1.03	1.01	1.00	-	4
24.00	1.02	1.02	1.01	-	4
26.00	1.01	1.02	1.01	-	3
28.00	1.01	1.02	1.01	-	3
30.00	1.00	1.02	1.01	-	2
32.00	1.01	1.02	1.01	-	3
34.00	1.01	1.02	1.01	-	3
36.00	1.02	1.02	1.00	-	4
38.00	1.03	1.02	1.00	-	5
40.00	1.04	1.02	1.00	-	6
42.00	1.05	1.01	.99	1	6
44.00	1.06	1.01	.99	1	7
46.00	1.07	1.01	.98	2	8
48.00	1.07	1.00	.98	2	7
50.00	1.06	1.00	.97	3	6
52.00	(1.06)	.99	.97	3	(6)
54.00	(1.06)	.99	.96	4	(6)
56.00	(1.06)	.98	.96	4	(6)
58.00	(1.06)	.98	.95	5	(6)
60.00	(1.06)	.97	.95	5	(6)
62.00	(1.06)	.97	.94	6	(6)

Table D-3. Q^2 ComparisonA. E_0 Higher 1% (S=10.45)

Q^2 (GeV/c) ²	Ratio	Error	Spline Approximation
4.42	.964	.074	.975
7.00	.967	.053	.998
9.00	1.059	.049	1.011
11.00	.954	.037	1.022
13.00	1.061	.042	1.029
15.00	1.073	.042	1.033
17.00	1.091	.043	1.036
19.00	1.062	.043	1.037
21.89	1.024	.031	1.035
25.91	1.003	.032	1.028
30.77	.987	.029	1.017
39.82	1.010	.024	.993
64.67	.992	.018	.992

B. Magnetic Field Higher 1% (S=23.20)

4.46	1.106	.088	.980
7.00	.925	.051	.988
9.00	.964	.043	.992
11.00	1.098	.044	.996
13.00	.989	.038	.998
15.00	.930	.034	.999
17.00	1.055	.042	.999
19.00	.955	.037	.998
21.89	1.046	.031	.996
25.91	.973	.031	.991
30.77	.992	.029	.984
39.07	.968	.024	.973
62.50	1.022	.018	1.022

C. Magnetic Field Lower 1% (S=16.90)

4.42	.979	.074	.941
7.00	.960	.050	.959
9.00	.965	.043	.971
11.00	.938	.036	.981
13.00	.998	.039	.990

Table D-3.(continued)

Q^2 (GeV/c) ²	Ratio	Error	Spline Approximation
15.00	1.075	.042	.997
17.00	1.015	.040	1.003
19.00	.948	.037	1.007
21.89	1.024	.031	1.012
25.91	1.022	.033	1.015
31.58	1.011	.026	1.015
51.81	1.012	.015	1.012

D. Individual and Summed Maximum Contributions

Q^2 (GeV/c) ²	E_o High	\bar{B} High	\bar{B} Low	Maximum	
				Above 1.00	Below (%)
4.00	.97	.98	.94	9	-
6.00	.99	.98	.95	6	-
8.00	1.01	.99	.97	3	1
10.00	1.02	.99	.98	2	2
12.00	1.03	1.00	.99	1	3
14.00	1.03	1.00	.99	1	3
16.00	1.03	1.00	1.00	-	3
18.00	1.04	1.00	1.01	-	5
20.00	1.04	1.00	1.01	-	5
22.00	1.03	1.00	1.01	-	4
24.00	1.03	.99	1.01	1	4
26.00	1.03	.99	1.01	1	4
28.00	1.02	.99	1.02	1	4
30.00	1.02	.98	1.02	2	4
32.00	1.01	.98	1.01	2	2
34.00	1.01	.98	1.01	2	2
36.00	1.00	.98	1.01	2	1
38.00	1.00	.97	1.01	3	1
40.00	.99	.97	1.01	4	1
42.00	.99	.97	1.01	4	1
44.00	.98	.97	1.01	5	1
46.00	.98	.97	1.01	5	1
48.00	.98	.97	1.01	5	1
50.00	.97	.97	1.01	6	1
52.00	.97	.98	(1.01)	5	(1)
54.00	.97	.98	(1.01)	5	(1)
56.00	.97	.99	(1.01)	4	(1)
58.00	.97	1.00	(1.01)	3	(1)
60.00	.98	1.01	(1.01)	2	(1)
62.00	.98	1.02	(1.01)	2	(2)
64.00	.99	(1.02)	(1.01)	1	(2)

Table D-4. x Comparison

A. E_0 Higher 1% (S=29.15)

x	Ratio	Error	Spline Approximation
.01	.850	.061	.927
.03	1.048	.031	1.002
.05	1.000	.027	1.005
.07	.948	.028	.989
.09	1.091	.036	.999
.11	.973	.035	1.028
.13	.984	.038	1.055
.16	1.185	.038	1.067
.20	1.005	.035	1.039
.25	.986	.032	.990
.32	.977	.033	.974
.48	1.120	.022	1.120

B. Magnetic Field Higher 1% (S=57.90)

.03	1.044	.029	1.027
.05	1.009	.027	1.002
.07	.979	.029	.988
.09	.910	.029	.980
.11	.933	.033	.974
.13	1.037	.041	.970
.16	1.140	.035	.964
.20	.946	.033	.960
.24	.834	.032	.965
.30	1.065	.035	.991
.47	1.023	.019	1.024

Table D-4. (continued)

x	Ratio	Error	Spline Approximation
C. Magnetic Field Lower 1% (S=21.80)			
.01	.834	.058	.904
.03	.997	.029	.969
.05	1.005	.027	1.005
.07	1.027	.030	1.019
.09	.962	.031	1.017
.11	1.052	.038	1.005
.14	.991	.028	.977
.18	.975	.033	.945
.22	.844	.031	.935
.28	1.038	.032	.968
.38	1.015	.030	1.029
.57	1.124	.027	1.123

D. Individual and Summed Maximum Contributions

x	E ₀ High	B̄ High	B̄ Low	Maximum Below Above 1.00(%)	
.01	.93	1.05	.90	17	5
.02	.98	1.03	.94	8	3
.03	1.00	1.02	.97	3	2
.04	1.01	1.01	.99	1	2
.05	1.00	1.00	1.01	-	1
.06	1.00	.99	1.01	1	1
.07	.99	.99	1.02	2	2
.08	.99	.98	1.02	3	2
.09	1.00	.98	1.02	2	2
.10	1.01	.98	1.01	2	2
.11	1.03	.97	1.00	3	3
.12	1.04	.97	1.00	3	4
.13	1.06	.97	.99	3	6
.14	1.06	.97	.98	3	6
.15	1.07	.97	.97	4	7
.16	1.07	.96	.96	4	7
.17	1.06	.96	.95	5	6
.18	1.06	.96	.94	6	6
.19	1.05	.96	.94	6	5
.20	1.04	.96	.94	6	4
.21	1.03	.96	.93	7	3
.22	1.02	.96	.94	6	2

Table D-4. (continued)

x	E _o High	\bar{B} High	\bar{B} Low	Maximum Below Above 1.00(%)	
.23	1.01	.96	.94	6	±
.24	1.00	.97	.94	6	-
.25	.99	.97	.95	6	-
.26	.98	.97	.96	6	-
.27	.98	.98	.96	6	-
.28	.97	.98	.97	6	-
.29	.97	.99	.98	5	-
.30	.97	.99	.98	5	-
.31	.97	1.00	.99	4	-
.32	.98	1.01	1.00	2	1
.33	.98	1.01	1.00	2	1
.34	.98	1.02	1.01	2	2
.35	.99	1.02	1.01	1	2
.36	1.00	1.03	1.02	-	3
.37	1.01	1.03	1.02	-	4
.38	1.01	1.03	1.03	-	4
.39	1.02	1.04	1.03	-	6
.40	1.03	1.04	1.04	-	7
.41	1.04	1.04	1.04	-	8
.42	1.05	1.04	1.05	-	10
.43	1.06	1.04	1.05	-	11
.44	1.08	1.04	1.06	-	14
.45	1.09	1.03	1.06	-	15
.46	1.10	1.03	1.07	-	17
.47	1.11	(1.03)	1.07	-	(18)
.48	(1.11)	(1.03)	1.08	-	(19)
.49	(1.11)	(1.03)	1.08	-	(19)
.50	(1.11)	(1.03)	1.09	-	(20)
.51	(1.11)	(1.03)	1.09	-	(20)
.52	(1.11)	(1.03)	1.10	-	(21)
.53	(1.11)	(1.03)	1.10	-	(21)
.54	(1.11)	(1.03)	1.11	-	(22)
.55	(1.11)	(1.03)	1.11	-	(22)
.56	(1.11)	(1.03)	1.12	-	(23)

Table D-5. W^2 ComparisonA. E_0 Higher by 1% (S=24.00)

W^2 (GeV) ²	Ratio	Error	Spline Approximation
15.33	1.031	.039	1.083
35.29	1.188	.046	1.063
54.83	1.077	.042	1.035
72.45	.924	.041	1.009
89.97	.970	.035	.987
110.00	.993	.038	.974
129.80	.990	.038	.978
149.80	.968	.039	.994
169.90	.995	.038	1.015
192.50	1.070	.038	1.034
217.40	1.084	.038	1.041
242.40	.994	.035	1.036
267.40	1.054	.037	1.028
292.40	1.007	.038	1.022
319.70	1.023	.035	1.023
349.70	.979	.036	1.017
383.90	1.038	.040	.974
420.90	.816	.049	.846

B. Magnetic Field Higher 1% (S=24.00)

15.35	.985	.036	1.013
35.14	1.088	.042	1.013
52.38	.987	.043	1.000
67.33	.938	.041	.984
85.01	1.037	.040	.965
104.90	.899	.034	.949
125.10	.978	.037	.946
145.00	.896	.033	.952
164.90	.983	.037	.965
187.50	1.062	.037	.981
210.00	.955	.037	.995
232.50	.987	.034	1.006
257.50	1.032	.037	1.015
282.50	1.038	.037	1.021
310.00	1.019	.034	1.024

Table D-5. (continued)

W^2 (GeV) ²	Ratio	Error	Spline Approximation
339.90	.989	.037	1.028
372.00	1.083	.043	1.034
410.50	1.035	.051	1.052

C. Magnetic Field Lower 1% (S=30.00)

18.59	.981	.033	.978
37.51	.994	.044	1.021
52.47	.984	.044	.965
67.30	.967	.043	.912
82.44	.835	.036	.918
99.95	1.057	.041	.960
120.00	.929	.035	.988
142.60	1.079	.037	1.000
164.80	.983	.038	1.016
184.90	.964	.036	1.030
207.50	1.098	.039	1.036
232.40	1.026	.037	1.033
257.50	1.066	.039	1.024
282.50	1.000	.036	1.011
307.40	.978	.036	1.000
334.80	.965	.035	.986
367.10	1.000	.037	.963
408.20	.904	.039	.914

D. Individual and Summed Maximum Contributions

W^2 (GeV) ²	E_0 High	\bar{B} High	\bar{B} Low	Maximum Below Above 1.00(%)	
15.00	1.08	1.01	.94	6	9
20.00	1.08	1.01	.99	1	9
25.00	1.07	1.02	1.02	-	9
30.00	1.07	1.01	1.03	-	10
35.00	1.06	1.01	1.03	-	9
40.00	1.06	1.01	1.01	-	7
45.00	1.05	1.01	1.00	-	6
50.00	1.04	1.00	.98	2	4
55.00	1.04	1.00	.95	5	4
60.00	1.03	.99	.93	7	3
65.00	1.02	.99	.92	8	2
70.00	1.01	.98	.91	9	1
75.00	1.01	.98	.91	9	1
80.00	1.00	.97	.91	9	0

Table D-5. (continued)

W^2 (GeV) ²	E_0 High	\hat{B} High	\hat{B} Low	Maximum Below Above 1.00(%)	
85.00	.99	.97	.92	9	-
90.00	.99	.96	.94	7	-
95.00	.98	.96	.95	7	-
100.00	.98	.95	.96	7	-
105.00	.98	.95	.97	7	-
110.00	.97	.95	.98	8	-
115.00	.97	.95	.98	8	-
120.00	.97	.95	.99	8	-
125.00	.98	.95	.99	7	-
130.00	.98	.95	.99	7	-
135.00	.98	.95	1.00	7	-
140.00	.99	.95	1.00	6	-
145.00	.99	.95	1.00	6	-
150.00	.99	.95	1.00	6	-
155.00	1.00	.96	1.01	4	1
160.00	1.00	.96	1.01	4	1
165.00	1.01	.96	1.02	4	3
170.00	1.02	.97	1.02	3	4
175.00	1.02	.97	1.02	3	4
180.00	1.02	.98	1.03	2	5
185.00	1.03	.98	1.03	2	6
190.00	1.03	.98	1.03	2	6
195.00	1.04	.99	1.03	1	7
200.00	1.04	.99	1.04	1	8
205.00	1.04	.99	1.04	1	8
210.00	1.04	1.00	1.04	-	8
215.00	1.04	1.00	1.04	-	8
220.00	1.04	1.00	1.04	-	8
225.00	1.04	1.00	1.04	-	8
230.00	1.04	1.01	1.03	-	7
235.00	1.04	1.01	1.03	-	7
240.00	1.04	1.01	1.03	-	7
245.00	1.04	1.01	1.03	-	7
250.00	1.03	1.01	1.03	-	6
255.00	1.03	1.01	1.02	-	5
260.00	1.03	1.02	1.02	-	5
265.00	1.03	1.02	1.02	-	5
270.00	1.03	1.02	1.02	-	5
275.00	1.03	1.02	1.02	-	5
280.00	1.02	1.02	1.01	-	4

Table D-5. (continued)

W^2 (GeV) ²	E_0 High	\bar{B} High	\bar{B} Low	Maximum Below Above 1.00(%)	
285.00	1.02	1.02	1.01	-	4
290.00	1.02	1.02	1.01	-	4
295.00	1.02	1.02	1.01	-	4
300.00	1.02	1.02	1.00	-	4
305.00	1.02	1.02	1.00	-	4
310.00	1.02	1.02	1.00	-	4
315.00	1.02	1.02	1.00	-	4
320.00	1.02	1.03	.99	1	5
325.00	1.02	1.03	.99	1	5
330.00	1.02	1.03	.99	1	5
335.00	1.02	1.03	.99	1	5
340.00	1.02	1.03	.98	2	5
345.00	1.02	1.03	.98	2	5
350.00	1.02	1.03	.98	2	5
355.00	1.01	1.03	.97	3	4
360.00	1.01	1.03	.97	3	4
365.00	1.00	1.03	.96	4	3
370.00	1.00	1.03	.96	4	3
375.00	.99	1.03	.96	5	3
380.00	.98	1.04	.95	7	4
385.00	.97	1.04	.94	9	4
390.00	.96	1.04	.94	10	4
395.00	.95	1.04	.93	12	4
400.00	.93	1.05	.93	14	5
405.00	.91	1.05	.92	17	5
410.00	.90	1.05	(.92)	(18)	5
415.00	.87	(1.05)	(.92)	(21)	(5)
420.00	.85	(1.05)	(.92)	(23)	(5)

APPENDIX E

APPENDIX E

THE TOROID MAGNETIC FIELD

A short summary of the toroid magnetic field is presented here, as excerpted from the Ph.D. thesis⁽²⁸⁾ of Steve Herb. Each toroid magnet consists of four toroids flame cut from ~7 5/8" thick, hot-rolled, low carbon, steel plate, bound together by tack welds and welded straps. The coils are #8 PVC insulated wire, about 460 turns spaced uniformly about the circumference.

B(H) was measured for a smaller toroid cut from the same material. From this measurement, B(R) for the full toroids was predicted with the aid of the relation

$$H = \frac{1250}{R(\text{in})} \cdot \frac{I(\text{A})}{35} \quad (\text{E-1})$$

Next, B(R) was measured by monitoring flux changes through coils wound through 1/4" holes drilled at different positions in one of the four toroidal pieces of the larger magnet. The effect of the holes on the measurement was measured to be less than 0.1%, and the results of the measurement agreed with the predictions from the small toroid to within 1%.

Finally, the total flux in each magnet was measured using a single coil wound around the entire magnet. These measurements were uniform to within $\pm 1\%$. They were repeated for this experiment with the same resultant uniformity (Table E-1).

The previous experiments test measurements with 33A current are shown in Figure E-1, and are 0.9% lower than measurements at 35A, independent of the radius. The measurements were performed in a "standard" situation with two magnets connected in series. With four magnets, the measured field was 1.0% to 1.5% lower. The single loop, total flux measurements for this experiment were an average 1.3% lower than those from the previous measurements, so that the values measured with all eight magnets powered are predicted to be 1.4% to 1.9% lower than the curve of Figure E-1. Calculations using the coefficients of Table II-7 yield results which are 1.0% to 1.4% lower than the curve predictions, values within the measured range of uniformity.

The conclusion, based on the single loop flux measurements and the agreement between the small toroid predictions and the flux loop radial measurements, is that the polynomial in R (Table II-7) accurately predicts $B(R)$, subject to a $\pm 1\%$ systematic uncertainty.

Table E-1. Integral Field Measurements in Spectrometer Toroidal Magnets

Magnet	\bar{B} in E26 at 35A (kG)	\bar{B} in E319 at 36.6A (M even) and 34.5A (M odd) (kG)
1	17.4	17.10
2	17.3	17.20
3	17.4	17.08
4	17.4	17.27
5	17.3	17.10
6	17.4	17.25
7	17.6	17.08
8	17.5	17.35

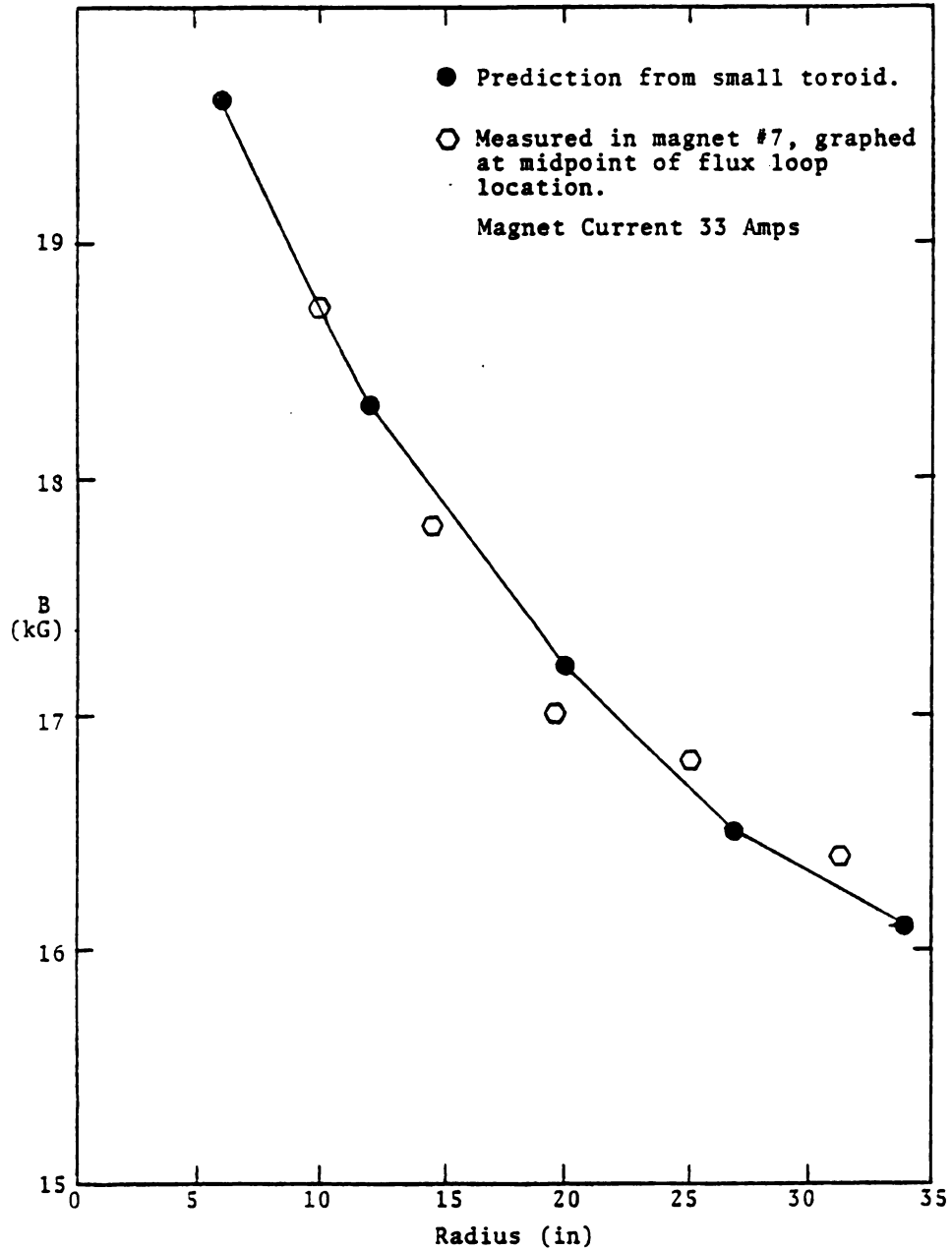


Figure E-1. B(R) in Spectrometer Toroidal Magnets

REFERENCES

1. M. Breidenbach et al., Physical Review Letters 23 (1969) 935.
2. R. P. Feynman, Photon-Hadron Interactions, Benjamin, New York, N.Y., 1972.
J. D. Bjorken, Physical Review 179 (1969) 1547.
3. D. H. Perkins, Introduction to High Energy Physics, Addison-Wesley, Reading, Mass., 1972.
4. Barger and Phillips, Nuclear Physics B 73 (1974) 269.
5. C. Chang et al., Physical Review Letters 35 (1975) 901.
Y. Watanabe et al., ibid., 898.
6. D. Fox et al., Physical Review Letters 33 (1974) 1504.
7. H. Anderson et al., Physical Review Letters 37 (1976) 4.
8. E.g. G. Sterman and S. Weinberg, Physical Review Letters 39 (1977) 1436.
9. A. J. Buras and K. J. Gaemers, Nuclear Physics B 132 (1978) 249.
10. R. E. Taylor, Proceedings of the XIX International Conference on High Energy Physics, Tokyo, August, 1978.
11. E. D. Bloom et al., Physical Review Letters 23 (1969) 930.
12. H. L. Anderson et al., FERMILAB-Pub-79/30, submitted to Physical Review D.
13. J. Friedman and H. Kendall, Annual Review of Nuclear Science 22 (1972) 203.
14. E. D. Bloom and F. J. Gilman, Physical Review Letters 25 (1970) 1140.

15. A. Bodek, Ph.D. thesis, Massachusetts Institute of Technology, 1968.
16. M. S. Chanowitz and S. D. Drell, Physical Review D 9 (1974) 2078.
17. Fermilab Experiment 319 Proposal, 1974.
18. S. Stein et al., Physical Review D 12 (1975) 1884.
19. Gross and Wilczek, Physical Review Letters 30 (1973) 1343.
20. D. Bailen, Weak Interactions, Sussex University Press, 1977.
21. Bardeen, Fritzsche, and Gell-Mann, CERN Report No. CERN-TH-1538, 1972.
22. A. J. Buras, Nuclear Physics B 125 (1977) 125.
23. H. Anderson et al., Physical Review Letters 38 (1977) 1450.
24. E. M. Riordan et al., SLAC-PUB-1634, 1975.
25. Y. Watanabe, Ph.D. thesis, Cornell University, 1975.
26. C. Chang, Ph.D. thesis, Michigan State University, 1975.
27. P. Schewe, Ph.D. thesis, Michigan State University, 1978.
28. S. Herb, Ph.D. thesis, Cornell University, 1975.
29. D. Bauer, Ph.D. thesis, Michigan State University, 1979.
30. J. Kiley, Ph.D. thesis, Michigan State University, 1979.
31. S. Loken, DROS-11, A Disk Based Real-Time Operating System for the PDP-11, 1973 (unpublished).
32. Review of Particle Properties, Physics Letters 75B No. 1, April, 1978.
33. J. D. Jackson, Classical Electrodynamics, Wiley and Sons, New York, N.Y., 1975.
34. D. Bauer, EXP 319 internal memo, March, 1979.
35. B. Rossi, High Energy Particles, Prentice-Hall Inc., Englewood Cliffs, N.J., 1965.

36. L.C.L. Yuan and C. Wu, Methods of Experimental Physics 5A, Academic Press, New York, N.Y. (1961).
37. Joseph, NIM 75 (1969) 13.
38. Tsai, Review of Modern Physics 46 (1974) 815.
39. Tannenbaum, FNAL Summer Study, 1970.
40. Drees, preprint, Dept. of Physics, U. of Wuppertal, Germany, April, 1978.
41. Mo and Tsai, Review of Modern Physics 41 (1969) 205.
42. Tsai, SLAC publication 848, January, 1971.
43. A. Kotlewski, FNAL Exp. 26 internal memo, February, 1975.
44. Y. Watanabe, FNAL Exp. 26 internal memo, July, 1974.
45. M. Strovink, FNAL Exp. 26 internal memo, July, 1974.
46. P. Dierckx, Journal of Computational and Applied Mathematics 3 (1977) 113.
47. A. Van Ginneken, Fermi National Accelerator Lab., personal communication.
48. International Mathematical and Statistical Library, Houston, Texas, 1977.
49. Abramowitz and Stegun, Handbook of Mathematical Functions, Dover Publications Inc., New York, N.Y., 1970.
50. J. L. Dye and V. A. Nicely, "KINFIT4, A General Non-Linear Curvefitting Program," Chemistry Dept., Michigan State University, 1977.
51. R. Marshall, "Final States in Electroproduction and Photoproduction at Low and Medium Energies," Proceedings of 1977 International Symposium on Lepton and Photon Interactions at High Energies, Hamburg, 1977.
52. J.G.H. de Groot et al., preprint submitted to Physics Letters B, 1979.
53. A. J. Buras et al., Nuclear Physics B 131 (1977) 308.

54. P. Dierckx, Journal of Computational and Applied Mathematics 1 (1975) 165.
- P. Dierckx and R. Piessens, Katholieke Universiteit Leuven, Belgium, Applied Mathematics and Programming Division, Report TW 32, June, 1977.
55. Ball et al., Physical Review Letters 42 (1979) 866.